Aluminum-Air Batteries Across Scales: A Multiscale Framework for Electrochemical Characterization, Materials Optimization, and Electric Vehicle Integration

by
Yasmin Shabeer

A thesis
presented to the University of Waterloo
in fulfilment of the
thesis requirement for the degree of
Doctor of Philosophy
in
Chemical Engineering

Waterloo, Ontario, Canada, 2026
© Yasmin Shabeer 2026

Examining Committee Membership

The following served on the Examining Committee for this thesis. The Committee's decisions are made by majority vote.

External Examiner:	Dr. Gisele Azimi Professor, Department of Chemical Engineering and Applied Chemistry, University of Toronto
Supervisor	Dr. Michael Fowler Professor, Department of Chemical Engineering, University of Waterloo
Co-Supervisor	Dr. Satyam Panchal Adjunct Assistant Professor, Department of Chemical Engineering, University of Waterloo
Internal Member	Dr. Aiping Yu Professor, Department of Chemical Engineering, University of Waterloo
Internal-External Member	Dr. Xiaoyu Wu Assistant Professor, Department of Mechanical and Mechatronics Engineering, University of Waterloo

Author's Declaration

This thesis consists of material all of which I authored or co-authored: see Statement of Contributions included in the thesis. This is a true copy of the thesis, including any required final revisions, as accepted by my examiners.

I understand that my thesis may be made electronically available to the public.

Statement of Contributions

I, Yasmin Shabeer, am the sole author of Chapters 1 and 7, which were written under the direct supervision of Dr. Michael Fowler for the sole purpose of this thesis and were not published prior to this. Chapters 2 to 6 were adapted from manuscripts published in peer-reviewed journals or currently under review, developed by the author during the doctoral program.

Chapter 2 & 3: Shabeer Y, Madani SS, Panchal S, Mousavi M, Fowler M. "Different Metal-Air Batteries as Range Extenders for the Electric Vehicle Market: A Comparative Study." Batteries 2025;11:35. https://doi.org/10.3390/BATTERIES11010035.

Chapter 4: Shabeer Y, Madani SS, Panchal S, Fowler M. "Performance optimization of high energy density aluminum-air batteries: Effects of operational parameters and electrolyte composition." Future Batteries 2025;6:100082. https://doi.org/10.1016/J.FUB.2025.100082.

Chapter 5: Shabeer Y, Madani SS, Panchal S, Fowler M. "Artificial Neural Network-Genetic Algorithm Prediction of Aluminum Anode Corrosion Kinetics in High-Concentration NaOH and KOH." Frontiers in Batteries and Electrochemistry.

Chapter 6: Shabeer Y, Madani SS, Panchal S, Fowler M. "System-Level Modeling and Integration of Al-air Batteries in Dual-Energy-Storage Electric Vehicles." World Electr. Veh. J. 2026, 17(6), 296; **https://doi.org/10.3390/wevj17060296**.

All work presented across all chapters was carried out by the author, including conceptualization of the research, design of experiments, data compilation, development and implementation of models, simulation, analysis, interpretation of results, and preparation of manuscripts.

Abstract

Aluminum-air (Al-air) batteries have emerged as a promising energy storage technology due to their exceptionally high theoretical energy density, material abundance, and potential for low-cost deployment. However, their practical implementation remains constrained by challenges related to electrochemical performance, parasitic corrosion, electrolyte management, and system-level integration. This thesis presents a comprehensive multiscale investigation of Al-air batteries, integrating techno-economic analysis, experimental characterization, data-driven modeling, and system-level simulation to evaluate their viability as advanced energy storage systems and range extenders in electric vehicles (EVs). The study begins with a techno-economic assessment of metal-air batteries in EV applications. A comparative framework is developed to evaluate the performance of Al-air systems relative to conventional lithium-ion batteries, incorporating key metrics such as gravimetric energy density, vehicle energy consumption, and cost. The analysis shows that Al-air batteries, with practical energy densities of approximately 700-900 Wh kg^{-1}, significantly outperform Li-ion systems (150-250 Wh kg^{-1}), offering strong potential for range extension. Simulated vehicle scenarios indicate that Al-air integration can extend driving range by a factor of 2-5, depending on system configuration and operating conditions. However, these benefits are offset by trade-offs related to system complexity, auxiliary components, and cost, highlighting the need for integrated evaluation frameworks. Experimental investigations are conducted to examine the electrochemical performance of Al-air batteries under varying electrolyte compositions and operating conditions. Using a novel galvanic generator-type Al-air system with a rotating electrode configuration, multiple prototype units provided by AlumaPower were evaluated. The rotating electrode design enhances mass transport, reduces passivation, and promotes uniform anodic dissolution, enabling improved discharge stability compared to conventional static systems. Systematic experiments reveal the alkaline electrolytes, particularly in the range of 6-8 M concentration, provide optimal performance by balancing ionic conductivity and electrochemical kinetics. Peak power densities exceeding 500 mW cm^{-2} are achieved under controlled conditions, while discharge tests at moderate current densities (~80-100 mA cm^{-2}) exhibit stable voltage profiles in the range of 1.0-1.2 V. The results further demonstrate that increasing electrolyte concentration beyond optimal levels accelerates parasitic corrosion and hydrogen evolution, leading to reduced efficiency and highlighting the importance of electrolyte optimization. To address the critical challenge of aluminum corrosion, a data-driven predictive

modeling framework is developed. Artificial neural networks (ANNs) are trained on experimental datasets to model the relationship between electrolyte composition, temperature, and electrochemical variables with corrosion metrics such as corrosion potential (Ecorr) and corrosion current density (Icorr). The ANN models achieve high predictive accuracy, with coefficient of determination (R^2) values exceeding 0.99, demonstrating their capability to capture complex nonlinear relationships in electrochemical systems. To further enhance system performance, genetic algorithms (GA) and multi-objective optimization (NSGA-II) are integrated with the ANN framework to identify optimal operating conditions. The optimization results reveal trade-offs between maximizing Ecorr and minimizing Icorr, enabling the identification of optimal electrolyte conditions that balance performance and degradation. This integrated modeling approach represents a significant advancement over conventional empirical methods by enabling predictive and systematic optimization of corrosion behavior. At the system level, the thesis develops a comprehensive modeling framework for integrating Al-air batteries within EV architectures. Using MATLAB and Simulink, a dual-energy storage system is implemented in which Al-air batteries function as range extenders for lithium-ion battery packs. The system incorporates experimentally informed battery models and employs state-of-charge (SOC)-based control strategies to manage power flow between energy sources. Simulations conducted under standard driving cycles, including UDDS, WLTP, and HWFET, demonstrate that Al-air integration can significantly mitigate SOC depletion and extend vehicle range, particularly in reduced-capacity Li-ion configurations (e.g., 50% and 35% baseline energy). The results highlight the importance of control strategy design, power limitations, and system configuration in achieving optimal performance. Collectively, the findings of this thesis establish a comprehensive framework linking electrochemical behavior, corrosion kinetics, and system-level performance of Al-air batteries. The integration of experimental characterization, data-driven modeling, and vehicle-level simulation provides new insights into the practical feasibility of Al-air systems and identifies key design and operational parameters governing their performance. The use of industrially relevant prototype systems further enhances the applicability of the research and bridges the gap between laboratory studies and real-world implementation. This work demonstrates that Al-air batteries, supported by optimized electrolyte conditions, predictive corrosion modeling, and intelligent system integration, represent a viable pathway for next-generation energy storage and EV range extension, while advancing both scientific understanding and practical development.

Acknowledgements

I would like to begin by expressing my deepest gratitude to my supervisor, *Michael Fowler,* for his exceptional guidance, support, and mentorship throughout the course of this research. His commitment as a supervisor consistently went above and beyond expectations, and I am especially grateful for his understanding and compassion during one of the most difficult periods of my life, when my father was critically ill. His support during that time played a crucial role in helping me regain focus and continue this work. I would also like to sincerely thank *Samantha Fowler,* whose encouragement and guidance were instrumental in helping me overcome a significant mental block and move forward with confidence. I am deeply thankful to my industrial collaborators at AlumaPower for their support and collaboration. In particular, I would like to acknowledge *Maya Mousavi* for her mentorship during the early stages of my work, where I was introduced to a completely new class of battery systems. Her guidance was invaluable in shaping my understanding and approach. I also extend my sincere thanks to *Kelly Stinson* and *Henk VandenEnde*, whose insights, encouragement, and even brief conversations left a lasting impact on me. Their depth of knowledge and perspective are truly inspiring, and I feel fortunate to have interacted with such individuals. I would also like to express my sincere appreciation to *Satyam Panchal*, who acted as a co-supervisor and mentor throughout this journey and to my postdoc *Seyed Saeed Madani,* their technical guidance, thoughtful discussions, and continued encouragement were invaluable to the progression of this work. I am grateful to my research group members, *Carlo Cunnan, Anosh Mevawalla, Mahn Kien Tran, Andre DaCosta*, *Khaja Wahab Ahmed* and most recently *Ananthu Shibu Nair*, for their support, collaboration, and the positive research environment they fostered. I would also like to extend my thanks to the co-op students who contributed significantly by assisting with experimental work, often taking on challenging tasks that enabled the progress of this research. My sincere thanks go to the administrative staff, particularly *Judy Caron*, whose consistent support and assistance made many aspects of this journey smoother. I am also grateful to my colleagues and friends, including *Arun Prabaharan, Andrew Stella, Monica Ho, Amirhossein Amirsoleymani, Abhishek Mishra, and Adhitya Legala*, among many others, for their camaraderie, encouragement, and the shared experiences that made this journey memorable. Finally, I would like to thank my friends outside of the university, across different phases of my life, whose unwavering support, understanding, and encouragement have been a constant source of strength.

Dedication

"Whatever else is unsure in this stinking dunghill of a world, a mother's love is not"

- James Joyce

This is deeply personal to me. I dedicate this thesis, with all that I am and all that I hope to become, to my mother, Ruckmanidevi R. She walked through fire so I could one day stand in the light. Her life has been a testament to courage, resilience, and a quiet, unyielding strength that I have spent my whole life trying to understand. I have never known a braver woman, and I do not believe I ever will.

Love, I have learned, does not come in a single form. But the love she has given me feels closest to the divine, steady, sacrificial, and boundless. If there is something sacred in this world, I have known it through her. For the longest time, I believed I would never love anyone the way my mother has loved me, and then, in the quiet unfolding of life, I found that I do.

Thus, naturally, I also dedicate this work to the love of my life, my eternity, Pramoth Varsan. He chose to stand beside me, not because he had to, but because he wanted to, through uncertainty, through struggle, through every season that tested us. In him, I have found a love that is patient, grounding, and enduring; a love that meets me where I am and grows with me into who I am becoming.

Between them, I have known two kinds of love, one that raised me, and one that walks with me. Everything I am, and everything within these pages, exists because of them.

With all the love in every fibre of my being,
-Yasmin

Table of Contents

Examining Committee Membership ii
Author's Declaration iii
Statement of Contributions iv
Abstract v
Acknowledgements vii
Dedication viii
List of Figures xiii
List of Tables xix
List of Abbreviations xxi
Graphical Abstract xxiii
Chapter 1 Introduction 1
1.1 Motivation 1
1.2 Research Objectives 3
1.3 Thesis Outline 5
Chapter 2 Literature Review 7
2.1 Metal-Air Batteries 15
2.1.1 Lithium-Air Batteries 24
2.1.2 Zinc-Air Batteries 32
2.1.3 Magnesium-Air Batteries 35
2.1.4 Sodium-Air and Potassium-Air Batteries 39
2.1.5 Other Metal-Air Batteries 42
2.2 Aluminum-Air Batteries: Fundamentals and Challenges 44
2.3 Corrosion Behavior of Aluminum in Alkaline Electrolytes 50
2.4 Data-Driven Modeling and Optimization in Electrochemical Systems 51
2.5 Battery and System-Level Modeling Approaches 53
2.6 Research Gaps and Thesis Positioning 55

2.7 Novelty and Contributions of the Thesis 56

Chapter 3 Techno-Economic Case Study of Metal-Air Batteries as Range Extenders in Electric Vehicles 58

3.1 Introduction 58

3.2 Methodology 59

3.3 Input Parameters and Case Definitions 65

3.4 Results and Discussion 70

3.5 Conclusions 76

3.6 Future Work 77

Chapter 4 Performance Optimization of High Energy Density Aluminum-Air Batteries: Effects of Operational Parameters and Electrolyte Composition 79

4.1 Introduction 79

4.2 Materials and Methods 85

4.2.1 Prototype-1 85

4.2.2 Prototype-2 85

4.2.3 Potentiostatic Polarization and Voltage-Current Profiles 86

4.2.4 Galvanostatic Discharge Profiles 87

4.3 Results and Discussion 88

4.3.1 Prototype-1: Impact of ACD 88

4.3.2 Prototype-1: Impact of electrolyte temperature and flowrate 91

4.3.3 Prototype-2: Effect of Electrolyte Concentration 95

4.4 Conclusion 101

Chapter 5 Artificial Neural Network-Genetic Algorithm Prediction of Aluminum Anode Corrosion Kinetics in High-Concentration NaOH and KOH 104

5.1 Introduction 104

5.2 Experimental Methods 108

5.2.1 Materials 108

5.2.2 Cell Setup 109
5.2.3 Procedure 110
5.2.4 Open-Circuit Voltage 111
5.2.5 Potentiodynamic Polarization (Tafel Analysis) 111
5.2.6 Electrochemical Impedance Spectroscopy (EIS) 112
5.2.7 X-ray Diffraction 113
5.3 Modeling Methodology 113
5.3.1 Artificial Neural Network Structure and Data 117
5.3.2 Grid-Based Hyperparameter Optimization 118
5.3.3 Data Normalization and Performance Assessment 118
5.3.4 Dataset Visualization and Input-Output Interactions 118
5.3.5 Genetic Algorithm Optimization 120
5.3.6 Multi-Objective Optimization Using NSGA-II 120
5.4 Results and Discussion 121
5.4.1 Experimental Corrosion Trends 122
5.4.2 Mechanistic Interpretation from Electrochemical Impedance 130
5.4.3 X-ray Diffraction Analysis 134
5.4.4 ANN Model Performance and Predictive Accuracy 135
5.4.5 GA and NSGA-II Optimization Outcomes 139
5.5 Conclusions 141
Chapter 6 System-Level Modeling and Integration of Al-air Batteries in Dual-Energy-Storage Electric Vehicles 143
6.1 Introduction 143
6.1.1. Motivation and limitations of Li-ion-only EVs 143
6.1.2. Rationale for metal-air batteries as secondary energy sources 144
6.1.3. Gaps in existing metal-air electric vehicle integration studies 145

6.1.4. Objective and contributions of the present work 146
6.1.5. Layout 147
6.2 System-Level Modeling Framework 147
6.2.1 Vehicle Powertrain Architecture 147
6.2.2 Traction Battery and Al-air Cell-Level Modeling 155
6.2.3 Energy Management and Control Strategy 164
6.2.4 Simulation Setup and Scenarios 169
6.2.5 Auxiliary Power Demand 175
6.3 Results and Discussions 178
6.3.1 SOC depletion behavior and Range 180
6.3.2 Battery Pack Characteristics 183
6.3.3 Impact of Al-air Integration 188
6.3.4 Aluminum-air as an Auxiliary Power Unit 201
6.3.5 Comparison with Literature Metal-Air Range Extenders 204
6.3.6 Practical Implications and Limitations 206
6.4 Conclusions 207
6.5 Future Work 208
Chapter 7 Conclusions and Future Work 209
References 212

List of Figures

Figure 2. 1: (a) Regional quarterly electric car sales (2021-2024), (b) the difference in sales-weighted average prices between traditional and electric vehicles in specific countries, before subsidies, by vehicle size (2018-2022), and (c) energy demand for electric vehicles, categorized by mode and region (2023-2035) [40]. 9

Figure 2. 2: Compilation of EV fire occurrences from January 2019 to August 2021: (a) Monthly count of EV fire incidents (b) Comparison of annual EV fire incidents and the total number of EVs sold (c) Distribution of accidents attributed to various types of Li-ion battery [41]. 11

Figure 2. 3: Comparison of the performance of several metal-air batteries, highlighting the theoretical specific energy, volumetric energy density and nominal cell voltage..... 12

Figure 2. 4: Abundance vs. cost of metal-air battery elements. Refer to the inset (a) for the earth's crustal distribution (Based on data from [60,61]) and inset (b) for a radar chart illustrating the benefits and drawbacks of various types of metal-air batteries based on research articles collected from the Web of Science between 2000 and 2023 (Adapted from [57]). 14

Figure 2. 5: Illustration of different configurations of MABs, including a conventional static battery setup (a), a cell design with electrolyte flow (b), and a novel flexible cell design (c); (d) and (e) are the representation of non-aqueous and aqueous electrolytes MABs respectively [63]; (f) and (g) depict the phase boundary diagram for both aqueous and non-aqueous electrolytes (Modified from [61]).... 16

Figure 2. 6: The metal's mass and volume define the theoretical (a) specific energy and (b) volumetric energy density of MABs, whereas the plots (c) and (d) include the discharged products [80]..... 21

Figure 2. 7: Classification of Li-air battery technologies with schematic representations. Modified from [87]. 25

Figure 2. 8: Rechargeable Zn-air battery designs: (a) Planar architecture with aqueous electrolyte, (b) Planar architecture with gel electrolyte, (c) Electrolyte flow-through design, (d) Flexible configuration (Adapted from [171]). 33

Figure 2. 9: Mg-air battery configurations: (a) Planar architecture with aqueous electrolyte [182], (b) Two-layer gel electrolyte structure [183], (c) Flexible configuration [184], (d) Hybrid electrolyte design [185]..... 36

Figure 2. 10: Graphical depiction of the operational mechanisms and cell configurations of (a) Na-air cell with organic electrolyte [189], (b) Na-air cell with hybrid electrolyte [189], (c) Planar K-O_2 cell [190], (d) K-O_2 cell with Na-K alloy anode [191]..... 40
Figure 2. 11: (a) Cell structure of a Si-air battery [204] (b) Working illustration of a Mg/Ca-O_2 battery [206]..... 43
Figure 2. 12: Al-air battery configurations: (a) Planar architecture with aqueous electrolyte [215], (b) Al-air battery stack architecture [53], (c) Electrolyte flow-through design [45], (d) Flexible configuration [216]. 45
Figure 3. 1: Comparative characteristics of various MABs and Li-ion cells. The data represents the practical value ranges at the cell level, derived from existing literature. ……71
Figure 3. 2: Vehicle cost vs. driving range and cost of additional range vs. driving range. Plots in (a,c,e) are computed from the equations R_V and $C_{V,T}$ while (b,d,f) are plotted from calculating the tangents of the curves of (a,c,e) respectively. (a,b): mini-vehicle; (c,d): mid-size vehicle; (e,f): semi-trailer truck. 74
Figure 4. 1: Comparison of metal-air batteries based on theoretical specific energy, gravimetric and volumetric energy densities, and nominal cell voltage [258] ……81
Figure 4. 2: Schematic representation of the two-electrode Aluminum-air battery..... 83
Figure 4. 3: Schematic representations of prototype-1 (a) and prototype-2 (b) with their components. 86
Figure 4. 4: The graphs above give the polarization and power density curves at a constant ACD of 3 mm with varying electrolyte flowrates and temperatures. (a), (b), (c), and (d) are the results for the runs (1), (2), (5), and (6) respectively..... 89
Figure 4. 5: A bar plot depicting the power density values for all eight combinations. 90
Figure 4. 6: The graphs above give the polarization and power density curves at a constant ACD of 10 mm with varying electrolyte flowrates and temperatures. (a), (b), (c), and (d) are the results for the combinations (3), (4), (7), and (8) respectively..... 92
Figure 4. 7: Galvanostatic discharge curves for all eight runs in Table 1 for prototype-1..... 94
Figure 4. 8: (a) Voltage vs. current density curves for KOH electrolytes at concentrations ranging from 1 M to 10 M. (b) Power density vs. current density curves for KOH electrolytes at concentrations ranging from 1 M to 10 M. (c) Voltage vs. current density curves for NaOH electrolytes at concentrations ranging from 1 M to 10 M. (d) Power density vs. current density

curves for NaOH electrolytes at concentrations ranging from 1 M to 10 M. These figures illustrate the electrochemical performance of Al-air batteries for both NaOH and KOH electrolytes across all tested concentrations. 95
Figure 4. 9: Galvanostatic discharge curves at a constant current density of 80 mA/cm^2 for electrolytes KOH (a) and NaOH (b) with varying concentrations from 1 M to 10 M over 120 minutes. 98
Figure 4. 10: Plots of energy density (a); energy and current efficiency (b) comparing KOH and NaOH electrolytes across concentrations from 1 M to 10 M. 100
Figure 5. 1: Schematic illustration of the experimental procedure and three-electrode electrochemical corrosion test configuration. ……..110
Figure 5. 2: Overview of the modelling methodology, showing data preprocessing, grid-based hyperparameter optimization, ANN training for prediction of Ecorr and Icorr, and subsequent GA and NSGA-II optimization. 117
Figure 5. 3: Pairwise scatter matrix for key electrochemical variables: concentration, Ecorr, Icorr, voltage, and log current density. The plots visualize electrolyte-dependent clustering for NaOH and KOH electrolytes, reveal nonlinear relationships among parameters, and highlight distributional characteristics that informed the ANN model design. 120
Figure 5. 4: Comprehensive electrochemical characterization of the commercial Al alloy in 1-5 M KOH, showing (a) open-circuit voltage evolution, (b) anodic and cathodic Tafel behaviours, (c) corrosion potential (Ecorr) as a function of electrolyte concentration, (d) corrosion current density (Icorr) trends, (e) estimated anode lifetime based on Icorr, (f) the relationship between Ecorr and Icorr, (g) Nyquist impedance response, (h) Bode magnitude of impedance $|Z|$ across frequency, and (i) corresponding phase-angle behaviour. 123
Figure 5. 5: Comprehensive electrochemical characterization of the commercial Al alloy in 6-10 M KOH, showing (a) open-circuit voltage evolution, (b) anodic and cathodic Tafel behaviours, (c) corrosion potential (Ecorr) as a function of electrolyte concentration, (d) corrosion current density (Icorr) trends, (e) estimated anode lifetime based on Icorr, (f) the relationship between Ecorr and Icorr, (g) Nyquist impedance response, (h) Bode magnitude of impedance $|Z|$ across frequency, and (i) corresponding phase-angle behaviour. 124
Figure 5. 6: Comprehensive electrochemical characterization of the commercial Al alloy in 1-5 M NaOH, showing (a) open-circuit voltage evolution, (b) anodic and cathodic Tafel behaviours,

(c) corrosion potential (Ecorr) as a function of electrolyte concentration, (d) corrosion current density (Icorr) trends, (e) estimated anode lifetime based on Icorr, (f) the relationship between Ecorr and Icorr, (g) Nyquist impedance response, (h) Bode magnitude of impedance $|Z|$ across frequency, and (i) corresponding phase-angle behaviour. 127
Figure 5. 7: Comprehensive electrochemical characterization of the commercial Al alloy in 6-10 M NaOH, showing (a) open-circuit voltage evolution, (b) anodic and cathodic Tafel behaviours, (c) corrosion potential (Ecorr) as a function of electrolyte concentration, (d) corrosion current density (Icorr) trends, (e) estimated anode lifetime based on Icorr, (f) the relationship between Ecorr and Icorr, (g) Nyquist impedance response, (h) Bode magnitude of impedance $|Z|$ across frequency, and (i) corresponding phase-angle behaviour. 128
Figure 5. 8: X-ray diffraction patterns of the commercial aluminum alloy before (blank) and after exposure to KOH and NaOH electrolytes over the concentration range of 1-10 M. The normalized intensity patterns (left panels) and vertically offset patterns (right panels) show dominant reflections at approximately 38.5°, 44.7°, 65.1°, and 78.2°, corresponding to the (111), (200), (220), and (311) planes of face-centered cubic aluminum. 134
Figure 5. 9: Performance of the ANN modelling and GA optimization workflow, including (a) training and validation loss evolution, (b-e) parity plots comparing predicted and experimental/normalized Icorr, and (f) convergence of the GA showing best-objective and best-Icorr trends across generations..... 137
Figure 5. 10: NSGA-II Pareto front illustrating the trade-off between corrosion potential and corrosion current density, with identification of the knee point and scalar GA optimum. 139
Figure 6. 1: Conventional electric vehicle powertrain architectures: (a) Battery electric vehicle (BEV) configuration and (b) series hybrid electric vehicle (HEV) configuration (c) series- parallel HEV (d) plug-in hybrid electric vehicle (PHEV) ……150
Figure 6. 2: High-Level Architecture of the Baseline BEV Modeling Framework..... 152
Figure 6. 3: Subsystem-level representation of the baseline BEV model, illustrating the internal powertrain, chassis, and control components implemented within the vehicle model 153
Figure 6. 4: Conceptual architecture of the dual-energy-storage electric vehicle integrating Al-air battery through a DC-DC converter for range-extender and auxiliary power operation 154
Figure 6. 5: Open circuit voltage-SOC curves of lithium iron phosphate battery at different temperatures. (Adapted from [413]) 156

Figure 6. 6: Comparison of experimental polarization data and semi-empirical robust model fit for the Al-air cell (6 M KOH, 40 °C)..... 158
Figure 6. 7: Al-air stack model (a) and the single-cell model (b) with aluminum consumption tracking 161
Figure 6. 8: Control logic and operational flowchart for the Al-air range extender integrated with the Li-ion battery system based on SOC thresholds and aluminum fuel availability..... 165
Figure 6. 9: Simulink implementation of the Al-air enable-disable control logic based on Li-ion SOC thresholds and aluminum fuel availability constraints..... 166
Figure 6. 10: Comparative performance of baseline and auxiliary electric vehicle configurations under standard driving cycles: range, SOC evolution, and energy consumption 171
Figure 6. 11: Baseline Li-ion battery pack electrical response under standard driving cycles (UDDS, WLTP, HWFET, FTP-75)..... 173
Figure 6. 12: Baseline Li-ion battery pack response under constant 3000 W auxiliary load (UDDS, HWFET, WLTP)..... 177
Figure 6. 13: Performance comparison of reduced-capacity Li-ion packs (50% and 65%) under baseline (a,b,c,g,h,i) and under constant 3000 W auxiliary load (d,e,f,j,k,l) across standard driving cycles..... 181
Figure 6. 14: Electrical response of the baseline Li-ion battery pack with 50% reduction in total energy capacity under UDDS, HWFET, AND WLTP driving cycles 183
Figure 6. 15: Electrical response of the baseline Li-ion battery pack with 65% reduction in total energy capacity under UDDS, HWFET, AND WLTP driving cycles 184
Figure 6. 16: Electrical response of the baseline Li-ion battery pack with 50% reduction in total energy capacity under constant 3000 w auxiliary load (UDDS, HWFET, WLTP)..... 185
Figure 6. 17: Electrical response of the baseline Li-ion battery pack with 65% reduction in total energy capacity under constant 3000 w auxiliary load (UDDS, HWFET, WLTP)..... 186
Figure 6. 18: Range performance, state-of-charge evolution, and net energy consumption for reduced Li-ion energy capacity configurations integrated with an Al-air range extender under UDDS, HWFET, and WLTP drive cycles..... 189
Figure 6. 19: Operational validation of SOC-window-controlled aluminum-air range extender and fuel consumption behavior..... 192

Figure 6. 20: Battery pack current, voltage, power, and power loss profiles under Al-air assisted operation with 50% reduced Li-ion energy capacity 193
Figure 6. 21: Battery pack current, voltage, power, and power loss profiles under Al-air assisted operation with 65% reduced Li-ion energy capacity 196
Figure 6. 22: Lithium-ion battery electrical response when auxiliary loads are supplied by the aluminum-air auxiliary power unit under UDDS, HWFET, and WLTP drive cycles, showing battery current, voltage, power, and power loss profiles. 202
Figure 6. 23: Vehicle range and lithium-ion battery state-of-charge evolution for the aluminum-air auxiliary power unit configuration under UDDS, HWFET, and WLTP drive cycles. 203

List of Tables

Table 2. 1: Key performance indicators and corresponding formulae for metal-air batteries 19
Table 2. 2: Theoretical parameter comparison across various metal-air batteries 23
Table 2. 3: Various metal anodes with electrolytes used in MABs: cell descriptions, electrode reactions, redox reactions, and electrochemical potentials. 27
Table 3. 1: Vehicle Parameters Used in the Study. ……65
Table 3. 2: Battery Properties for All Different MABs 66
Table 3. 3: Representative Electric Vehicle Dataset for Model Calibration (July 2024) 68
Table 4. 1: Summary of Test Conditions with Varying Operating Parameters ……87
Table 4. 2: Peak power densities and energy densities for prototype-1 91
Table 5. 1: Chemical composition of the commercial Al-Mg-Si alloy used in this study …….108
Table 5. 2: Summary of all equations used for data normalization, ANN modeling, hyperparameter optimization, GA search, and performance evaluation.....114
Table 5. 3: Comparison of corrosion potential (Ecorr) and corrosion current density (Icorr) of the commercial Al-Mg-Si alloy in KOH and NaOH electrolytes over the concentration range of 1-10 M. 129
Table 5. 4: Fitted electrochemical impedance parameters for the commercial Al alloy in KOH and NaOH electrolytes over the concentration range of 1-10 M. 130
Table 5. 5: ANN hyperparameter search results, including tuning grid and selected optimal configuration. 136
Table 5. 6: Summary of the optimized ANN model architecture and training configuration used for Ecorr and Icorr prediction. 138
Table 6. 1: Parameters for Al-air polarization curve model (6 M KOH, 40 °C, rotating anode, circulating electrolyte). ……159
Table 6. 2: Representative auxiliary power demands reported in the literature [432,433]. 175
Table 6. 3: Energy consumption and achievable range of baseline and reduced-capacity Li-ion configurations under standard drive cycles..... 181
Table 6. 4: Root-mean-square error between reference and simulated vehicle speed under reduced-capacity Li-ion configurations and auxiliary loading. 187
Table 6. 5: Energy Consumption and Performance Metrics for Al-air Enabled Range-Extender Configurations with Reduced Li-ion Energy Capacity. 188

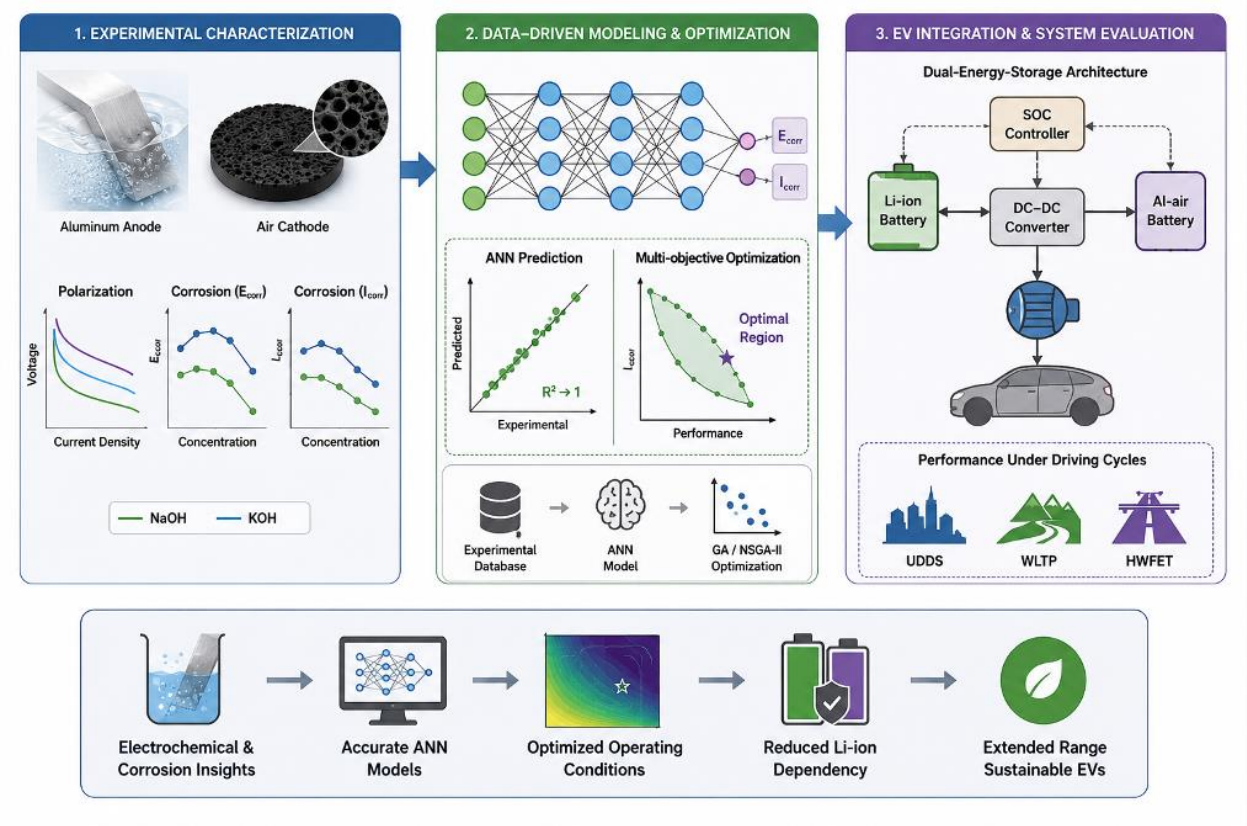
Table 6. 6: Mass breakdown and total range for reduced-energy Li-ion configurations with and without Al-air range extender. 197
Table 6. 7: Pack capital cost assumptions and total CAPEX for configurations evaluated. 199

List of Abbreviations

- Ag/AgCl: Silver/silver chloride reference electrode
- ACD: Anode-cathode distance
- Al-air: Aluminum-air battery
- Al-Mg-Si: Aluminum-magnesium-silicon alloy system
- ANN: Artificial neural network
- APU: Auxiliary power unit
- BEV: Battery electric vehicle
- Cdl: Double-layer capacitance
- CPE: Constant phase element
- DOD: Depth of discharge
- Ecorr: Corrosion potential
- EIS: Electrochemical impedance spectroscopy
- EV: Electric vehicle
- FCC: Face-centered cubic lattice structure
- FTP-75: Federal Test Procedure
- GA: Genetic algorithm
- GHGs: Greenhouse gases
- HER: Hydrogen evolution reaction
- HEVs: Hybrid electric vehicles
- HWFET: Highway Fuel Economy Test
- Icorr: Corrosion current density
- KOH: Potassium hydroxide
- LFP: Lithium iron phosphate
- Li-ion: Lithium-ion battery
- LIBs: Lithium-ion batteries
- MAE: Mean absolute error
- MSE: Mean squared error
- NaOH: Sodium hydroxide

- NMC: Nickel manganese cobalt
- NSGA-II: Non-dominated sorting genetic algorithm II
- OCV: Open-circuit voltage
- ORR: Oxygen reduction reaction
- PHEVs: Plug-in hybrid electric vehicles
- R^2: Coefficient of determination
- Rct: Charge-transfer resistance
- ReLU: Rectified linear unit activation function
- REEV: Range-extended electric vehicle
- RMSE: Root mean squared error
- R_s: Solution resistance
- SOC: State of charge
- UDDS: Urban Dynamometer Driving Schedule
- WLTP: Worldwide Harmonized Light Vehicles Test Procedure
- XRD: X-ray diffraction
- Zn-air: Zinc-air battery

Graphical Abstract



Chapter 1 Introduction

1.1 Motivation

The global energy landscape is undergoing a rapid transformation driven by the urgent need to mitigate climate change, reduce greenhouse gas emissions, and transition toward sustainable energy systems. Within this context, the transportation sector remains a major contributor to global carbon emissions, accounting for a significant fraction of fossil fuel consumption [1]. Electrification of transportation, particularly through battery electric vehicles (BEVs), has emerged as a critical pathway toward achieving decarbonization targets. Advances in lithium-ion (Li-ion) battery technology have enabled the commercialization of BEVs with improved energy density, longer driving ranges, and enhanced performance. However, despite these advancements, several inherent limitations of Li-ion systems continue to pose challenges for large-scale adoption [2].

One of the primary constraints of Li-ion batteries is their limited specific energy relative to the requirements of long-range transportation. Increasing the driving range of BEVs often necessitates larger battery packs, which in turn lead to increased vehicle weight, higher costs, and reduced overall efficiency [3]. Additionally, Li-ion batteries rely on critical raw materials such as lithium, cobalt, and nickel, which are associated with supply chain vulnerabilities, geopolitical constraints, and environmental concerns related to mining and processing. These factors highlight the need for alternative or complementary energy storage technologies that can overcome the limitations of conventional Li-ion systems while maintaining compatibility with existing electric vehicle architectures [4].

Metal-air batteries have emerged as a promising class of energy storage systems due to their exceptionally high theoretical energy densities and the use of oxygen from ambient air as a reactant. This unique configuration significantly reduces the weight of the battery system, as one of the reactants is not stored internally [5]. Among the various metal-air chemistries, aluminum-air (Al-air) batteries offer distinct advantages, including the abundance and low cost of aluminum, high theoretical specific energy, and well-established recycling infrastructure. Aluminum is one of the most widely produced metals globally, and its recyclability contributes to a potentially sustainable energy cycle. These characteristics position Al-air batteries as strong candidates for applications requiring high energy density, such as long-range electric mobility [6].

However, the practical realization of Al-air battery systems is hindered by several technical challenges. A critical issue is the parasitic corrosion of the aluminum anode in alkaline electrolytes, which leads to self-discharge and reduced system efficiency [7]. This corrosion is often accompanied by hydrogen evolution reactions, further decreasing coulombic efficiency and posing safety and operational challenges. Additionally, electrolyte management remains a significant concern, as changes in electrolyte composition, concentration, and water content during operation can affect both performance and durability. The formation of by-products such as aluminum hydroxides can also lead to clogging and reduced mass transport, further limiting system performance [8].

Beyond materials-level challenges, Al-air batteries are characterized by relatively low power density compared to Li-ion systems. While their high energy density makes them suitable for sustained energy delivery, their ability to meet transient high-power demands, such as acceleration in electric vehicles, is limited [9,10]. This mismatch between energy and power capabilities restricts the use of Al-air batteries as standalone power sources in dynamic applications. Consequently, there is a growing interest in hybrid energy storage architectures that combine the high energy density of Al-air systems with the high-power density and fast response characteristics of Li-ion batteries [11].

In such hybrid configurations, Al-air batteries can function as range extenders or auxiliary power units, providing sustained energy to recharge or support the primary Li-ion battery during operation. This approach enables a reduction in the required size of the Li-ion pack, thereby lowering system cost and weight while maintaining or even extending the overall driving range. However, the successful implementation of such systems requires careful consideration of system-level dynamics, including power flow management, control strategies, and efficiency trade-offs. In particular, the interaction between the two energy storage systems must be optimized to ensure stable operation, effective utilization of the Al-air battery, and minimal degradation of the Li-ion system [12].

Despite the potential advantages of Al-air integration, existing research has largely focused on either fundamental electrochemical studies or high-level system concepts, with limited efforts directed toward bridging these scales [13-15]. A comprehensive understanding of Al-air battery behavior requires a multiscale approach that integrates experimental characterization, predictive modeling, and system-level simulation. At the electrochemical level, detailed investigation of

corrosion mechanisms and performance under varying electrolyte conditions is essential to identify optimal operating regimes. At the modeling level, data-driven approaches can provide insights into complex relationships between operating parameters and degradation behavior, enabling predictive capability and optimization. At the system level, integration within electric vehicle platforms requires simulation frameworks that capture real-world driving conditions and evaluate performance metrics such as energy consumption, range, and state-of-charge dynamics.

Furthermore, the development of such integrated systems must account for practical considerations, including system efficiency, thermal effects, hydrogen management, and electrolyte handling. These factors play a critical role in determining the feasibility and scalability of Al-air technologies for real-world applications. In addition, economic and sustainability considerations, such as material costs, recyclability, and lifecycle impacts, must be evaluated to position Al-air systems within the broader energy landscape.

In this context, there exists a clear need for a unified framework that systematically addresses the challenges associated with Al-air batteries across multiple scales. This thesis is motivated by the objective of developing such a framework, combining experimental electrochemical analysis, machine learning-based predictive modeling, and system-level integration within electric vehicles. By linking fundamental material behavior to practical system performance, this work aims to provide critical insights into the viability of Al-air batteries as a complementary energy storage technology for next-generation electric mobility.

Ultimately, the integration of Al-air batteries with Li-ion systems represents a promising pathway toward overcoming the limitations of current battery technologies. By leveraging the strengths of both systems, it is possible to achieve a balance between energy density, power capability, cost, and sustainability. The outcomes of this research are expected to contribute to the advancement of hybrid energy storage architectures and support the development of more efficient, cost-effective, and sustainable electric transportation systems.

1.2 Research Objectives

The overarching objective of this thesis is to establish a comprehensive, multiscale framework for the development and integration of Al-air battery systems, addressing key challenges from materials-level degradation to vehicle-level performance optimization.

To achieve this goal, the following specific objectives are defined:

1. Electrochemical Performance Evaluation of Al-air Systems

To experimentally investigate the electrochemical behavior of a commercial Al-Mg-Si alloy in alkaline electrolytes, with a focus on understanding the influence of electrolyte composition and concentration on key performance metrics, including open-circuit voltage (OCV), corrosion potential (Ecorr), corrosion current density (Icorr), and impedance characteristics.

2. Corrosion Behavior Analysis and Predictive Modeling

To develop a data-driven framework for predicting corrosion behavior using artificial neural networks (ANN), incorporating electrochemical inputs such as electrolyte type, concentration, temperature, voltage, and current density. This objective includes optimization of corrosion performance using genetic algorithms (GA) and non-dominated sorting genetic algorithms (NSGA-II), as well as interpretability analysis using feature importance methods.

3. Development of Semi-Empirical Electrochemical Models

To construct and validate semi-empirical models that capture the polarization behavior of Al-air cells, enabling accurate representation of voltage losses associated with activation, ohmic, and mass transport phenomena under varying operating conditions.

4. System-Level Integration of Al-air Batteries in Electric Vehicles

To implement and evaluate Al-air battery systems within a BEV simulation framework, focusing on dual energy storage system architectures where Al-air batteries function as range extenders or auxiliary power units. This includes the development of control strategies based on state-of-charge (SOC) thresholds and analysis of power flow dynamics.

5. Performance Assessment under Standard Driving Cycles

To quantify the impact of Al-air integration on vehicle performance metrics, including energy consumption, driving range, and SOC evolution, under standardized driving cycles such as UDDS, WLTP, and HWFET. This objective also includes sensitivity analysis with respect to Li-ion battery sizing.

6. Evaluation of Practical Constraints and Design Trade-offs

To identify key limitations associated with Al-air systems, including power density constraints, system efficiency losses, hydrogen evolution, and electrolyte management challenges, and to assess their implications for real-world deployment in electric vehicles.

1.3 Thesis Outline

This thesis is structured to develop a comprehensive and multiscale understanding of Al-air battery systems, progressing from literature synthesis to experimental analysis, data-driven modeling, and system-level integration within electric vehicles.

- Chapter 2 presents a detailed literature review on metal-air battery technologies, with particular emphasis on Al-air systems. The chapter discusses fundamental electrochemical mechanisms, corrosion behavior of aluminum in alkaline electrolytes, and key factors influencing performance and degradation. In addition, prior studies on metal-air battery integration in electric vehicles are critically reviewed to identify existing gaps in both materials-level understanding and system-level implementation.
- Chapter 3 investigates the techno-economic feasibility of metal-air batteries as range extenders in electric vehicles. This chapter evaluates the potential of metal-air systems in comparison to conventional Li-ion configurations, considering key metrics such as energy density, system mass, cost, and vehicle range. The analysis provides a quantitative foundation for assessing the viability of Al-air batteries in real-world transportation applications.
- Chapter 4 focuses on the experimental performance evaluation of high energy density Al-air batteries. The effects of operational parameters, including electrolyte type, concentration, and temperature, on electrochemical performance are systematically examined. Key metrics such as open-circuit voltage, polarization behavior, corrosion potential, corrosion current density, and impedance characteristics are analyzed to identify optimal operating conditions and performance limitations.
- Chapter 5 presents a data-driven approach for modeling and predicting aluminum anode corrosion kinetics using artificial neural networks combined with genetic algorithms. The developed framework enables accurate prediction of corrosion behavior under varying operating conditions and facilitates multi-objective optimization of system performance. Feature importance analysis is also conducted to provide insight into the dominant factors influencing corrosion.
- Chapter 6 addresses the system-level modeling and integration of Al-air batteries within dual-energy-storage electric vehicle architectures. A simulation framework is developed to evaluate the interaction between Al-air and Li-ion systems, including control strategies

based on state-of-charge thresholds. The performance of the integrated system is assessed under standard driving cycles, with analysis of energy consumption, power flow, and range extension capabilities.

- Chapter 7 concludes the thesis by summarizing the key findings and contributions across all chapters. The chapter also outlines directions for future research, including the development of higher-fidelity electrochemical models, improved system efficiency, and experimental validation of integrated Al-air battery systems for electric vehicle applications.

Chapter 2 Literature Review

*** Chapter 2 is adapted from Shabeer Y, Madani SS, Panchal S, Mousavi M, Fowler M. "Different Metal-Air Batteries as Range Extenders for the Electric Vehicle Market: A Comparative Study." Batteries 2025;11:35. https://doi.org/10.3390/BATTERIES11010035.

The extensive use of fossil fuels has been the primary driver of long-term climate change for the past 150 years, responsible for a staggering 75% of global greenhouse gas emissions and 90% of global carbon dioxide (CO_2) emissions. As fossil fuel reserves continue to dwindle and geopolitical tensions heighten over their supply, the imperative to develop alternative energy sources becomes increasingly urgent in modern civilizations. Solar, wind, wave, biomass, and other renewable energy sources hold promise as alternatives to reduce dependence on fossil fuels. However, their widespread adoption faces significant challenges related to efficiency and regulatory hurdles. There is still a significant distance to cover in addressing the ecological damage brought on by the exploitation of fossil fuels by transitioning to renewable energy sources [16-23].

Motivated to decrease carbon emissions and dependence on fossil energy, a global transition towards electric vehicles (EVs) signifies a critical juncture in the automotive sector. Evidently, the ambitious goal of significantly reducing CO_2 emissions necessitates a multifaceted approach that includes the widespread deployment of EVs alongside a strategic focus on integrating renewable energy sources into the grid [24,25]. Although there have been notable improvements in EV technology, the restricted range of existing battery systems hinders widespread adoption. This limitation translates into a critical concern for the EV industry in the form of range anxiety. Consumers remain apprehensive about the driving distance achievable on a single charge, ultimately dampening consumer confidence and hindering the overall growth of the EV market [26-31]. The rapid progress of energy storage technologies has been crucial in promoting the widespread use of battery-powered solutions in the automotive industry. Batteries are the core component of EVs and are essential in determining the driving range and overall performance of these environmentally friendly battery electric vehicles (BEVs). Advancements in battery technology are crucial for overcoming range limitations while alleviating concerns like range anxiety. This will demonstrably improve consumer acceptance of EVs, thereby expediting their universal adoption as a sustainable transportation solution [32].

Lithium-ion (Li-ion) currently dominates the battery industry, powering not only EVs but also a myriad of consumer electronics. They experienced a significant advancement in energy density, rising from around 90 Wh kg^{-1} to a contemporary range of 100 to 250 Wh kg^{-1} between the 1990s and now. Though this advancement has permitted larger vehicles to cover typical driving patterns this is insufficient for BEVs striving to outperform internal combustion engine vehicles (ICEVs), that typically, achieve a mileage equivalent of about 7 to 11 kilometres per litre of gasoline, varying based on the model [33-37]. Contrariwise, lithium-powered systems are unable to meet the escalating demand for energy storage, particularly within the automotive sector. In the wake of recent regulations and the fact that lithium comprises only 0.0017% of the crust, the demand for electric vehicle batteries is anticipated to increase substantially over the next decade [38,39].

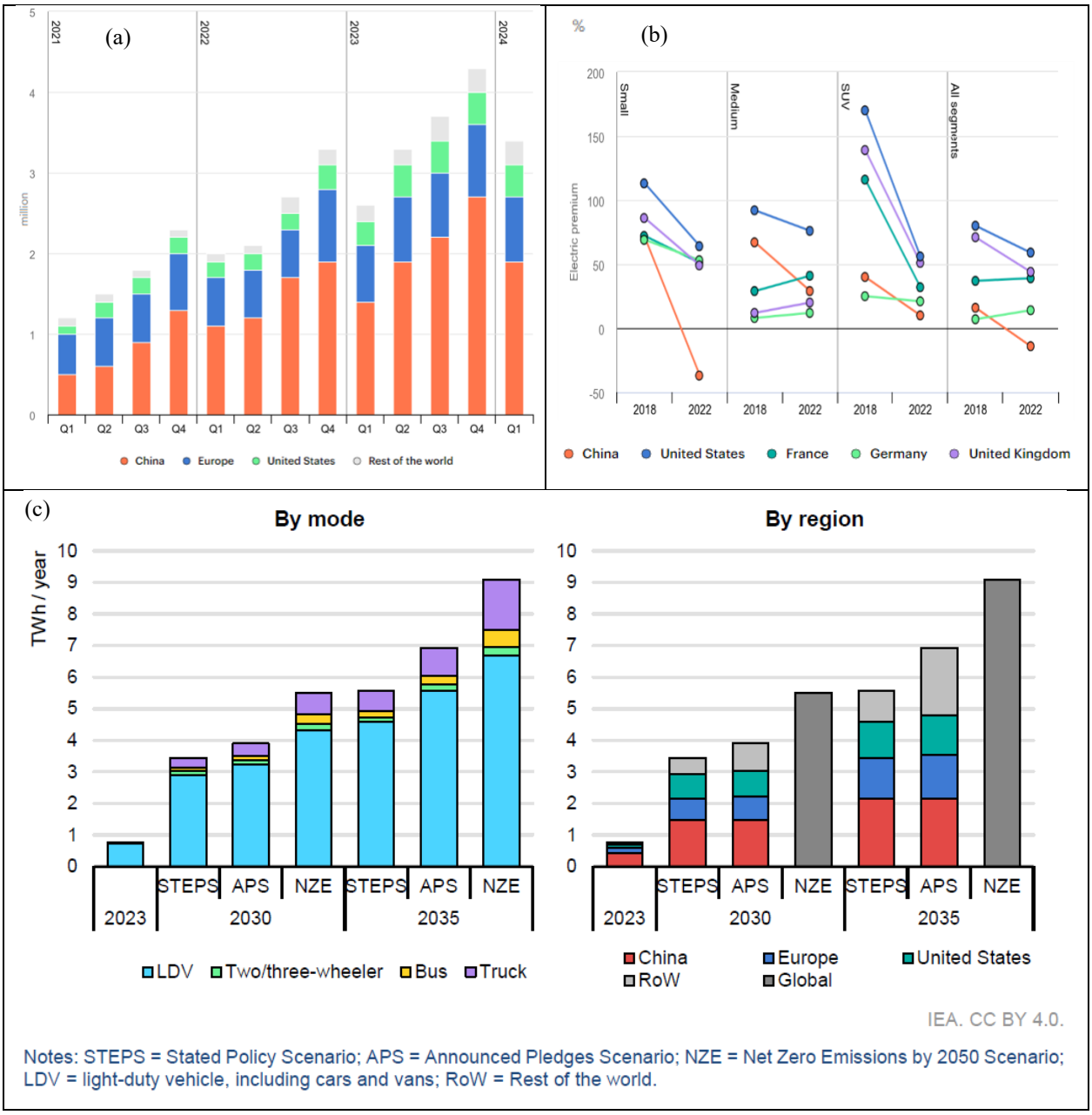


Figure 2. 1: (a) Regional quarterly electric car sales (2021-2024), (b) the difference in sales-weighted average prices between traditional and electric vehicles in specific countries, before subsidies, by vehicle size (2018-2022), and (c) energy demand for electric vehicles, categorized by mode and region (2023-2035) [40].

According to the International Energy Agency's (IEA) global EV outlook released in 2024, electric car sales continue to rise and could reach approximately 17 million in 2024, making up more than one in five cars sold globally and the pricing strategies of car manufacturers will perform a key role in increasing affordability, along with the rate at which EV battery prices

decrease as evidenced by the trends shown in Figure 2.1. Under current projections, EV energy demand is expected to increase significantly by 2035. By 2030, demand could grow up to 4.5 times compared to 2023, and nearly 7 times by 2035. In more ambitious scenarios, demand may rise 5 to 7 times by 2030, and 9 to 12 times by 2035. For context, in 2035, weekly EV battery demand could match the total annual demand recorded in 2019 [40]. To accommodate this driving patterns, BEV manufacturers are compelled to include large and bulky Li-ion battery packs, which are both heavy and expensive, thereby limiting the ability of EVs to compete with standard ICEVs. Furthermore, safety issues related to Li-ion systems are of the primary concern due to the significant potential risks to users resulting from battery malfunctions. This failure can occur due to an electrical shortage caused by the formation of dendritic lithium during rapid charging, or thermal runaway resulting from overcharging/discharging. These failures could potentially cause fires due to the highly combustible electrolyte used in Li-ion cells, consequently leading to a multitude of accidents involving these batteries, as analyzed by Yu et al. [41] in Figure 2.2. A further significant concern is the negative environmental impact of Li-ion systems. The extraction, production, and indiscriminate disposal of these batteries contribute to environmental issues, primarily because of the existence of hazardous substances and specifically, heavy metals classified as such, including nickel and cobalt. The recycling of the Li-ion system continues to pose challenges, primarily stemming from economic feasibility issues and the complexity of the disassembly process. Consequently, the combination of lithium scarcity, limited energy capacities, extended charging durations, adverse environmental effects and safety apprehensions surrounding their components collectively hinder the widespread adoption and commercialization of Li-ion, particularly within the realm of the EV industry [42-48].

To address the challenges posed by Li-ion systems and meet the growing demands in the energy sector, researchers are focusing on the advancements of metal-air/oxygen batteries. Metal-air batteries (MABs), consisting of electrolytes and bifunctional air electrodes, typically function by extracting atmospheric oxygen and simultaneously converting metal anodes into their oxide forms. The batteries utilize a range of metal electrodes, including alkali metals like potassium (K), lithium (Li), and sodium (Na), metalloids like germanium (Ge) and silicon (Si) as well as transition metals, and post-transition metals such as aluminum (Al), calcium (Ca), iron (Fe), magnesium (Mg), tin (Sn), zinc (Zn) and vanadium (V). MABs have a remarkable theoretical

energy density that falls within the range of 1353 to 11429 Wh kg^{-1} (per unit weight) based on calculations for common MABs including those utilizing Li, Zn, Al, and Mg [49,50].

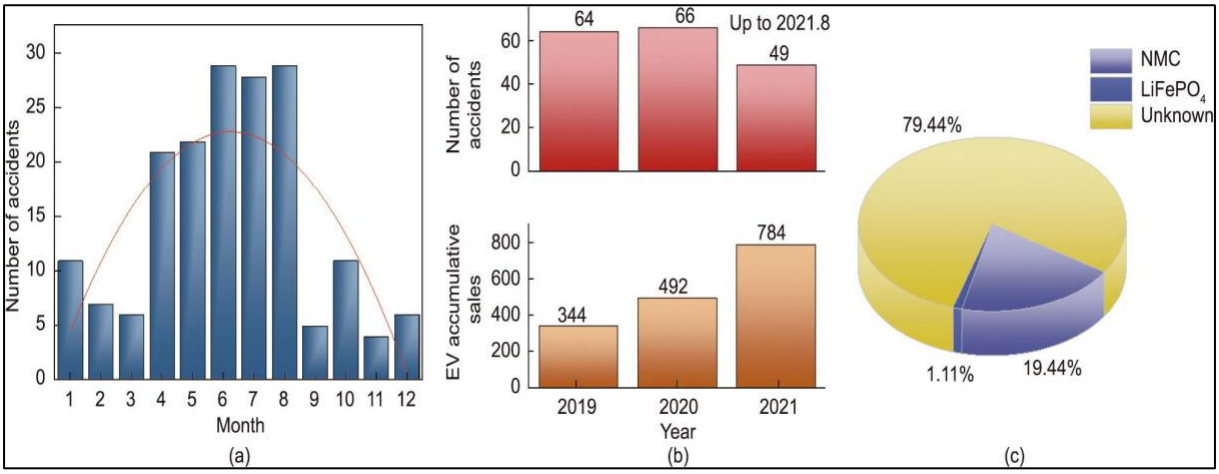


Figure 2. 2: Compilation of EV fire occurrences from January 2019 to August 2021: (a) Monthly count of EV fire incidents (b) Comparison of annual EV fire incidents and the total number of EVs sold (c) Distribution of accidents attributed to various types of Li-ion battery [41].

The essence of MABs lies in their innovative design, where electrical energy is generated through the reaction of atmospheric oxygen with a metallic electrode. The process underscores the pivotal role of air in facilitating the electrochemical reactions within these batteries, resulting in efficient energy conversion and storage. This dynamic offers a promising avenue for advancing energy storage technologies toward higher performance and sustainability through the unique interplay between air and metal electrodes. Thus, MABs are anticipated to have a significant impact in the markets of automobile, consumer electronics, stationary storage, defence, marine, and aviation markets [51].

MABs have become prominent because of their efficient operation in outdoor settings, making them ideal for meeting the high energy requirements of EVs. Researchers anticipate that specific MABs will directly replace Li-ion batteries, while others will act as range extenders. This feature reduces range anxiety, enhances safety, and improves cost efficiency by decreasing the size of Li-ion batteries when they are not replaced directly. Figures 2.3 and 2.4 give a visual summary of essential parameters influencing the selection and utilization of various metals in MAB technologies. Figure 2.3 presents a comparative analysis of the energy parameters of different metals used in MABs, highlighting the theoretical volumetric energy density in Wh L^{-1}, specific energy in Wh kg^{-1}, and nominal cell voltage in V. Concurrently, Figure 2.4 illustrates

the cost and abundance of these elements, offering insights into their economic feasibility and natural availability.

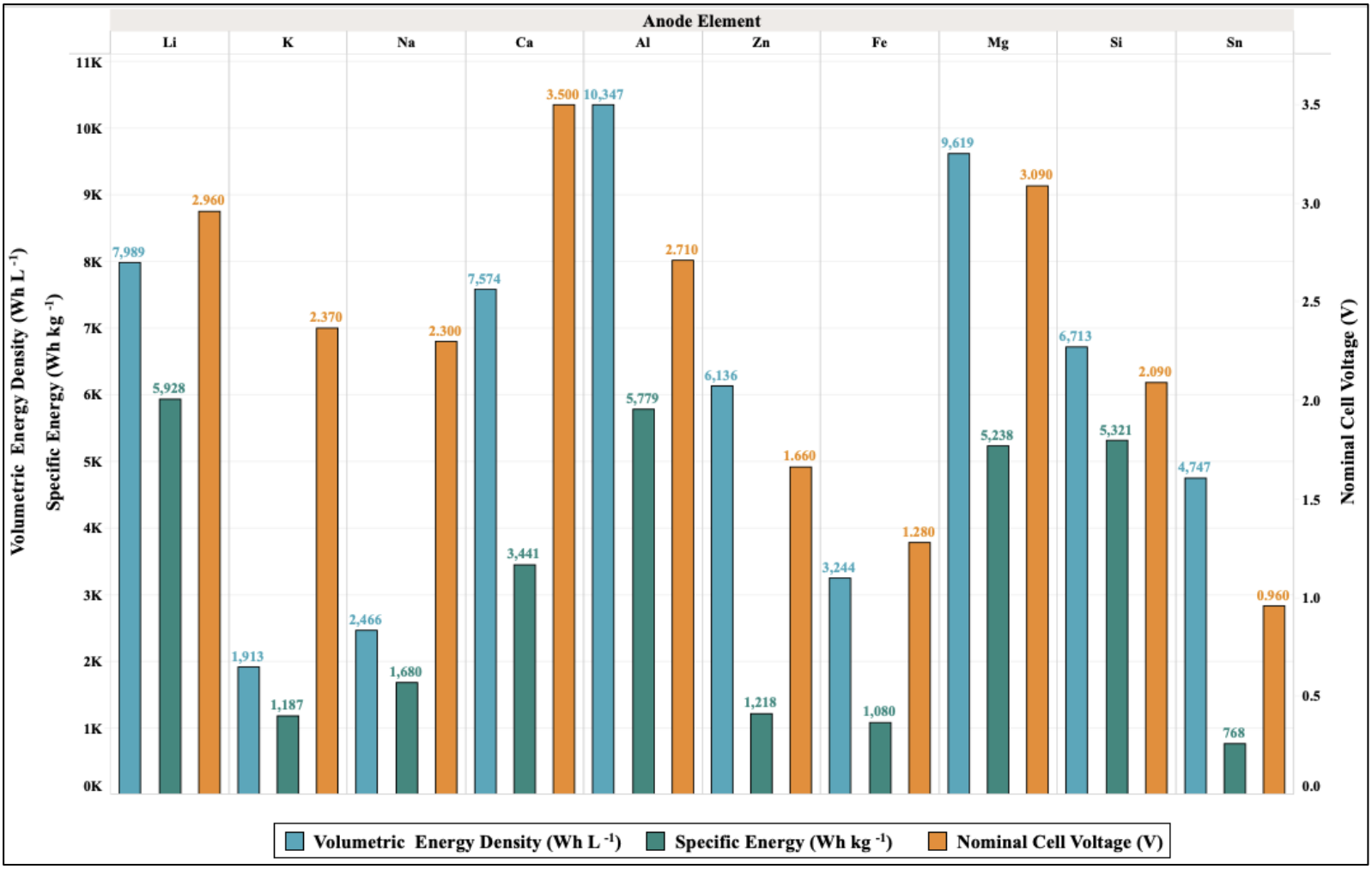


Figure 2. 3: Comparison of the performance of several metal-air batteries, highlighting the theoretical specific energy, volumetric energy density and nominal cell voltage.

Together, these Figures 2.3 and 2.4 present a holistic perspective on the essential parameters that must be considered when evaluating the practicality and efficiency of using these different metals. From the graph, lithium appears as a very effective anode because of its superior theoretical specific energy of 5928 Wh kg^{-1} and an open circuit voltage (OCV) of 2.96 V. Nevertheless, the very low abundance (< 0.0017 %) and high cost of lithium metal (46 US$ kg^{-1}), combined with its intrinsic instability when it comes into contact with air and aqueous electrolytes, present significant challenges [52]. Subsequently, Al metal emerges as a promising

candidate due to its exceptional theoretical specific energy of 5779 in Wh kg^{-1} and an energy density of 10347 Wh L^{-1}. Al metal is also known for its high safety, cost-effectiveness and abundance. However, its high corrosion rate in aqueous electrolytes, coupled with parasitic reactions, diminishes its overall performance [53]. The appeal of employing Mg metal in MABs lies in their ability to achieve uniform metal deposition and significant theoretical energy potentials (energy density of 9619 Wh L^{-1}, specific energy of 5238 Wh kg^{-1} and OCV of 3.090 V). However, the ubiquitous usage of magnesium electrodes in aqueous electrolytes is impeded by significant corrosion challenges and high self-charge characteristics. The high corrosion rates compromise the electrode's longevity and performance, posing a substantial barrier to its practical application [54]. Additionally, the cost of magnesium, approximately 11.02 US$ kg^{-1}, coupled with its relatively limited abundance of only 2.10 %, further limits its viability as a sustainable material in large-scale energy storage solutions.

It should be noted that, as of this point, in the context of aqueous MABs, only MABs with Zn anodes can be electrically recharged while Mg and Al employing air batteries require mechanical replacement of these metal anodes due to their inability to be directly converted from ions to metal [55]. Given this unique advantage, employing Zn as the metal anode presents promising opportunities for the development and enhancement of MAB technology. Zn is one of the widely researched anodes for MABs with a high theoretical energy density of 6136 Wh L^{-1} and a specific energy of 1218 Wh kg^{-1}. However, limitations such as the formation of Zn dendrites and low cycle life need to be addressed to enhance their commercial viability [56,57]. While Na and K metals exhibit some chemical similarities to Li, their application as a viable battery alternative face substantial hurdle. These hurdles include the lack of comprehensive understanding of the underlying electrochemistry, the development of stable electrolytes, and the design of high-performance electrode materials for these batteries [58,59]. Other metal anodes such as Fe, Si, Ca, and Sn, while less extensively researched, show promising potential due to their high crustal abundance and lower costs.

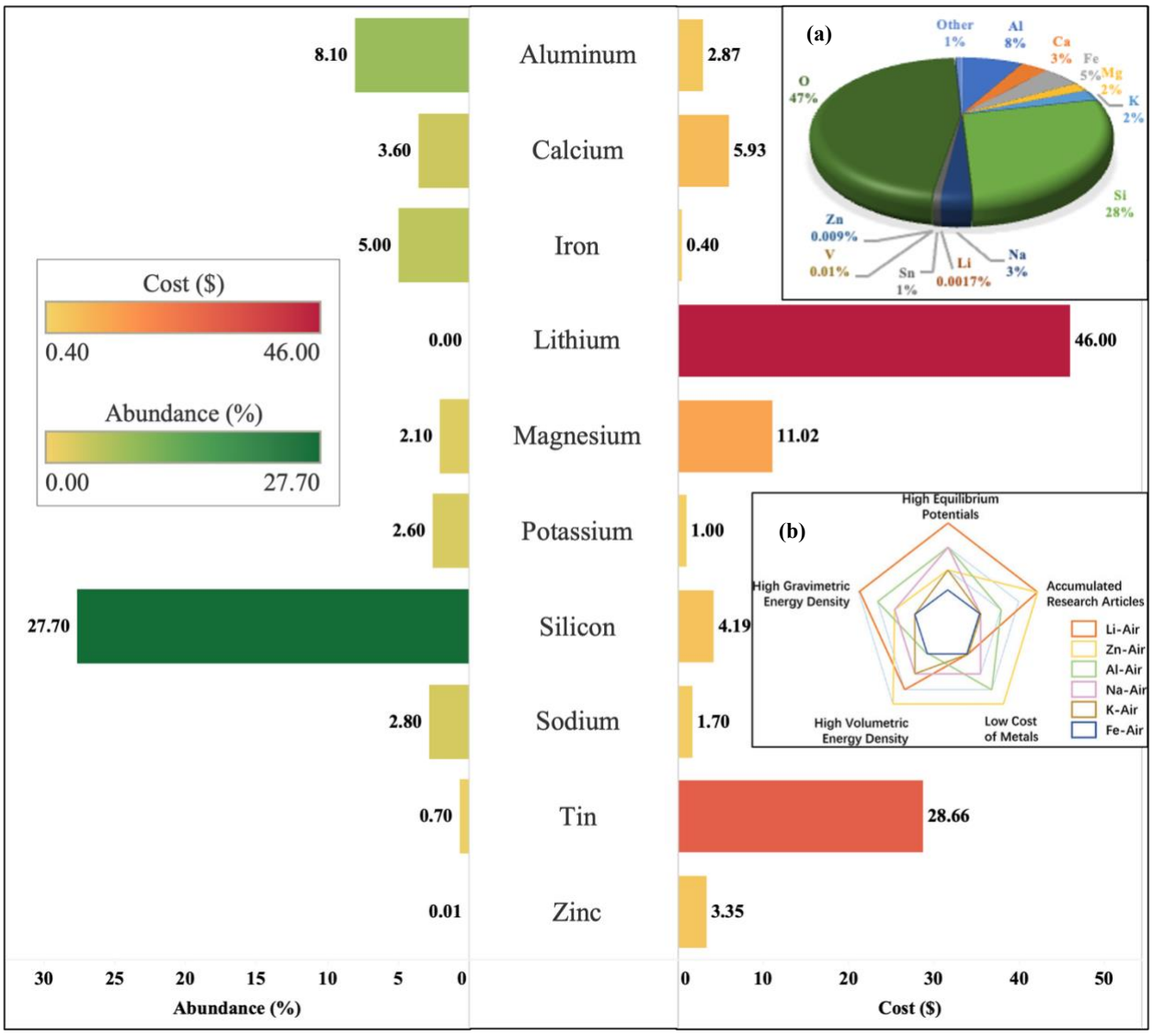


Figure 2. 4: Abundance vs. cost of metal-air battery elements. Refer to the inset (a) for the earth's crustal distribution (Based on data from [60,61]) and inset (b) for a radar chart illustrating the benefits and drawbacks of various types of metal-air batteries based on research articles collected from the Web of Science between 2000 and 2023 (Adapted from [57]).

Currently, none of these battery chemistries have achieved the technological maturity required for widespread industrial adoption. As a result, their potential to either replace or supplement Li-ion batteries as the primary power source or range extenders for future EVs remains highly uncertain. Although some studies explore the potential of specific MABs like Li-air or Zn-air batteries as range extenders, they do not offer a comprehensive comparison of all MABs

currently being studied in the field. Thus, this comparative review aims to bridge this knowledge gap by offering a comprehensive analysis of different MABs as potential EV range extenders. We will delve into their structural compositions, operational principles, performance metrics, and existing challenges. By critically evaluating the strengths and limitations of each battery type, the goal is to illuminate their suitability for integration into the rapidly evolving EV market. *Chapter 2* introduces MABs as energy storage systems and delves into specific types with different anodes, describing in detail their types, working principles, advantages, and challenges. *Chapter 3* provides a comparison of the practical properties of these MABs, focusing on factors such as driving range, battery pack volume, and total vehicle cost. *Chapter 4* concludes with summarizing remarks, encapsulating the observations made throughout the review.

2.1 Metal-Air Batteries

The operational mechanisms of both aqueous and non-aqueous MABs and the various configurations are depicted in Figure 2.5 [62]. In essence, these batteries consist of three key parts: an anode (metal), an electrolyte solution positioned between the electrodes, and a permeable air-cathode. The categorization of MABs by Wang et al. [49] includes three distinct types: static battery setups with multiple cells, cell configurations with electrolyte flow, and innovative flexible battery designs.

In conventional static electrochemical setups, such as the one depicted in Figure 2.5(a), four critical components are employed: a cathode, a separator, an electrolyte, and an anode. The anode reaction exhibits rapid kinetics, while the oxygen reduction reaction (ORR) at the positive electrode is kinetically slow. This sluggishness is attributed to the reaction occurring at a three-phase (solid catalyst, liquid electrolyte, and gaseous oxygen) that is crucial for the ORR. Furthermore, the oxygen evolution reaction (OER) proceeds concurrently on the cathode at a two-phase boundary, consisting solely of the catalyst and electrolyte. Achieving optimal performance for both the OER and ORR necessitates the use of highly efficient dual-functional catalysts. However, a significant obstacle for conventional static designs is the accumulation of solid byproducts on the surfaces of both electrodes during the cycling of the cell. These deposits can block electrode pores, impeding air diffusion and ultimately reducing battery performance. Flow batteries (Figure 2.5(b)) include electrodes, an electrolyte, a separator, and an additional reservoir for storing the electrolyte, often accompanied by a pump to facilitate electrolyte flow. This

flowing-electrolyte configuration mitigates some issues related to both positive and negative electrodes.

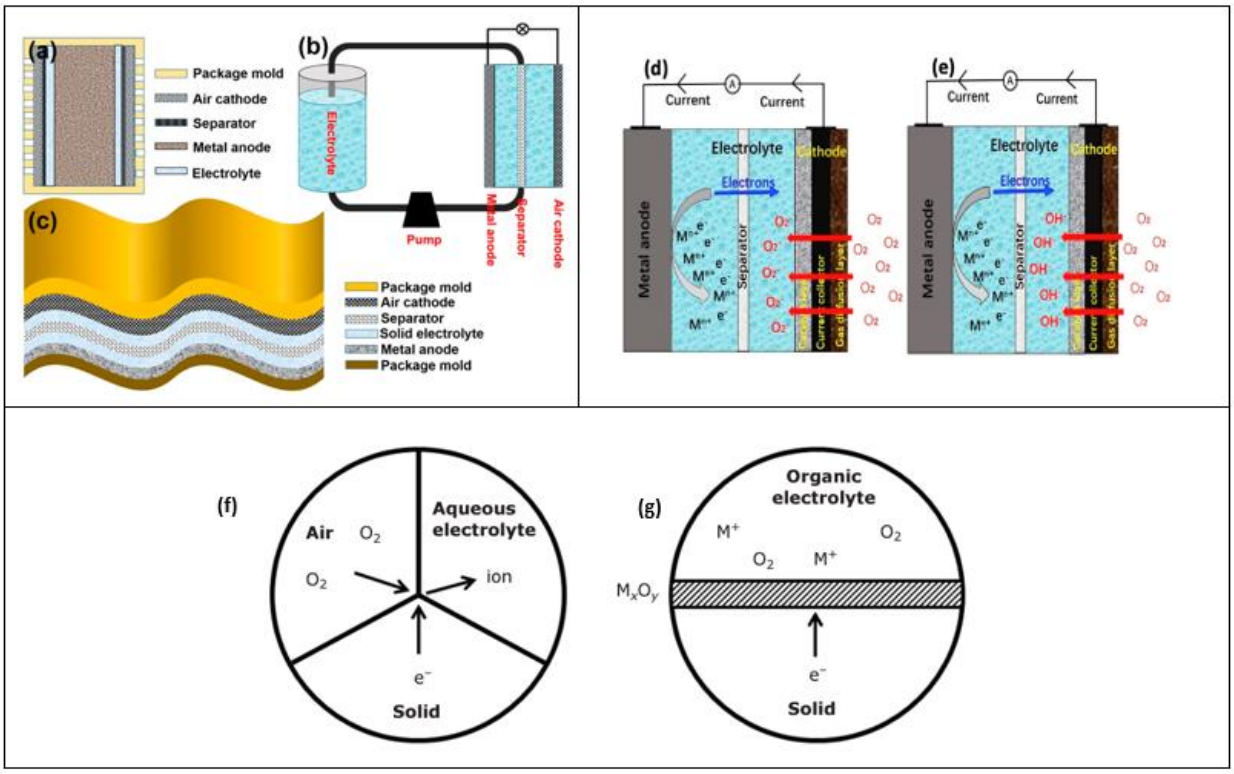


Figure 2. 5: Illustration of different configurations of MABs, including a conventional static battery setup (a), a cell design with electrolyte flow (b), and a novel flexible cell design (c); (d) and (e) are the representation of non-aqueous and aqueous electrolytes MABs respectively [63]; (f) and (g) depict the phase boundary diagram for both aqueous and non-aqueous electrolytes (Modified from [61]).

For example, in Zn-Ni battery types, a large volume of flowing electrolyte helps prevent dendrite growth and uneven zinc geometry variations, thus mitigating passivation through enhanced current uniformity and reduced concentration disparities. Despite these advantages, the complex configuration of flowing electrolytes introduces drawbacks such as decreased energy efficiency and volumetric density, along with the necessity for auxiliary flow channels and pumps to enhance electrolyte circulation during cell operation. Han et al. [64] conducted an extensive review comparing static and flow batteries, providing a detailed analysis of their respective advantages and challenges. Flexible batteries (Figure 2.5(c)) have gained significant attention recently due to the rising demand for portable electronics. These miniaturized batteries prioritize high energy density within a lightweight form factor. They achieve this through a combination of electrodes, a separator, and a high-conductive (often solid-state) electrolyte. The small thickness

of the metal anode further reduces the overall mass of the cell. Different nanomaterials like graphene, carbon nanotubes and fibres are investigated for optimal cathode performance. Flexible battery technology is transitioning beyond basic chemistries, with the emerging lithium-based and metal-air options. Notably, Zinc and Aluminum-based MABs are currently favoured for the application of flexible electronics owing to their massive specific energy, safety profile, and cost-effectiveness [65-67].

Regarding the categorization of MABs depending on the electrolyte types, there are various kinds of electrolytes employed: aqueous (water-based), non-aqueous (organic solvent-based), solid-state (no liquid component), and hybrid (combinations of the above). Metal electrodes that are highly water-sensitive, such as those in lithium, potassium and sodium-air batteries, cannot utilize aqueous electrolytes, as these alkali metals react vigorously with water, often leading to hazardous situations. In contrast, other types of MABs, including those with aluminum, zinc, iron, or magnesium electrodes, which are compatible with water, can use both aqueous and non-aqueous electrolytes, among others [68,69]. The distinctions between reactions in aqueous and non-aqueous MABs pose unique challenges for technological implementation, as elucidated in the review by Hardwick et al [51]. In non-aqueous MABs, the ORR leads to the generation of metal oxides that precipitate on the surface of the permeable air-cathode itself. Conversely, in alkaline-based aqueous MABs, the anodic metallic ions do not arrive at the positive electrode; instead, precipitation of these metal ions occurs by the reaction with hydroxide ions (OH^-), or they form a complex with a negative charge, such as the zincate anion ($Zn(OH)_4^{2-}$) near the anode, preventing its migration to the cathode. Aqueous MABs encounter the additional hurdle of low oxygen solubility in water (0.2 mM) under atmospheric pressure, necessitating the utilization of gaseous oxygen. Atmospheric oxygen permeates into the air-cathode propelled by the pressure gradient between the cell's interior and exterior. Catalysts enable the formation of hydroxyl (OH^-) ions in the basic media by oxygen reduction, with electrons produced at the negative electrode, potentially resulting in the production of metal hydroxides in solid form. This three-phase reaction involves a solid catalyst, a liquid electrolyte, and gaseous oxygen, as depicted in Figure 2.5(f). Meanwhile, Figure 2.5(g) portrays the boundary diagram of non-aqueous MABs, facilitating a comparison between them [70-76]. Within aqueous MABs, the anode undergoes an oxidation reaction during discharge, releasing electrons and simultaneously forming metal hydroxide as the metal cations react with OH^- ions,

$$M + nOH^- \rightarrow M(OH)_n + ne^- \quad (2.1)$$

Here, M represents the metal and n stands for the valence metal ions. The liberated electrons (e^-) travel via the closed circuit and arrive at the positive electrode to engage in the ORR. There, the molecules of oxygen present in the ambient air, coupled with the e^- and water, undergo reduction to produce OH^- ions.

$$\frac{n}{4}O_2 + ne^- + \frac{n}{2}H_2O \rightarrow nOH^- \quad (2.2)$$

The produced OH^- ions move from the cathode to the metal anode, closing the loop. By combining Equations (2.1) and (2.2), we can derive the overall reaction [49].

$$M + \frac{n}{4}O_2 + \frac{n}{2}H_2O \rightarrow M(OH)_n \quad (2.3)$$

Similarly, in non-aqueous MABs, the metal undergoes oxidation to form metal cations and electrons at the anode,

$$M \leftrightarrow M^+ + e^- \quad (2.4)$$

whereas, at the cathode, the metal cations react with O_2 and e^- to give metal oxides [50],

$$xM^+ + O_2 + xe^- \leftrightarrow M_xO_2 \ (x = 1 \ or \ 2) \quad (2.5)$$

To quantify the performance of MABs, parameters like cell voltage, specific capacity, and energy density are used. These are crucial parameters for evaluating MAB performance. To calculate these metrics and gain a deeper understanding of MAB behaviour, we can utilize various formulas based on the underlying electrochemical reactions. Table 2.1 summarizes the formulae employed for calculating these key performance indicators of MABs.

Table 2. 1: Key performance indicators and corresponding formulae for metal-air batteries

Parameter	Formula	Units	Explanation	Ref.
Specific Capacity	$C = \frac{(I \times t)}{m}$	mAh g^{-1}	I is discharge current, t is discharge time, m is mass of the electrode	[77]
Capacity Density	$Q = \frac{It}{\Delta m}$	mA cm^{-2}	I is current in mA, t is discharge time in hours, Δm is weight loss in g	[45]
Power Density	$P = \frac{EI}{S}$	mW cm^{-2}	E is average discharge voltage (V), I is current in mA, S is active surface area in cm^2	45]
Specific Energy	$SE = \frac{V \times C}{M_B}$	Wh kg^{-1}	SE is specific energy, V is nominal battery voltage in V, C is rated battery capacity in Ah and M_B is the battery mass	78]
Energy Density	$W = \frac{EIt}{\Delta m}$	mWh g^{-1}	E is average discharge voltage (V), I is current in mA, t is discharge time in hours, Δm is weight loss in g	[45]
Instantaneous Specific Energy (including oxygen)	$\frac{F \cdot n \cdot OCV}{3.6}[\frac{\ln[(M_{M+O}/M_{Metal})}{M_{M+O} - M_{Metal}}]$	Wh kg^{-1}	F is Faraday constant, n is the number of electrons transferred per metal ion, OCV is nominal voltage, M_{Metal} is molar mass of metal anode, M_{M+O} is the combined molar mass of metal anode and stoichiometric amount of oxygen that enters the battery	[52]
Energy Density (including	$Volumetric\ Energy\ Density = (SE) \cdot (OAD)$	Wh L^{-1}	SE is specific energy in Whkg^{-1}, OAD is Oxidizing anode density in kgL^{-1}	[52]
Nernst Equation	$E = E^{\circ} - \frac{RT}{nF} lnQ$	V	R is the gas constant, T is the temperature in K, F is Faraday's constant, n is the number of moles of electrons transferred, Q is the reaction quotient	[79]

Parameter	Formula	Units	Explanation	Ref.
Gibbs Free Energy	$\Delta G^{\circ} = -nFE^{\circ} = \Delta H^{\circ} - T\Delta S^{\circ}$	J	T is the temperature in K, F is Faraday's constant, n is the number of moles of electrons transferred, S is entropy, H is Enthalpy	[79]
Current Efficiency	$\eta_a = \frac{Q}{Q_0}$	%	Q is the actual capacity density in $mAcm^{-2}$ and Q_0 is the theoretical capacity density in $mAhg^{-1}$	[45]
Energy Efficiency	$\eta_{fuel} = \frac{W}{W_0} \times 100$	%	W is the actual energy density in $mWHg^{-1}$ and W_0 is the theoretical energy density in $mWhg^{-1}$	[45]
Charging Energy Efficiency	$\eta_{charge} = \frac{\int_{SOC(0)}^{SOC(t)} U_{OCV} C_n d\ SOC}{\int_{SOC(0)}^{SOC(t)} U_{charge} C_n d\ SOC}$	%	Numerator = net energy, Denominator = charge energy, SOC = state of charge, U = battery voltage, C_n = battery standard capacity	[79]
Discharging Energy efficiency	$\eta_{disch} = \frac{\int_{SOC(0)}^{SOC(t)} U_{disch} C_n d\ SOC}{\int_{SOC(0)}^{SOC(t)} U_{OCV} C_n d\ SOC}$	%	Numerator = discharge energy, Denominator = net energy, SOC = state of charge, U = battery voltage, C_n = battery standard capacity	[79]
Charge-discharge Energy Efficiency	$\eta_{battery} = \frac{\int_{SOC(0)}^{SOC(t)} U_{disch} C_n d\ SOC}{\int_{SOC(0)}^{SOC(t)} U_{charge} C_n d\ SOC}$	%	Numerator = discharge energy, Denominator = charge energy, SOC = state of charge, U = battery voltage, C_n = battery standard capacity	[79]
Vehicle Range	$R_V = \frac{E_B}{ECE_V\left(M_V + \frac{E_B\, k_{m,B}}{SE_{BC}}\right)}$	km	E_B is battery pack energy in Wh, ECE_V is the energy consumption efficiency of the vehicle in Wh km^{-1} kg^{-1}, M_V is vehicle mass without battery pack in kg, $k_{m,B}$ is the battery mass overhead and SE_{BC} is specific energy of the battery cell in $Whkg^{-1}$	[30]
Total Vehicle Cost	$C_{V,T} = C_V + C_B E_B$	US$	C_V is vehicle cost without battery pack in US$, and C_B is battery pack cost in US$ kWh^{-1}	[29]
Battery Pack Volume	$Vol_B = \frac{E_B \times k_{vol,B}}{ED_{BC}}$	L	$k_{vol,B}$ is the battery volume overhead and ED_{BC} is energy density of the battery cell in WhL^{-1}	[29]

MAB has a clear advantage in terms of energy storage capacity. When compared to a standard lithium/manganese dioxide (Li/MnO_2) battery with an assumed voltage of 3 V, MABs boast a much higher theoretical specific energy (Wh g^{-1}) and volumetric energy density (Wh cm^{-3}). This is illustrated in Figures 2.6(a) and (b), where the values for MABs are significantly greater.

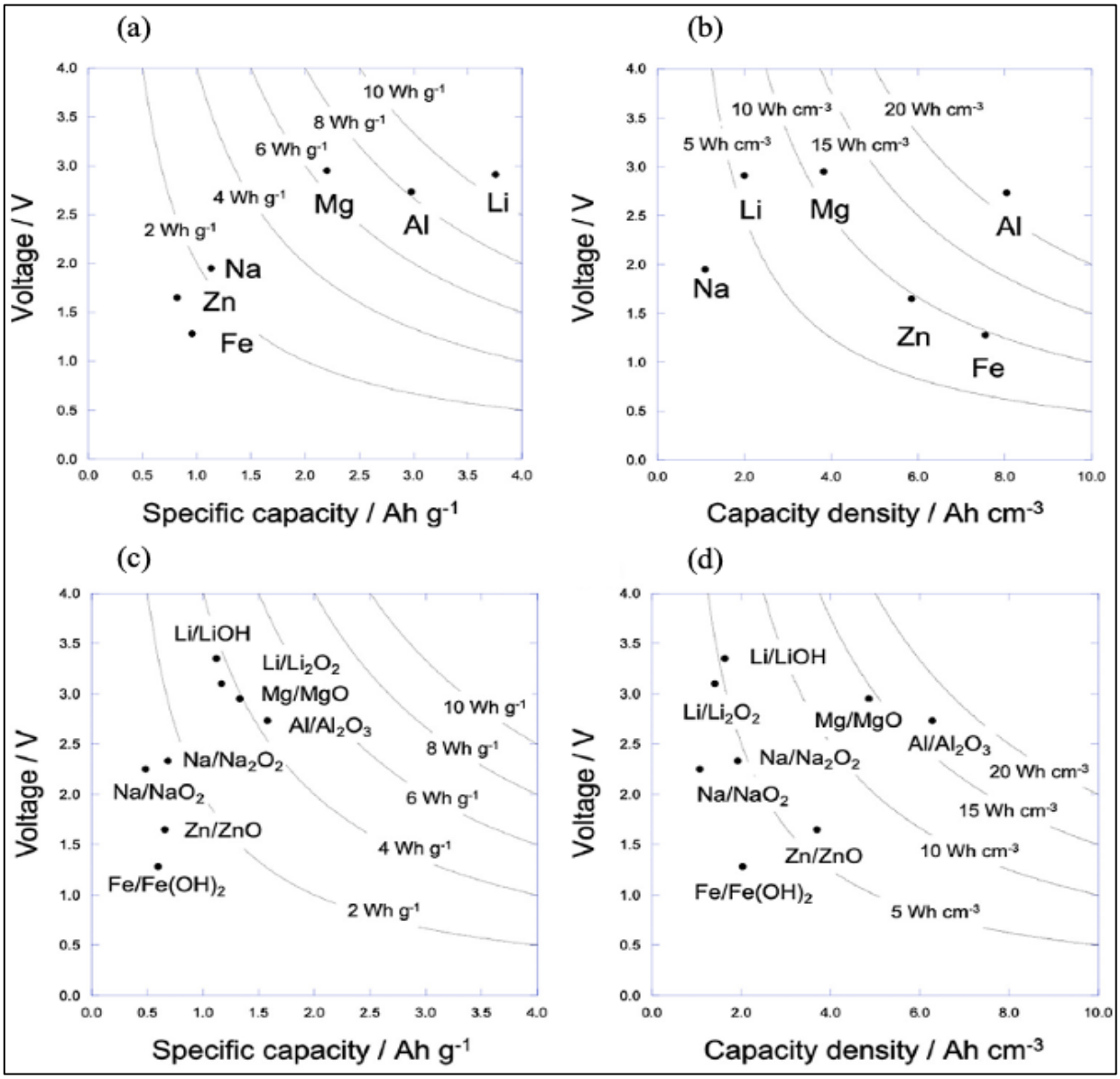


Figure 2. 6: The metal's mass and volume define the theoretical (a) specific energy and (b) volumetric energy density of MABs, whereas the plots (c) and (d) include the discharged products [80].

It's important to note that for rechargeable MABs (either electrically or mechanically), a more precise comparison would involve using data from discharged states. This is because the discharged material tends to be heavier and larger than its charged counterparts. Figures 2.6(c) and (d) showcase the theoretical energy storage potential including the discharged materials. Here, this potential is reduced as the by-products dissolve in the electrolyte. For comparison, the theoretical values for a common Li-ion battery ($LiCoO_2$) are 2.9 Wh cm^{-3} and 0.78 Wh g^{-1}, which in turn highlights the significant theoretical advantage of MABs for energy storage capacity. Accompanying this discussion is a comprehensive table that outlines the key theoretical parameters for each anode material, serving as a reference point for understanding the performance expectations of these technologies. In Table 2.2, specific energy values were determined by numerically integrating the oxygen uptake between the completely charged and completely discharged states of the battery. Volumetric energy densities were evaluated based on the anode density in its completely discharged state. Please refer to Table 2.1 for the equations used to calculate the specific energy values.

However, a significant drawback lies in their discharge behaviour. Unlike Li-ion batteries, where electrode volume changes are minimal, the volume of MABs can increase by several tens of percent during discharge. This can pose challenges for their reusability. Interestingly, some MAB configurations can be manufactured pre-discharged (for instance, an anode built of metal oxide) and then activated through charging. The voltage output of MABs is typically stable and flat, reflecting a straightforward two-phase reaction between the metal anode and its products. The non-conductive nature of these discharged materials, compared to the highly conductive metals in their initial state, leads to voltage drops during discharge cycles [80-83].

To learn more about the potential and limitations of MABs, it is essential to explore the specific characteristics of each battery chemistry. While the general principles of MABs provide a foundational overview, the unique properties and performance metrics of individual MAB types are critical in determining their suitability for various applications, particularly in EVs. This detailed examination will not only highlight the distinct advantages and challenges associated with each type but will also provide valuable insights into their theoretical performance parameters. To facilitate this analysis, the following sections will delve into the specific MAB chemistries, beginning with Li-air batteries, to examine their design, functionality, and practical implications.

Table 2. 2: Theoretical parameter comparison across various metal-air batteries

Parameter	Li-air	K-air	Na-air	Mg-air	Al-air	Zn-air	Ca-air	Fe-air	Sn-air	Si-air	Ge-air
Specific Energy (Wh kg^{-1})	5928	187	680	5238	5779	1218	3441	1080	768	5321	2214
Specific Power (W kg^{-1})	-	-	12-300	20-550	15-130	10-200	-	-	-	-	-
Specific Capacity (Ah kg^{-1})	2003	501	730	1695	2132	733	983.1	844	800	2548	1223
Volumetric Capacity density (Ah L^{-1})	2699	807	1072	3112	3817	3694	2164	2537	4944	3212	2633
Volumetric Energy Density (Wh L^{-1})	7989	1913	2466	9619	10347	6136	7574	3244	4747	6713	4766
Theoretical Open Circuit Voltage (V $cell^{-1}$)	2.96	2.37	2.3	3.09	2.71	1.66	3.5	1.28	0.96	2.09	1.81
Energy Efficiency (%)	68-94	-	-	-	70	-	-	96	70-90	-	-
Operational Temperature Range (°C)	10-40	-	105-110	420-620	30-50	-20-70	-	-	-	-	-
Cost ($\$kg^{-1}$)	46	13.02	1.7	11.02	2.866	3.351	5.93	0.4	28.66	4.19	1400

2.1.1 Lithium-Air Batteries

Lithium-air (Li-air) batteries were first conceptualized in 1976, though it wasn't until 1996 that Abraham et al. successfully demonstrated a practical Li-air battery using a non-aqueous electrolyte [84]. This technology has garnered significant attention due to its unique properties. Li-air batteries utilize lithium, the lightest element, and boast a remarkable theoretical specific energy. This value can reach 13000 Wh kg^{-1} calculated solely on the mass of lithium metal. However, considering the weight of the entire oxidized Li anode, the specific energy is still high at 5928 Wh kg^{-1}. Additionally, Li-air batteries possess an exceptional specific capacity of 2003 Ah kg^{-1} and operate at a voltage of 2.91 V [85-87]. Several Li-air battery architectures have been researched, including liquid electrolytes (aqueous and non-aqueous), hybrid (combining liquid and solid-state approaches), and the solid-state electrolyte system.

Driven by their high theoretical energy capacity and comparatively simpler construction, Li-air batteries with non-aqueous electrolytes have accumulated immense research effort [88-90]. These batteries (Figure 2.7) rely on a Li metal for the anode and an air electrode that reacts with oxygen from the atmosphere. The components are isolated by a thin membrane, while an organic electrolyte enables the mobility of Li ions during operation. The reaction produces solid, insoluble Li_2O_2 as the discharge product and the corresponding reactions are shown in Table 2.3 [91,92]. Though these batteries possess a substantial amount of theoretical energy densities (3505 Wh kg^{-1} and 3436 Wh L^{-1}), they exhibit high decomposition overpotential during the charging cycle. Additionally, during the discharge cycle, pore clogs of lithium oxide (Li_2O_2) within the cathode structure reduce the overall performance, and there is a necessity for pure oxygen as fuel limiting the design configurations. Moreover, unfavourable side reactions are observed, stemming from reactions with water and carbon dioxide at both electrodes.

The aqueous Li-air battery (Figure 2.7) offers an alternative approach to the non-aqueous design. The electrolyte is placed in the cathode compartment to address safety concerns and prevent lithium from reacting with water. This battery also employs a special Li ion conducting separator between the anode and the electrolyte [93-95]. The reactions at the cathode differentiate between aqueous and non-aqueous Li-air batteries. This complexity arises from the dependence of these cathodic reactions on electrolyte pH. At low pH (acidic environment), oxygen consumes H^+ ions to form water, while an alkaline environment promotes a reaction with H_2O to produce

OH^- ions. This contrasting behaviour significantly impacts the standard reaction potential (Refer to Table 2.3 for the relevant reactions).

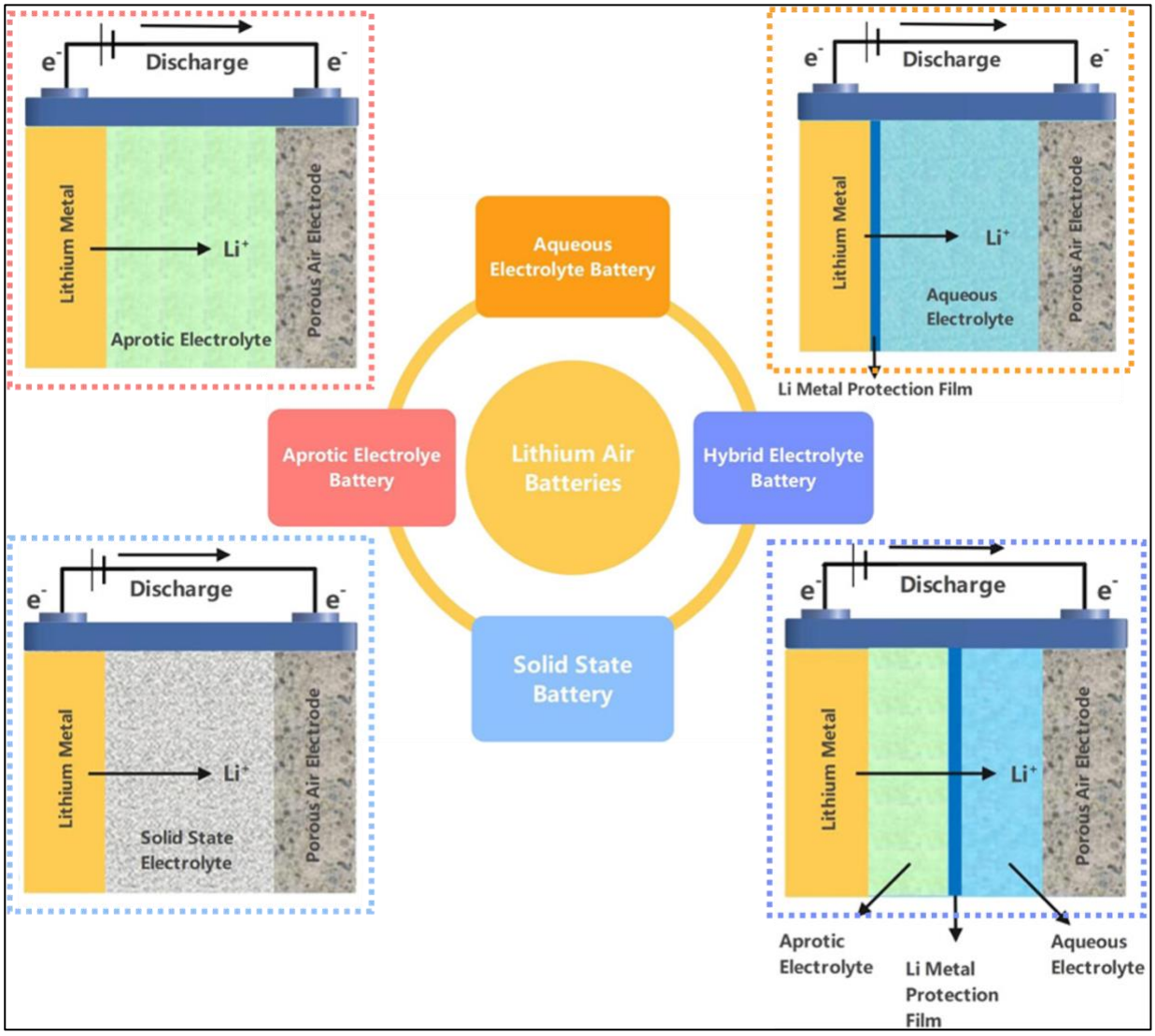


Figure 2. 7: Classification of Li-air battery technologies with schematic representations. Modified from [87].

While the theoretical energy density of aqueous Li-air batteries (1910 Wh kg^{-1}) falls short of their non-aqueous counterparts (3505 Wh kg^{-1}), it still surpasses the energy potential of gasoline. However, the key strength of aqueous Li-air batteries lies in their inherent compatibility with atmospheric air. Unlike non-aqueous Li-air systems, where severe water contamination from the environment can occur, aqueous designs are less susceptible to this issue. Furthermore,

the discharge product, LiOH, exhibits solubility within the aqueous electrolyte. This characteristic offers the potential for significantly reduced overpotential during the charging cycle and improved areal discharge capacity [96]. However, the lithium anode struggles with long-term stability, forcing efforts to maintain a neutral pH and minimize corrosion of the separator. Additionally, the battery's discharge capacity is reduced because of the limited conductivity of the separator at room temperature. While high temperatures can improve conductivity, they introduce other problems like electrolyte evaporation and higher corrosion rates. Furthermore, LiOH precipitation on the cathode during discharge hinders performance, requiring novel cathode designs with improved air channels [97-105]. By examining and comparing the pros and cons of both aqueous and non-aqueous Li-air battery technologies, it becomes evident that despite their promising theoretical and practical aspects, they encounter substantial challenges that necessitate significant advancements before achieving widespread commercialization.

To address some of the above-mentioned limitations, a hybrid electrolyte system was put forward in 2010 [98,100]. This design combines a Li negative electrode in a non-aqueous electrolyte (organic) with an oxygen reduction cathode in an aqueous electrolyte, separated by a LISICON (lithium superionic conductor) plate. This innovative strategy offers the potential to overcome some of the significant challenges plaguing conventional non-aqueous Li-air batteries. These challenges include lithium metal corrosion Li_2O_2 clogging of cathode pores, and comparatively lower voltage output. By strategically separating the Li anode and the oxygen reduction cathode using a LISICON plate, the hybrid system appears to circumvent these limitations [98,100]. However, a critical hurdle lies in the mechanical and chemical stability of the LISICON separator. For instance, at higher pH levels, the corrosion rate of the LISICON plate accelerates, significantly compromising its stability and long-term performance within the battery. The Li dendrites developed during the charging of the battery negatively react with LISICON. Thus, the plate's durability decreases and has a short-term functionality within the battery system. Furthermore, developing low-cost, highly efficient carbon-based composite catalysts for these batteries remains a challenge [106].

Solid-state electrolytes present a paradigm shift in Li-air battery development, offering a confluence of higher energy density and safety. These solid-state Li-air batteries typically comprise three key components: an air cathode, an electrolyte, and a Li anode (as illustrated in

Figure 2.7). Their exceptional mechanical strength and electrochemical stability enable the strategic integration of high-energy-density Li metal anodes and higher potential cathode materials. This synergy unlocks the potential for significant advancements in energy density without compromising safety. Additionally, solid-state electrolytes simplify the manufacturing process due to their inherent ease of preparation, shaping, and large-scale production. This translates to streamlined battery management systems and potentially reduced production costs. Finally, the thermal stability and safety of solid electrolytes eliminate the need for intricate encapsulated cooling systems, further contributing to cost reductions and overall system optimization [107-109]. While solid-state electrolytes present a favourable avenue for futuristic Li-air batteries, their widespread adoption hinges on overcoming several critical limitations. A significant challenge lies in the inherently low electrolytic conductivity of many solid-state electrolytes, particularly at lower temperatures. This limitation directly impacts the battery's ability to charge and discharge efficiently. Furthermore, high interfacial resistance at the solid-electrolyte interface hinders the flow of ions, further compromising overall battery performance. Additionally, compatibility issues can arise between certain solid-state electrolytes (SSE) and Li metal cathodes, leading to degradation and a decline in performance over time. Finally, the weak physical stability observed in some electrodes can induce significant interfacial stress changes, ultimately contributing to mechanical failure and a shortened battery lifespan [110-112]. In recognition of the crucial role that solid-state electrolytes play in enabling efficient ionic transport between the anode and cathode, researchers [113-121] are diligently pursuing solutions to address the limitations. This multi-pronged approach encompasses advancements in SSE materials, cathode materials, and anode materials. Notably, optimizing the properties of SSEs remains a key factor in unlocking the utmost capability of solid-state Li-air batteries [122].

Table 2. 3: Various metal anodes with electrolytes used in MABs: cell descriptions, electrode reactions, redox reactions, and electrochemical potentials.

Metal	Electrolyte	Cell Description	Reaction	Potential	Cell Reaction (Overall)	Refs.
Aluminum (Al)	Aqueous-Neutral	Anode: Aluminum Cathode: Air-breathing Electrolyte: Any neutral media	Anode: $Al + 3H_2O \rightarrow Al(OH)_3 + 3H^+ + 3e^-$ Cathode: $O_2 + 4e^- + 2H_2O \rightarrow 4OH^-$	Anode: -1.47 V Cathode: 0.81 V	$Al + \frac{3}{4}O_2 + \frac{3}{2}H_2O \rightarrow Al(OH)_3$ (2.28 V)	[123,124]
	Aqueous-Alkaline	Anode: Aluminum Cathode: Air-breathing Electrolyte: Any basic media	Anode: $Al + 4OH^- \rightarrow Al(OH)_4^- + 3e^-$ Cathode: $O_2 + 4e^- + 2H_2O \rightarrow 4OH^-$ Side: $Al + 3H_2O + OH^- \rightarrow Al(OH)_4^- + \frac{3}{2}H_2$	Anode: -2.35 V Cathode: 0.39 V	$Al + \frac{3}{4}O_2 + \frac{3}{2}H_2O + OH^- \rightarrow Al(OH)_4^-$ (2.75 V)	[125]
	Aqueous-Acidic	Anode: Aluminum Cathode: Air-breathing Electrolyte: Any acidic media	Anode: $Al \rightarrow Al^{3+} + 3e^-$ Cathode: $O_2 + 4e^- + 4H^+ \rightarrow 2H_2O$ Side: $Al + 3H^+ \rightarrow Al^{3+} + \frac{3}{2}H_2$	Anode: -1.66 V Cathode: 1.23 V	$Al + \frac{3}{4}O_2 + 3H^+ \rightarrow Al^{3+} + \frac{3}{2}H_2O$ (2.89 V)	[17]
	Organic Solvent Based: Solid-State Gel Polymer Electrolyte	Anode: Aluminum Cathode: Air-breathing (carbon and polymer-based) Electrolyte: PVA/LiCl polymer	Anode: $Al + 3OH^- \rightarrow Al(OH)_3 + 3e^-$ Cathode: $O_2 + 4e^- + 2H_2O \rightarrow 4OH^-$	Anode: -2.3V Cathode: 0.81 V	$Al + 3H_2O \rightarrow Al(OH)_3 + 3H^+$ (3.31 V)	[17,126]
	Room Temperature Ionic Liquid (RTIL) Based	Anode: Aluminum Cathode: Air-breathing Electrolyte: Aprotic room temperature ionic liquids	Anode: $Al + 7AlCl_4^- \rightarrow 4Al_2Cl_7^- + 3e^-$ Cathode: $H_2O_2 + 2H^+ + 2e^- \rightarrow 2H_2O$	Anode: -1.3 V Cathode: 0.695 V	$Al + 7AlCl_4^- + \frac{3}{2}H_2O_2 + 3H^+ \rightarrow 4Al_2Cl_7^- + 2H_2O$ (1.995* V)	[127-129]
Calcium (Ca)	Non-Aqueous: (Aprotic) Organic Electrolyte	Anode: Calcium Cathode: Air-breathing Electrolyte: Aprotic liquid	Anode*: $Ca \rightarrow Ca^{2+} + 2e^-$ Cathode 1*: $Ca^{2+} + 2O_2 + 2e^- \rightarrow Ca(O_2)_2$ Cathode 2*: $Ca^{2+} + O_2 + 2e^- \rightarrow CaO_2$ Cathode 3*: $Ca^{2+} + \frac{1}{2}O_2 + 2e^- \rightarrow CaO$	Anode: -2.368 V Cathode: varies	$Ca + 2O_2 \rightarrow Ca(O_2)_2$ (3.25 V) $Ca + O_2 \rightarrow CaO_2$ (3.28 V) $Ca + \frac{1}{2}O_2 \rightarrow CaO$ (3.13 V)	[130-133]
	Non-Aqueous-Ionic Liquid	Anode: Calcium Cathode: Carbon nanotube sheet Electrolyte: Ca salt in 1:1 EMIM-BF_4/DMSO solution	Anode: $Ca \rightarrow Ca^{2+} + 2e^-$ Cathode 1: $O_2 + 2Ca^{2+} + 4e^- \rightarrow 2CaO$ Cathode 2: $2O_2 + 2Ca^{2+} + 4e^- \rightarrow 2CaO_2$	Anode: -2.868 V Cathode: 0.715 V* Cathode: 0.265 V*	$O_2 + 2Ca \rightarrow 2CaO$ (3.583 V*) $2O_2 + 2Ca \rightarrow 2CaO_2$ (3.133 V*)	[134]

Metal	Electrolyte	Cell Description	Reaction	Potential	Cell Reaction (Overall)	References
Iron (Fe)	Aqueous-Alkaline	Anode: Iron Cathode: Air-breathing Electrolyte: Basic media	Anode: $3Fe + 8OH^- \rightarrow Fe_3O_4 + 4H_2O + 8e^-$ Cathode: $O_2 + 4e^- + 2H_2O \rightarrow 4OH^-$ Side: $2H_2O + 2e^- \rightarrow H_2 + 2OH^-$	Anode: -0.88 V Cathode: 0.401 V	$3Fe + 2O_2 \rightarrow Fe_3O_4$ (1.28 V)	[135,136]
	Solid Oxide	Anode: Ni-Fe alloy Cathode: $Ba_{0.6}La_{0.4}CoO_3$ Electrolyte: LSGM Fuel: Iron powder	Anode: $H_2 + O^{2-} \rightarrow H_2O + 2e^-$ Cathode: $\frac{1}{2}O_2 + 2e^- \rightarrow O^{2-}$ Iron Powder: $3Fe + 4H_2O \rightarrow Fe_3O_4 + 4H_2$	Anode: - Cathode: -	$3Fe + 2O_2 \rightarrow Fe_3O_4$ (0.97 V)	[137-141]
Lithium (Li)	Aprotic Solvent	Anode: Lithium Cathode: Porous carbon Electrolyte: Aprotic liquid	Anode: $Li \rightarrow Li^+ + e^-$ Cathode: $O_2 + Li^+ + e^- \rightarrow LiO_2$ Cathode: $LiO_2 + Li^+ + e^- \rightarrow Li_2O_2$ Cathode: $O_2 + 2Li^+ + 2e^- \rightarrow Li_2O_2$ Cathode: $Li_2O_2 + 2Li^+ + 2e^- \rightarrow 2Li_2O$ Cathode: $O_2 + 4Li^+ + 4e^- \rightarrow 2Li_2O$	Anode: -3.0401 V Cathode: varies	$O_2 + Li \rightarrow LiO_2$ (3.0 V) $LiO_2 + Li \rightarrow Li_2O_2$ (2.96 V) $O_2 + 2Li \rightarrow Li_2O_2$ (3.10 V) $Li_2O_2 + 2Li \rightarrow 2Li_2O$ (2.91 V) $O_2 + 4Li \rightarrow 2Li_2O$ (2.91 V)	[142-145]
	Aqueous-Acidic	Anode: Lithium Cathode: Air-breathing Electrolyte: Acidic media	Anode: $Li \rightarrow Li^+ + e^-$ Cathode: $\frac{1}{2}O_2 + 2e^- + 2H^+ \rightarrow H_2O$	Anode: -3.0401 V Cathode: 1.229 V	$2Li + \frac{1}{2}O_2 + 2H^+ \rightarrow H_2O + 2Li^+$ (4.274 V)	[146]
	Aqueous-Alkaline	Anode: Lithium Cathode: Air-breathing Electrolyte: Basic media	Anode: $Li \rightarrow Li^+ + e^-$ Cathode: $\frac{1}{2}O_2 + H_2O + 2e^- \rightarrow 2OH^-$	Anode: -3.0401 V Cathode: 0.401 V	$2Li + \frac{1}{2}O_2 + H_2O \rightarrow 2LiOH$ (3.44 V)	[146]
Magnesium (Mg)	Aqueous-Neutral	Anode: Magnesium (or alloy) Cathode: Air-breathing Electrolyte: Saline	Anode: $Mg \rightarrow Mg^{2+} + 2e^-$ Cathode: $O_2 + 4e^- + 2H_2O \rightarrow 4OH^-$ Side: $2H_2O + 2e^- \rightarrow H_2 + 2OH^-$	Anode: -2.37V Cathode: 0.81V	$2Mg + O_2 + 2H_2O \rightarrow 2Mg(OH)_2$ (3.1 V)	[127]
Potassium (K)	K Salt Ether Solvent, Potassium Superoxide	Anode: Potassium Cathode: Air-breathing Electrolyte: Organic	Anode: $K \rightarrow K^+ + e^-$ Cathode: $O_2 + e^- \rightarrow {O_2}^-$	Anode: -2.931 V Cathode: -0.451V*	$K + O_2 \rightarrow KO_2$ (2.48 V)	[127,147]

Metal	Electrolyte	Cell Description	Reaction	Potential	Cell Reaction (Overall)	References
Silicon (Si)	Non-Aqueous - RTIL: EMIm (HF) 2.3F	Anode: Silicon Cathode: Air-breathing Electrolyte: Room temperature ionic liquids	Anode: $Si + 12(HF)_2F^- \rightarrow SiF_4 + 8(HF)_3F^- + 4e^-$ Cathode: $O_2 + 12(HF)_3F^- + 4e^- \rightarrow 2H_2O + 16(HF)_2F^-$ SiO_2 formation: $SiF_4 + 2H_2O + 4(HF)_2F^- \rightarrow SiO_2 + 4(HF)_3F^-$	Anode: -2.71 V Cathode: 0.40 V	$Si + O_2 \rightarrow SiO_2$ (2.21 V)	[148]
	Aqueous - Alkaline: KOH	Anode: Silicon Cathode: Air-breathing Electrolyte:	Anode: $Si + 4OH^- \rightarrow Si(OH)_4 + 4e^-$ Cathode: $O_2 + 4e^- + 2H_2O \rightarrow 4OH^-$	Anode: -2.71 V Cathode: -0.44 V Alternate: -0.38	$Si + O_2 + 2H_2O \rightarrow Si(OH)_4$ (2.09 V)	[148]
Sodium (Na)	Aqueous-Neutral	Anode: Sodium Cathode: Air-breathing Electrolyte: Saline	Anode: $Na \rightarrow Na^+ + e^-$ Cathode: $O_2 + 4e^- + 2H_2O \rightarrow 4OH^-$	Anode: -0.96 V Cathode: 0.33 V	$4Na + O_2 + 2H_2O \rightarrow 4NaOH$ (3.11 V)	[149]
	Aprotic Solvent	Anode: Sodium Cathode: Air-breathing Electrolyte: Aprotic solvent	Anode: $Na \rightarrow Na^+ + e^-$ Cathode: $O_2 + e^- \rightarrow {O_2}^-$ Alternate Cathode: $O_2 + 2e^- \rightarrow {O_2}^{2-}$	Anode: -2.71 V Cathode: -0.44 V Alternate: -0.38V	$Na + O_2 \rightarrow NaO_2$ (2.27 V) $2Na + O_2 \rightarrow Na_2O_2$ (2.33 V)	[149,150]
Tin (Sn)	Solid Oxide	Anode: Tin Alloy Cathode: LSM/LSM-GDC Electrolyte: Ethylene glycol with tin powder (high temperature)	Anode: $Sn + 2{O_2}^{2-} \rightarrow SnO_2 + 4e^-$ Cathode*: $O_2 + 2e^- \rightarrow {O_2}^{2-}$	Anode: -0.96 V Cathode: 0.33 V	$Sn + 2O_2 \rightarrow SnO_2$ (1.29 V)	[151]
Vanadium (Va)	Aqueous-Acidic	Anode: Zinc Cathode: Air-breathing	Anode: $V^{2+} \rightarrow V^{3+} + e^-$ Cathode: ${VO_2}^+ + 2H^+ + 2e^- \rightarrow VO^{2+} +$	Anode: -0.26 V Cathode: 1.0 V	${V^{2+}} + {VO_2}^+ + 2H^+ \rightarrow V^{3+} + VO^{2+} + H_2O$ (1.26 V)	[152-154]
	Vanadium-Oxygen Fuel Cell	Anode: Vanadium Cathode: Oxygen diffusion electrode Electrolyte:	Anode: $V^{2+} \rightarrow V^{3+} + e^-$ Cathode: $O_2 + 4e^- + 4H^+ \rightarrow 2H_2O$	Anode: -0.26 V Cathode: 1.23 V	$4V^{2+} + O_2 + 4H^+ \rightarrow 4V^{3+} + 2H_2O$ (1.49 V)	[153]

Metal	Electrolyte	Cell Description	Reaction	Potential	Cell Reaction (Overall)	References
Zinc (Zn)	Aqueous-Neutral	Anode: Zinc Cathode: Air-breathing Electrolyte: any neutral media	Anode: $Zn \rightarrow Zn^{2+} + 2e^-$ Cathode: $O_2 + 4e^- + 2H_2O \rightarrow 4OH^-$	Anode: -0.762 V Cathode: 0.817 V	$2Zn + O_2 + 2H_2O \rightarrow 2Zn(OH)_2$ (1.579 V)	[155]
	Aqueous-Alkaline	Anode: Zinc Cathode: Air-breathing Electrolyte: any basic media	Anode: $Zn + 2OH^- \rightarrow ZnO + H_2O + 2e^-$ Cathode: $O_2 + 4e^- + 2H_2O \rightarrow 4OH^-$	Anode: -1.26 V Cathode: 0.40 V	$2Zn + O_2 \rightarrow 2ZnO$ (1.66 V)	[156]
	Non-Aqueous: Protic Room Temperature Ionic Liquids	Anode: Zinc Cathode: Air-breathing Electrolyte: Protic room temperature ionic liquid	Anode: $Zn \rightarrow Zn^{2+} + 2e^-$ Cathode: $O_2 + 2H^+ + 2e^- \rightarrow H_2O_2$	Anode: -0.7618 V Cathode: 0.695 V	$Zn + O_2 + 2H^+ \rightarrow Zn^{2+} + H_2O_2$ (1.457 V)	[157]
Germanium (Ge)	Aqueous-Alkaline: 1- 6M KOH	Anode: Germanium wafers Cathode: Air-breathing Electrolyte: Aqueous KOH	Anode: $Ge + 4OH^- \rightarrow Ge(OH)_4 + 4e^-$ Cathode: $O_2 + 4e^- + 2H_2O \rightarrow 4OH^-$ Passivation: $Ge(OH)_4 \rightarrow GeO_2 + 2H_2O$	Anode: 1.0 V Cathode: 0.81 V	$Ge + O_2 + 2H_2O \rightarrow Ge(OH)_4$ (1.81 V)	[158]

2.1.2 Zinc-Air Batteries

Zinc-air (Zn-air) batteries currently hold the distinction of being the sole commercially available metal-air battery technology worldwide. Their extensive history underscores their efficacy in low-current, long-duration applications such as hearing aids. Early prototypes of Zn-air batteries date back to the 1870s. Advancements in electrode design soon followed, paving the way for the primary Zn-air batteries to the market in the 1930s, ultimately leading to their widespread adoption in hearing aids by the 1970s [159,160]. While zinc exhibits a lower specific capacity (733 Ah kg^{-1}) compared to certain alternative metals investigated for MABs (e.g., lithium and aluminum), they continue to demonstrate notable performance. This is evidenced by their impressive theoretical specific energy and energy density as mentioned earlier. Furthermore, Zn-air batteries boast high anode utilization and compatibility with alkaline electrolytes. This compatibility offers a distinct advantage, as the comparatively slower reaction rate between the alkaline electrolyte and zinc minimizes hydrogen evolution, a significant challenge encountered in other metal-air chemistries (like Al and Mg-based MABs). These properties position them as strong contenders in the development of next-generation portable, flexible electronics, and in the electrification of automobiles [161-164]. Zn-air batteries can be broadly classified into primary, mechanically rechargeable, and electrically rechargeable types. A typical primary Zn-air cell comprises several key components such as a zinc anode, a separator, an electrolyte and an air cathode [165]. Mechanically rechargeable Zn-air batteries operate as functionally similar to primary batteries, relying on replacing the Zn anode and electrolyte during recharge. This distinct characteristic necessitates the use of only ORR electrocatalysts at the cathode [166]. Commercially proven primary Zn-air batteries, known for their high energy density, are used in power hearing aids (in the form of button cells) and even telecommunications and satellite systems in prismatic pouch formats. One key challenge associated with primary or replenishable primary Zn-air batteries is the potential for electrolyte evaporation. This evaporation can disrupt ionic conductivity within the battery, ultimately leading to performance degradation [167-170].

Rechargeable Zn-air batteries come in various arrangements, differing in their electrolyte types and design configurations. The most common design, depicted in Figure 2.8(a), utilizes a simple "sandwich" framework with four key components. The first is a zinc anode. The second component, the air electrode, incorporates bifunctional oxygen electrocatalysts, a gas diffusion layer (GDL), and a current tab. Finally, the design is completed by a liquid electrolyte and a

separator. This configuration allows for easy assembly in research labs using readily available materials like rubber gaskets, steel or plastic plates, and chambers.

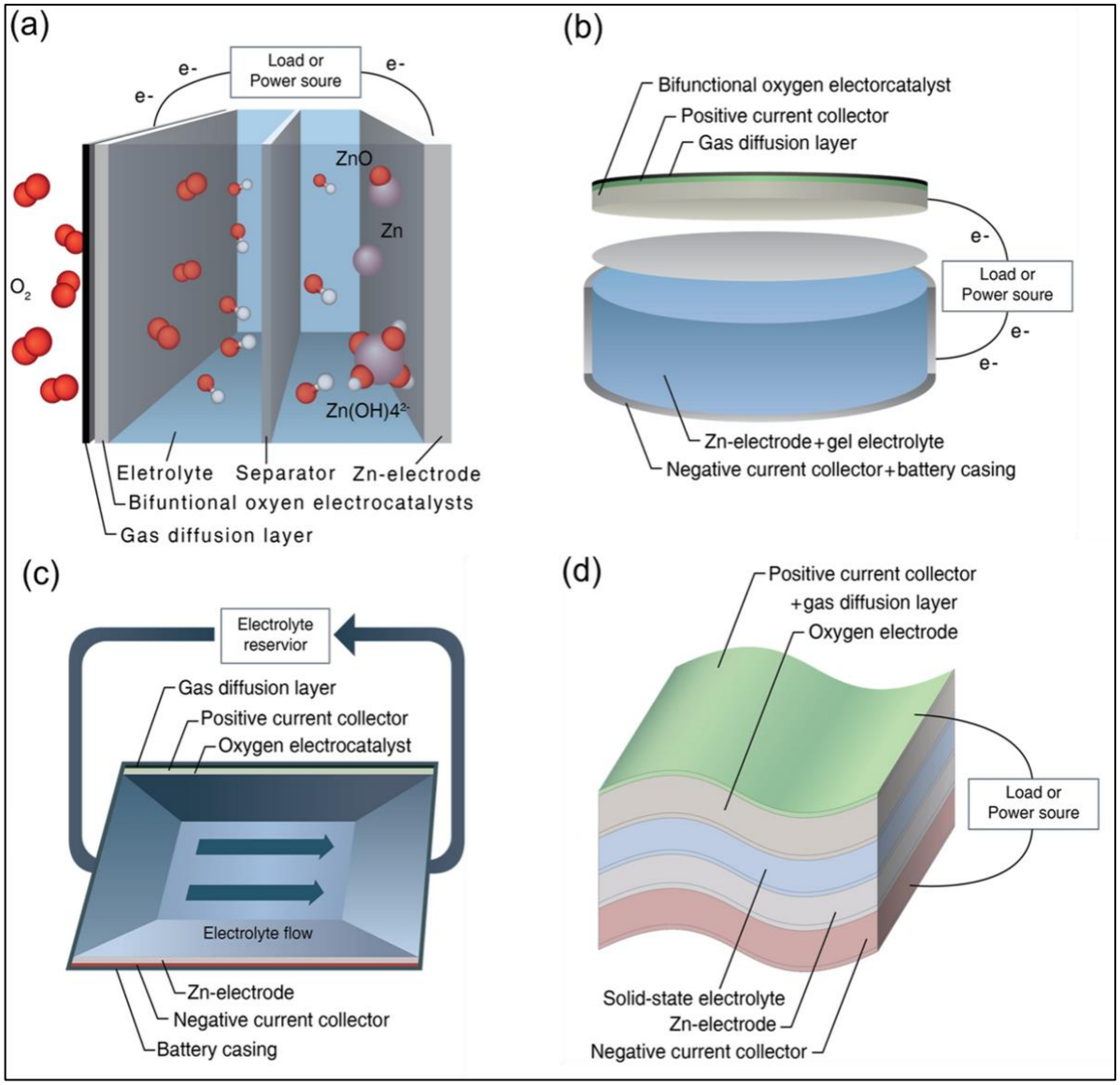


Figure 2. 8: Rechargeable Zn-air battery designs: (a) Planar architecture with aqueous electrolyte, (b) Planar architecture with gel electrolyte, (c) Electrolyte flow-through design, (d) Flexible configuration (Adapted from [171]).

Although planar Zn-air batteries can be arranged either horizontally or vertically, the vertical configuration is preferred to avoid electrolyte evaporation issues and ensure better ionic connectivity. While commercially available rechargeable Zn-air batteries are not yet widespread,

their simple design offers potential advantages for EVs and other applications, owing to their high energy density and lightweight properties. In contrast, the planar design can lead to challenges, such as electrolyte loss in horizontal setups, which hampers the commercial viability of these batteries [172].

Building on the foundational principles of conventional planar Zn-air batteries, the planar gel electrolyte architecture shown in Figure 2.8(b) represents an advanced iteration that addresses electrolyte evaporation loss and enhances efficiency using gel polymer electrolytes (GPEs). GPEs possess properties intermediate between liquid and solid states. Notably, they have high ionic conductivity (10^{-4} to 10^{-3} S cm^{-1} at ambient temperature), flexibility, and efficient electrolyte retention. As ionic conductors and separators, GPEs facilitate ion transport through a mechanism similar to liquid electrolytes. Despite significant advancements in GPEs, they still face challenges in making Zn-air batteries suitable for consumable electronics and EVs. Alkaline GPEs tend to generate carbonates which diminishes battery reversibility. Given the ongoing research into electrolytes, further advancements are essential to address these limitations [173].

A Zn-air flow battery (Figure 2.8(c)) utilizes a circulating electrolyte design to enhance performance and mitigate degradation issues associated with both the anode and cathode. On the metal anode side, the larger volume flowing electrolyte improves the current distribution and reduces concentration gradients, which helps prevent shape change, dendrite formation, and passivation. The precipitated carbonate layer on the cathode can be washed away by the flowing electrolyte and removed using an external filter. This design is comparable to the approach utilized in alkaline fuel cells, where circulating electrolytes are employed to prevent carbonate precipitation on the cathode surface. Consequently, rechargeable Zn-air flow batteries are expected to offer longer cycle life compared to traditional static electrolyte configurations. However, Zn-air flow batteries also come with certain disadvantages. The increased complexity of the system, which includes the need for pumps, tubing, and circulating the electrolyte, results in decreased energy efficiency. Additionally, the excess volume of electrolytes and the associated components lead to lower specific and volumetric energy density [174-176].

A Zn-air flexible battery (Figure 2.8(d)) is an innovative power source designed to be flexible, making it suitable for various applications such as wearable technology. They are preferred due to their cost-effectiveness, high energy density, and intrinsic safety, which obviates the need for a rigid protective casing. Many studies are exploring methods and materials to

produce flexible Zn-air batteries, including thin-film “wearable” designs, cylindrical cable-type batteries, and biocompatible flexible batteries. The key challenge in developing flexible Zn-air batteries is their exposure to the air, making the use of liquid electrolytes undesirable due to risks of evaporation or leakage onto sensitive electronic equipment. Consequently, current research efforts are centred on developing a solid-state electrolyte that is mechanically flexible, durable, and exhibits adequate ionic conductivity. Additionally, the electrodes and other cell components must be capable of withstanding and maintaining operation under significant bending. Despite these challenges, the advantages of flexibility, safety, and high energy density make Zn-air flexible batteries a promising choice for future energy storage solutions [177-179].

2.1.3 Magnesium-Air Batteries

In 1966, Carson and Kent conducted conceptual and practical investigations into high-performance magnesium-air (Mg-air) primary cells, termed the "Magair" cell. This system employed an air cathode, a Mg alloy anode, and a neutral salt electrolyte, achieving a nominal voltage of 1.60 V. During discharge, the cell exhibited voltages of 1.30 V and 1.00 V at current densities of 10 and 60 mA cm^{-2}, respectively. The authors also demonstrated the concept of mechanical rechargeability through periodic replenishment of the anode and electrolyte salt [180]. While Mg-air batteries have received comparatively less attention than other MAB technologies, their potential as energy storage systems is compelling due to magnesium's abundance and the battery's high theoretical energy density. Moreover, when considering practical performance metrics, Mg-air batteries exhibit competitive advantages over Zn-air and Al-air technologies. Since their inception in the 1960s, studies on Mg-air cells have been mostly centered around the primary, or reserve-type, configurations. These batteries require activation before use and offer continuous discharge until anode depletion. Conversely, developing rechargeable Mg-air batteries has proven significantly more challenging [181].

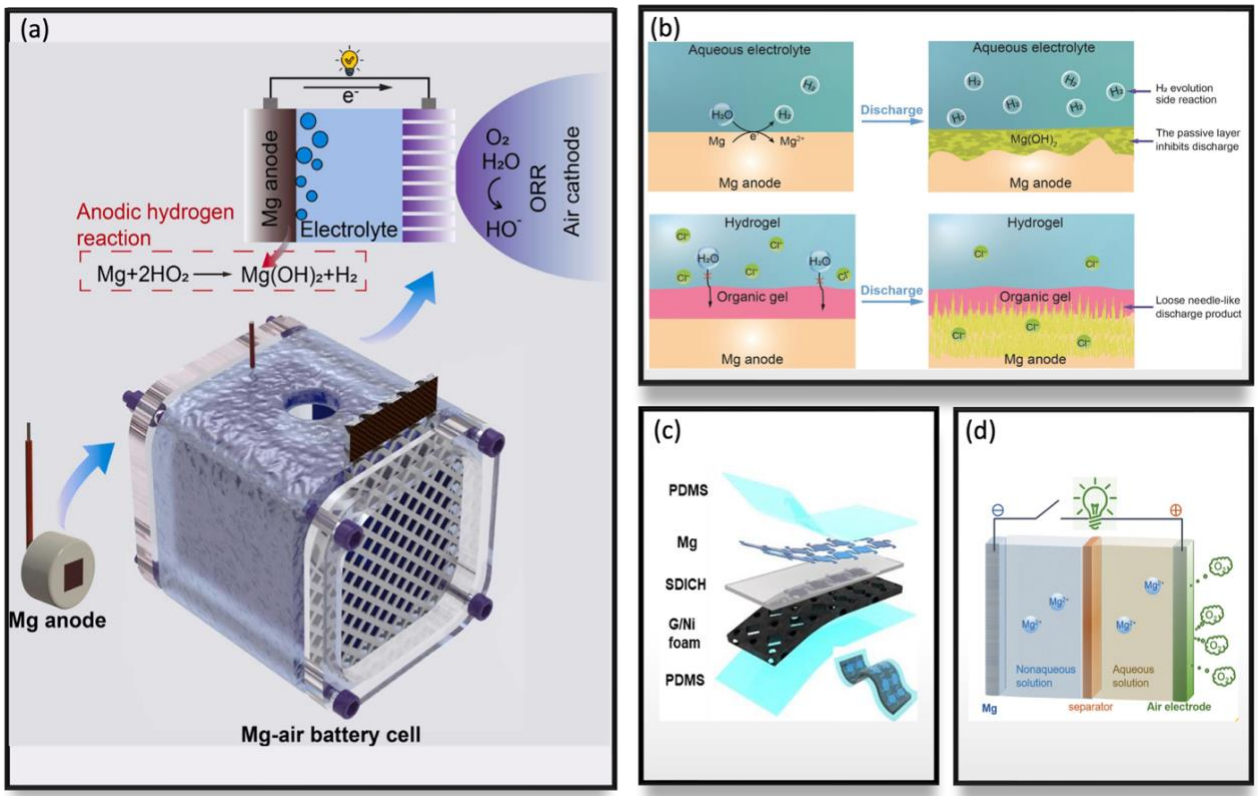


Figure 2. 9: Mg-air battery configurations: (a) Planar architecture with aqueous electrolyte [182], (b) Two-layer gel electrolyte structure [183], (c) Flexible configuration [184], (d) Hybrid electrolyte design [185].

In general, Mg-air batteries face several hurdles, including low working voltage and practical specific energy, substantially below theoretical values. These limitations stem largely from sluggish oxygen reduction kinetics and anode corrosion, common challenges in MAB systems. Magnesium's unique corrosion behaviour, exacerbated by impurities, further complicates the issue. Unlike most metals, magnesium exhibits a negative difference effect, where increasing cathodic current accelerates hydrogen evolution. Additionally, the poor conductivity and electrochemical activity of discharge products (MgO and MgO_2) hinder rechargeability [186]. Figure 2.9 illustrates various configurations of Mg-air batteries, categorized by cell architecture and electrolyte types.

Chen et al. [182] devised a planar structure utilizing ultra-high-purity (UHP) Mg-Ge anodes for Mg-air cells, enhancing their performance significantly as shown in Figure 2.9(a). The inclusion of Ge in the anode composition improves anodic reaction activity while effectively suppressing the anode hydrogen evolution reaction (HER). The electrolyte utilized in this system is a 3.5 wt. % NaCl solution, which facilitates ion transport during the electrochemical processes.

The UHP Mg-0.5Ge anode possessed an impressive cell voltage of 1.69 V at a current density of 0.5 mA cm^{-2} during discharge and achieved a high energy density of 2272 mWh g^{-1} at 20 mA cm^{-2}. These performance metrics surpass those of all previously researched Mg-based anodes. Moreover, the low content of impurity and the formation of a Ge-bearing surface layer results in a remarkable 95% discharge efficiency. This is 3.5 times greater than that of the frequently used AZ31 anode. Thus, the advantages include enhanced discharge characteristics and improved battery efficiency due to the low impurity content and a Ge-bearing surface film as mentioned. However, potential disadvantages may arise from the corrosive nature of the NaCl electrolyte, which might impact the longevity of the cell components, alongside the complexities associated with manufacturing high-purity materials, raising concerns about cost and scalability. Overall, the exceptional properties of the UHP Mg-Ge anode pave the way for significant advancements in Mg-air batteries.

Li et al. [183] employ a two-layer gel electrolyte structure that addresses significant performance limitations associated with Mg anodes. The architecture consists of a Mg anode, an air-breathing cathode and a two-layer gel electrolyte as described in Figure 2.9(b). The two layers built of an organic gel and hydrogel, were evenly coated on the surface of the anode. It serves two primary functions: the first layer prevents corrosion of the Mg anode, while the second layer inhibits the development of a thick, insoluble passive layer that forms on the Mg's surface during discharge and corrosion processes. This design enables effective interaction between the Mg anode and the electrolyte, facilitating the battery's operation. The working mechanism involves the reaction of Mg with water in the electrolyte, producing magnesium hydroxide and releasing H_2 gas, with electrons being transferred directly to the electrolyte. Key results from this study indicate that these Mg-air batteries achieved an impressive specific capacity of 2190 mAh g^{-1} based on the anode alone and an anode efficiency of 99.3%, alongside an energy density of 2282 Wh kg^{-1} based on the Mg anode and air electrode. The dual-layer architecture presents several advantages, including enhanced battery performance, improved efficiency, and high utilization of the Mg anode. However, it also has drawbacks, such as increased complexity in the cell's design and potential concerns regarding the long-range stability of the gel electrolyte in various environmental conditions.

The architecture of the cell is based on a completely flexible Mg-air battery that employs dual-ion-conducting hydrogels (SDICH) as illustrated in Figure 2.9(c). This design allows for

significant mechanical flexibility and stretchability, making it suitable for integration into biomedical devices. The materials used include a Mg anode, an air-breathing cathode, and an SDICH electrolyte. This combination produces electricity while maintaining the necessary flexibility and stretchability for biomedical applications. The battery successfully powered 120 light-emitting diodes (LEDs) for over 5 hours, demonstrating its capacity and efficiency. It exhibited stable electrical output even under mechanical stretching, indicating resilience to deformation without performance degradation. The biocompatibility of the battery was validated through in vitro and in vivo studies, showcasing its ability to be used in medical applications. The stretchable design allows the battery to be integrated into wearable and flexible devices, making it safe for use in biomedical applications, particularly in systems that are in contact with human tissue, such as wound dressings. However, the long-term stability of the dual-ion-conducting hydrogel under various environmental conditions may require further investigation. Additionally, the production of such advanced materials and architectures may be more complex and costly compared to simpler battery designs [184].

Hybrid electrolyte Mg-air batteries (Figure 2.9(d)) use both aqueous and non-aqueous electrolytes to improve the electrochemical reactions within the battery. This approach improves the characteristics of traditional Mg-air batteries by enhancing charge transport reactions, reducing polarization effects, and enabling recharging capabilities. Hybrid electrolyte Mg-air batteries offer several advantages. They can achieve up to 90% round-trip efficiencies, making them an attractive option for energy storage solutions. Their enhanced power density results from the integration of materials that facilitate fast charge transport and high current density. Furthermore, the design of hybrid electrolytes contributes to a longer battery lifespan by addressing issues such as self-corrosion and passivation of the Mg anode. However, there are notable disadvantages such as the Mg's self-corrosion which can produce insulating products like MgO and impedes battery performance by increasing overpotential and polarization. Additionally, parasitic reactions that produce hydrogen gas can disrupt the pressure balance within sealed cells, further increasing cell polarization. Thus, hybrid electrolytes carry inherent disadvantages, along with the complexity of managing both aqueous and non-aqueous components and the need for advanced electrocatalysts for effective oxygen reduction. These factors can reduce the operational stability of the batteries, impacting their overall efficiency and longevity [186].

2.1.4 Sodium-Air and Potassium-Air Batteries

Sodium-air (Na-air) and potassium-air (K-air) batteries demonstrate substantial energy densities in contrast to other battery technologies. Na-air batteries offer a specific energy of 1680 Wh kg^{-1} and a volumetric energy density of 2466 Wh L^{-1}, while K-air batteries exhibit a specific energy of 1187 Wh kg^{-1} and a volumetric energy density of 1913 Wh L^{-1}. These impressive figures underscore the significant potential of sodium and potassium-based systems for future energy storage applications. However, despite concerted research efforts during the last few decades, advancements in the research area of alkali MABs remain in their early stages. Peled et al. [187] introduced the theories of the Na-air batteries in 2011. This initial cell configuration employed a liquid sodium anode, a polymer electrolyte, and a commercial air cathode. To prevent sodium metal buildup on the air electrode, the system was run at a high temperature of 105°C to 110°C, exceeding sodium's melting point. Ren et al. [60] first illustrated the idea of a K-O_2 battery in 2013, showcasing decreased overpotentials by leveraging the reversibility of the O_2/O_2^- redox couple. For the first time, they reported a charge/discharge potential gap smaller than 50 mV at a current density of 0.16 mA cm^{-2}. Raman analyses and XRD verified the generation and decomposition of KO_2 during the battery cycle test. In the literature, K-air and K-O_2 batteries are often used interchangeably, but most research has been conducted with oxygen, with few works reported on dry ambient air [188].

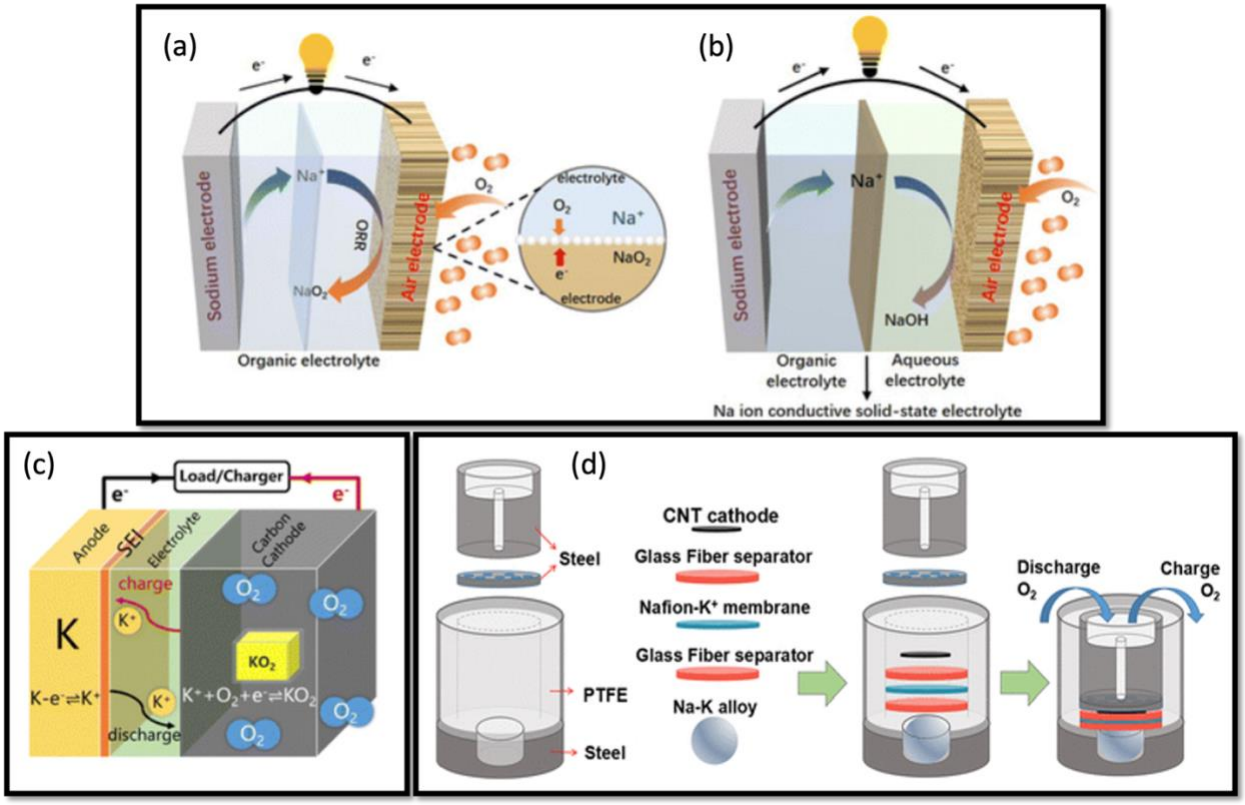


Figure 2. 10: Graphical depiction of the operational mechanisms and cell configurations of (a) Na-air cell with organic electrolyte [189], (b) Na-air cell with hybrid electrolyte [189], (c) Planar K-O_2 cell [190], (d) K-O_2 cell with Na-K alloy anode [191].

Among the various types of Na-air cells, hybrid electrolyte and organic electrolyte Na-air cells have been the most extensively studied. These two types differ primarily not only by the electrolyte type but also by their structural designs. Organic Na-air batteries constitute one primary research focus within the broader Na-air battery field. Their fundamental architecture, as depicted in Figure 2.10(a), centers around a Na anode, a porous bifunctional catalyst cathode, and an organic electrolyte-saturated separator. A range of organic solvents like dimethyl ether (DME) and diethylene glycol dimethyl ether (DEGDME), along with salts such as sodium hexafluorophosphate (NaPF6) and sodium bis(trifluoromethanesulfonyl)imide (NaTFSI), are used to modulate battery performance. The specific salt and its concentration significantly impact the battery's overall efficacy. Functionally akin to Li-O_2 due to the chemical parallels between sodium and lithium, organic Na-air batteries excel in lower overpotential and superior cycling stability [192-194].

In contrast, hybrid Na-air batteries diverge in their structural design. As shown in Figure 2.10(b), they incorporate a dual electrolyte system: an aqueous electrolyte at the anode and an organic electrolyte at the cathode, separated by a sodium ion-conductive solid electrolyte membrane, often NASICON ($Na_3Zr_2Si_2PO_{12}$). This configuration shields the anode from oxidative reactions while facilitating unidirectional sodium ion migration. The cathode electrolyte mirrors that of organic Na-air batteries, while the anode typically employs an aqueous NaOH solution. The energy storage mechanism in hybrid Na-air batteries is simpler, involving oxygen uptake and release at the positive electrode during the discharge and charge operations. This process corresponds to the ORR and OER, respectively. A key advantage of this design is the generation of a single discharge product, NaOH, which minimizes side reactions and enhances cycle life. Moreover, the solubility of NaOH in the electrolyte prevents accumulation on the air cathode, further improving efficiency. Unlike their organic counterparts, hybrid Na-air cells can function with atmospheric air and exhibit higher theoretical voltages. Both organic and hybrid Na-air batteries hold promise for diverse applications. However, they present distinct advantages and drawbacks. Organic Na-air batteries prioritize safety due to sodium's reactivity with water, but they suffer from higher costs, environmental concerns associated with organic electrolytes, and performance limitations caused by discharge product deposition. Additionally, they necessitate dry oxygen and gas purification systems, increasing operational expenses. In comparison, hybrid Na-air battery systems exhibit lower overpotentials, higher energy densities, and extended cycle life. Their ability to utilize ambient air and dissolve discharge products in the cathode electrolyte renders them more cost-effective and efficient. Consequently, hybrid Na-air batteries emerge as a compelling alternative to their organic counterparts [195-198].

Yu et al. [191] successfully showcased the novel K-O_2 battery that is dendrite-free operating at room temperature, utilizing a liquid Na-K alloy as the negative electrode, a Nafion-K^+ membrane separator, and a 0.5 M potassium hexafluorophosphate (KPF_6) in DEGDME electrolyte sandwiched between glass fibres and a carbon nanotube (CNT) as the cathode (Figure 2.10(b)). The cathode is made of carbon paper coated with carbon nanotubes. The primary discharge product is KO_2, with some KOH also formed, demonstrating the efficacy of the Na-K alloy anode. Without the Nafion-Na^+ membrane, the battery possesses a discharge capacity of around 2.0 mAh and an initial voltage of approximately 2.45 V. However, the Nafion membrane's ion selectivity restricts K^+ diffusion, hindering discharge capacity in Na-O_2 cells. This

configuration offers advantages like dendrite-free operation, effective anode performance, and reduced side reactions due to the Nafion membrane. Nevertheless, it suffers from limited discharge capacity due to ion selectivity, solvent decomposition, and sustainability concerns as the battery transitions from Na-O_2 to K-O_2 during discharge.

2.1.5 Other Metal-Air Batteries

In the realm of MABs, the utilization of semiconductors as anodes has opened new avenues for energy storage. Among these, silicon-air (Si-air) batteries are particularly noteworthy with a theoretical volumetric energy density of 6713 Wh L^{-1} and a specific energy of 5321 Wh kg^{-1}. The pioneering Si-air battery, developed by Cohn et al. [199] in 2009, maintained a consistent voltage between 1.0 and 1.2 V. This innovative design featured doped silicon wafers as the fuel, an air-breathing cathode, and a precisely engineered ionic liquid, 1-ethyl-3-methylimidazolium oligofluorohydrogenate (EMI·$(HF)_2$·3F), as the electrolyte. Recent research has concentrated on aqueous Si-air batteries utilizing conventional KOH electrolytes. Initial research emphasized the importance of micro- or nano-porous Si surfaces to maintain extended discharge times, achieving up to 30 hours at 0.05 mA cm^{-2} [200,201]. Without these surface modifications, the cell voltage drops sharply due to the formation of the passivation layer on the Si surface rapidly. The following studies demonstrated longer discharge times of up to 270 hours at the same current density using a refill-type cell setup with an unmodified Si anode. In cases where a thicker Si wafer (3 mm) was employed as the anode, the alkaline Si-air battery, utilizing a 5 M KOH electrolyte, sustained operation for up to 1100 hours at voltages above 1.1 V, delivering specific capacities of 115 mAh g^{-1} and anode mass conversion efficiencies around 3% [202]. More recent research has shown that reducing the KOH concentration to 0.5 M enhances Si anode utilization during discharge, with conversion efficiencies increasing to as much as 9% [203]. In 2024, Guerrero et al. [204] pioneered a study using both alkaline and non-aqueous Si-air batteries to power low-power transient electronics designed for partial self-destruction. The Si-air batteries demonstrate practical specific capacities and energies of 117 mAh g^{-1} and 123 Wh kg^{-1} for the alkaline system, and 1072 mAh g^{-1} and 841 Wh kg^{-1} for the non-aqueous system, until the active area of the Si anodes is fully consumed (Figure 2.11(a)). Nevertheless, Si-air batteries have several drawbacks. The silicon surface can quickly become passivated, causing a drop in voltage unless modified with micro- or nano-porous structures. The batteries also face mechanical stress due to silicon's expansion and

contraction during use, which can shorten their lifespan. Additionally, the electrolyte can be consumed during reactions, leading to corrosion. Production costs are high because of the need for pure silicon and specialized processes. Si-air batteries also have a shorter cycle life and can be less energy-efficient [205].

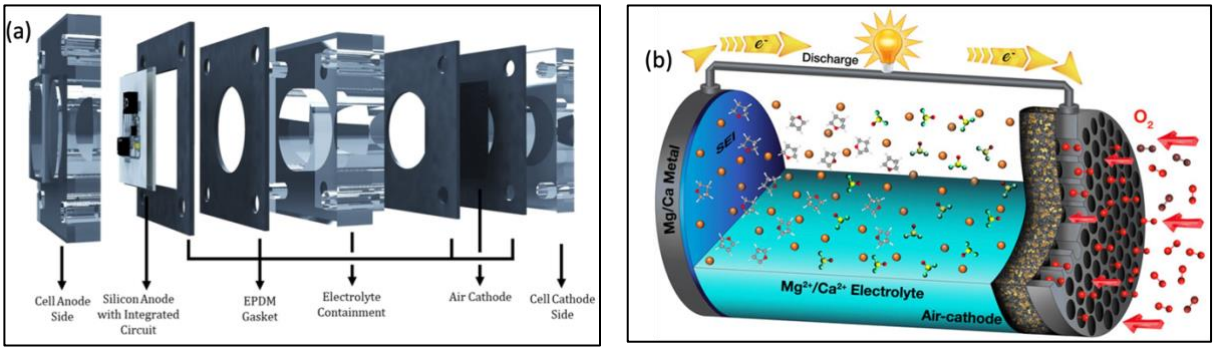


Figure 2. 11: (a) Cell structure of a Si-air battery [204] (b) Working illustration of a Mg/Ca-O_2 battery [206].

Germanium-air (Ge-air) batteries emerged shortly after Si-air batteries in 2013, by Ocon et al. [207], leveraging germanium's widespread use in Li-ion batteries. The cell featured a nanoporous Ge anode, a KOH electrolyte, and an air-breathing cathode. It operated at a sustained discharge and maintained a stable cell voltage of 0.42 V, with a power density of 0.21 mW cm^{-2} and a current density of 0.5 mA cm^{-2}. Remarkably, there were no signs of polarization, even at elevated current densities, as evidenced by the slight increase of potential after 200 hours of operation. However, since their introduction, there have been very few advancements in research on Ge-air batteries, and they remain a relatively unexplored area in the field.

The calcium-oxygen (Ca-O_2) battery presents a favourable avenue for rechargeable energy storage. These batteries are attractive due to their impressive theoretical volumetric energy density of 7574 Wh L^{-1}, a specific energy of 3441 Wh kg^{-1} and an incredibly high nominal voltage of 3.5 V. This electrochemical system employs a calcium anode and an air-breathing cathode, where O_2 is reversibly converted to calcium peroxide. An ionic liquid-based electrolyte, consisting of EMIM-BF_4 and dimethyl sulfoxide, provides a stable operating environment. Recent studies have highlighted the exceptional performance of Ca-O_2 batteries, including their longevity (700 recharge cycles), stability in ambient air, and adaptability to flexible textile formats for wearable applications [208]. Lu et al. [206] introduced the concept of Mg/Ca-O_2 where a Mg/Ca metal is

used as the anode. They conducted a comprehensive analysis of suitable electrolytes and identified key technological advancements required to address the challenges associated with this type of battery (Figure 2.11(b)). Challenges such as anode passivation and calcium ion transport limitations are yet to be addressed. Ca-O_2 batteries are in their initial research phase, and it will take considerable time and effort to realize their full potential.

The pioneering work on iron-air (Fe-air) batteries was first conducted by NASA in 1968. This concept was later adopted by the Swedish National Development Corporation in the 1970s to produce a 30 kWh battery for traction applications, achieving an energy density of 80 Wh/kg at a 5-hour discharge rate [136]. Fe-air batteries boast several advantages over traditional batteries. Theoretically, they possess a volumetric energy density of 3244 Wh L^{-1}, a specific energy of 1080 Wh kg^{-1} and an OCV of 1.28V. Notably, it eliminates the risk of iron dendrite formation during charging, ensuring safety and longevity. Furthermore, its iron negative electrode offers a remarkably high theoretical specific capacity of 960 mAh g^{-1}, promising exceptional energy density [209]. Finally, their composition and operational characteristics make it a more environmentally friendly and sustainable energy storage solution with many recent works to solve the issues associated with this battery type.

2.2 Aluminum-Air Batteries: Fundamentals and Challenges

Aluminum-air (Al-air) batteries have attracted sustained research interest due to their exceptionally high theoretical energy density, material abundance, and low cost. First introduced by Zaromb in 1962, Al-air systems operate as primary metal-air batteries in which aluminum serves as a sacrificial anode, reacting with oxygen from ambient air to generate electrical energy. Their high gravimetric and volumetric energy densities have positioned them as promising candidates for large-scale energy storage and transportation applications, particularly in electric vehicles (EVs) and grid-scale system [210].

A typical Al-air battery consists of an aluminum metal anode, a porous air cathode, and an aqueous electrolyte, commonly based on NaOH, KOH, or NaCl solutions. The electrochemical reactions governing the system are fundamentally driven by aluminum oxidation and oxygen reduction. At the anode, aluminum reacts with hydroxide ions to form soluble aluminate species while releasing electrons. Concurrently, oxygen reduction at the cathode consumes electrons and produces hydroxide ions, thereby sustaining ionic transport within the electrolyte.

While these reactions provide the basis for energy generation, the practical operation of Al-air batteries is strongly influenced by competing parasitic processes. A major side reaction is hydrogen evolution, which occurs due to the direct reaction of aluminum with water, independent of the external circuit. This parasitic reaction leads to continuous self-corrosion of the aluminum anode, resulting in material loss, reduced coulombic efficiency, and gas evolution that may compromise system safety. The competition between useful anodic oxidation and parasitic hydrogen evolution represents a central limitation in Al-air battery performance [211-214].

The corresponding reactions with various electrolyte types are summarized in detail in Table 2.3.

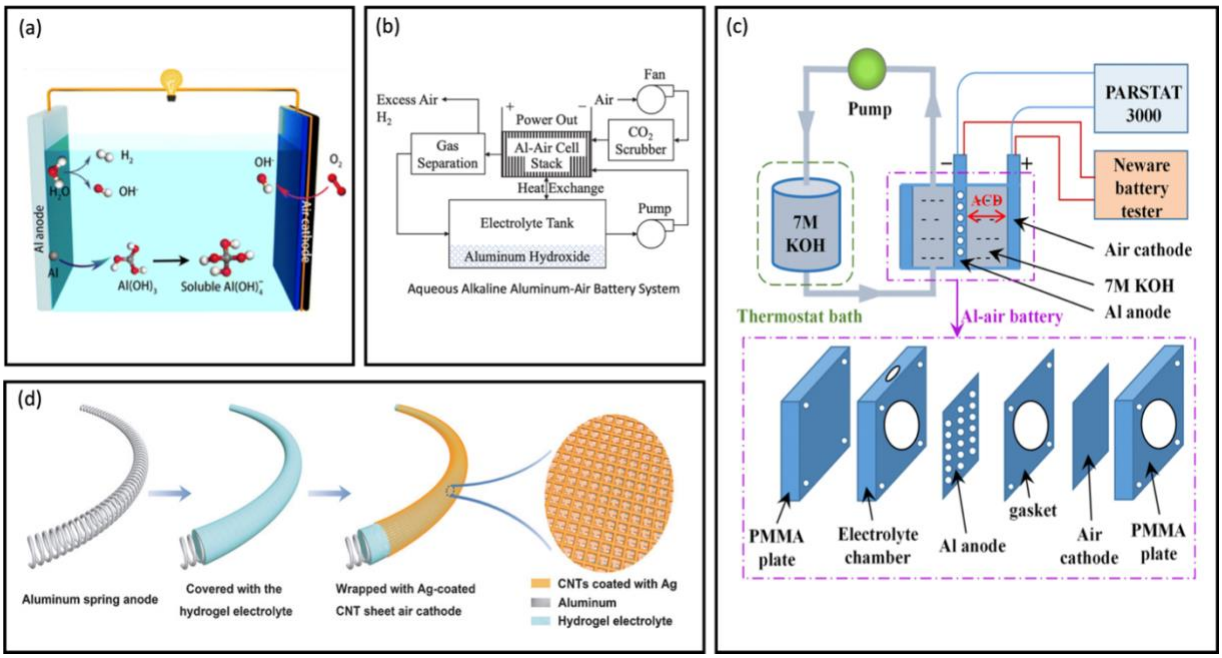


Figure 2. 12: Al-air battery configurations: (a) Planar architecture with aqueous electrolyte [215], (b) Al-air battery stack architecture [53], (c) Electrolyte flow-through design [45], (d) Flexible configuration [216].

Al-air batteries exhibit diverse configurations, varying in both electrolyte composition and design structure. As depicted in Figure 2.12(a), a planar structure refers to a flat, layered design where the components of the Al-air battery are arranged in flat sheets stacked either vertically or horizontally. Three types of aqueous electrolytes are used based on their pH: Neutral, acidic, and alkaline electrolytes. Neutral Al-air batteries are eco-friendly, utilizing non-toxic raw materials and generating non-hazardous by-products. The generated OH^- during the operation

quickly combines with aluminum ions to form aluminum hydroxide, keeping the electrolyte neutral. This neutrality offers a high level of safety to Al-air batteries, making them suitable for marine and consumer applications. Since the 1970s, large neutral Al-air battery stacks (Figure 2.12(b)) have been developed for marine use, leveraging seawater as a natural electrolyte. This allows offshore Al-air batteries to operate with only aluminum plates and air cathodes, as seawater can be utilized directly as an electrolyte. Neutral Al-air batteries have seen applications in consumer products, including wearable devices, small electronics, and other household appliances. However, these batteries are hindered by significant challenges, such as the intense polarization of the Al anode due to the passivation of the aluminum surface. This passivation layer impedes the migration of aluminum ions and electron transfer, reducing the battery's discharge performance. The presence of chloride ions can help reduce polarization by assisting in the dissolution of the oxide film [215].

To combat the disadvantages of anode passivation in neutral electrolytes, acidic electrolytes were proposed. Hydrochloric acid (HCl) and sulphuric acid (H_2SO_4) have been studied as possible options, offering the potential for higher voltages due to the high theoretical positive potential of the air cathode in low pH environments. However, the aluminum anode's thermodynamic properties in acidic electrolytes are unsatisfactory, with severe H_2 evolution side reactions occurring alongside the main reaction. The time needed for the disintegration of the oxide film in lower concentrations of acidic electrolytes is higher than in alkaline electrolytes, leading to longer activation processes and increased polarization. Moreover, acidic electrolytes can cause pitting corrosion, which is detrimental to smooth discharge. These practical limitations have hindered the usage of acidic electrolytes in Al-air batteries, though ongoing research aims to address these issues [217-219].

The introduction of alkaline electrolytes marked a breakthrough for Al-air batteries. KOH or NaOH-based electrolytes, quickly disintegrate the passivation layer on the aluminum, greatly increasing the kinetics of the charge transfer reactions. Insoluble aluminum hydroxide is converted into soluble tetrahydroxy aluminate ions, reducing polarization, and maintaining high ionic conductivity. Alkaline Al-air batteries can maintain high voltages under high current densities due to the intense destructive capacity of hydroxide ions on the oxide film, facilitating smoother ion mobility at the solid-electrolyte interface at the anode. However, alkaline electrolytes also have inherent flaws. The reactive aluminum is exposed to the electrolyte as the

passivation layer dissolves during discharge, leading to hydrogen evolution, which poses safety risks and reduces the energy density and specific capacity of the battery. Although high-concentration electrolytes and additive compounds are used to mitigate these issues, the actual anode potential in alkaline solutions remains lower than the theoretical value, indicating significant anode polarization [45,220]. Despite these challenges, alkaline Al-air batteries show promise for vehicle power supplies. Phinergy developed an electric car combining Al-air batteries and Li-ion batteries, extending the range of the Li-ion batteries from 60 km to 350 km [221]. Recently, a short-range aircraft powered by Al-air batteries was designed, showcasing significant advantages in weight and cost with a theoretical 950 nautical miles of mileage [222]. The primary barrier to commercialization lies in high anodic corrosion and complicated stack design. Many effective options to inhibit self-corrosion are studied, but achieving easy mechanical charging, simple, and safe replacement of aluminum anodes and electrolytes remains crucial for industrialization.

Al-air electrolyte flow batteries (Figure 2.12(c)) employ an electrolyte flow system to remove reaction by-products, thereby improving energy efficiency. This design leads to exceptional electrochemical performance, including excellent discharge capabilities and extended cycle life. There are two primary methods for facilitating electrolyte flow in Al-air electrolyte flow batteries: external mechanical pump-assisted driving and paper-based capillary action driving. The mechanical pump-assisted method, utilizing devices like peristaltic or syringe pumps, ensures a fast and stable electrolyte flow, significantly enhancing the performance of Al-air electrolyte flow batteries. However, the bulky and complex structure of this system makes it suitable only for large-scale applications. To reduce size and complexity, researchers have developed a paper-based microfluidic Al-air battery. In this system, the solution flow is driven by capillary action within the microchannels of cellulose paper. This approach offers a compact and simplified design but comes with limitations such as reduced energy storage capacity and shorter battery shelf life, resulting in weaker discharge behaviour compared to their larger counterparts [223]. Wen et al. [45] reported significant results using an Al-air electrolyte flow battery with a 7 M KOH electrolyte flowing externally. They reached a peak power density of 545 mW cm^{-2} in a pure O_2 environment, with optimal performance parameters including a 0.5 mm anode-cathode distance (physical distance between the two electrodes to prevent short-circuit), an operating temperature of 60°C, and an electrolyte flow rate of 15 mL min^{-1}. The

battery demonstrated an anode efficiency of 96.2% and energy efficiencies of 44.4% in air and 42.6% in pure O_2. Furthermore, their research indicated that the technology can be scaled to kilowatt-level packs, with energy densities of 700 Wh L^{-1} and 900 Wh kg^{-1}, making it promising for applications in EVs and large-scale energy storage systems. Huang et al. developed a novel acoustofluidic saltwater Al-air flow battery that uses ultrasonic vibrations to drive the electrolyte flow and create an ultrasonic field within the reaction chamber. This innovative approach led to a peak power density of 43.88 mW cm^{-2}, which is up to 7.5 times higher than that with static electrolytes and comparable to mechanical pumping systems. The optimization of reaction vessel thickness, ultrasonic vibration velocity and electrolyte concentration contributed to this performance enhancement. Additionally, the acoustofluidic system significantly decreases the energy usage, mass, and size of the electrolyte-driven component compared to traditional methods. This research highlights the potential of ultrasonic pump-based Al-air flow batteries for energy storage applications requiring eco-friendliness, cost efficiency, safety, and stable discharge performance [224].

A flexible Al-air battery (Figure 2.12(d)) is an advanced type of battery designed to offer both high energy density and mechanical flexibility. Unlike traditional rigid batteries, flexible Al-air batteries are constructed to be pliable and stretchable, allowing them to be integrated into various applications such as smart textiles and wearable electronics. Xu et al. presented a fibre-shaped flexible Al-air cell with notable advantages and performance. This design achieved an impressive energy density of 1168 Wh kg^{-1}, over 12 times greater than fibrous Li-ion batteries, and a specific capacity of 935 mAh g^{-1}, about six times higher than fibre-type zinc-carbon batteries. It maintained an output voltage above 1 V even when stretched by up to 30%, demonstrating excellent mechanical stability. The fibre design also allows for integration into textiles, making it suitable for flexible and wearable electronics. Key advantages include its environmental friendliness and the usage of a porous design with aligned carbon nanotubes and silver nanoparticles to enhance performance. However, practical energy density remains lower than theoretical values due to limitations in electrode materials, and there are concerns about the aluminum anode's self-corrosion and the complexity of the manufacturing process. Despite these challenges, the battery offers promising potential for innovative applications in smart textiles and wearable technology.

A notable advancement in Al-air battery technology is the galvanic generator-type system developed by AlumaPower [225], which integrates several of the aforementioned design advantages into a unified and practical architecture. This system employs a mechanically rechargeable configuration, wherein aluminum plates are consumed as fuel and periodically replaced, thereby decoupling energy storage from electrical recharging. A key innovation in this design is the incorporation of a patented rotating electrode mechanism, which continuously exposes fresh aluminum surface to the electrolyte while mitigating localized passivation and accumulation of discharge by-products such as $Al(OH)_3$. This dynamic electrode configuration enhances mass transport at the solid-liquid interface, promotes more uniform anodic dissolution, and reduces the formation of insulating oxide layers, thereby improving discharge stability and overall system efficiency. In addition, the flow-assisted electrolyte management within the galvanic generator facilitates effective removal of reaction products and sustains ionic conductivity, addressing key limitations associated with stagnant electrolyte systems. Collectively, these features enable improved control over parasitic corrosion, hydrogen evolution, and polarization behavior, which are central challenges in conventional Al-air battery designs. The present thesis builds upon this novel system by utilizing multiple prototype units provided by AlumaPower for systematic experimental investigation. These prototypes enabled controlled evaluation of electrolyte composition, operational parameters, and electrochemical performance under realistic conditions, thereby bridging the gap between laboratory-scale studies and practical system-level implementation. This collaboration not only grounds the research in an industrially relevant design but also provides a unique platform for advancing both performance optimization and predictive modeling of Al-air battery behavior.

Overall, although Al-air batteries offer a compelling combination of high energy density and material sustainability, their performance is fundamentally constrained by the interplay between electrochemical kinetics, parasitic corrosion, and electrolyte dynamics. A comprehensive understanding of these coupled phenomena, particularly the effects of electrolyte composition and operating conditions on corrosion and performance metrics, remains incomplete. This gap highlights the need for systematic experimental investigation and predictive modeling frameworks, which form a central focus of the subsequent chapters in this thesis.

2.3 Corrosion Behavior of Aluminum in Alkaline Electrolytes

The performance and durability of Al-air batteries are fundamentally governed by the corrosion behavior of aluminum in aqueous electrolytes. Unlike conventional battery systems, where degradation is often a secondary concern, corrosion in Al-air systems occurs concurrently with the primary electrochemical reaction, directly impacting efficiency, capacity utilization, and system stability. In alkaline environments, corrosion is driven by both electrochemical and chemical processes, with aluminum dissolution competing with parasitic reactions such as hydrogen evolution [226].

Electrochemical corrosion of aluminum is commonly analyzed using polarization techniques, where the relationship between electrode potential and current density follows Tafel behavior. The extrapolation of anodic and cathodic branches enables the determination of key corrosion parameters, including the corrosion potential (Ecorr) and corrosion current density (Icorr). Ecorr represents the mixed potential at which anodic dissolution and cathodic reduction reactions are balanced, while Icorr provides a quantitative measure of the corrosion rate. In the context of Al-air batteries, lower Icorr values indicate reduced parasitic material loss, whereas more positive Ecorr values suggest improved thermodynamic stability of the aluminum anode [227]. The governing electrochemical relationships and mathematical formulations describing these parameters are discussed in detail in Chapter 5.

A dominant cathodic process contributing to aluminum corrosion in alkaline electrolytes is the hydrogen evolution reaction (HER), which proceeds via the reduction of water to produce hydrogen gas and hydroxide ions. This reaction occurs spontaneously on the aluminum surface, independent of external current flow, and therefore represents a major pathway for self-corrosion. The coexistence of anodic aluminum dissolution and HER leads to significant efficiency losses, reduced effective capacity, and potential safety concerns due to gas accumulation [228]

Electrolyte concentration plays a critical role in modulating corrosion behavior. Increasing the concentration of alkaline electrolytes such as NaOH or KOH enhances ionic conductivity and promotes dissolution of the native oxide layer on aluminum, thereby improving electrochemical kinetics. However, higher concentrations also accelerate parasitic corrosion and hydrogen evolution, resulting in increased Icorr and reduced anode utilization efficiency. Temperature further amplifies these effects by enhancing reaction kinetics and diffusion processes, often leading to accelerated corrosion rates and altered polarization characteristics [11].

Material composition of the aluminum anode also significantly influences corrosion behavior. In practical systems, alloys such as a commercial Al-Mg-Si alloy are commonly employed. Alloying elements affect surface chemistry, oxide layer stability, and electrochemical activity, thereby influencing both anodic dissolution and hydrogen evolution kinetics. Microstructural heterogeneities and intermetallic phases can introduce localized galvanic effects, contributing to non-uniform corrosion and pitting behavior [229].

Electrochemical impedance spectroscopy (EIS) provides additional insight into corrosion mechanisms by characterizing interfacial processes across a range of frequencies. Key parameters obtained from equivalent circuit modeling include solution resistance (Rs), charge transfer resistance (Rct), and constant phase elements (CPE), which account for non-ideal capacitive behavior associated with surface roughness and heterogeneity. Nyquist plots are used to evaluate charge transfer resistance and corrosion kinetics, while Bode plots provide complementary information on frequency-dependent impedance magnitude and phase response [230].

Despite extensive experimental characterization of aluminum corrosion using polarization and impedance techniques, the ability to predict corrosion kinetics under varying operating conditions remains limited. Most existing studies rely on empirical observations or simplified models that do not fully capture the coupled effects of electrolyte composition, temperature, and material properties. This limitation highlights the need for predictive, data-driven modeling frameworks, which are developed and validated in Chapter 5 of this thesis.

2.4 Data-Driven Modeling and Optimization in Electrochemical Systems

The increasing complexity of electrochemical systems, particularly metal-air batteries, has driven the adoption of data-driven modeling approaches to complement traditional experimental and physics-based methods. While classical electrochemical models provide valuable mechanistic insights, they often require simplifying assumptions and may not fully capture the nonlinear and coupled interactions between material properties, electrolyte composition, and operating conditions. As a result, machine learning (ML) techniques have emerged as powerful tools for modeling, prediction, and optimization in electrochemical systems [231].

Among these approaches, artificial neural networks (ANNs) have gained significant attention due to their ability to approximate complex nonlinear relationships without requiring explicit knowledge of the underlying governing equations. In the context of electrochemistry, ANNs have been successfully applied to predict battery performance, estimate state-of-charge

(SOC) and state-of-health (SOH), and model corrosion behavior under varying environmental and operational conditions. By learning directly from experimental datasets, ANNs can capture intricate dependencies between input variables such as electrolyte concentration, temperature, current density, and voltage, and output responses such as corrosion potential (Ecorr), corrosion current density (Icorr), and overall system performance [232]. The mathematical formulation and training methodology of ANN models employed in this thesis are discussed in detail in Chapter 5.

In addition to predictive modeling, optimization techniques are increasingly integrated with machine learning frameworks to identify optimal operating conditions in multidimensional parameter spaces. Genetic algorithms (GAs), inspired by principles of natural selection and evolution, have been widely used for global optimization of electrochemical systems. These algorithms iteratively evolve candidate solutions based on fitness functions, enabling efficient exploration of complex design spaces where gradient-based methods may be ineffective. In electrochemical applications, GAs have been employed to optimize electrode design, electrolyte composition, and operating parameters to enhance performance metrics such as energy efficiency and corrosion resistance [233].

For problems involving multiple competing objectives, multi-objective optimization techniques such as non-dominated sorting genetic algorithm II (NSGA-II) are particularly relevant. NSGA-II enables the simultaneous optimization of conflicting performance indicators, such as maximizing corrosion potential while minimizing corrosion current density. By generating Pareto-optimal solution fronts, these approaches provide valuable insight into trade-offs inherent in electrochemical systems and support informed decision-making for system design and operation .

Despite the growing application of machine learning and optimization techniques in electrochemical research, several limitations remain. Many existing studies focus either on predictive modeling or optimization in isolation, with limited integration between experimental datasets and multi-objective optimization frameworks. Furthermore, most models are developed for specific systems or conditions, limiting their generalizability across varying electrolyte compositions, temperatures, and material systems. In the context of Al-air batteries, the application of data-driven approaches to model corrosion kinetics and optimize operating conditions remains relatively underexplored.

Therefore, there is a clear need for integrated modeling frameworks that combine experimental electrochemical data with advanced machine learning and optimization techniques

to enable accurate prediction and systematic optimization of corrosion behavior. Addressing this gap, the present thesis develops an ANN-based predictive model coupled with genetic algorithm and NSGA-II optimization to characterize and optimize corrosion kinetics of a commercial Al-Mg-Si alloy under varying electrolyte conditions, as detailed in Chapter 5.

2.5 Battery and System-Level Modeling Approaches

Modeling of electrochemical energy storage systems plays a crucial role in bridging the gap between cell-level behavior and system-level performance, particularly in applications such as electric vehicles (EVs). While detailed electrochemical models provide fundamental insight into reaction mechanisms and transport phenomena, their high computational complexity often limits their applicability in large-scale simulations. Consequently, simplified modeling approaches have been developed to enable efficient integration of battery systems into vehicle-level frameworks.

Battery models are generally categorized into three main classes: empirical models, equivalent circuit models (ECMs), and physics-based electrochemical models. Empirical models rely on experimentally derived relationships to describe battery behavior under specific operating conditions, offering simplicity but limited generalizability. Physics-based models, such as those derived from porous electrode theory, provide detailed representation of electrochemical processes including ion transport, charge transfer, and diffusion. However, these models are computationally intensive and require extensive parameterization, making them less suitable for real-time or system-level simulations [234].

Equivalent circuit models (ECMs) represent a widely adopted compromise between accuracy and computational efficiency. These models approximate battery behavior using electrical components such as voltage sources, resistors, and capacitors to capture open-circuit voltage (OCV), internal resistance, and transient dynamics. ECMs are particularly advantageous for system-level studies due to their reduced computational burden and ease of implementation in simulation environments. In the context of metal-air batteries, ECM-based approaches can be extended to incorporate polarization behavior and discharge characteristics derived from experimental data, enabling practical representation of battery performance without requiring detailed electrochemical formulations [235].

At the system level, battery modeling is integrated within complete vehicle powertrain architectures to evaluate real-world performance under dynamic operating conditions. Modern EV powertrains consist of interconnected subsystems, including the energy storage unit, power

electronic converters, electric motor, drivetrain, and vehicle dynamics modules. Simulation of such systems is commonly performed using platforms such as MATLAB and Simulink, which enable modular and physics-informed representation of complex multi-domain systems. These environments provide pre-configured vehicle models and allow for the integration of custom battery subsystems, facilitating the analysis of interactions between electrochemical behavior and powertrain performance [236].

Within these frameworks, battery models are subjected to standardized driving cycles such as UDDS, WLTP, and HWFET to evaluate performance metrics including energy consumption, state-of-charge (SOC) evolution, power demand, and vehicle range. The coupling between the battery and the powertrain is governed by power flow dynamics, where battery output must satisfy motor and auxiliary loads while maintaining operational constraints. This integrated approach enables a more realistic assessment of battery performance beyond laboratory-scale characterization [237].

Hybrid and dual-energy storage system architectures have gained increasing attention as a means to leverage complementary characteristics of different energy storage technologies. In such configurations, high-power-density systems such as lithium-ion batteries are combined with high-energy-density systems such as metal-air batteries. Effective integration of these systems requires the implementation of control strategies, commonly based on SOC thresholds, to manage power distribution and ensure stable operation. These strategies enable metal-air systems to function as range extenders or auxiliary power sources, supplementing the primary battery during high energy demand or low SOC conditions within the vehicle powertrain [238].

Despite these advancements, several challenges remain in system-level modeling of metal-air batteries. Most existing studies rely on simplified assumptions regarding battery behavior, often neglecting the influence of electrochemical degradation mechanisms such as corrosion, electrolyte depletion, and mass transport limitations. Additionally, limited efforts have been made to integrate experimentally validated Al-air battery models into realistic EV powertrain simulation platforms. As a result, the translation of cell-level performance to system-level impact remains inadequately understood.

Therefore, there is a need for modeling frameworks that balance electrochemical fidelity with computational efficiency, while enabling seamless integration into vehicle powertrain simulations. Addressing this gap, the present thesis develops a system-level modeling approach

implemented in MATLAB/Simulink, incorporating experimentally informed battery representations and integrating Al-air systems within a dual-energy storage EV architecture, as detailed in Chapter 6.

2.6 Research Gaps and Thesis Positioning

Despite significant advancements in metal-air battery research, particularly in aluminum-air (Al-air) systems, existing studies remain largely fragmented across electrochemical, material, and system-level domains. While substantial progress has been made in understanding individual aspects of Al-air batteries, a comprehensive and integrated framework that connects fundamental electrochemical behavior with practical system-level performance is still lacking. This disconnect limits the ability to assess the true potential of Al-air technology in real-world applications, particularly in electric vehicles (EVs). The present thesis addresses these limitations by systematically bridging gaps across multiple scales, from electrochemical processes to vehicle-level integration.

- Gap 1: Lack of integrated techno-economic evaluation of Al-air batteries in EV applications.

Current literature primarily evaluates metal-air batteries based on theoretical energy densities or isolated performance metrics, with limited emphasis on practical feasibility in transportation systems. While some studies have explored the potential of metal-air batteries as range extenders, these analyses often lack a comprehensive techno-economic perspective that incorporates vehicle constraints, energy consumption, and cost implications simultaneously. As a result, the viability of Al-air systems within realistic EV architectures remains insufficiently understood. This gap is addressed in Chapter 3, which presents a detailed techno-economic case study evaluating the feasibility of metal-air batteries as range extenders, incorporating vehicle-level performance metrics and cost considerations.

- Gap 2: Limited understanding of electrolyte-driven performance optimization in Al-air batteries.

Electrolyte composition and operating conditions play a critical role in determining the electrochemical performance of Al-air systems. Although prior studies have investigated the effects of electrolyte type, concentration, and temperature, these investigations are often conducted in isolation and lack systematic analysis across a broad parameter space. Furthermore, the interplay between electrolyte properties, discharge behavior, and degradation mechanisms remains

inadequately characterized. This gap is addressed in Chapter 4, which presents a comprehensive experimental investigation into the performance optimization of Al-air batteries, focusing on the effects of electrolyte composition and operational parameters on discharge characteristics and efficiency.

- Gap 3: Absence of predictive frameworks for corrosion kinetics in Al-air systems.

Corrosion of the aluminum anode, driven by parasitic reactions such as hydrogen evolution, remains a dominant limitation in Al-air batteries. While experimental techniques such as Tafel analysis and electrochemical impedance spectroscopy have been widely used to characterize corrosion behavior, existing studies are largely empirical and lack predictive capability. There is a clear absence of integrated modeling approaches capable of capturing the nonlinear relationships between electrolyte conditions, temperature, material composition, and corrosion metrics such as Ecorr and Icorr. This gap is addressed in Chapter 5, which develops a data-driven predictive framework based on artificial neural networks coupled with genetic algorithm and multi-objective optimization techniques to model and optimize corrosion kinetics.

- Gap 4: Lack of system-level integration of Al-air batteries in EV architectures.

Although the high energy density of Al-air batteries makes them attractive for EV applications, most existing studies focus on cell-level performance without considering integration into vehicle powertrain systems. Limited work has been conducted on incorporating Al-air batteries within dual-energy storage architectures, and even fewer studies utilize realistic driving cycles or validated simulation environments. Consequently, the system-level impact of Al-air batteries on vehicle performance, energy consumption, and range remains poorly understood. This gap is addressed in Chapter 6, which develops a system-level modeling framework implemented in MATLAB/Simulink, integrating Al-air batteries within a dual-energy storage EV architecture using SOC-based control strategies.

2.7 Novelty and Contributions of the Thesis

First, this thesis establishes a techno-economic evaluation framework that bridges the gap between theoretical battery performance and practical EV feasibility. By incorporating vehicle-level metrics, energy consumption, and cost considerations, this work provides a realistic assessment of Al-air batteries as range extenders, moving beyond conventional theoretical analyses.

Second, the thesis presents a systematic experimental investigation of electrolyte-driven performance optimization, examining the influence of electrolyte composition, concentration, and operating conditions on Al-air battery behavior. This work provides detailed insight into the relationships between electrochemical performance, discharge characteristics, and degradation mechanisms, contributing to a more comprehensive understanding of Al-air system operation.

Third, a key novelty of this thesis is the development of a data-driven predictive modeling framework for corrosion kinetics, combining artificial neural networks with genetic algorithm and multi-objective optimization techniques. Unlike traditional empirical approaches, this framework enables accurate prediction and optimization of corrosion behavior across multidimensional parameter spaces, representing a significant advancement in the modeling of electrochemical degradation processes.

Fourth, the thesis introduces a system-level integration of Al-air batteries within EV powertrain architectures, implemented in MATLAB/Simulink using experimentally informed battery models. This work demonstrates the feasibility of dual-energy storage systems, where Al-air batteries function as range extenders or auxiliary power sources, and evaluates their impact under realistic driving cycles.

Finally, the thesis is grounded in a novel industrially relevant Al-air battery design, leveraging prototype systems based on a galvanic generator configuration with a rotating electrode mechanism. The use of these prototypes enables experimental validation under practical operating conditions, enhancing the relevance and applicability of the research.

Collectively, the contributions of this thesis establish a multiscale framework that links electrochemical behavior, corrosion kinetics, and system-level performance, providing new insights into the design and application of Al-air batteries in advanced energy systems.

Chapter 3 Techno-Economic Case Study of Metal-Air Batteries as Range Extenders in Electric Vehicles

*** Chapter 3 is adapted from Shabeer Y, Madani SS, Panchal S, Mousavi M, Fowler M. "Different Metal-Air Batteries as Range Extenders for the Electric Vehicle Market: A Comparative Study." Batteries 2025;11:35. https://doi.org/10.3390/BATTERIES11010035.

3.1 Introduction

The increasing demand for extended driving range, cost reduction, and system-level efficiency in EVs has exposed critical limitations in current battery technologies. Li-ion batteries have enabled the rapid growth of electrified transportation, their incremental improvements in energy density and cost are approaching practical limits, particularly for applications requiring long-range capability or high energy throughput. Increasing battery capacity to extend range introduces significant penalties in mass, cost, and packaging complexity, ultimately constraining further performance gains at the vehicle level [239].

In this context, alternative energy storage systems are being explored to complement conventional Li-ion batteries rather than replace them entirely. Among these, MABs have attracted significant attention due to their exceptionally high theoretical energy densities and the use of atmospheric oxygen as a reactant, which eliminates the need to store the oxidizer within the system. This fundamental advantage offers the potential for substantial improvements in energy storage capacity compared to closed battery systems. However, despite their promising electrochemical characteristics, most MAB technologies remain limited by low energy efficiency, parasitic reactions, system complexity, and challenges in practical implementation [240].

Rather than functioning as standalone energy sources, MABs are increasingly considered for use as range extenders, where they operate alongside a primary battery system to supplement energy supply during vehicle operation. In such configurations, the high energy density of MABs can be leveraged to extend driving range, while the primary battery provides the required power density and operational stability. This hybrid approach enables a more efficient utilization of each technology and represents a promising pathway for overcoming the limitations of single-chemistry battery systems [241].

Despite extensive research on MABs at the material and cell levels, a critical gap remains in understanding their system-level performance within electric vehicles. Most existing studies focus on electrochemical properties such as specific energy, power density, and reaction kinetics, with limited attention given to how these characteristics translate into practical metrics such as vehicle range, total cost, and battery pack volume. As a result, the feasibility of integrating different MAB chemistries into EV platforms remains insufficiently quantified.

To address this gap, this chapter develops a techno-economic evaluation framework that directly links battery characteristics to vehicle-level performance. The framework integrates key parameters, including specific energy, energy density, cost, and system overhead factors, with vehicle properties such as mass and energy consumption. Through this approach, the performance of multiple battery chemistries, including Li-ion and various metal-air systems, is evaluated under consistent conditions.

The analysis focuses on three critical performance indicators: driving range, total vehicle cost, and battery pack volume, enabling a comprehensive comparison of different technologies. In addition, the study introduces a marginal cost analysis to quantify the cost efficiency of extending vehicle range, providing further insight into the economic viability of each battery system. By translating electrochemical properties into system-level outcomes, this chapter provides a realistic assessment of the potential of metal-air batteries as range extenders in EVs. The results offer valuable insights into the trade-offs between energy density, cost, efficiency, and packaging constraints, and identify the most promising battery chemistries for practical deployment. Most importantly, this work demonstrates that vehicle-level performance is governed not solely by material properties, but by the integration of battery systems within the broader vehicle architecture, highlighting the necessity of system-level design in the development of next-generation energy storage solutions.

3.2 Methodology

To evaluate the feasibility of metal-air batteries as range extenders in electric vehicles, a system-level modelling framework is developed to bridge the gap between electrochemical properties and real-world vehicle performance. While conventional battery studies focus on cell-level metrics such as specific capacity, voltage, and energy density, these parameters do not directly translate into meaningful vehicle-level outcomes. Therefore, this framework integrates

electrochemical relations with vehicle dynamics and economic considerations to quantify performance in terms of driving range, cost, and packaging constraints.

The methodology is structured around three interconnected layers: electrochemical performance, battery system scaling, and vehicle-level impact. Electrochemical equations are first used to define intrinsic battery properties such as capacity and energy. These properties are then scaled to system-level parameters by incorporating mass and volume overheads associated with real battery packs. Finally, these system-level values are integrated with vehicle parameters to determine driving range and total cost.

The fundamental electrochemical performance of each battery system is quantified using standard relationships between current, time, voltage, and mass.

The specific capacity of the battery is calculated as [77,78]:

$$C_{\text{spec}} = \frac{I \cdot t}{m} \tag{3.1}$$

where I is the discharge current, t is the discharge time, and m is the mass of the active material. This parameter represents the total charge delivered per unit mass and reflects the efficiency of electrochemical utilization.

The power density is defined as [45]:

$$P = V \cdot I \tag{3.2}$$

or in area-normalized form:

$$P_{\text{dens}} = V \cdot J \tag{3.3}$$

where V is the operating voltage and J is the current density. This describes the rate of energy delivery, which is important for evaluating whether the system can support vehicle load demands.

The specific energy is calculated as [78]:

$$SE = V \cdot C \tag{3.4}$$

where V is the nominal voltage and C is the capacity. This parameter represents the total energy stored per unit mass and is the primary determinant of achievable driving range.

Similarly, the energy density is given by [45]:

$$ED = \frac{E}{V_{\text{cell}}} \tag{3.5}$$

where $E$is total energy and $V_{\text{cell}}$is the volume of the battery system.

The total energy delivered during discharge is determined using [78]:

$$E = \frac{V \cdot I \cdot t}{m} \tag{3.6}$$

This equation links electrochemical performance directly to usable energy output and accounts for both operating voltage and discharge duration.

Additionally, the theoretical specific energy based on Faraday's law is expressed as [78]:

$$SE_{\text{theoretical}} = \frac{n \cdot F \cdot \text{OCV}}{M} \tag{3.7}$$

where:

- n= number of electrons transferred
- F= Faraday constant
- M= molar mass of the metal

This provides the upper bound of energy storage for each metal-air chemistry.

The equilibrium voltage of the battery is described by the Nernst equation [79]:

$$E = E^{\circ} - \frac{RT}{nF} \ln Q \tag{3.8}$$

where:

- E°= standard potential
- R= gas constant
- T= temperature
- Q= reaction quotient

This equation accounts for deviations from ideal conditions and explains variations in cell voltage during operation.

The total energy delivered by a battery during discharge is calculated as the product of average voltage, current, and discharge time, normalized by the mass of the active material. This

formulation captures the cumulative effect of electrochemical reactions over time and provides a realistic measure of usable energy.

To evaluate practical performance, several efficient metrics are incorporated. Current efficiency quantifies the fraction of total current that contributes to the desired electrochemical reaction, accounting for losses due to parasitic reactions such as hydrogen evolution in metal-air systems. Energy efficiency compares the useful energy output to the input energy, reflecting losses due to overpotentials and internal resistance.

Charging and discharging efficiencies are also considered separately, enabling a more detailed assessment of round-trip efficiency. These parameters are particularly important for rechargeable systems such as Zn-air batteries, whereas mechanically rechargeable systems like Al-air are primarily evaluated based on discharge efficiency.

To evaluate real-world performance, efficiency terms are introduced.

The energy efficiency is defined as [79]:

$$\eta_{\text{energy}} = \frac{E_{\text{out}}}{E_{\text{in}}} \tag{3.9}$$

The charge-discharge efficiency is given by [79]:

$$\eta_{\text{cycle}} = \frac{E_{\text{discharge}}}{E_{\text{charge}}} \tag{3.10}$$

These parameters capture losses due to overpotential, internal resistance, and parasitic reactions, which are particularly significant in metal-air systems.

To translate battery energy into vehicle performance, the total battery pack energy is coupled with vehicle energy consumption. The driving range is determined by dividing the available battery energy by the energy consumption per unit distance, while accounting for the effect of battery mass on overall vehicle weight.

This formulation captures a critical trade-off: increasing battery capacity improves energy availability but also increases vehicle mass, which in turn raises energy consumption. As a result, the relationship between battery size and driving range is inherently non-linear, with diminishing returns at higher energy capacities.

For metal-air batteries, this effect is amplified by the inclusion of additional system components such as air cathodes, electrolyte reservoirs, and flow systems. These components

increase the effective battery mass, reducing the net gain in driving range despite high intrinsic energy density.

The driving range of the vehicle is calculated as [30]:

$$R_V = \frac{E_B}{E_{CEV} \cdot (M_V + M_B)} \tag{3.11}$$

where:

- E_B= battery energy
- E_{CEV}= energy consumption per unit mass
- M_V= vehicle mass
- M_B= battery mass

This formulation incorporates the mass penalty effect, where increasing battery mass leads to increased energy consumption, resulting in diminishing returns in driving range.

To account for real-world implementation, the intrinsic properties of battery materials are scaled to system-level values using mass and volume overhead factors. These factors represent additional components required for safe and efficient operation, including structural supports, air management systems, and thermal regulation units.

Battery pack mass is calculated by dividing the total energy requirement by the specific energy of the battery and multiplying by a mass overhead factor. Similarly, battery volume is obtained by dividing the energy requirement by the volumetric energy density and applying a volume overhead factor.

These scaling relationships are essential for realistic comparisons, as they reveal that high theoretical energy density does not necessarily translate into compact or lightweight systems. In metal-air batteries, the need for auxiliary systems can significantly increase both mass and volume, offsetting their intrinsic advantages

The battery mass is calculated as [30]:

$$M_B = \frac{E_B}{SE_{BC}} \cdot k_{m,B} \tag{3.12}$$

where:

- SE_{BC}= specific energy
- $k_{m,B}$= mass overhead factor

This accounts for additional system components such as structural supports and auxiliary systems. The battery volume is determined using [30]:

$$V_B = \frac{E_B}{ED_{BC}} \cdot k_{vol,B} \tag{3.13}$$

where:

- ED_{BC}= energy density
- $k_{vol,B}$= volume overhead factor

This equation defines the packaging constraint that limits maximum achievable range.

The total cost of the vehicle is determined by combining the base vehicle cost with the cost of the battery pack, which is proportional to its energy capacity. This approach enables direct comparison of different battery technologies in terms of their economic impact on vehicle design.

To further evaluate economic performance, the marginal cost of extending driving range is calculated as the derivative of vehicle cost with respect to range. This metric provides insight into how efficiently additional energy translates into increased driving distance and highlights the diminishing returns associated with large battery systems.

The total vehicle cost is expressed as [30]:

$$C_{V,T} = C_V + C_B \cdot E_B \tag{3.14}$$

where:

- C_V= base vehicle cost
- C_B= battery cost per kWh

This enables evaluation of economic feasibility across battery technologies.

In addition to energy, cost, and mass considerations, practical constraints such as battery volume limits and system efficiency are incorporated into the model. The maximum achievable range is restricted by the available space within the vehicle, beyond which further increases in battery capacity are not feasible.

Furthermore, efficiency losses associated with electrochemical reactions, auxiliary systems, and power conversion are included to ensure that the analysis reflects realistic operating conditions. These constraints are particularly important for metal-air batteries, where system-level inefficiencies can significantly reduce overall performance. Thus, the methodology provides a comprehensive framework for evaluating battery technologies at the vehicle level. By integrating

electrochemical equations with system-level scaling and vehicle dynamics, the approach enables a realistic comparison of different battery chemistries under consistent conditions.

This framework forms the foundation for the subsequent analysis, where the performance of multiple metal-air battery systems is evaluated in terms of driving range, cost, and volumetric feasibility.

3.3 Input Parameters and Case Definitions

The accuracy and relevance of the techno-economic evaluation depend strongly on the selection of input parameters used to represent both battery technologies and vehicle systems. In this study, a comprehensive dataset is constructed by integrating values from literature with calculated system-level adjustments to reflect realistic operating conditions.

The input parameters are categorized into three groups:

1. Vehicle parameters, defining baseline vehicle characteristics
2. Battery properties, representing intrinsic electrochemical performance
3. System-level correction factors, accounting for practical implementation constraints

This structured approach ensures that all battery chemistries are evaluated under consistent and comparable conditions, enabling a fair assessment of their performance as range extenders.

To capture a wide spectrum of real-world applications, three representative vehicle categories are considered: a mini vehicle, a mid-size passenger vehicle, and a heavy-duty vehicle. These categories differ significantly in mass, cost, and energy consumption characteristics, allowing the analysis to reflect diverse operational requirements. The vehicle parameters used in this study are summarized in Table 3.1.

Table 3. 1: Vehicle Parameters Used in the Study

Vehicle Type	Base Vehicle Mass (kg)	Base Cost ($)	Energy Consumption (Wh km^{-1} kg^{-1})
Mini EV	650	10,000	0.08
Mid-size EV	1500	25,000	0.06
Heavy-duty	24,000	100,000	0.0334

The selected vehicle categories represent typical use cases across the EV market. The average values were obtained by collecting various EV data and categorizing them based on their size (Table 3.3). Mini vehicles emphasize affordability and urban mobility, while mid-size vehicles

reflect mainstream consumer demand for range and performance [30]. Heavy-duty vehicles represent high-energy-demand applications where battery energy density becomes a dominant constraint. Energy consumption values are expressed on a mass-normalized basis to capture the influence of vehicle weight on efficiency. This formulation is critical for evaluating battery technologies, as increases in battery mass directly affect vehicle energy consumption and therefore overall range.

The battery technologies evaluated in this study include lithium-ion and a range of metal-air chemistries such as Li-air, Zn-air, Al-air, Mg-air, Fe-air, Na-air, and K-air. The key performance parameters for each chemistry are compiled from literature sources and include:

- Specific energy (Wh kg^{-1})
- Energy density (Wh L^{-1})
- Battery cost (\$ kWh^{-1})
- Efficiency (%)

These parameters define the intrinsic energy storage capability and economic characteristics of each battery system.

Table 3. 2: Battery Properties for All Different MABs

Parameter	**Li-air**	**Zn-air**	**Mg-air**	**Al-air**	**Na-air**	**Fe-air**	**K-air**	**Si-air**	**Sn-air**	**Ca-air**	**Li-ion**
Specific Energy (Wh/kg)	523-800	180-500	400-700	300-900	200-400	200-400	95-105	124-640	250-420	—	269-350
Energy Density (Wh/L)	620-1125	160-1400	800-1200	100-700	100-200	400-600	47.5-52.5	61.75-320	800-1000	—	750-810
Specific Power (W/kg)	—	10-200	20-550	15-130	12-300	—	—	—	—	—	500-20,000
Energy Cost ($/kWh)	70-200	70-160	200-400	31-37	100-150	150-250	70-154	70-160	30-50	—	70-250
Cycle Life (cycles)	20-100	150-450	50-100	0-30	40-150	6-500	8-80	—	100-1000	100-700	1000-6000

Energy Efficiency (%)	—	64-74	60-90	15-45	75-84	70-80	94.2-96.1	—	—	—	95
Operating Temp (°C)	10-40	-20-70	420-620	30-50	25-110	23-650	23-44	23-800	25-750	25-100	-20-60
Safety (Index)	4	8	8	9	4	8	4	8	5.5-7.5	4-6.5	6-10
Mass Overhead Factor	2	1.7	1.5-1.7	1.7-1.8	1.7-2	2-2.3	1.7-2	1.7-1.9	2.5-3	2-2.5	1.3-1.7
Volume Overhead Factor	2.9-6	2-2.5	2-2.5	2-2.5	2.5-2.9	2.4-2.8	2.5-2.9	2.2-2.4	3-3.5	2.7-3	1.2-1.4

The dataset (Table 3.2) used in this study incorporates a combination of reported values and carefully derived estimates to ensure completeness across all battery chemistries. In cases involving Li-ion systems, certain maximum values are assumed based on configurations employing a lithium metal anode, representing an upper-bound performance scenario. Additional data and projections are adopted from established literature sources, including Cano et al. [30], to maintain consistency with widely accepted benchmarks. Cycle life is defined as the number of cycles or operational years before the battery capacity degrades to 80% of its initial value, providing a standardized basis for comparison across technologies. For parameters where direct experimental data are unavailable, such as volumetric energy density in some metal-air systems, values are estimated from reported capacity densities by assuming a representative cell density, typically around 2 kg L^{-1}. Similarly, adjustments are applied where original literature values are reported on an anode-mass basis, converting them to cell-level metrics using appropriate scaling factors. System-level parameters, including battery mass overhead and volume overhead, are derived using a comparative estimation approach. This method benchmarks well-characterized systems such as Li-ion, Li-air, and Zn-air batteries, and extends these relationships to other metal-air chemistries by accounting for differences in metal density, packing efficiency, electrochemical behavior, and auxiliary system requirements. A similar comparative framework is applied to assign safety indices, where relative values are determined based on material reactivity, electrolyte

characteristics, and overall system design considerations. While these estimations introduce a degree of uncertainty, they provide a consistent and physically grounded basis for evaluating a wide range of battery chemistries within a unified techno-economic framework.

Table 3. 3: Representative Electric Vehicle Dataset for Model Calibration (July 2024)

Model	Range (km)	Battery (kWh)	Curb Weight (kg)	GVWR (kg)	Energy Consumption (Wh km^{-1} kg^{-1})	Price ($)	Segment
Tesla Model Y	531.1	75	1995	2405	0.0587	44,990	Mid-size SUV
Tesla Model S	651.8	100	2162	2720	0.0564	72,990	Full-size Car
Ford Mustang Mach-E	397.5	70	1959	2690	0.0655	39,995	Mid-size SUV
Chevrolet Bolt	416.8	65	1628	2062	0.0756	41,577	Subcompact SUV
Volkswagen ID.4	442.6	82	2235	2750	0.0674	39,735	Mid-size SUV
Nissan Leaf	341.2	40	1591	2210	0.0530	28,040	Compact Car
Audi e-tron	363.7	95	2615	3205	0.0815	70,800	Mid-size SUV
Tesla Model 3	437.7	60	1836	2149	0.0638	38,990	Mid-size Car
Hyundai Kona Electric	415.2	39	1685	2160	0.0435	33,550	Compact SUV
BMW i4 (2025)	515	81.3	2065	2605	0.0606	52,200	Mid-size Car
Hyundai Ioniq 5	385	77.4	2275	2660	0.0756	41,800	Compact SUV
Polestar 2 (2024)	470	79	2030	2500	0.0672	54,950	Compact Sedan
GMC Hummer EV	482.8	170	3928	4785	0.0736	79,995	Pickup Truck
Kia Niro EX	385	64.8	2200	2200	0.0765	29,190	Subcompact SUV
Mazda MX-30	169.0	35.5	1548	2119	0.0991	42,650	Compact SUV
Subaru Solterra	365.3	64	1975	2550	0.0687	44,995	Compact SUV
Ford F-150 Lightning	370.1	131	3109	3856	0.0918	62,995	Pickup Truck
Rivian R1T	415.2	141.5	3242	3870	0.0881	71,700	Pickup Truck
Heavy-Duty Electric Vehicles							

Model	Range (km)	Battery (kWh)	GVWR (kg)	Energy Consumption (Wh km^{-1} kg^{-1})	Segment
Daimler eActros 600	500	600	22,000	0.0545	Semi-truck
Freightliner eCascadia	354	438	37,195	0.0333	Semi-truck
Volvo VNR Electric	370	—	14,969	0.0085	Semi-truck
Nikola Tre	531.1	738	37,195	0.0374	Semi-truck

The vehicle dataset (Table 3.3) used in this study is constructed from a representative selection of commercially available electric vehicles spanning multiple segments, including compact cars, mid-size vehicles, sport utility vehicles, and heavy-duty trucks. The dataset includes key parameters such as driving range, battery capacity, vehicle mass, and energy consumption efficiency, enabling a realistic calibration of the vehicle-level model. Energy consumption is expressed in a mass-normalized form (Wh km^{-1} kg^{-1}), allowing consistent comparison across vehicles of different sizes and classes. The inclusion of heavy-duty electric trucks extends the applicability of the analysis to high-energy-demand scenarios, where battery performance constraints are more pronounced. Average values derived from this dataset are used as baseline inputs in the techno-economic model, ensuring that the results reflect real-world vehicle performance rather than idealized assumptions. This approach provides a robust foundation for evaluating the impact of different battery chemistries on driving range and system-level efficiency.

To ensure consistency across all evaluated battery technologies, several simplifying assumptions are applied:

- Battery systems are assumed to operate under steady-state conditions
- Power limitations are not explicitly considered, as the focus is on energy delivery
- Efficiency values are treated as constant across the operating range
- Environmental and degradation effects are not included

These assumptions allow the analysis to isolate the impact of fundamental battery properties on vehicle performance, while maintaining computational tractability.

All input parameters are normalized and applied uniformly across the three vehicle categories. This ensures that differences in performance arise solely from the intrinsic properties of battery technologies rather than inconsistencies in modelling assumptions. Furthermore, midpoint values are used where parameter ranges are reported, providing a balanced representation

of expected performance. This approach avoids bias towards either optimistic or conservative estimates.

3.4 Results and Discussion

The developed framework is applied to evaluate the techno-economic performance of multiple battery chemistries across different vehicle classes. As mentioned earlier, studying practical performance metrics is crucial as they provide real-world insights into the efficiency and limitations of MABs, beyond what theoretical parameters can predict. Thus, Figure 3.1 compares the practical characteristics of various MABs to better understand the potential of these candidates for next-generation EVs, alongside those of Li-ion batteries. The data is compiled from the latest literature showcasing the practical value ranges at the cell level whereas energy storage cost is the price of a battery pack or system level. Safety ratings for various battery types are determined qualitatively on a scale of 1 to 10 based on factors like the risk of toxic material release, overheating and electrolyte flammability. Li-ion, Li-air, and Zn-air batteries are rated directly based on these criteria, while other MAB types are evaluated by comparing their properties to those of the known Li-ion, Li-air, and Zn-air batteries. Adjustments are made to account for differences in metal reactivity, electrochemical properties, and cell components. This approach provides a logical framework for assigning relative safety values. Li-ion batteries have a variable safety profile, with ratings ranging from 6 to 10, indicating that their safety can vary significantly depending on specific conditions or configurations. Certain MABs show higher safety ratings, with Al-air batteries (aqueous electrolytes) rated at 9 and other types (Zn-air, Mg-air, Fe-air, and Si-air) rated at 8. Practical evaluation of certain battery metrics, such as energy storage cost, energy density, and specific energy in Figure 3.2, can be achieved by approximating their influence on battery pack volume (Vol_B), total vehicle cost ($C_{V,T}$), and vehicle range (R_V). These metrics are directly correlated with the battery pack's energy (E_B) and can be calculated using the equations adapted from [30] and shown in Table 3.3. The overhead factors quantify the necessary safety and air management equipment for each battery type, especially for MABs. This estimation approach for battery system mass overhead and battery system volume overhead uses comparative analysis based on the known properties of MABs Li-air and Zn-air batteries and adjusts them according to the specific characteristics of other MABS such as the density of the metal used, packing efficiency, electrochemical properties, and cell components.

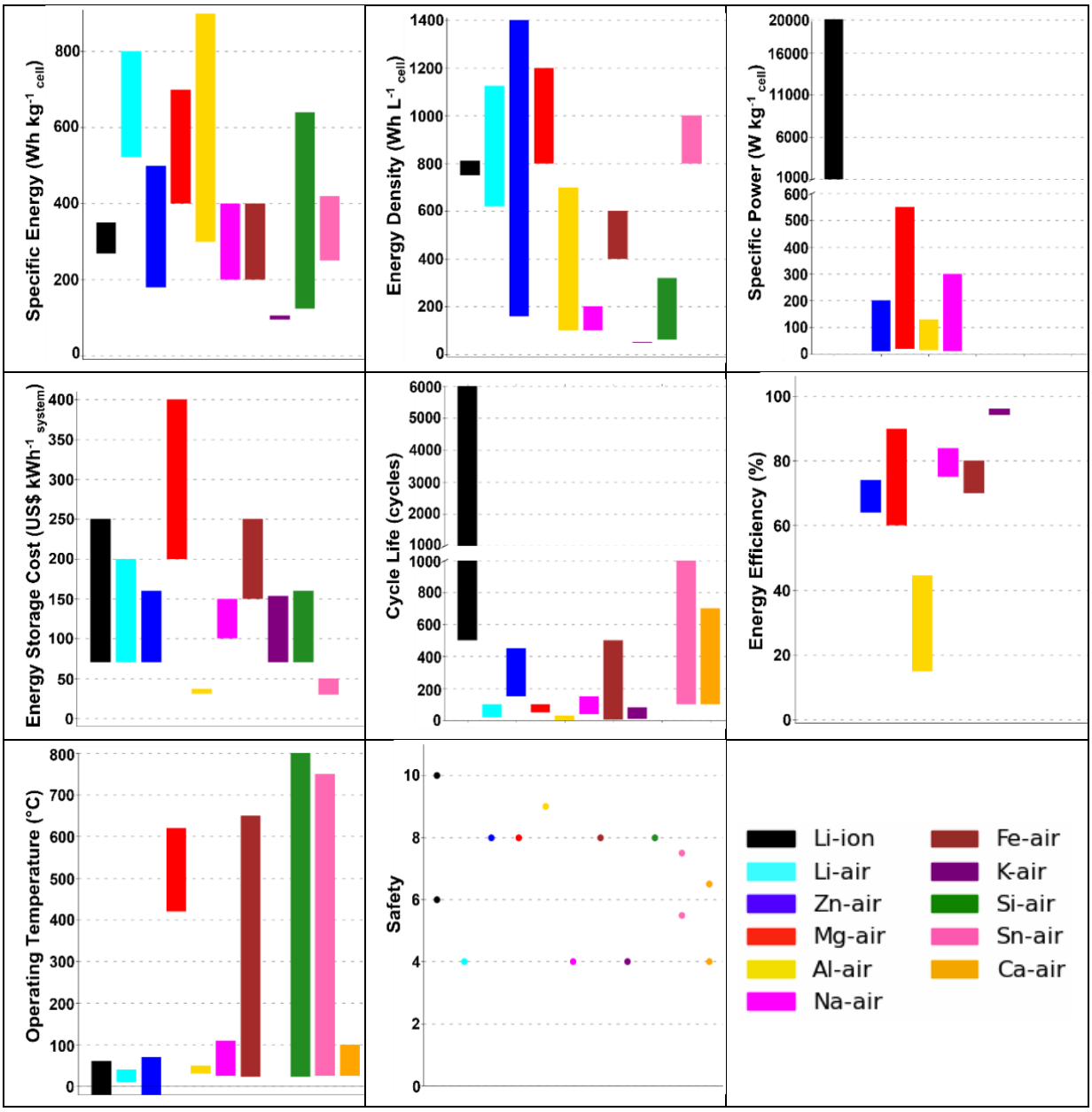


Figure 3. 1: Comparative characteristics of various MABs and Li-ion cells. The data represents the practical value ranges at the cell level, derived from existing literature.

In addition to safety, it is important to recognize that practical performance metrics such as specific energy, energy density, and cost must be interpreted collectively rather than independently. A battery system exhibiting high specific energy may still underperform at the vehicle level if its efficiency, cycle life, or system overheads are unfavorable. Therefore, Figure 3.1 should be interpreted as a multi-parameter comparison, highlighting that no single

battery chemistry simultaneously optimizes all performance metrics. This observation reinforces a key system-level insight: the suitability of a battery technology for EV applications is governed not by peak material properties, but by the balance between energy density, efficiency, safety, and system integration requirements. This forms the basis for the subsequent techno-economic evaluation.

Li-ion batteries, being a well-established and widely used technology, offer a highly balanced profile with their excellent cycle life (1000-6000) and consistently high energy efficiency (95%). Analyzing the capabilities of MABs, their effectiveness as range extenders is significantly shaped by their cycle life, energy efficiency and safety profile. Zn-air batteries offer a balanced compromise with a cycle life ranging from 150 to 450 cycles and efficiency between 64% and 74%. This makes them a viable option as a range extender, given their moderate performance in both longevity and energy efficiency. In comparison, Fe-air batteries achieve a slightly higher maximum cycle life of up to 500 cycles and an efficiency of 80%. However, their relatively lower energy density and specific energy results in an unfavourable trade-off for a range extender. Among relatively high-efficiency, mechanically rechargeable batteries with moderate cycle life, Li-air and Al-air batteries stand out. Currently, Li-air batteries offer up to 100 cycles (electrically rechargeable), while Al-air batteries exhibit efficiencies as high as 45%. Both types show impressive energy metrics and driving range, demonstrating significant potential. However, further research and development are needed to standardize these battery designs and address their current limitations. For enhanced safety in hybrid vehicles, Al-air and Zn-air batteries are preferable to Li-air, as seen from the safety profile. K-air batteries, while boasting a high efficiency of 94.2-96.1% but a poor cycle life of 8-80 cycles, also fall short in other key energy metrics, making them unsuitable for range-extending applications in the near term. Similarly, Na-air batteries, with their moderate cycle life and efficiency, also present less favourable trade-offs. Meanwhile, Si-air, Sn-air, and Ca-air batteries lack sufficient data for immediate application but could offer unique advantages or potential for future use as research and technology progress.

A critical implication of these results is that high efficiency alone does not guarantee suitability for EV integration. For example, K-air batteries demonstrate excellent energy efficiency but are limited by extremely low cycle life, rendering them impractical for repeated vehicle use. Conversely, Zn-air batteries, while less efficient, offer a more balanced combination of cycle life and performance, making them more suitable for near-term deployment. This highlights a

fundamental design principle for range extender systems: moderate efficiency combined with acceptable durability is often more valuable than extreme performance in a single parameter. Therefore, battery selection must prioritize balanced performance across multiple criteria rather than optimizing a single metric.

Figure 3.2 illustrates results for three vehicle categories: a mini vehicle (Figures 3.2 (a) and (b)), typically found in markets that prioritize affordability; a mid-size vehicle (Figures 3.2 (c) and (d)), prevalent in markets emphasizing range; and a semi-trailer truck (Figures 3.2 (e) and (f)), representing heavy-duty applications. Figures 3.2 (a), (c), and (e) show the vehicle cost as it relates to the driving range, plotted until the battery volume surpasses the designated space limit within each vehicle.

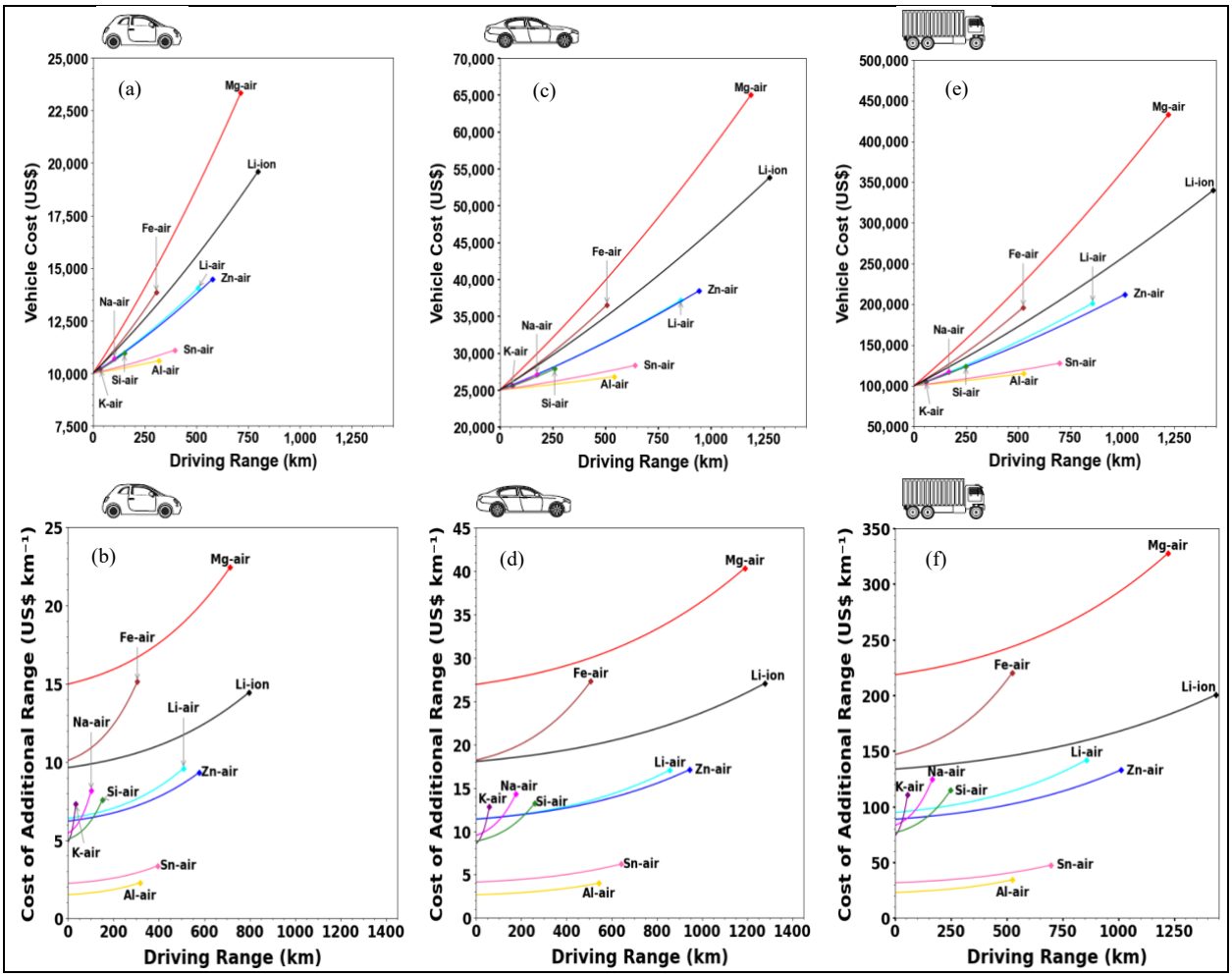


Figure 3. 2: Vehicle cost vs. driving range and cost of additional range vs. driving range. Plots in (a,c,e) are computed from the equations R_V and $C_{V,T}$ while (b,d,f) are plotted from calculating the tangents of the curves of (a,c,e) respectively. (a,b): mini-vehicle; (c,d): mid-size vehicle; (e,f): semi-trailer truck.

For the mini-vehicle, the vehicle cost is \$10,000, with a mass of 650 kg and an energy consumption efficiency of 0.08 $Whkm^{-1}kg^{-1}$. For the mid-size vehicle, the vehicle cost is \$25000, with a mass of 1500 kg and an energy consumption efficiency of 0.06 $Whkm^{-1}kg^{-1}$ and the semi-trailer truck has a vehicle cost of \$100000, a mass of 24000 kg, and an energy consumption efficiency of 0.0334 $Whkm^{-1}kg^{-1}$. These curves use midpoint values for battery system overhead ranges, energy storage cost, volumetric energy density, and specific energy (Table 3.2). The cost-range relationship exhibits a distinctly non-linear behavior across all vehicle categories. At lower ranges, cost increases gradually as battery capacity is added. However, beyond a threshold range,

the cost increases more rapidly due to the combined effects of battery mass, system overhead, and volumetric constraints. This behavior is particularly pronounced in heavy-duty vehicles, where energy requirements are significantly higher.

In Figures 3.2 (b), (d), and (f), the cost of adding range per km is plotted against the vehicle's range. The curves are generated by calculating the tangents of the respective curves from Figures 3.2 (a), (c), and (e). While these plots illustrate the inherent capability of each battery type to reduce costs and extend the driving range, it does not consider factors such as power metrics, electric grid compatibility, self-discharge rate, cycle life, efficiency, and safety, which are essential for reliable operation in an electric vehicle. Na-air, K-air, and Si-air batteries have significant drawbacks due to their low energy densities, resulting in limited driving range extensions. Their cost per additional range is still greater than that of Li-air, Zn-air, and Al-air batteries, which offer comparable driving ranges at a significantly lower cost than Li-ion batteries across all three vehicle types. This metric provides a more practical perspective than absolute vehicle cost, as it directly quantifies the economic efficiency of extending driving range. Technologies with low marginal cost of range, such as Al-air, are particularly attractive for range extender applications, even if their overall efficiency is lower.

With the equipment to safeguard against atmospheric carbon dioxide and moisture, the utmost volumetric energy density of Li-air batteries at the vehicle level is projected to be only 384 WhL^{-1}. This volumetric limitation hinders their ability to achieve significantly longer driving ranges compared to Li-ion batteries. On the flip side, Zn-air batteries, offering lower costs and greater range than Li-air batteries, are favoured by researchers for forthcoming EVs because of their superior practical energy density. Despite their potential, substantial improvements in energy efficiency, specific power, and cycling stability are necessary for the successful integration of Zn-air batteries, into electric vehicles in a dual-battery configuration. While Al-air batteries offer the lowest cost per additional kilometer, their low energy efficiency and complex mechanical recharge design may hinder their adoption. However, the combination of attributes such as low cost and high safety could indirectly boost range by powering auxiliary units, reducing the load on the main battery. The Fe-air battery has the second-highest cost for additional range, only surpassed by Mg-air. Although Mg-air batteries provide a driving range comparable to Li-ion batteries, their cost is significantly higher, exceeding what the average EV customer might expect to pay. Unless the estimated cost for both Fe-air and Mg-air is substantially reduced, these batteries may not be

suitable for high-usage EVs. These results collectively indicate that metal-air batteries are not universally suitable as standalone replacements for Li-ion systems. Instead, their optimal role lies in hybrid configurations, where their high energy density can be leveraged without being constrained by their lower power capability and efficiency.

Thus, this chapter has conducted a comprehensive analysis of MAB parameters in the context of EVs, focusing on their impact on driving range, total vehicle cost, and battery volume. By considering these practical factors along with the information on battery chemistry, cell design, and cell working, we have gained valuable insights into the trade-offs involved in optimizing MAB performance. The findings presented in this chapter can serve as a valuable resource for researchers, engineers, and policymakers working to advance the development of high-performance and cost-effective electric vehicles. These findings also provide a quantitative foundation for the integration of metal-air batteries into dual-energy storage architectures, which is further explored in subsequent chapters of this thesis.

3.5 Conclusions

This study presents a comprehensive techno-economic evaluation of metal-air batteries (MABs) for electric vehicle applications by translating electrochemical properties into vehicle-level performance metrics. The analysis reveals several key quantitative insights regarding the feasibility of different battery chemistries. At the vehicle level, the average energy consumption derived from a representative EV dataset is approximately 0.0704 Wh km^{-1} kg^{-1}, with compact vehicles exhibiting lower values (~0.0603 Wh km^{-1} kg^{-1}) compared to mid- and full-size vehicles (~0.0675 Wh km^{-1} kg^{-1}). These values highlight the strong dependence of range on vehicle mass and reinforce the importance of gravimetric efficiency in battery selection. Lithium-ion batteries demonstrate the most balanced performance, with a cycle life of 1000-6000 cycles and energy efficiency of ~95%, establishing them as the benchmark for reliability and performance. However, their specific energy range (269-350 Wh kg^{-1}) limits further range extension without significant increases in system cost and mass. Among metal-air systems, Zn-air batteries exhibit a favorable balance between performance and practicality, with specific energy ranging from 180-500 Wh kg^{-1}, cycle life of 150-450 cycles, and efficiency between 64-74%. This positions Zn-air as one of the most promising candidates for near-term range extender applications. Al-air batteries demonstrate the lowest economic barrier for range extension, with energy storage costs as low as

31-37 \$ kWh^{-1}, resulting in the lowest cost per additional kilometer across all vehicle categories. However, their relatively low energy efficiency (15-45%) and limited rechargeability constrain their use to mechanically rechargeable or auxiliary applications. Li-air batteries exhibit the highest theoretical energy potential, with specific energy up to 800 Wh kg^{-1}, but practical limitations reduce their effective volumetric energy density to approximately 384 Wh L^{-1} at the system level, significantly limiting their achievable range advantage. Additionally, their cycle life (~100 cycles) and system complexity remain major barriers to implementation. Mg-air and Fe-air batteries, despite moderate performance, are limited by economic constraints. Mg-air systems exhibit high energy potential but energy storage costs of 200-400\$ kWh^{-1}, making them economically unfavorable. Similarly, Fe-air batteries, while achieving up to 500 cycles and ~80% efficiency, suffer from lower energy density and relatively high cost per additional range.

The cost-range analysis reveals a non-linear relationship between vehicle cost and driving range, where marginal cost increases sharply beyond a threshold due to mass and volumetric constraints. This effect is most pronounced in heavy-duty vehicles, where energy requirements are significantly higher.

Importantly, the marginal cost of extending range provides a more meaningful metric than total cost. Al-air batteries exhibit the lowest marginal cost, followed by Zn-air, while Li-ion systems show higher incremental costs at extended ranges.

3.6 Future Work

While this study provides a comprehensive techno-economic evaluation, several areas require further investigation to enable practical implementation of metal-air batteries in EV systems:

- Dynamic vehicle-level modelling: Integration of metal-air batteries into time-dependent driving cycles (e.g., UDDS, WLTP) to evaluate real-time performance.
- Power and transient behavior: Inclusion of power density constraints and transient response to assess compatibility with vehicle load demands.
- Electrochemical degradation modelling: Incorporation of cycle life degradation, self-discharge, and electrolyte degradation effects.
- System-level efficiency improvements: Optimization of air management, electrolyte circulation, and auxiliary subsystems.

- Hydrogen and by-product management: Particularly critical for Al-air and Zn-air systems to ensure safety and operational stability.
- Integration with control strategies: Development of SOC-based or demand-based control logic for hybrid Li-ion-MAB systems.

Future work will extend this analysis through high-fidelity system-level modelling using MATLAB/Simulink, where metal-air batteries are integrated as range extenders within a dual-energy storage architecture. This will enable evaluation under realistic driving conditions and provide deeper insight into control strategies and system performance.

Chapter 4 Performance Optimization of High Energy Density Aluminum-Air Batteries: Effects of Operational Parameters and Electrolyte Composition

*** Chapter 4 is adapted from Shabeer Y, Madani SS, Panchal S, Fowler M. "Performance optimization of high energy density aluminum-air batteries: Effects of operational parameters and electrolyte composition." Future Batteries 2025;6:100082. https://doi.org/10.1016/J.FUB.2025.100082.

4.1 Introduction

The overuse of fossil fuels has triggered not only a climate crisis but also a range of socio-economic challenges, such as disruptions in supply chains that threaten supply security. The excessive reliance on these fuels has significantly increased the emission of harmful greenhouse gases (GHGs) worldwide. In response, many nations have prioritized efforts to curb GHG emissions. For instance, Canada has committed to reducing its GHG emissions by 80% by 2050, compared to 2007 levels. Among various sectors, transportation is the largest contributor to GHG emissions. In Canada, for example, the transportation sector accounts for 82.5% of the country's overall national transportation emissions, primarily due to the reliance on fossil fuels in internal combustion engine vehicles (ICEVs) [242].

A promising alternative to fossil fuels is the generation of electricity from renewable energy sources, particularly as electrical energy begins to replace gasoline. To meet global GHG reduction targets, it is projected that nearly 90% of electricity generation worldwide must come from renewable sources, with solar and wind energy contributing close to 70% [4]. This shift underscores the urgent need for the development of advanced energy storage systems. The growing reliance on renewable energy has created a significant demand for robust storage solutions to support both on-grid and off-grid energy applications [23,243-245].

In light of these challenges, significant efforts are underway to develop alternative battery systems for energy storage applications [246]. Innovations in battery storage hold immense promise for addressing the vulnerabilities of renewable energy generation systems [18]. Among the current technologies, lithium-ion batteries (LIBs) have become dominant in the battery market

due to their high charge-discharge efficiencies and superior energy density [247,248]. However, LIBs face several critical limitations. Resource availability is a significant concern, as the global distribution and limited abundance of lithium and other essential elements, such as cobalt, raise supply chain challenges. With the anticipated growth of electric grid storage and electric mobility, the demand for these materials will surge, exacerbating these issues [249]. Safety is another pressing concern for LIBs, with increasing reports of fire incidents in aircraft and electric vehicles as their usage expands. Problems such as thermal runaway, lithium dendrite-induced short circuits, and toxic gas emissions contribute to these risks [47,250]. Additionally, LIBs pose environmental challenges, including the ecological damage caused by the extraction and production of raw materials and the improper disposal of toxic elements like cobalt and nickel. Recycling efforts are hampered by economic and technical barriers, such as complex disassembly processes and low profitability [251]. Given these drawbacks, the development of next-generation battery technologies for sustainable energy storage is not just desirable but essential.

Metal-air batteries are notable for their exceptionally high specific energies, as they leverage oxygen from the air as a reactant on the cathode side. Both rechargeable and non-rechargeable metal-air batteries, utilizing anodes such as lithium (Li), magnesium (Mg), potassium (K), sodium (Na), zinc (Zn), aluminum (Al), and iron (Fe), have garnered significant attention in recent years [252-254]. Figure 4.1 [52] illustrates the gravimetric energy densities, nominal cell voltages, and energy densities of various metal-based negative electrodes in metal-air batteries. Lithium has drawn the most academic focus due to its exceptionally high theoretical specific energy of 5928 Wh kg^{-1} and a high nominal cell voltage of 2.96 V. However, lithium's inherent instability in contact with air and aqueous electrolytes poses significant challenges [255]. Both aluminum and magnesium battery systems are compatible with aqueous electrolytes and can achieve power densities comparable to lithium-air cells. Nevertheless, magnesium's lower reduction potential often results in pronounced self-discharge and poor coulombic efficiency, limiting its practical applications [256].

Among the many emerging metal-air battery technologies, aluminum-air (Al-air) batteries stand out due to their advantageous properties. These batteries boast a theoretical energy density of 8 kWh/kg and a practical energy density of approximately 4 kWh/kg, making them a highly energy-efficient option. Al-air batteries also provide superior safety features, attributed to the low

reactivity of aluminum, making them easier to handle compared to other battery technologies. Aluminum's abundance- it is the third most plentiful material on earth- contributes to its cost-efficiency. Additionally, aluminum is lightweight, non-toxic, safe, and recyclable, further enhancing its appeal for use in energy storage systems [257].

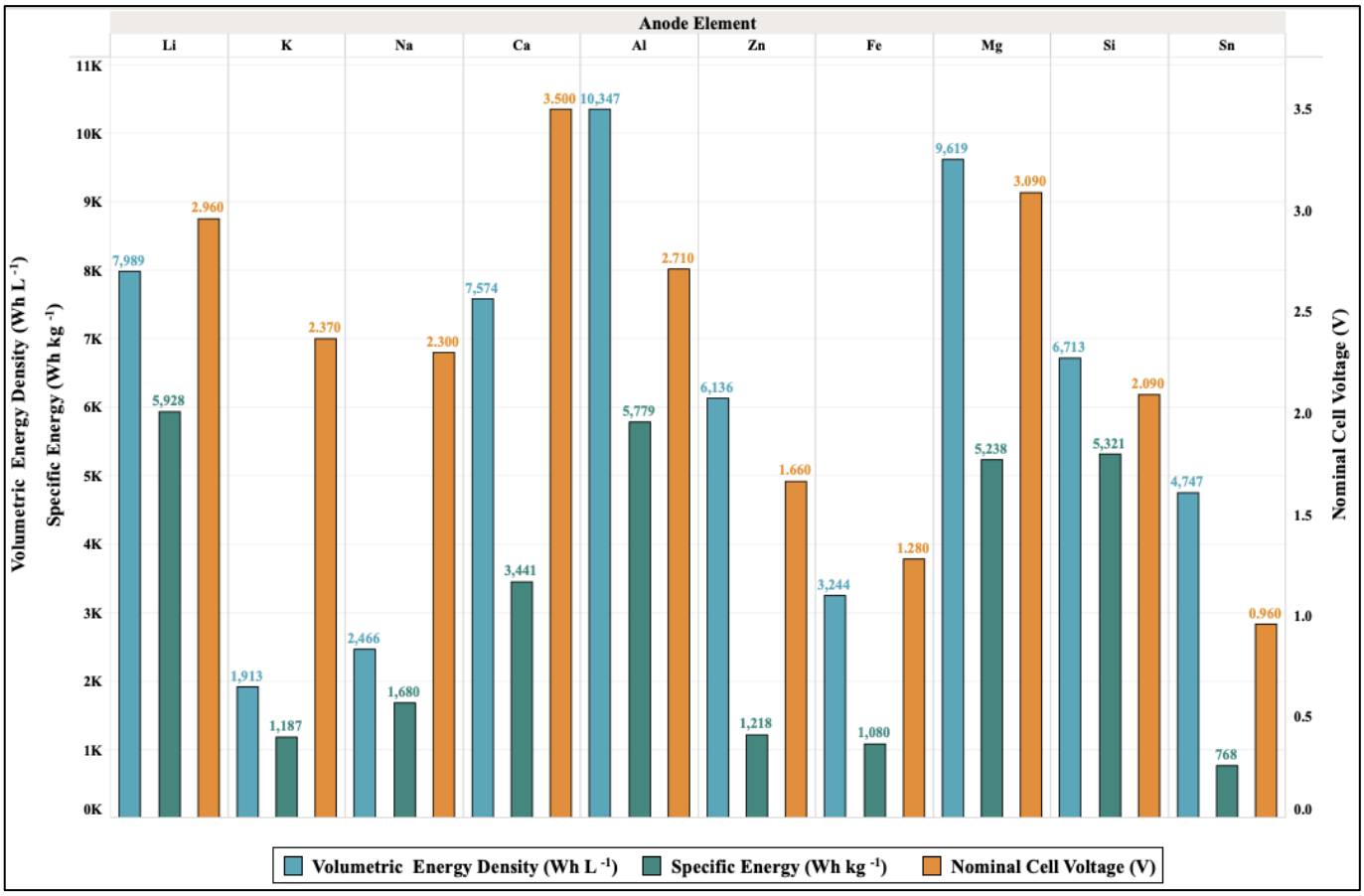


Figure 4. 1: Comparison of metal-air batteries based on theoretical specific energy, gravimetric and volumetric energy densities, and nominal cell voltage [258]

An Al-air battery comprises several key components, including an aluminum anode, an air cathode, an aqueous alkaline electrolyte, an external load, and a peristaltic pump for electrolyte circulation. The system also includes anolyte and catholyte chambers, current collectors, separators, and additional electronics. The specific configuration and design of the battery influence the choice and arrangement of these components. In operation, the Al anode connects to the air cathode through an external load circuit, as depicted in Figure 4.2. The alkaline electrolyte, which is ionically conductive, facilitates electrochemical interactions between the two electrodes.

During discharge, hydroxide ions (OH^-) oxidize the Al anode, producing tetrahydroxy aluminate ions and releasing three electrons, as shown in Equation 1. These electrons flow through the external circuit, powering the load, while oxygen at the air cathode consumes the electrons via the oxygen reduction reaction (ORR). To maintain electrolyte neutrality, the OH^- ions produced at the air cathode diffuse to the Al anode, where they are consumed. The overall electrochemical reaction achieves a nominal cell voltage (E^0) of approximately 2.75 V, as described in Equation 3. The individual reactions at the anode and cathode, along with the overall cell reaction, are detailed below [259-261].

The anode cell reaction is,

$$Al + 4OH^- \rightarrow Al(OH)_4^- + 3\,e^- \qquad E^0 = -2.35\ V \qquad (4.1)$$

In cathodic reduction, the oxygen from the air reacts with water in the electrolyte as follows,

$$O_2 + 2H_2O + 4e^- \rightarrow 4OH^- \qquad E^0 = +0.40\ V \qquad (4.2)$$

The overall cell reaction is,

$$4Al + 3\,O_2 + 6H_2O + 4OH^- \rightarrow 4Al(OH)_4^- \qquad E^0 = 2.75\ V \qquad (4.3)$$

While Al-air batteries offer significant advantages, including high energy density and low cost, they face several challenges that hinder large-scale commercialization. These include complex mechanical rechargeability, low coulombic efficiency, and limited power density. Despite these limitations, Al-air batteries hold great potential as range extenders in electric vehicles when paired with lithium-ion batteries. In this configuration, the Al-air battery pack activates when the charge level of the lithium-ion battery drops below a predetermined threshold during long-range journeys. This hybrid approach combines the high energy density and cost-effectiveness of Al-air batteries with the performance benefits of LIB technology. Beyond their use in electric vehicles, Al-air batteries have promising applications in stationery and portable systems. They are being considered for use in sectors such as aviation, maritime, and military, as well as in long-lasting portable electronics. Additionally, Al-air batteries can serve as reliable power sources in remote locations or for underwater vehicles, showcasing their versatility. Given

their unique properties, the potential applications of Al-air batteries are extensive and varied [212,213].

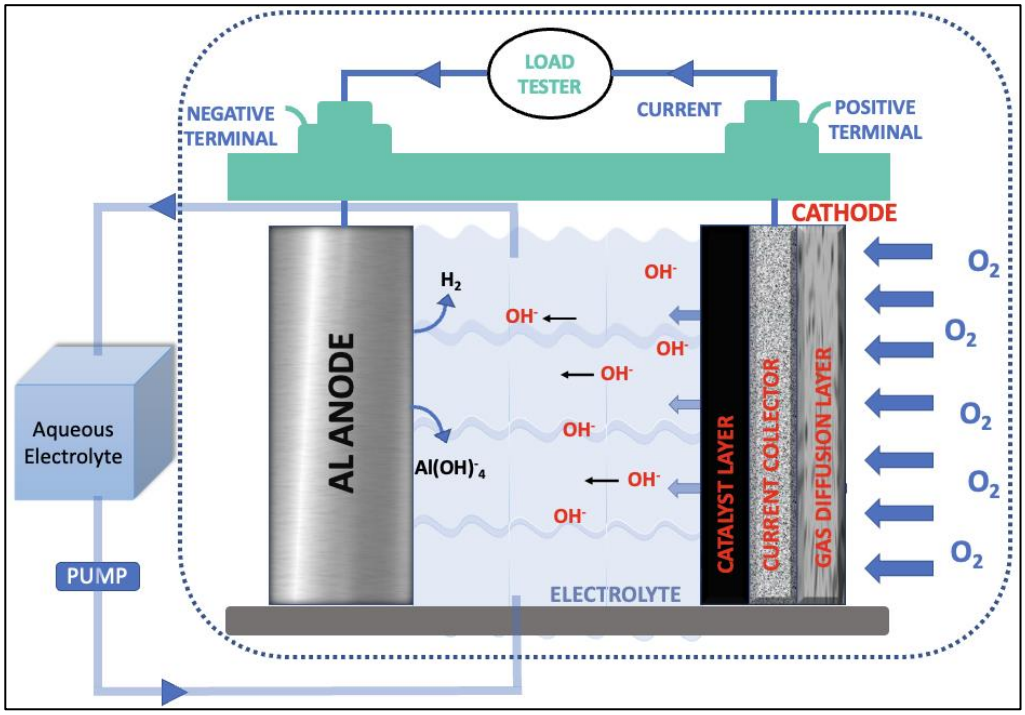


Figure 4. 2: Schematic representation of the two-electrode Aluminum-air battery

This paper investigates two distinct rotating disk prototypes of high-energy-density Al-air batteries. For Prototype-1, three critical operational parameters, such as the anode-cathode distance (ACD), electrolyte flowrate, and temperature are systematically evaluated. While previous studies have examined these parameters individually, their combined effects remain largely unexplored. This research aims to elucidate the synergistic interactions of these parameters across varying levels. Insights gained from prototype-1 are utilized to optimize the design of the advanced prototype-2, which features a larger active electrode surface area with an electrode cartridge system for enhanced usability and ease of maintenance. The performance of Al-air batteries is strongly influenced by the electrolyte composition, which affects the electrochemical reactions at both the anode and cathode, thereby impacting the overall efficiency and energy output. Sodium hydroxide (NaOH) and potassium hydroxide (KOH) are commonly studied electrolytes due to their ability to enhance conductivity and promote more efficient aluminum oxidation. Mokhtar et al. (2015) [44] reviewed alkaline electrolytes used in Al-air batteries up until 2015, noting that 4 M KOH and 4 M NaOH were among the most widely employed concentrations. In addition, Wang et al. (2019) [262] investigated the effect of NaOH concentrations ranging from 1 M to 5 M in one

molar increment, finding a steady increase in power density with higher concentrations, suggesting a positive correlation between concentration and battery performance. Few studies have also examined higher concentrations, such as 7 M KOH [45] and 8 M NaOH [263], but without a clear explanation for the selection of these values. These findings highlight the importance of understanding the role of electrolyte concentration in optimizing Al-air battery performance. By examining the effects of varying NaOH and KOH concentrations, insights can be gained into their impact on efficiency, stability, and longevity, which are crucial for developing high-performance, sustainable Al-air batteries. Section 2 provides a comprehensive overview of the materials and methodologies employed in the development and evaluation of both prototypes, including detailed descriptions of the electrochemical tests conducted to assess their performance. Section 3 presents an in-depth analysis of the results, exploring the individual and combined effects of operational parameters on battery performance. This section includes a comparative evaluation of the two alkaline electrolytes, also highlighting improvements in energy efficiency, current density, and operational stability in prototype-2. Additionally, it identifies the critical factors influencing the prototypes' performance and offers insights into the mechanisms underlying the observed trends. Section 4 concludes with the key findings, summarizing the study's contributions to optimizing the Al-air batteries and outlining potential directions for future research.

4.2 Materials and Methods

Two novel designs are tested for Al-air batteries: one with a 5 cm Al anode diameter and the other with a larger anode of 7.5 cm diameter featuring a more practical and easier setup with convenient cathode cartridges.

4.2.1 Prototype-1

Prototype-1 is designed with metal and acrylic plates and silicone gaskets, all secured by nuts and bolts for easy assembly and maintenance of the electrodes. The prototype schematic in Figure 4.3 illustrates an Al-air cell that uses a rotating anode and a stationary cathode. The housing assembly includes a fixed anolyte chamber made from 3D-printed poly(methyl methacrylate) (PMMA). The aluminum disc anode (5.08 cm in diameter) is sanded and weighed, then attached to a brass cylindrical current collector that acts as a rotating shaft. Silicone gaskets prevent electrode contact and maintain the ACD. Commercial air cathodes are cut into appropriate shapes slightly larger than the anode to ensure a tight seal and prevent electrolyte leakage. The cathode is placed over a silicone gasket with its activated carbon layer facing the anode and the gas diffusion layer facing outward. Another gasket and a PMMA plate secure the cathode in place. The anolyte chamber and cathode are then secured between steel plates in the housing assembly and fastened with screws and nuts. A peristaltic pump circulates a 250 mL 4M NaOH electrolyte through the anolyte chamber to ensure uniform flow. Compressed air at 5 psi is supplied to the system.

4.2.2 Prototype-2

Prototype-2 is designed to hold the anode and cathode cartridges, incorporating gears and tubing to facilitate the rotation of the anode and the circulation of electrolytes through the cell. The cell is first cleaned using deionized (DI) water. Electrolyte solutions of varying concentrations are then prepared separately by dissolving potassium hydroxide (KOH) and sodium hydroxide (NaOH) pellets (Sigma Aldrich Chemicals) in DI water, with the electrolyte maintained at a temperature of 40°C using a water bath. The aluminum anode is sanded and weighed. A commercial air cathode embedded in a cartridge is inserted into the cell, and the anode is screwed into the cell compartment with current tabs at the end. The distance between the anode and cathode is set to 1.5 mm. After testing, the anode is weighed again to determine its mass loss, which is also recorded. The prototypes built and tested in this paper are protected by the following patents [264,265] with further patents pending. Please note that AlumaPower have several patent families

(same invention covered in multiple countries, you can find the countries in the worldwide application section), each country issued patent number should be included.

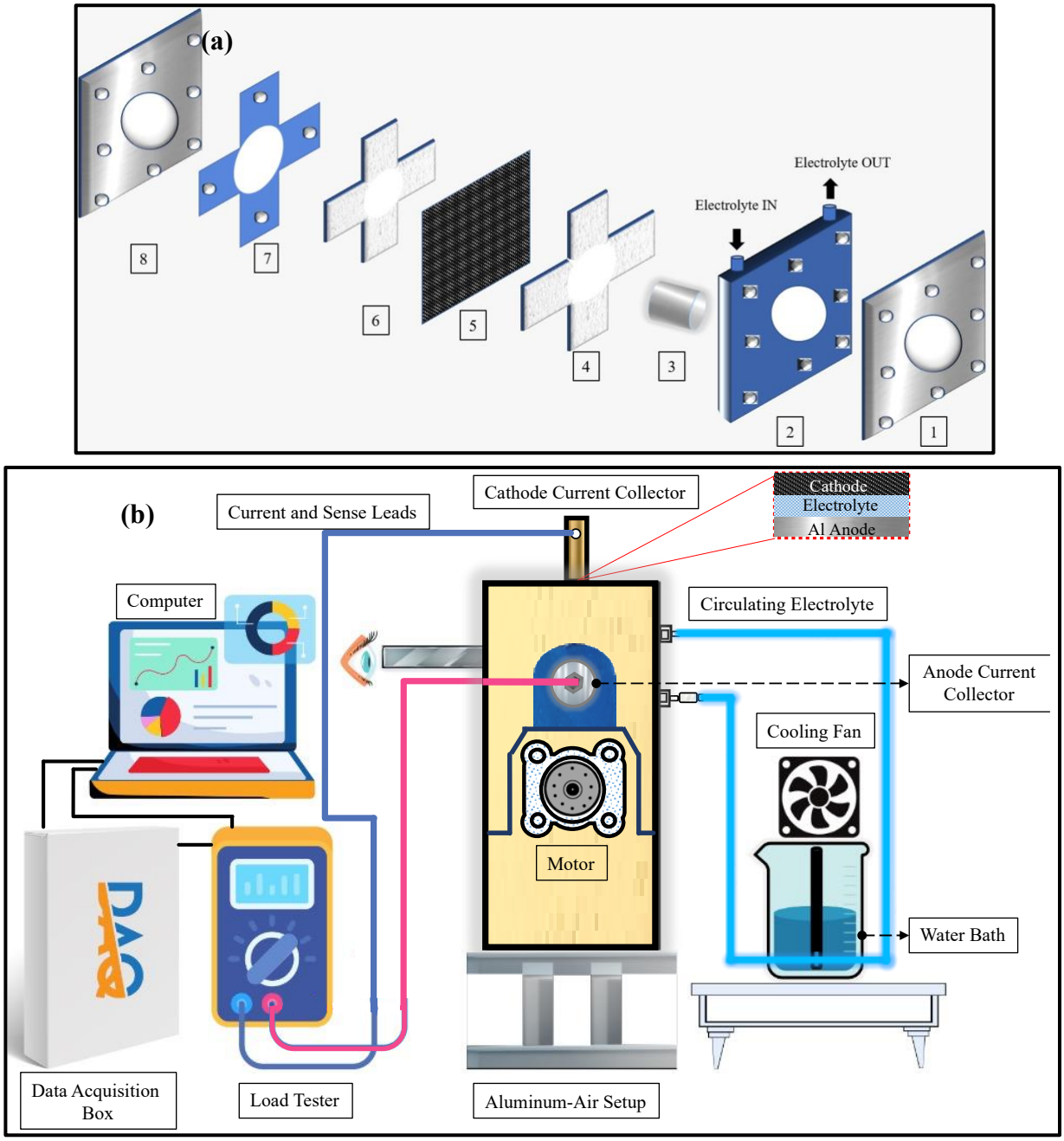


Figure 4. 3: Schematic representations of prototype-1 (a) and prototype-2 (b) with their components.

4.2.3 Potentiostatic Polarization and Voltage-Current Profiles

A potentiostatic polarization curve illustrates the relationship between voltage and current density in a battery, providing critical insights into performance characteristics. This curve enables

the identification of key losses, including ohmic, activation, and concentration losses, which influence overall efficiency [266,267]. The voltage-current (V-I) curve represents the relationship between voltage and current in a battery, providing essential insights into its behaviour under varying loads. This curve is instrumental in evaluating the battery's capacity, efficiency, and overall performance. Additionally, it is particularly valuable for assessing the rate capability, which reflects the battery's ability to deliver power at different discharge rates [268]. The voltage is recorded over one minute at varying current density loads, ranging from 0 mA/cm^2 to 300 mA/cm^2 in increments of 20 mA/cm^2 for prototype-1 and up to 200 mA/cm^2 for prototype-2. For the prototype-1 the tests are conducted in a 4M NaOH solution at varying combinations of operating parameters as shown in Table 4.1. Whereas for the prototype-2 the tests are conducted at a constant temperature of 40°C, ACD of 1 mm and an electrolyte flowrate of ~150 RPM at varying concentrations of electrolytes from 1 M to 10 M of NaOH and KOH solutions in increments of 1 M.

Table 4. 1: Summary of Test Conditions with Varying Operating Parameters

Runs	Temperature of electrolyte	Anode cathode distance	Electrolyte flowrate
1	40°C	3 mm	65 ml/min
2	50°C	3 mm	65 ml/min
3	40°C	10 mm	65 ml/min
4	50°C	10 mm	65 ml/min
5	40°C	3 mm	80 ml/min
6	50°C	3 mm	80 ml/min
7	40°C	10 mm	80 ml/min
8	50°C	10 mm	80 ml/min

4.2.4 Galvanostatic Discharge Profiles

A Galvanostatic discharge curve is a plot that represents the voltage of a battery as a function of time or capacity during a constant current discharge. The curve typically starts at the battery's open-circuit voltage (OCV) and decreases as the battery discharges [269,270]. The

discharge curves were measured at a constant current density of 120 mA/cm^2 for prototype-1 and 80 mA/cm^2 for prototype-2.

4.3 Results and Discussion

The performance evaluation of the Al-air battery is conducted under eight distinct test conditions, as summarized in Table 4.1. These conditions are designed to investigate the influence of electrolyte temperature, ACD, and electrolyte flowrate on the battery's electrochemical behaviour. By systematically varying these parameters, key insights into the operational efficiency and performance characteristics of the battery are obtained, providing a comprehensive understanding of its behaviour under diverse conditions.

4.3.1 Prototype-1: Impact of ACD

The results are categorized based on ACD measurements of 3 mm and 10 mm as shown in Figures 4.4 and 4.6 respectively. The distance between the anode and cathode in a battery significantly influences its efficiency and performance. A shorter ACD reduces internal resistance, thereby enhancing efficiency by minimizing energy loss as heat during electrochemical reactions. Additionally, decreasing this distance increases the power density of the battery, allowing it to deliver more power for a given volume, which is particularly advantageous for high-power applications. The ease of ion transport is also affected by the ACD; a shorter distance facilitates faster ion movement, improving the battery's discharge rates. Furthermore, in certain battery designs, a reduced ACD can enhance electrolyte utilization, leading to better overall performance and efficiency [271,272]. In the context of Al-air batteries, a smaller ACD not only decreases internal resistance but also contributes to reducing the cell's overall size and weight. To determine the optimal ACD, a silicone rubber gasket with a thickness of 1.5 mm is employed to simulate ACDs of 3 and 10 mm. The desired ACD values are achieved by stacking multiple gaskets. The tests are conducted under various combinations of electrolyte temperature and flowrate, allowing for the analysis of their combined effects.

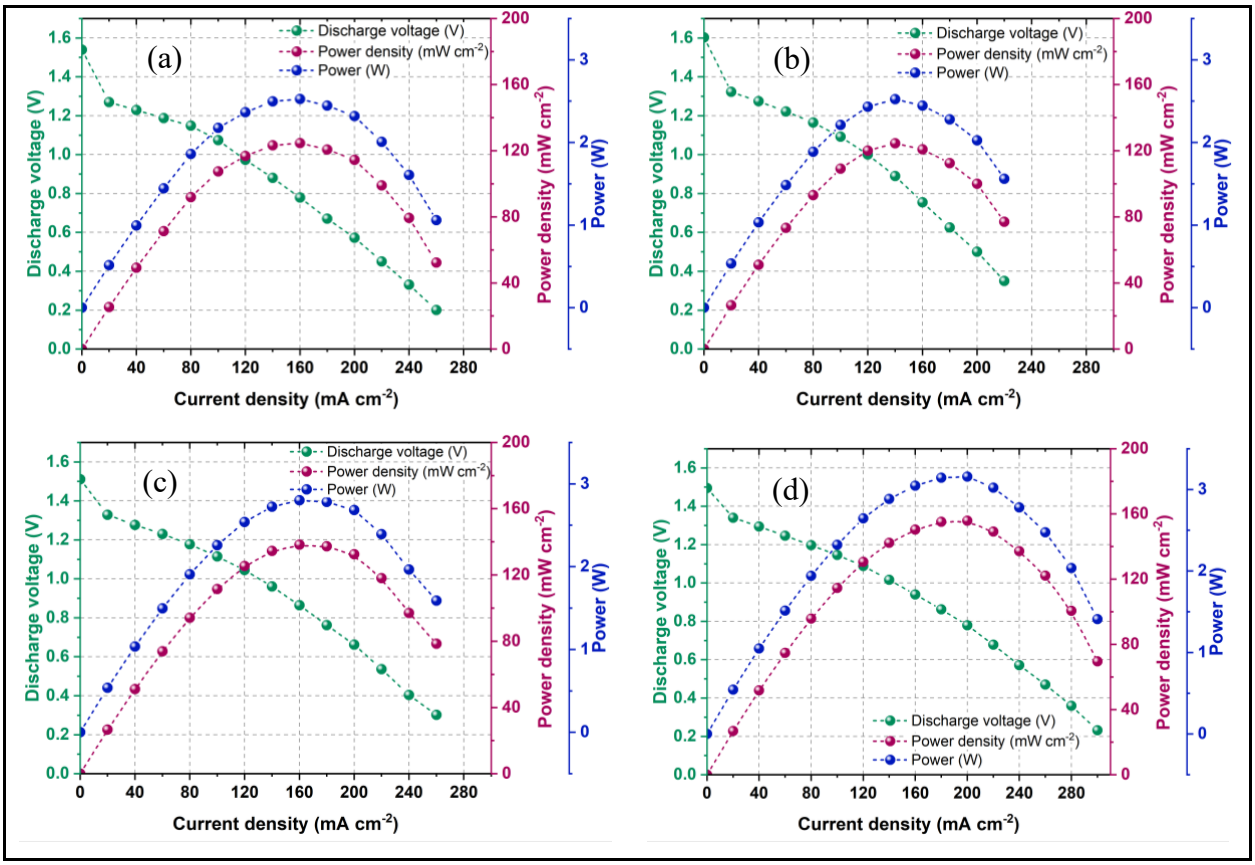


Figure 4. 4: The graphs above give the polarization and power density curves at a constant ACD of 3 mm with varying electrolyte flowrates and temperatures. (a), (b), (c), and (d) are the results for the runs (1), (2), (5), and (6) respectively.

A comparison of Figures 4.4 and 4.6, corresponding to ACDs of 3 mm and 10 mm respectively, reveals notable differences in the V-I curves, particularly in the regions influenced by ohmic and concentration overpotentials. Ohmic overpotential occurs at moderate current densities, where the voltage drop increases linearly with the current due to the resistance of the electrolyte and other cell components. Higher voltages are observed in the ohmic overpotential region for all four instances with a 3 mm ACD. For instance, at 120 mA/cm^2, the voltage remains above 1 V. In contrast, a 10 mm ACD decreases to a range of 0.65-0.85 V. This disparity arises from the increased ACD distance, which substantially affects the measured electrode potentials and power output. Larger ACDs lead to greater ohmic losses, reducing the voltage output due to their impact on cell potential and electrolyte resistivity, with higher resistive losses observed at larger separations [273,274]. Similarly, at high current densities exceeding 200 mA/cm^2, low voltage readings are observed for a 10 mm ACD, primarily due to increased concentration overpotential losses. Concentration overpotential arises from the rate-limiting movement of ions through the electrolyte

to the electrode surfaces [275]. With a greater ACD, ions require more time to reach the electrodes, resulting in the buildup of concentration gradients. This accumulation leads to higher overpotentials and reduced voltage output. Concentration overpotential becomes particularly significant at high current densities, where the voltage drop is governed by mass transport limitations of reactants to the electrode surfaces [276].

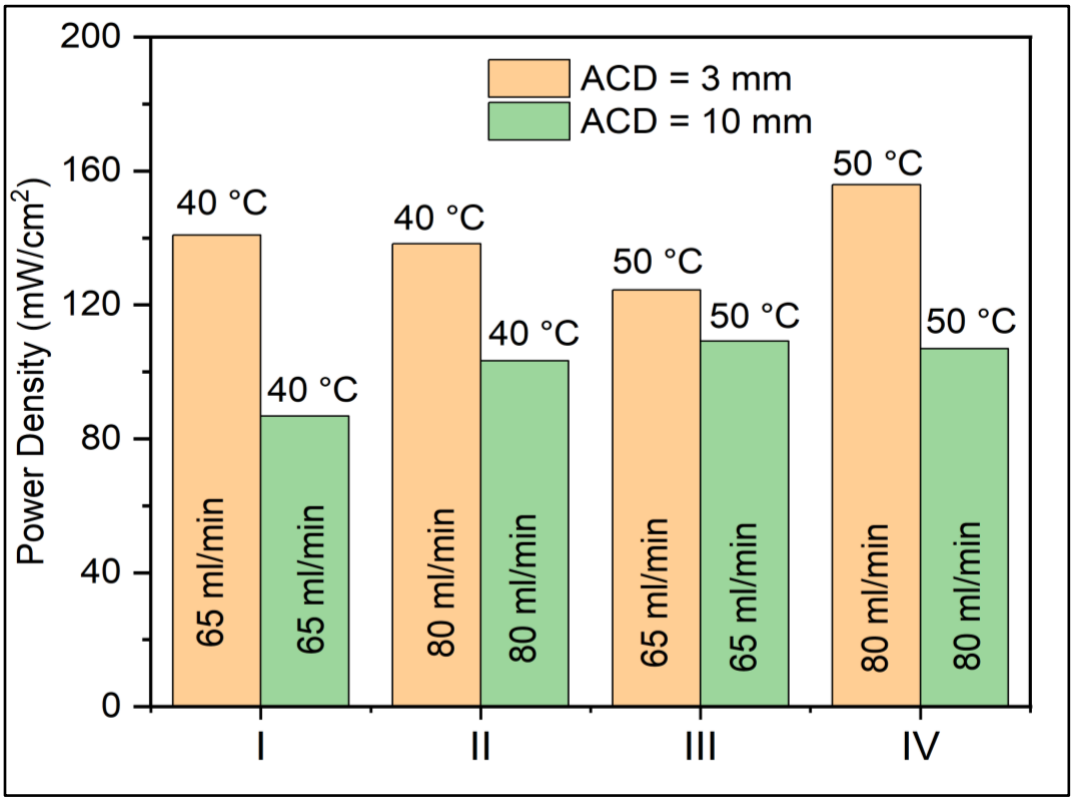


Figure 4. 5: A bar plot depicting the power density values for all eight combinations.

The peak power densities from Figures 4.4 and 4.6 are presented in a bar graph (Figure 4.5) to illustrate the observed trend: higher peak power densities are associated with a smaller ACD (3 mm), while lower peak power densities are linked to a larger distance (10 mm ACD). This relationship underscores the critical influence of ACD on the performance of Al-air batteries. Increasing the ACD leads to a decline in cell voltage and discharge capacity due to heightened internal resistance and mass transport limitations, which result in greater ohmic overpotential. Conversely, reducing the distance can improve electrical performance but may introduce challenges such as electrode fouling and reduced long-term cell stability, particularly in prolonged operation or under high current densities. Thus, optimizing the ACD is essential for balancing performance and stability. A carefully selected ACD minimizes resistive and transport losses while avoiding detrimental effects like fouling, ensuring improved efficiency, power density, and

operational reliability of Al-air batteries. Significant variations are observed in the power density curves with changes in ACD. A lower ACD of 3 mm demonstrated higher peak power densities, ranging from 155.87 mW/cm^2 to 124.51 mW/cm^2, whereas an increased ACD of 10 mm resulted in reduced power densities, ranging from 109.17 mW/cm^2 to 86.77 mW/cm^2, as detailed in Table 4.2. This reduction in power density at larger ACDs can be attributed to diminished mass transport efficiency and increased ohmic losses.

Table 4. 2: Peak power densities and energy densities for prototype-1

Runs	Peak Power Density (mW/cm^2)	Energy density (Wh/kg)
1	140.84	816.5
2	124.51	924.14
3	86.77	516.77
4	109.17	738.90
5	138.24	987.17
6	155.87	789.08
7	103.31	954.09
8	106.90	481.75

4.3.2 Prototype-1: Impact of electrolyte temperature and flowrate

Temperature significantly influences the performance and longevity of Al-air batteries [277]. Elevated temperatures enhance reaction rates at the electrode-electrolyte interface, thereby improving the battery's overall performance. However, excessively high temperatures accelerate the corrosion of the aluminum anode and degrade other battery components, ultimately reducing the battery's lifespan. Conversely, lower temperatures adversely affect the battery's capacity and energy delivery efficiency due to the reduced rate of chemical reactions within the battery [278,279].

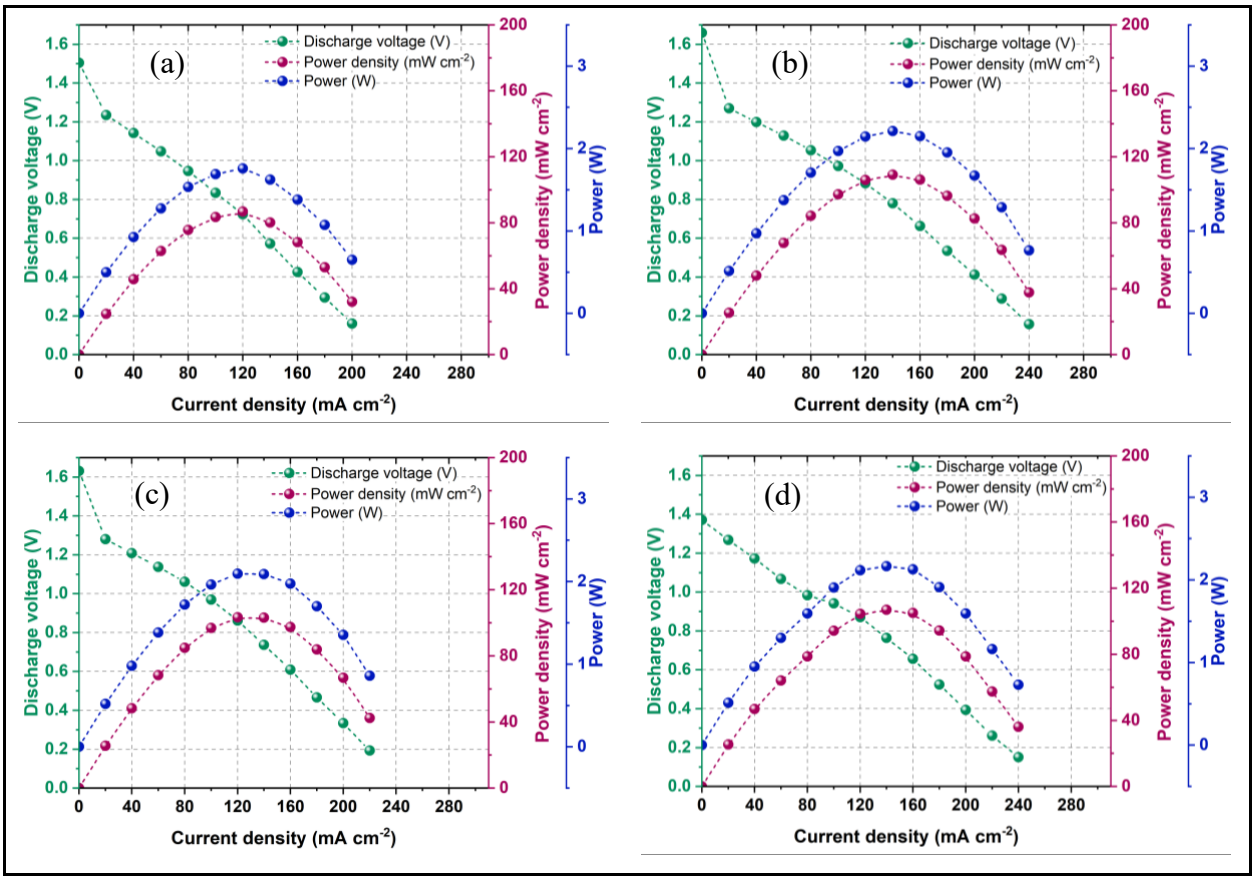


Figure 4. 6: The graphs above give the polarization and power density curves at a constant ACD of 10 mm with varying electrolyte flowrates and temperatures. (a), (b), (c), and (d) are the results for the combinations (3), (4), (7), and (8) respectively.

The peak power density for test run (5) at 40ºC is 138.24 mW/cm^2, while for run (6) at 50ºC, it increases to 155.87 mW/cm^2, representing a 12% improvement at a fixed ACD and flowrate (3 mm and 80 ml/min) with the temperature rise from 40ºC to 50ºC. However, this temperature increase also results in a higher parasitic corrosion rate of the anode, increased evaporation rate of the electrolyte and reduced solubility of O_2 in the electrolyte [280]. Despite the observed improvement in power density, the energy density decreases by 20% under the same conditions due to the increased parasitic reactions. These reactions accelerate the loss of anode mass due to increased hydrogen evolution, contributing to the decline in energy density. Similar trends are evident in the data from Figure 4.6 c, d. This indicates that increasing temperature has a combined impact on battery performance, improving power density while adversely affecting energy density. Detailed values of peak power densities and calculated energy densities for all experimental combinations are provided in Table 4.2.

In Al-air batteries, electrolyte circulation improves mass transport, thereby minimizing electrode polarization and enhancing overall performance. Higher flowrates facilitate efficient ion transport and the effective removal of reaction by-products, resulting in increased power densities. Optimizing the electrolyte flowrate is crucial for maximizing battery efficiency by mitigating polarization effects. Consequently, circulating electrolyte-based systems typically exhibit superior performance compared to stationary configurations[281-283]. The polarization graphs (Figure 4.6 b, d) reveal distinct behaviours in the low current density region, where the activation and ohmic regions exhibit similar characteristics regardless of changes in electrolyte flowrate. However, in the concentration overpotential region at higher current densities, significant differences are observed with an increased electrolyte flowrate of 80 ml/min. Specifically, the discharge voltage remains higher (approximately 0.8 V) at a current density of 200 mA/cm^2 under higher flowrates, whereas it drops to 0.6 V for the same current density at lower flowrates. This improvement at higher flowrates can be attributed to enhanced mass transport processes. The increased flowrate likely facilitates better interaction between dissolved O_2 in the electrolyte and the cathode catalysts, while also effectively removing reaction products from the electrode surface. This reduces concentration polarization, thereby improving performance [284]. The impact of flowrate is further corroborated by comparing the peak power density values for two test runs, (2) and (6), which share the same temperature and ACD for fair comparison. At lower flowrates, run (2) achieves a peak power density of 124.51 mW/cm^2, whereas the higher flowrate in combination (6) results in a significantly higher peak power density of 155.87 mW/cm^2.

In the analysis of the combined effect of the three operating conditions, as anticipated, the highest power density of 155.87 mW/cm^2 was achieved under the optimal combination of high electrolyte temperature, high flow rate, and low ACD. However, for energy density, a 10°C increase in temperature resulted in a decrease in energy density due to the increased corrosion rate of aluminum. Consequently, the highest energy density of 987.17 Wh/kg is observed for the test run conducted at a lower temperature of 40°C, higher electrolyte flowrate, and low ACD. Thus, a synergistic effect is observed, where power density and energy density are influenced by distinct combinations of the operating conditions.

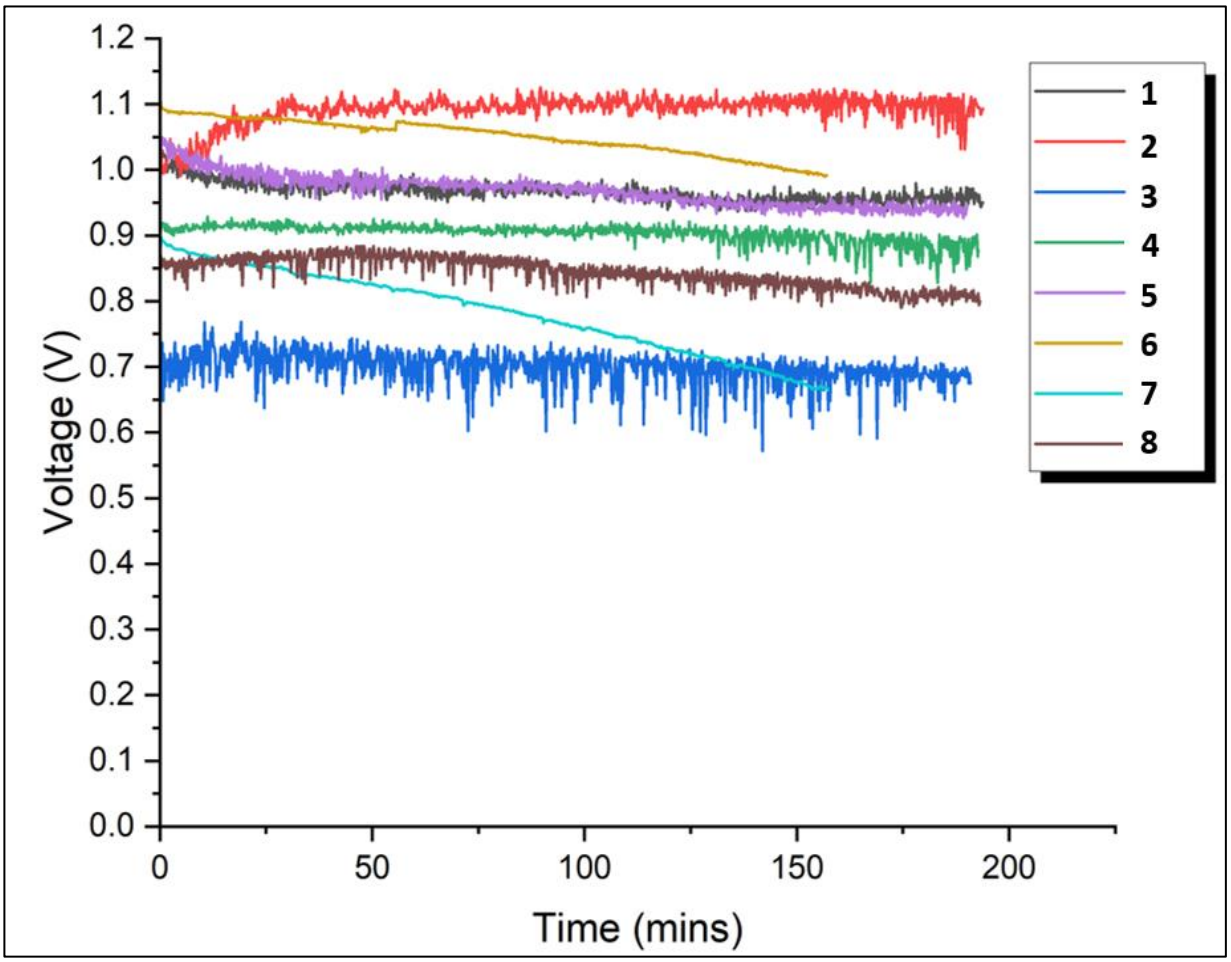


Figure 4. 7: Galvanostatic discharge curves for all eight runs in Table 4.1 for prototype-1.

The discharge performance of runs 2 and 6 from Figure 4.7 is significantly better than that of the other runs, maintaining a stable average voltage of 1.1 V. Both these runs were conducted at a high temperature of 50°C and a low ACD of 3 mm, albeit with varying flowrates. These results indicate that changes in flow rate do not substantially influence discharge performance over a short period of 200 minutes. In contrast, temperature and ACD appear to play a critical role in enhancing discharge performance. Furthermore, a comparison of discharge performance between prototype 1 (Figure 4.7) and prototype-2 (Figure 4.9) reveals that prototype-1 exhibited noisy and unstable discharge curves, reflecting system instability. In contrast, prototype-2 demonstrated stable and uniform discharge curves, highlighting its superior performance.

4.3.3 Prototype-2: Effect of Electrolyte Concentration

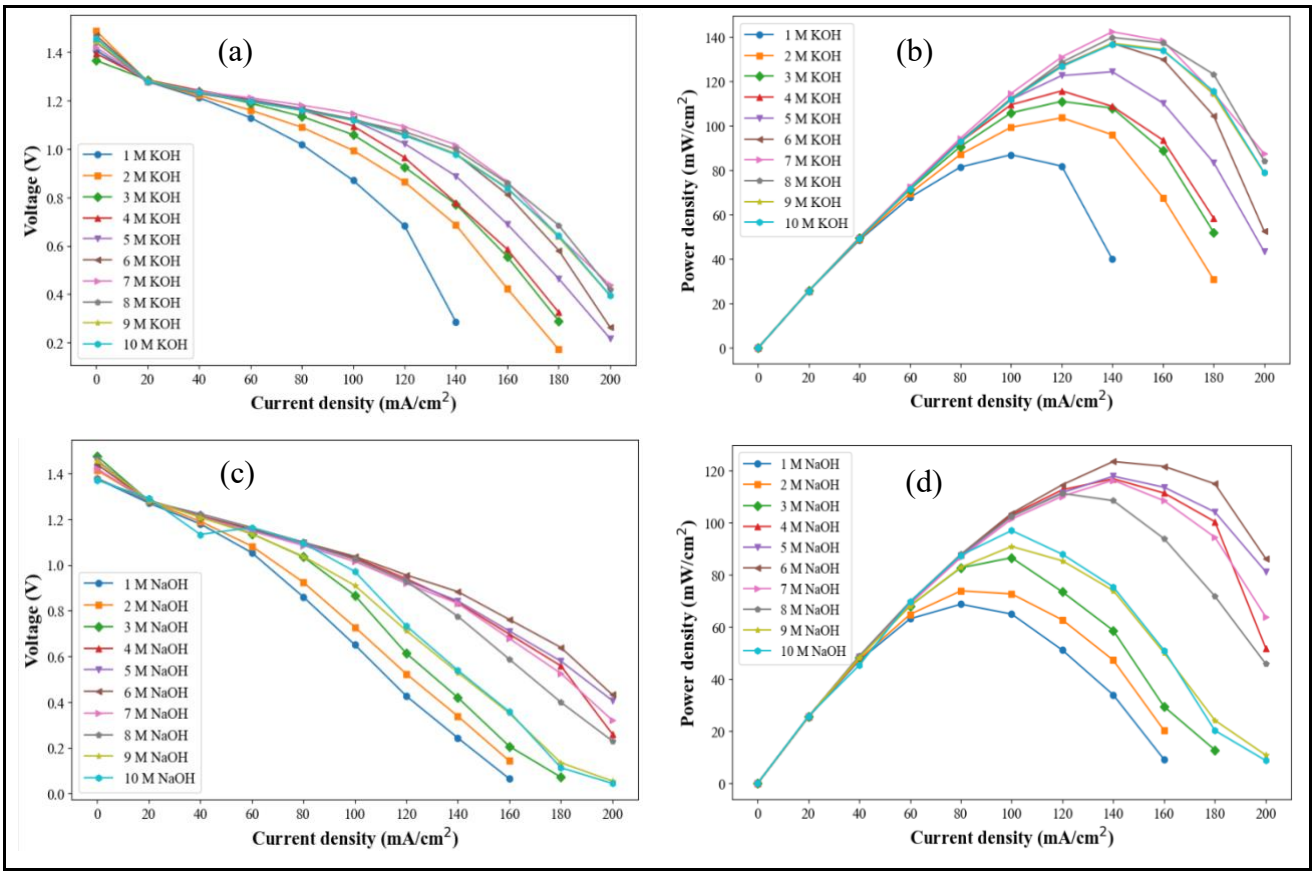


Figure 4. 8: (a) Voltage vs. current density curves for KOH electrolytes at concentrations ranging from 1 M to 10 M. (b) Power density vs. current density curves for KOH electrolytes at concentrations ranging from 1 M to 10 M. (c) Voltage vs. current density curves for NaOH electrolytes at concentrations ranging from 1 M to 10 M. (d) Power density vs. current density curves for NaOH electrolytes at concentrations ranging from 1 M to 10 M. These figures illustrate the electrochemical performance of Al-air batteries for both NaOH and KOH electrolytes across all tested concentrations.

The electrolyte concentration plays a critical role in the performance of Al-air batteries, influencing both the anode and cathode reactions. As mentioned earlier, previous studies have highlighted the use of NaOH and KOH in varying concentrations, with a positive correlation between concentration and power density but only random concentrations. In this study, experiments are conducted for both NaOH and KOH electrolytes, with concentrations increasing from 1 M to 10 M increments, to further investigate their impact on battery performance. Figure 4.8 shows the electrochemical performance of Al-air batteries with KOH and NaOH electrolytes

across concentrations from 1 M to 10 M. Panel (a) and (b) display the voltage vs. current density and power density vs. current density curves for KOH, respectively, while panels (c) and (d) show the corresponding curves for NaOH.

The OCV of Al-air cells shows minimal variation with changes in electrolyte concentration, remaining limited to a range of 1.35 to 1.5 V for both KOH and NaOH. This low OCV is largely due to the substantial activation overpotential of the Al anode. The range of current densities at which voltage is recorded increases with higher concentrations of KOH and NaOH electrolytes. For KOH, the range remains between 140 and 200 mA/cm^2, while for NaOH, it spans from 160 to 200 mA/cm^2. For KOH, the polarization curves exhibit a linear relationship between cell voltage and current density up to 140 mA/cm^2, suggesting that the voltage drop at higher current densities is primarily governed by the ohmic losses between the Al anode and air cathode [262]. Higher voltages are observed across various current densities as the electrolyte concentration increases from 1 M to 7 M, but a voltage drop is noted at concentrations of 8, 9, and 10 M. This decline is attributed to the increased viscosity and reduced conductivity of KOH at higher concentrations [285]. The conductivity of the KOH electrolyte increases steadily from 0.2592 S/cm at 1 M to 0.8117 S/cm at 7 M but decreases from 0.7950 S/cm to 0.7249 S/cm between 8 M and 10 M at 40°C [286]. This results in the accumulation of reaction products at the aluminum electrode, which obstructs diffusion in the solution. The experiments reveal a clear trend of increasing power density with KOH concentration, from 1 M to 7 M, followed by a gradual decrease and levelling off between 8 M and 10 M. The peak power density of 142.4 mW/cm^2 is recorded at 7 M KOH with a current density of 140 mA/cm^2, followed by concentrations of 8 M, 9 M, 10 M, and 6 M. Similarly, for NaOH, voltages increase with rising current densities up to 140 mA/cm^2 across concentrations from 1 M to 6 M, after which they gradually decrease and stabilize between 7 M and 10 M. Power density follows a similar trend, increasing from 1 M to 6 M and then declining and levelling off from 7 M to 10 M. The highest peak power density, approximately 120 mW/cm^2, is observed for 6 M NaOH at 140 mA/cm^2, followed by concentrations of 5 M, 4 M, and 7 M. The decline in power density at higher concentrations can be attributed to several factors, including higher viscosities, reduced ionic conductivity, restricted ion mobility, and increased mass transfer resistance. Comparing the peak power densities of both electrolytes, KOH exhibits a peak at 7 M, while NaOH reaches its peak at 6 M. Despite similar trends in both electrolytes, the highest peak power density was observed for the KOH electrolyte.

The higher peak power density observed in batteries using KOH compared to NaOH can be attributed to several key factors. Firstly, KOH exhibits higher ionic conductivity, facilitating faster ion transport and enhancing electrochemical reactions. Additionally, KOH demonstrates better compatibility with electrode materials, reducing resistance at the electrode-electrolyte interface and improving overall battery performance. Furthermore, KOH solutions offer superior solubility and stability, contributing to more consistent and efficient battery operation. Lastly, potassium ions (K+) are generally more electrochemically active than sodium ions (Na+), leading to improved energy and power density [287-289].

The discharge curves for KOH and NaOH electrolytes across concentrations from 1M to 10M reveal clear trends in performance and stability as shown in Figure 4.9a, b. Both electrolytes show an initial rapid voltage drop at the start of the discharge, which stabilizes over time, followed by relatively steady discharge behaviour. However, there are notable differences between the two electrolytes in terms of peak performance, stability, and the effects of concentration. For KOH, the discharge voltage stabilizes quickly after the initial drop and remains consistent over 120 minutes for most concentrations. The highest performance is observed at 5 and 6 M, which maintains the highest steady-state voltage. As the concentration increases beyond 6 M (i.e., 7 to 10 M), the voltage begins to plateau or slightly decrease. This decline can be attributed to the higher viscosity of concentrated KOH solutions, which increases mass transfer resistance, and the reduced ionic conductivity that limits ion mobility. At lower concentrations (1 M and 2 M), KOH exhibits significantly lower discharge voltages, indicating insufficient ionic conductivity to sustain efficient electrochemical reactions. In comparison, NaOH shows similar trends but with some key differences. The peak performance is observed at a concentration of 8 M, beyond which the voltage decreases steadily for higher concentrations (9 and 10 M). The reduction in performance at higher concentrations is likely due to similar reasons as KOH: increased viscosity and mass transfer resistance.

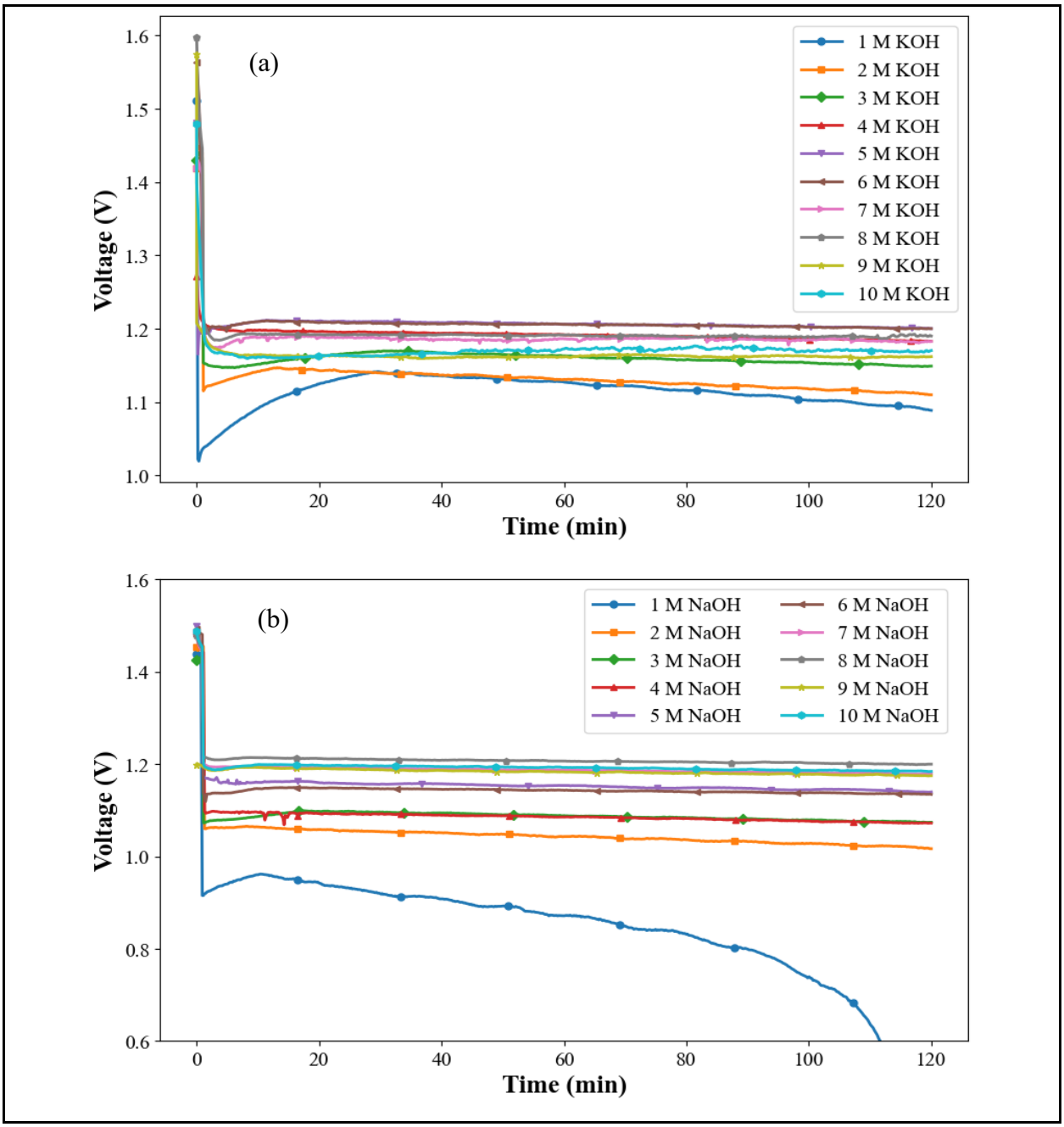
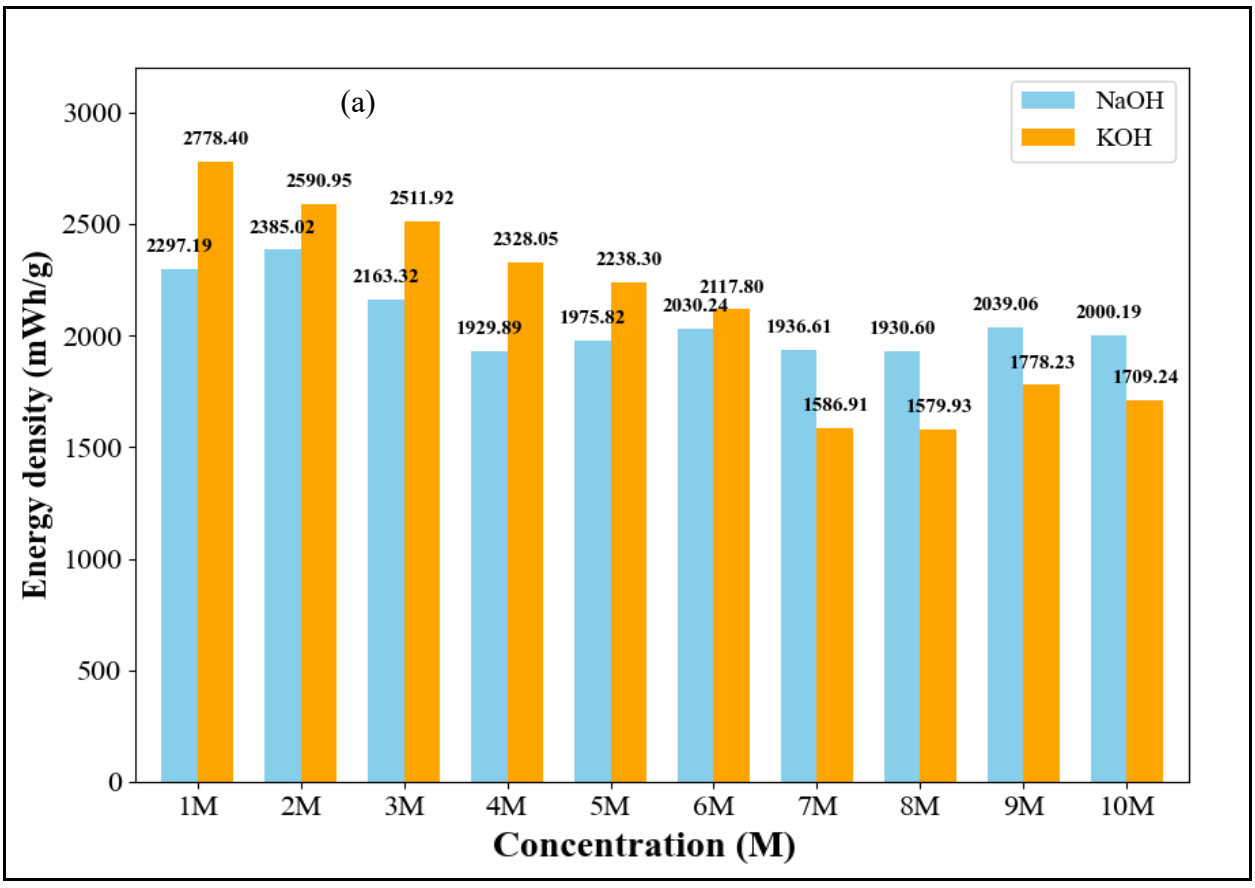


Figure 4. 9: Galvanostatic discharge curves at a constant current density of 80 mA/cm^2 for electrolytes KOH (a) and NaOH (b) with varying concentrations from 1 M to 10 M over 120 minutes.

However, NaOH exhibits less stability in the steady-state region, as evidenced by more pronounced fluctuations in the discharge voltage over time. At lower concentrations (1 M and 2 M), NaOH performs significantly worse than KOH, with the 1 M curve showing a notable decline in voltage over time. This suggests that the ionic conductivity of NaOH is more severely impacted

at lower concentrations compared to KOH, resulting in less effective ion transport and poorer discharge behaviour. When comparing the two electrolytes, KOH consistently demonstrates superior stability and discharge performance across the range of concentrations. The higher peak voltage at 5 and 6 M for KOH, compared to 8 M for NaOH, indicates that KOH supports more efficient electrochemical reactions under similar operating conditions. Additionally, KOH exhibits a more stable voltage profile over time, even at higher concentrations. In contrast, NaOH experiences greater performance degradation at lower concentrations and less stability at higher concentrations, likely due to differences in the physical properties (solubility, stability) and electrochemical activity of the two electrolytes as mentioned earlier [287-289].



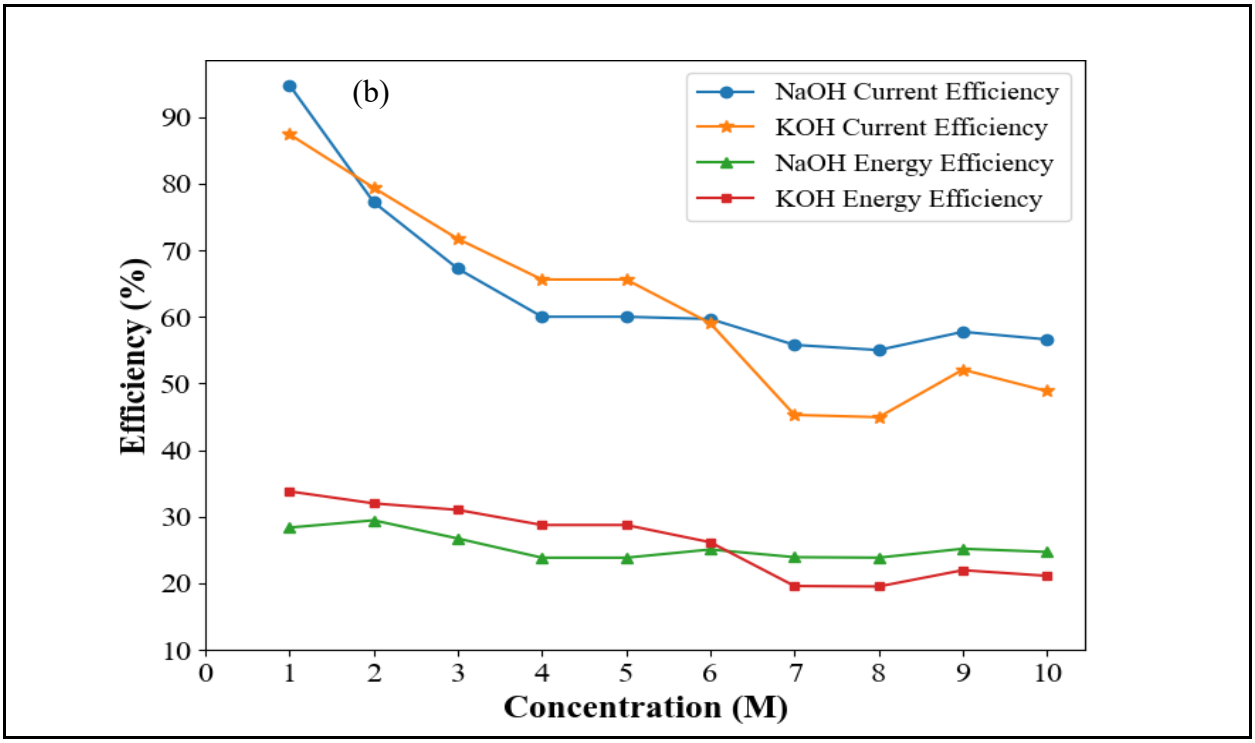


Figure 4. 10: Plots of energy density (a); energy and current efficiency (b) comparing KOH and NaOH electrolytes across concentrations from 1 M to 10 M.

The energy density plot for KOH and NaOH electrolytes across varying concentrations (1 M to 10 M) reveals distinct trends and comparative performance insights as shown in Figure 4.10 a. For KOH, the highest energy density of 2,778.40 mWh/g is observed at 1 M, with a gradual decline as the concentration increases. NaOH achieves its peak energy density of 2,385.02 mWh/g at 2 M. Both electrolytes show optimal performance at lower concentrations due to the decreased corrosion (loss of Al anode) at lower concentrations. Both electrolytes exhibit a consistent decline in energy density as the concentration increases from 3 M to 10 M. The decline is more gradual for NaOH compared to KOH, suggesting that NaOH maintains a more stable energy density profile across the concentration range. For KOH, concentrations between 1 M and 3 M offer high energy densities, after which the decline becomes more pronounced. For NaOH, the range from 2 M to 5 M demonstrates moderate energy densities, with a slower decrease beyond this range. At higher concentrations, both electrolytes exhibit reduced energy densities, with NaOH performing slightly better than KOH. For instance, at 10 M, KOH has an energy density of 1,709.24 mWh/g, while NaOH achieves 2,000.19 mWh/g, showing less degradation for NaOH at very high concentrations. Higher concentrations exacerbate hydrogen evolution reaction (HER), consuming current that

would otherwise contribute to useful energy production. This phenomenon is more pronounced in KOH due to its potentially higher catalytic activity for HER [290-292].

The plot in Figure 4.10b compares the current and energy efficiencies of NaOH and KOH electrolytes across varying concentrations. NaOH exhibits higher current efficiency than KOH, starting at approximately 92% at 1 M and decreasing sharply to about around 55% at 4 M, stabilizing around 60% at higher concentrations. KOH follows a similar trend but starts lower at approximately 85% and levels off slightly above 40%. In terms of energy efficiency, both electrolytes perform significantly lower than their current efficiencies. NaOH maintains energy efficiency between 25% and 30% across all concentrations, while KOH remains stabilizing between 20% and 35%. The initial sharp decline in current efficiency for both electrolytes at higher concentrations is likely due to increased ionic conductivity leading to parasitic side reactions, such as hydrogen evolution, which reduce effective current utilization. The subsequent stabilization may indicate the saturation of these parasitic effects [293,294]. The low energy efficiencies highlight significant energy losses, possibly caused by high overpotentials and heat dissipation. Optimal performance for both electrolytes is observed at lower concentrations (1-3 M), where efficiency is higher and side reactions are less pronounced. At higher concentrations, increased electrolyte viscosity, diffusion resistance, and hydrogen evolution adversely affect performance. The superior performance of NaOH at higher concentrations can be attributed to better compatibility with aluminum and relatively lower hydrogen evolution [285,295-297].

4.4 Conclusion

The performance of prototype-1 was significantly influenced by the ACD, electrolyte temperature, and flowrate. A shorter ACD of 3 mm achieved higher power densities (155.87-124.51 mW/cm^2) compared to 10 mm (109.17-86.77 mW/cm^2) due to reduced internal resistance and improved ion transport. However, a reduced ACD may increase electrode fouling and compromise long-term stability. Higher temperatures (50°C) enhanced power density by 12% compared to 40°C, driven by faster reaction kinetics, though this also increased aluminum corrosion, reducing energy density by 20%. This trade-off highlights the need to balance power and energy efficiency. Increased electrolyte flowrates (80 ml/min) improved performance by enhancing mass transport and reducing concentration polarization, maintaining higher discharge voltages at high current densities. The optimal combination of low ACD, high temperature, and

high flowrate yielded the highest power density (155.87 mW/cm^2), while the highest energy density (987.17 Wh/kg) occurred at lower temperatures and higher flowrates. Discharge stability was primarily influenced by ACD and temperature, with flowrate showing minimal short-term impact. The unstable discharge curves observed in prototype-1 underscored the need for improvements, which were addressed in prototype-2. Using prototype-2, this study investigated the effects of varying concentrations on Al-air battery performance for two commonly used electrolyte types: KOH and NaOH. The results revealed that KOH consistently outperformed NaOH across key performance metrics. The highest power density of 142.4 mW/cm^2 was achieved with KOH at a 7 M concentration, attributed to its superior ionic conductivity, solubility, and compatibility with electrode materials. Conversely, NaOH exhibited a peak power density of 120 mW/cm^2 at 6 M but showed lower overall performance due to reduced ionic conductivity and higher viscosity at similar concentrations. KOH also demonstrated superior discharge stability, maintaining steady voltage over time, particularly at concentrations of 5-6 M. Beyond 7 M, both electrolytes experienced performance declines caused by increased viscosity, reduced ion mobility, and greater mass transfer resistance. Although NaOH displayed its peak performance at 8 M, its discharge curves were less stable, particularly at lower and higher concentrations. In terms of energy density, KOH demonstrated higher overall energy density and peak performance, while NaOH offered greater stability at elevated concentrations. Additionally, NaOH slightly outperformed KOH in current and energy efficiency at lower concentrations, highlighting its advantages in specific scenarios. These findings emphasize the need to balance electrolyte concentration to minimize side reactions and energy losses while maximizing reaction kinetics. Ultimately, this study provides a comprehensive analysis of the factors influencing Al-air battery performance, offering valuable insights into the trade-offs between KOH and NaOH. It enables researchers to make informed decisions tailored to the specific requirements of their applications, emphasizing the importance of optimizing performance and stability when selecting electrolytes for Al-air batteries.

Future work in this area should focus on addressing the limitations observed in both prototypes and further optimizing the performance of Al-air batteries. Investigating advanced electrode materials and surface modifications could help mitigate challenges such as electrode fouling and aluminum corrosion, particularly at shorter ACDs and higher temperatures. Developing novel electrolytes or hybrid electrolyte systems that combine the advantages of KOH

and NaOH, or incorporating additives to enhance ionic conductivity and reduce viscosity, could improve both power and energy density. Additionally, studies on the long-term stability and degradation mechanisms of electrodes and electrolytes under varying operational conditions are critical for practical applications. The impact of dynamic flowrates and temperature cycling on battery performance and stability warrants detailed exploration to mimic real-world scenarios. Finally, integrating advanced modeling and simulation techniques to predict performance metrics and optimize design parameters could accelerate the development of high-performance, cost-effective Al-air batteries for commercial and industrial applications.

Chapter 5 Artificial Neural Network-Genetic Algorithm Prediction of Aluminum Anode Corrosion Kinetics in High-Concentration NaOH and KOH

*** Chapter 5 is adapted from Shabeer Y, Madani SS, Panchal S, Fowler M. "Artificial Neural Network-Genetic Algorithm Prediction of Aluminum Anode Corrosion Kinetics in High-Concentration NaOH and KOH." Frontiers in Batteries and Electrochemistry.

5.1 Introduction

The global transition toward cleaner energy systems has positioned electric vehicles (EVs) at the forefront of sustainable transportation [298]. As nations implement stricter emission regulations and invest in renewable energy infrastructure, the demand for efficient, cost-effective, and environmentally friendly energy storage and conversion technologies has accelerated [299-302]. Lithium-ion batteries, which currently dominate the EV market, have achieved remarkable improvements in energy density and cost reduction [303]. However, limitations related to the availability of critical raw materials, recycling complexity, and safety concerns under high-energy operation continue to restrict their scalability and sustainability [304,305]. This situation has stimulated research into alternative chemistries capable of complementing or extending the range of conventional EV batteries [258]. Among these emerging technologies, metal-air systems have gained increasing attention for their potential to deliver high energy density while maintaining simple and lightweight configurations [306].

Aluminum-air (Al-air) batteries represent a promising direction for the next generation of energy systems due to aluminum's natural abundance, low cost, and inherent recyclability [307]. Aluminum possesses one of the highest theoretical gravimetric energy densities among metals (8.1 kWh kg^{-1}), making it an attractive anode material for vehicular energy applications [308]. The reaction of aluminum with oxygen in an alkaline electrolyte produces electrical energy with water and aluminum hydroxide as benign by-products, reinforcing its environmental appeal [309]. These characteristics make Al-air systems highly suitable as potential range extenders for electric vehicles, where secondary Li-ion packs may be complemented by lightweight and high-energy aluminum-based cells to achieve longer driving distances with minimal additional mass [310].

Furthermore, aluminum's established industrial supply chain and recycling infrastructure provide additional advantages over more resource-limited chemistries, supporting the circular economic goals of modern transportation systems [311,312].

Despite these benefits, widespread commercialization of Al-air batteries has been constrained by one critical issue: the corrosion of aluminum in alkaline electrolytes [313]. Spontaneous parasitic corrosion and hydrogen evolution during open-circuit and discharge conditions lead to the loss of active material, reduced anode utilization, and gas accumulation that degrades system reliability [314]. These challenges are particularly severe in highly concentrated alkaline electrolytes, such as sodium hydroxide (NaOH) and potassium hydroxide (KOH), which are commonly used due to their ability to enhance ionic conductivity and dissolution kinetics [45,315,316]. The corrosion behavior of aluminum is complex, influenced by alloy composition, surface passivation, electrolyte concentration, and temperature. Besides, aluminum's corrosion behavior in alkaline electrolytes is strongly dependent on the OH^- concentration, resulting in distinct kinetic regimes characterized by film stability and dissolution processes. In weaker alkaline solutions, the corrosion process is dominated by the hydrolysis and subsequent dissolution of the passivating oxide layer [317,318].

- Film Transformation and Penetration: The initial Al_2O_3 layer undergoes hydrolysis to form more porous and hydrated species, such as AlOOH or $Al(OH)_3$. Water molecules and OH^- ions then penetrate this hydrated film to initiate corrosion at the Al/film interface.
- Dissolution and Rate Control: Simultaneously, the hydroxide precipitate $Al(OH)_3$ at the film/electrolyte interface dissolves through complexation with OH^- ions :

$$Al(OH)_3 + OH^- \rightarrow Al(OH)_4^- \tag{5.1}$$

The dissolution of the foundational Al_2O_3film also yields the soluble tetrahydroxoaluminate ion ($Al(OH)_4^-$):

$$Al_2O_3 + OH^- + H_2O \rightarrow Al(OH)_4^- \tag{5.2}$$

In this regime, the diffusion of OH^- ions toward the surface and the $Al(OH)_4^-$ product away from the interface is generally considered the rate-controlling step. It is important to note that the direct ejection of Al^{3+} into the alkaline solution is thermodynamically prohibited. In highly

concentrated alkaline electrolytes, the aggressive environment leads to the complete breakdown of the protective mechanism, resulting in active corrosion.

- Film Breakdown and Direct Attack: The excessive concentration of OH^- causes the complete dissolution of any surface oxide or hydroxide film. Consequently, OH^- ions directly attack the bare aluminum surface, which is the primary corrosion reaction in these highly caustic environments:

$$Al + 4OH^- \rightarrow Al(OH)_4^- \quad (5.3)$$

- Kinetic Dominance: Due to the high concentration of OH^- and the high solubility of the product, the influence of ion diffusion on the corrosion rate becomes negligible. The corrosion kinetics are instead governed by the rate of the surface chemical reaction (Eqn 3). This rapid, film-free mechanism is directly responsible for the significant self-discharge and material consumption observed in Al anodes used in Al-air batteries under conditions of excessive electrolyte alkalinity [319].

Among numerous aluminum systems, a commercial Al-Mg-Si alloy is frequently selected due to its favorable balance of mechanical robustness, corrosion resistance, and thermal transport properties [320]. Its controlled additions of magnesium and silicon enable a stable microstructure with good strength-to-weight characteristics, while maintaining relatively high thermal conductivity compared to higher-alloyed aluminum systems [321]. This combination supports efficient heat dissipation and mitigates localized thermal gradients during operation, which is advantageous for electrochemical environments where coupled thermal and corrosion effects can influence performance and degradation [322]. In contrast to higher-strength aluminum alloys with elevated alloying content, Al-Mg-Si compositions exhibit improved processability and reduced susceptibility to stress-assisted corrosion and cracking. These attributes, together with their widespread industrial use, reinforce the suitability of commercial Al-Mg-Si alloys for electrochemical applications that prioritize durability, manufacturability, and materials circularity [323].

Understanding and controlling the corrosion behavior of a commercial Al-Mg-Si alloy in alkaline environments is essential for advancing Al-air battery technology. However, despite extensive research on aluminum corrosion and separate investigations on Al-air systems, the corrosion kinetics of this alloy have not been systematically evaluated within the Al-air context.

Existing studies often employ limited or inconsistent electrolyte concentrations, making it difficult to establish a clear relationship between electrolyte strength and corrosion activity. Comparative evaluation in NaOH and KOH solutions is particularly valuable, as these two electrolytes differ in ionic characteristics, solubility, and aggressiveness toward passive film dissolution [324]. A structured investigation across a wide concentration range is therefore needed to generate a coherent understanding of electrolyte-dependent corrosion mechanisms and to guide the selection of optimal electrolyte formulations that minimize parasitic corrosion while maintaining electrochemical efficiency. Moreover, accurately predicting corrosion parameters such as corrosion potential (Icorr) and current density (Icorr) remain challenging because of the nonlinear and coupled effects of electrolyte composition, temperature, and surface state. These complexities highlight the need for data-driven approaches capable of modeling multivariate nonlinear systems beyond the capability of conventional empirical or regression-based models.

Artificial neural networks (ANNs) have shown increasing promise in electrochemical modeling, materials characterization, and corrosion prediction due to their ability to learn complex relationships directly from data. When combined with optimization techniques such as scalar genetic algorithms (GA) and non-dominated sorting genetic algorithm (NSGA-II) , ANN models can be further tuned to achieve superior prediction accuracy and generalization performance. Previous studies have demonstrated the potential of ANN models for corrosion prediction in several alloy systems [325,326]; however, no systematic effort has yet focused on modeling the corrosion kinetics of aluminum alloys in alkaline environments pertinent to Al-air technologies. Considering the growing global interest in Al-air technologies and the extensive datasets generated from electrochemical testing, integrating ANN-GA frameworks into corrosion studies provides a powerful avenue to predict kinetic parameters, optimize electrolyte composition, and support future digital-twin models for metal-air battery design and control.

This study systematically investigated the corrosion of a commercial Al-Mg-Si alloy in 1 M to 10 M NaOH and KOH electrolytes using an integrated experimental and computational approach. The key aspects of the work are summarized below:

- Experimental Techniques and Structural Analysis: Electrochemical measurements, including open-circuit voltage, potentiodynamic polarization, and electrochemical impedance spectroscopy, were employed to determine corrosion potential and corrosion

current density across varying electrolyte concentrations. Complementary phase identification of corrosion products was conducted using X-ray diffraction (XRD) to assess structural evolution during alkaline exposure.

- Comparative Analysis: The work provides a detailed comparative understanding of Al corrosion mechanisms between NaOH and KOH electrolytes.
- Predictive Modeling: An ANN model, optimized via scalar GA and NSGA-II, was developed and trained on experimental data to predict corrosion potential and current density as a function of electrolyte parameters.
- Novelty and Impact: This work is the first to couple systematic alkaline corrosion experiments of a commercial Al-Mg-Si anode across a wide concentration range with ANN-assisted genetic and multi-objective optimization, enabling quantitative identification of corrosion-optimal electrolyte conditions rather than empirical trial-and-error selection.

5.2 Experimental Methods

5.2.1 Materials

The working electrode material consists of samples of a commercial Al-Mg-Si alloy, machined to provide an exposed surface area of 0.79 cm^2 for electrochemical testing. The bulk alloy composition is summarized in Table 5.1. Prior to each experiment, the samples are mechanically sanded to remove surface impurities and native oxide layers, followed by cleaning with ethanol and air-drying at room temperature to ensure a reproducible and contaminant-free surface, as shown in Figure (5.1). Analytical-grade sodium hydroxide (NaOH, Sigma-Aldrich) and potassium hydroxide (KOH, Sigma-Aldrich) are used to prepare alkaline electrolytes in concentrations ranging from 1 M to 10 M using deionized water. All electrochemical tests are conducted at 25 °C.

Table 5. 1: Chemical composition of the commercial Al-Mg-Si alloy used in this study

Element	Al	Mg	Si	Fe	Cu	Cr	Ti	Others
Composition (wt%)	99	~1.0	~0.6	~0.3	~0.3	~0.1	~0.05	<0.05 (each)

5.2.2 Cell Setup

Electrochemical characterization is conducted using a conventional three-electrode corrosion test cell (Figure 5.1). The alloy sample functions as the working electrode, a carbon rod is used as the counter electrode, and an Ag/AgCl electrode serves as the reference. All potentials are measured relative to VAg/AgCl. Tests are performed under quiescent conditions to ensure uniformity across measurements.

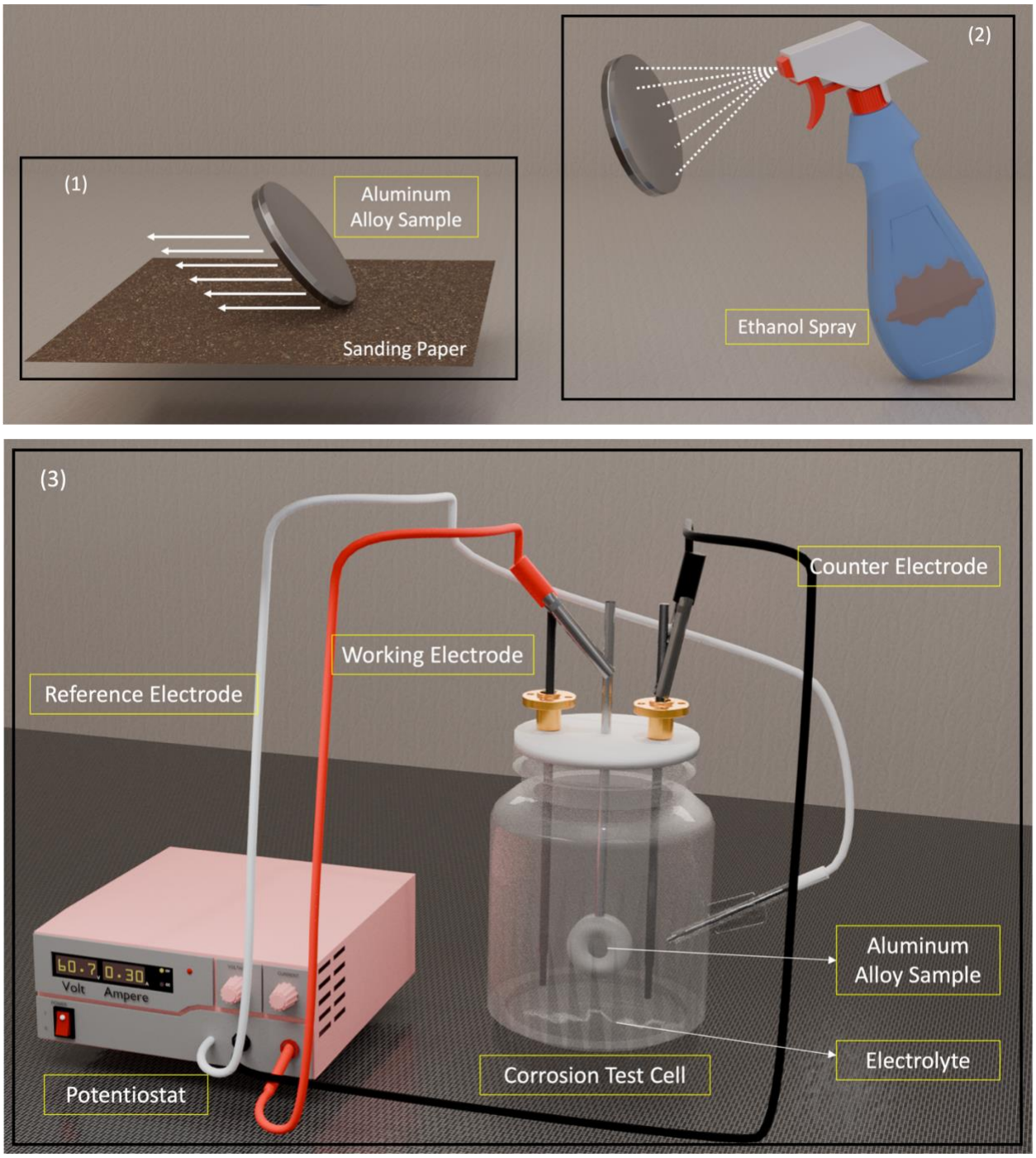


Figure 5. 1: Schematic illustration of the experimental procedure and three-electrode electrochemical corrosion test configuration.

5.2.3 Procedure

Prior to each experiment, the working electrode is immersed in the electrolyte and allowed to stabilize under open circuit voltage (OCV) for 15 minutes. This stabilization period removes

transient oxide films formed during sample preparation and ensures potential equilibrium. Measurements are carried out in NaOH and KOH electrolytes across concentrations ranging from 1 M to 10 M.

5.2.4 Open-Circuit Voltage

The OCV represents the natural potential of the alloy when no external current is applied. It indicates the initial corrosion tendency of the commercial Al alloy in each electrolyte. Measuring OCV for 15 minutes allows the system to reach a stable surface condition, ensuring that subsequent polarization and impedance tests begin from a steady and reproducible corrosion potential.

5.2.5 Potentiodynamic Polarization (Tafel Analysis)

Potentiodynamic polarization tests are performed over a potential range of -0.5 V to +0.5 V vs. VAg/AgCl at a sweep rate of 10 mVs^{-1} with a sampling interval of 1 s. Tafel extrapolation is used to extract the corrosion potential and corrosion current density (Icorr).

The current-potential behavior is described by the Butler-Volmer equation:

$$I = I_{corr}\left[\exp\left(\frac{\alpha nF(E-E_{corr})}{RT}\right) - \exp\left(-\frac{(1-\alpha)nF(E-E_{corr})}{RT}\right)\right] \quad (5.4)$$

The current-potential response of the alloy in alkaline solution is described by the Butler-Volmer equation, which relates the measured current density I to the applied potential E relative to the corrosion potential Ecorr. In this expression, the net current is governed by the corrosion current density Icorr and the anodic and cathodic exponential terms, each dependent on the charge-transfer coefficient α, the number of electrons involved in the electrochemical reaction n, the Faraday constant F, the universal gas constant R, and the absolute temperature T. The equation captures how the anodic and cathodic reactions accelerate as the electrode potential deviates from Ecorr, providing a fundamental description of the electrochemical kinetics that govern corrosion behavior in alkaline media.

At small overpotentials, this simplifies the Tafel relationship [327],

$$\eta = a + b\log i \quad (5.5)$$

where a and b are the anodic and cathodic Tafel constants. Tafel slopes are obtained by fitting tangents to the anodic and cathodic branches, and their intersection is used to determine Ecorr and Icorr.

5.2.6 Electrochemical Impedance Spectroscopy (EIS)

EIS measurements are conducted using an AC perturbation amplitude of 10 mV rms over a frequency range of 1 x 10^5 Hz to 1 x 10^{-1} Hz, with 10 points per decade. Impedance spectra are analyzed to extract charge-transfer resistance and double-layer capacitance, providing insight into corrosion mechanisms and surface film behavior. The following expressions constitute the fundamental relationships underlying the EIS analysis.

Randles circuit impedance [328],

$$Z(\omega) = R_s + \frac{R_{ct}}{1+j\omega R_{ct}C_{dl}} \tag{5.6}$$

Constant phase element [328],

$$Z_{CPE} = \frac{1}{Q(j\omega)^n} \tag{5.7}$$

Combined Rct-CPE impedance [328],

$$Z(\omega) = R_s + \frac{1}{\frac{1}{R_{ct}} + Q(j\omega)^n} \tag{5.8}$$

In EIS, the measured impedance reflects contributions from the solution resistance Rs, the charge-transfer resistance Rct, and the interfacial capacitance associated with the electrochemical double layer. For a simple Randles-type system, the total impedance is expressed through Rs, which represents the resistance of the bulk electrolyte, and Rct, which describes the resistance to electron transfer during the corrosion reaction, while Cdl denotes the ideal double-layer capacitance formed at the alloy-electrolyte interface. The double-layer term is more accurately represented using a constant phase element, characterized by the parameters Q and n, where Q reflects the magnitude of the non-ideal interfacial capacitance and n (ranging between 0 and 1) quantifies the degree of deviation from ideality. When incorporated into the charge-transfer process, the CPE modifies the impedance expression such that the system response depends on both Rct and the frequency-dependent term $(j\omega)^n$, where ω is the angular frequency, and j is the imaginary unit. Together, these parameters describe how the corrosion reaction and interfacial processes contribute to the

semicircle in the Nyquist plot and the characteristic phase behavior in the Bode spectra, allowing Rct to be extracted as a measure of corrosion resistance and providing insight into the electrochemical behavior of the commercial Al-Mg-Si alloy in alkaline electrolytes.

5.2.7 X-ray Diffraction

X-ray diffraction (XRD) is performed on post-corrosion samples to identify crystalline corrosion products formed during immersion in NaOH and KOH. Diffraction patterns allow detection of aluminum hydroxides, oxide phases, and other species that form because of alloy dissolution and surface film transformation in alkaline environments. Comparing XRD profiles across electrolyte concentrations provides insight into differences in film stability and phase composition between NaOH and KOH systems.

5.3 Modeling Methodology

The machine-learning model was developed using a curated dataset comprising electrochemical measurements collected across a range of alkaline electrolyte conditions (Section 2.1.2). Each entry in the dataset represents a unique electrolyte configuration and its corresponding polarization response, encoded through five descriptive input features: electrolyte type (encoded as KOH = 1, NaOH = 2)), electrolyte concentration (M), solution temperature (°C), applied potential (V), and measured current density (A cm^{-2}). These variables capture the physicochemical environment governing anodic dissolution and serve as the predictors in the ANN framework. The associated outputs consist of the experimentally derived Ecorr and Icorr, which are key indicators of alloy degradation and performance in alkaline media. The dataset was refined through consistency checks and removal of incomplete entries, resulting in a final set suitable for supervised learning. Predicting Ecorr and Icorr directly from easily measurable electrochemical inputs provides an efficient pathway for rapid corrosion assessment and supports the development of optimization strategies for alkaline aluminum-based energy systems. The overview of the modeling methodology is represented in Figure (5.2). All mathematical operations associated with data preprocessing, ANN training, optimization, and model evaluation are summarized in Table 5.2 to consolidate the computational framework used throughout this study [329-337].

Table 5. 2: Summary of all equations used for data normalization, ANN modeling, hyperparameter optimization, GA search, and performance evaluation

Category	Equation	Description	Symbol Explanation	Eqn no.
Feature Normalization	$X_{normalized} = \frac{(X - X_{min})}{(X_{max} - X_{min})}$	Scales each input feature to the range [0,1] prior to ANN training	X : original feature; $X_{\min}$, $X_{\max}$: min and max of feature; X_{norm}: normalized feature	(9)
ANN Activation Function	$ReLU\ (x) = \max\ (0, x)$	Introduces nonlinearity and improves gradient propagation in hidden layers	x : neuron input value	(10)
ANN Output Mapping	$\hat{y} = f_\theta(X)$	Forward pass of the ANN using model parameters (θ)	$\hat{y}$: predicted outputs; X: input vector; f_θ: ANN function; θ: model weights	(11)
Adam Optimizer - First Moment	$m_t = \beta_1 m_{t-1} + (1 - \beta_1) g_t$	Exponentially weighted moving average of gradients	m_t : first moment; g_t: gradient at step t; β_1: decay rate	(12)
Adam Optimizer - Second Moment	$v_t = \beta_2 v_{t-1} + (1 - \beta_2) g_t^2$	Exponentially weighted moving average of squared gradients	v_t : second moment; g_t^2: squared gradient; β_2: decay rate	(13)
Adam Update Rule	$\theta_t = \theta_{t-1} - \alpha \frac{m_t}{\sqrt{v_t} + \epsilon}$	Parameter update using adaptive learning rates	θ_t : updated weight; α: learning rate; ϵ: small constant for numerical stability	(14)
Grid Search Criterion	$\theta^* = arg\ min_{\theta \epsilon \Theta}\ MSE_{val}\ (\theta)$	Selects hyperparameters that minimize validation error	Θ : hyperparameter space; θ^*: optimal hyperparameters	(15)

MAE	$MAE = \frac{1}{n}\sum_{j=1}^{n} \lvert y_j - \hat{y}_j \rvert$	Measures average prediction error	y_j : actual value; $\hat{y}_j$: predicted value; n : number of data points	(16)
MSE	$MSE = \frac{1}{n}\sum_{j=1}^{n} (y_j - \hat{y}_j)^2$	Penalizes large prediction errors quadratically	y_j : actual value; $\hat{y}_j$: predicted value; n : number of data points	(17)
RMSE	$RMSE = \sqrt{\frac{1}{n}\sum_{j=1}^{n} (y_j - \hat{y}_j)^2}$	Root of MSE; interpretable in original units	y_j : actual value; $\hat{y}_j$: predicted value; n : number of data points	(18)
R^2 (Coefficient of Determination)	$R^2 = 1 - \frac{\sum_{j=1}^{n}(y_j - \hat{y}_j)^2}{\sum_{j=1}^{n}(y_j - \bar{y})^2}$	Measures of fit relative to variance in the data	$\bar{y}$: mean of true values	(19)
Genetic Algorithm - Fitness Function	f(x)=objective score for candidate x	Converts ANN prediction accuracy or error into a scalar fitness value	x : candidate solution; f: fitness score	(20)
Genetic Algorithm - Parent Selection	$P(i) = \frac{f(i)}{\sum_j f(j)}$	Roulette-wheel probability of selecting individual $i$based on fitness	$P(i)$: selection probability; $f(i)$: fitness of individual i	(21)
Genetic Algorithm - Crossover	$x_{child}^{(k)} = x_{p1}^{(k)}\ or\ x_{p2}^{(k)}$	Component-wise mixing of parent vectors to form offspring	$x_{child}^{(k)}$: child's k-th gene, $x_{p1}^{(k)}$, $x_{p2}^{(k)}$; parent vectors	(22)
Genetic Algorithm - Mutation	$x' = x + \epsilon$	Random perturbation applied to maintain	x : original gene; x': mutated gene; ϵ: random noise	(23)

		population diversity		
Scalarized Objective Function	$f(x) = w_I\, I_{\text{norm}}(x) + w_E\, E_{\text{norm}}(x)$	Converts the bi-objective corrosion problem (min Icorr, max Ecorr) into a single scalar objective suitable for standard GA optimization	w_I, w_E : weighting coefficients; I_{norm}: normalized corrosion current (lower is better); E_{norm}: inverted normalized corrosion potential (higher Ecorr → lower cost); $f(x)$: scalar fitness value	(24)
Multi-objective Formulation	$F\ (x) = [f1(x), f2(x)]$	Defines the two-objective vector for NSGA-II (minimize Icorr, maximize Ecorr)	$f1$: corrosion current objective; f_2: inverted corrosion potential objective; x: candidate electrolyte condition	(25)
Pareto Dominance Rule	$x_i \prec x_j$ $if\ f_m(x_i) \leq f_m(x_j)\ \forall$ m and $f_m(x_i) < f_m(x_j)$ for at least one m	Defines dominance relationship used to construct Pareto fronts	x_i, x_j: candidate solutions; f_m: objective m	(26)
Non-Dominated Sorting	$F1 = \{x$:no solution dominates $x\}$	Partitions the population into ordered Pareto fronts	Fk: k-th Pareto front	(27)
Crowding Distance	$d_i = \sum_{m=1}^{M} \frac{f_m^{(i+1)} - f_m^{(i-1)}}{f_m^{max} - f_m^{min}}$	Measures solution density to preserve diversity on the Pareto front	d_i: crowding distance; f_m: objective m; indices $i \pm 1$: neighbors after sorting	(28)

NSGA-II Selection Rule	x_a wins if rank is lower or d is higher	Ensures elitist and diverse selection of parent solutions	rank: Pareto level; d: crowding distance	(29)
Knee Point Criterion	$x_{knee} = \arg min_x \parallel F(x) - F^* \parallel$	Identifies the least-compromise solution on the Pareto front	F^*: ideal objective vector; $F(x)$: candidate objectives	(30)

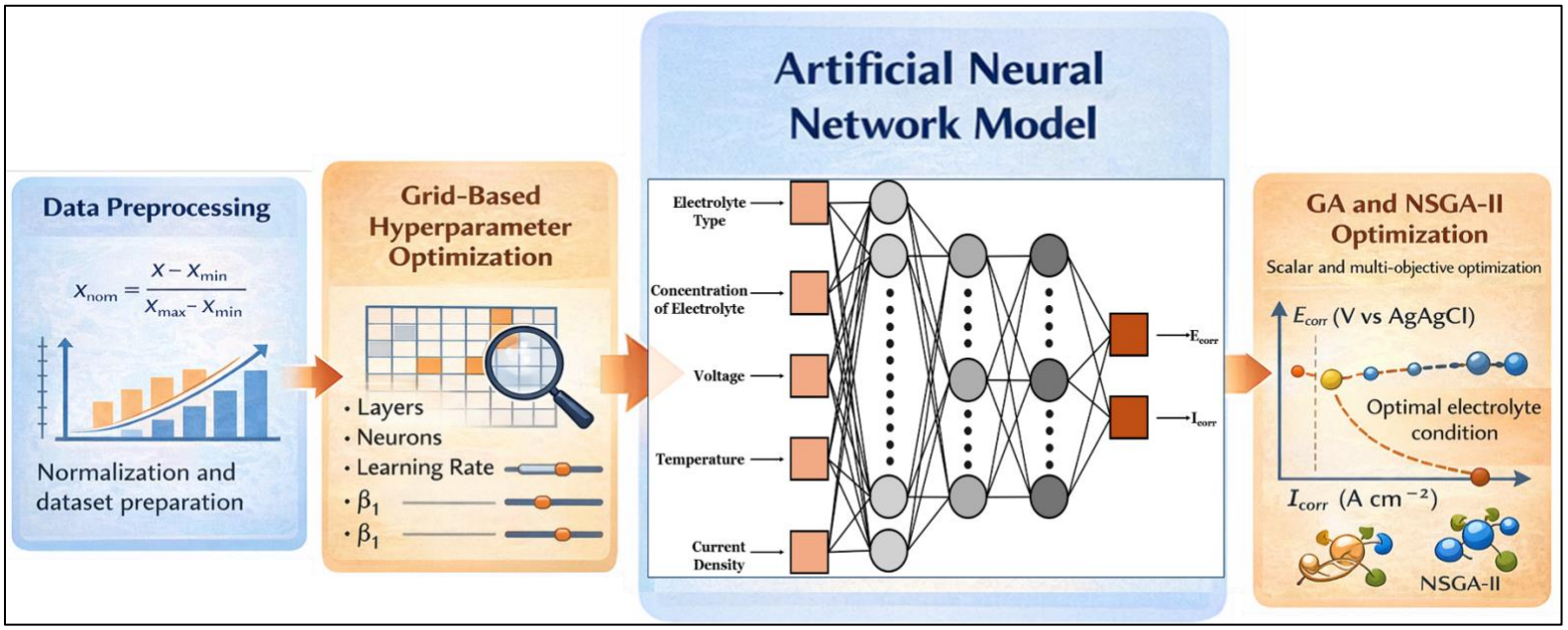


Figure 5. 2: Overview of the modelling methodology, showing data preprocessing, grid-based hyperparameter optimization, ANN training for prediction of Ecorr and Icorr, and subsequent GA and NSGA-II optimization.

5.3.1 Artificial Neural Network Structure and Data

ANNs are data-driven computational frameworks designed to learn nonlinear relationships from experimental observations. They consist of interconnected processing units (neurons) arranged in input, hidden, and output layers, where each connection is associated with a trainable weight. During model training, these weights are iteratively updated to minimize prediction error, allowing the network to identify complex patterns within the data [338]. Nonlinearity within the network is introduced through activation functions, with the rectified linear unit (ReLU, Eqn 10),

being one of the most commonly used due to its computational efficiency and its ability to mitigate vanishing-gradient issues in deeper architectures [339]. During forward propagation, the ANN maps its inputs to predicted outputs through the functional relationship defined in Eqn 11. Model optimization is performed using the Adam algorithm, an adaptive gradient-based optimizer that adjusts the learning rate for each weight by estimating the first (Eqn 12) and second moments (Eqn 13) of the gradient [340]. This results in stable and rapid convergence, even in high-dimensional and nonlinear datasets such as those associated with corrosion behavior. Several hyperparameters, including learning rate, number of hidden layers, number of neurons, number of epochs, β_1 and β_2 decay coefficients, and loss function, are tuned through systematic search.

5.3.2 Grid-Based Hyperparameter Optimization

To identify the most effective ANN configuration, a structured grid-based hyperparameter search was performed. Three model attributes were systematically varied: the number of hidden layers (1, 2, or 3), the number of neurons per layer (20, 25, or 30), and the Adam optimizer parameters, including three learning rates (0.00100, 0.00085, and 0.00070) and a range of β_1 values. The β_1 parameter was found to strongly influence convergence behavior, with $\beta_1 = 0.92$ consistently yielding the highest predictive accuracy.

5.3.3 Data Normalization and Performance Assessment

During preprocessing, all input features are scaled using min-max normalization to prevent variables with larger magnitudes from dominating the learning process (Eqn 9). This method rescales each feature to a dimensionless range between 0 and 1, improving numerical stability and convergence during model training [341]. Model performance is subsequently assessed using four standard regression metrics that quantify the accuracy of predicted corrosion parameters relative to experimentally measured values. These include mean absolute error (MAE), mean squared error (MSE), root mean squared error (RMSE) and the coefficient of determination (R^2) shown in Eqn (16-19) respectively. Lower MAE, MSE, and RMSE values indicate closer agreement between predicted and experimental corrosion parameters, while R^2 values approaching unity reflect high predictive capability and strong model generalization [342,343].

5.3.4 Dataset Visualization and Input-Output Interactions

To assess the structure of the experimental dataset and evaluate potential nonlinear relationships among variables, a pairwise scatter and kernel-density matrix was generated for all

key electrochemical parameters (Figure 5.3). The matrix includes electrolyte concentration, corrosion potential (Ecorr), corrosion current density (Icorr), applied voltage, and log-transformed current density. Scatter plots along the lower triangle illustrate how the distributions of Ecorr and Icorr shift between NaOH and KOH, while the diagonal kernel-density curves highlight differences in the statistical behavior of each variable. The scatter plots also reveal concentration-dependent clustering and asymmetric relationships, especially the strong electrolyte-dependent separation in both Ecorr and Icorr. This visualization provides an integrated overview of how experimental variables covary and demonstrates the presence of distinct nonlinear trends, supporting the motivation for developing an ANN-based predictive model.

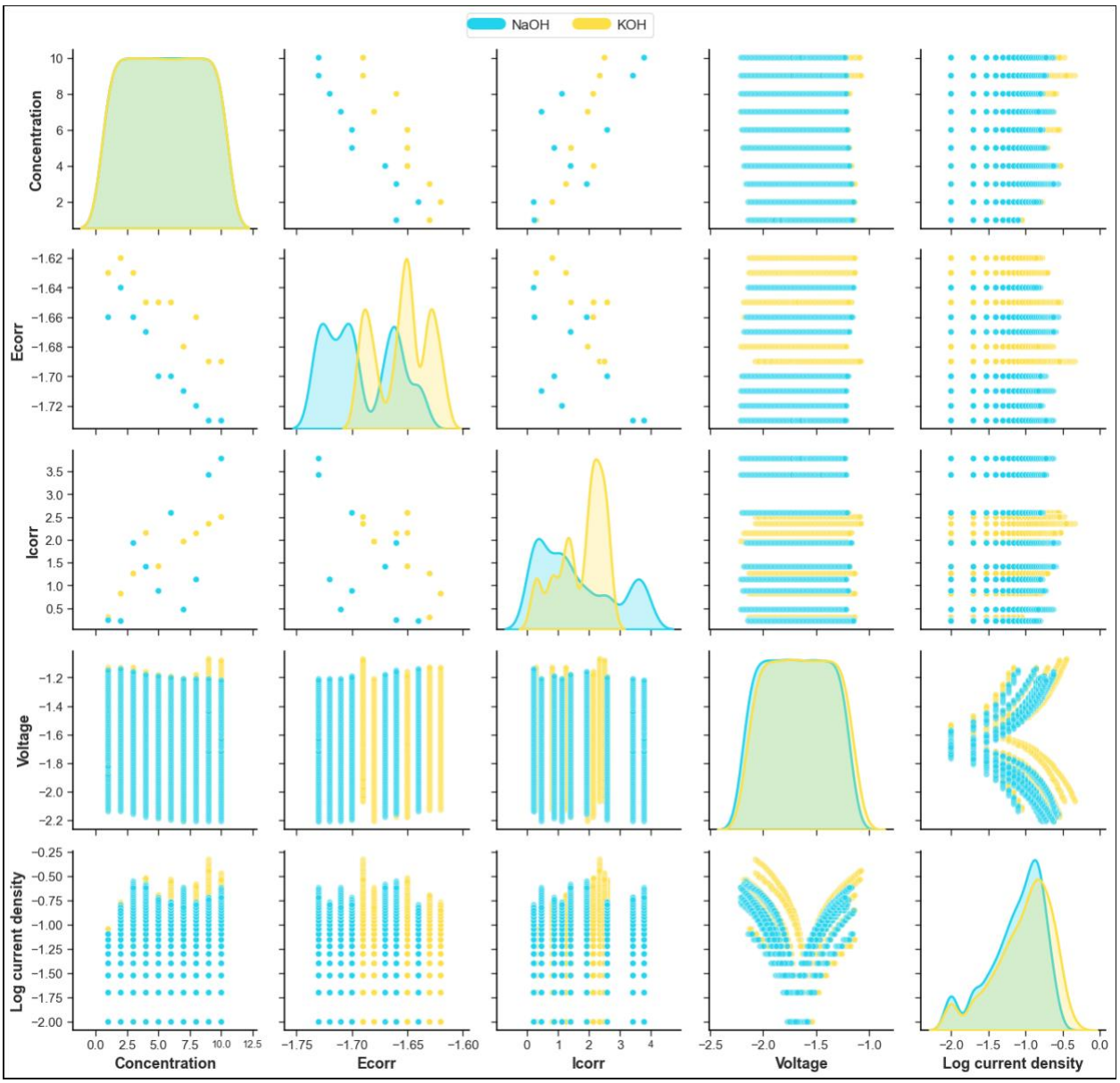


Figure 5. 3: Pairwise scatter matrix for key electrochemical variables: concentration, Ecorr, Icorr, voltage, and log current density. The plots visualize electrolyte-dependent clustering for NaOH and KOH electrolytes, reveal nonlinear relationships among parameters, and highlight distributional characteristics that informed the ANN model design.

5.3.5 Genetic Algorithm Optimization

A genetic algorithm (GA) was implemented to identify an optimal electrolyte condition that simultaneously promotes a high Ecorr while minimizing the Icorr. Because standard GAs are designed for single-objective searches [344], the two corrosion objectives were incorporated into a scalarized fitness function such that a single cost value could represent the combined corrosion response predicted by the trained ANN model. After ANN training, the model function (Eqn 11) was used to estimate Ecorr and Icorr from candidate input vectors representing electrolyte type and concentration, with the remaining operational variables (temperature, applied potential, and instantaneous current density) set to representative operating values.

To embed the two corrosion objectives into a single scalar score, Ecorr and Icorr were first normalized to the range [0,1] using min-max scaling (Eqn 9). To maintain a consistent minimization direction, Ecorr was inverted such that higher Ecorr values corresponded to lower normalized cost, while Icorr was used directly since lower Icorr values naturally indicate reduced corrosion. The scalar objective function for a candidate electrolyte condition was expressed as a weighted sum in Eqn 24, where $w_I = w_E = 0.5$ reflect an equal preference for reducing corrosion rate and increasing corrosion potential. This formulation transforms the bi-objective corrosion problem into a single-objective optimization that can be solved using standard GA operations (selection, crossover, and mutation; Eqns 21-23). A continuous search space was defined for concentration (1-10 M) and electrolyte type, which was discretized during evaluation to maintain its categorical nature (KOH = 1, NaOH = 2). The GA iteratively refined the population until convergence, and the candidate with the lowest objective value was designated as the scalar GA optimum. This optimum represents the best solution according to the chosen weights, rather than the full Pareto trade-off structure of the corrosion system.

5.3.6 Multi-Objective Optimization Using NSGA-II

To obtain a weight-free and physically interpretable characterization of the trade-off between Ecorr and Icorr, a non-dominated sorting genetic algorithm (NSGA-II) was implemented.

Unlike scalar GA, NSGA-II preserves the independence of both corrosion objectives and identifies the complete Pareto front, defined as the set of electrolyte conditions for which no further improvement in one objective is possible without degrading the other [345]. The two objectives were defined as (Eq. 25):

- Objective 1: minimize Icorr
- Objective 2: maximize Ecorr

To maintain a uniform minimization framework, the second objective was evaluated through its inverse, where larger Ecorr corresponds to lower objective value. For each candidate solution, the ANN model predicted Ecorr and Icorr, from which the objective pair was obtained. Pareto dominance between solutions followed the standard NSGA-II criterion (Eq. 26), and the formation of successive fronts was determined using fast non-dominated sorting (Eq. 27).

The NSGA-II algorithm proceeded through [345,346]:

- Fast non-dominated sorting, which partitions the population into hierarchical fronts based on Pareto dominance (Eq. 27).
- Crowding-distance assignment, which preserves diversity along the front (Eq. 28).
- Tournament selection, crossover, and polynomial mutation to generate the next population, with selection comparing solutions by Pareto rank and crowding distance (Eq. 29).
- Elitist replacement, ensuring that high-quality Pareto solutions are retained across generations.

The final NSGA-II front represents the complete corrosion trade-off landscape across electrolyte type and concentration. From this front, a knee point was identified using the minimum-distance-to-ideal method (Eq. 30), where the ideal point corresponds to the maximum Ecorr and minimum Icorr present on the Pareto front. The knee point therefore represents the least-compromise solution, where simultaneous improvements in Ecorr and Icorr become mutually limiting due to the curvature of the trade-off surface.

5.4 Results and Discussion

The electrochemical behaviour of the commercial Al alloy across the full 1-10 M concentration range in KOH and NaOH electrolytes was evaluated using OCV, potentiodynamic polarization, and EIS. To present these data without excessive crowding and to preserve clarity in

trend interpretation, the results are organized into four concentration windows: 1-5 M KOH, 6-10 M KOH, 1-5 M NaOH, and 6-10 M NaOH. Each window consolidates the complete electrochemical response, including OCV evolution, Tafel behaviour, Ecorr and Icorr values, estimated anode lifetime, and impedance characteristics. This structured presentation enables direct comparison within each electrolyte across its full molarity range, followed by cross-electrolyte interpretation that highlights mechanistic differences between KOH and NaOH .

5.4.1 Experimental Corrosion Trends

Across both electrolytes and the full concentration range, the open-circuit voltage profiles exhibit a consistent two-stage behavior, characterized by an initially rapid shift toward more positive potential followed by stabilization to a quasi-steady plateau within the first 200-400 s of immersion. This early-time evolution reflects rapid interfacial adjustment upon exposure to alkaline media, during which the native surface film is chemically modified, and the mixed potential evolve as anodic aluminum dissolution and cathodic hydrogen evolution approach a steady balance.

For KOH in the low-to-moderate concentration range (1-5 M, Figure 5.4a), the stabilized OCV displays a clear but non-monotonic dependence on concentration. The most positive steady potential is observed at 2 M, while both lower (1 M) and higher concentrations (4-5 M) stabilize at more negative values. This behavior suggests that intermediate hydroxide concentrations may temporarily favor partial surface stabilization, whereas higher concentrations promote more aggressive dissolution of surface films and a shift toward a more active corrosion state [347]. In the higher concentration KOH regime (6-10 M, Figure 5.5a), the OCV curves converge closely and stabilize at similarly negative plateau values, indicating that once a sufficiently high hydroxide activity is reached, the surface rapidly transitions to a comparable actively corroding steady state across concentrations, with further increases in molarity exerting a limited influence on the final mixed potential. All curves exhibit an upward drift in potential as the native Al_2O_3/AlOOH surface layer gradually dissolves and the interface transitions toward an actively corroding state. This monotonic shift indicates that higher OH^- activity accelerates removal of the initial, thereby promoting earlier exposure of metallic Al and facilitating the onset of anodic dissolution [348].

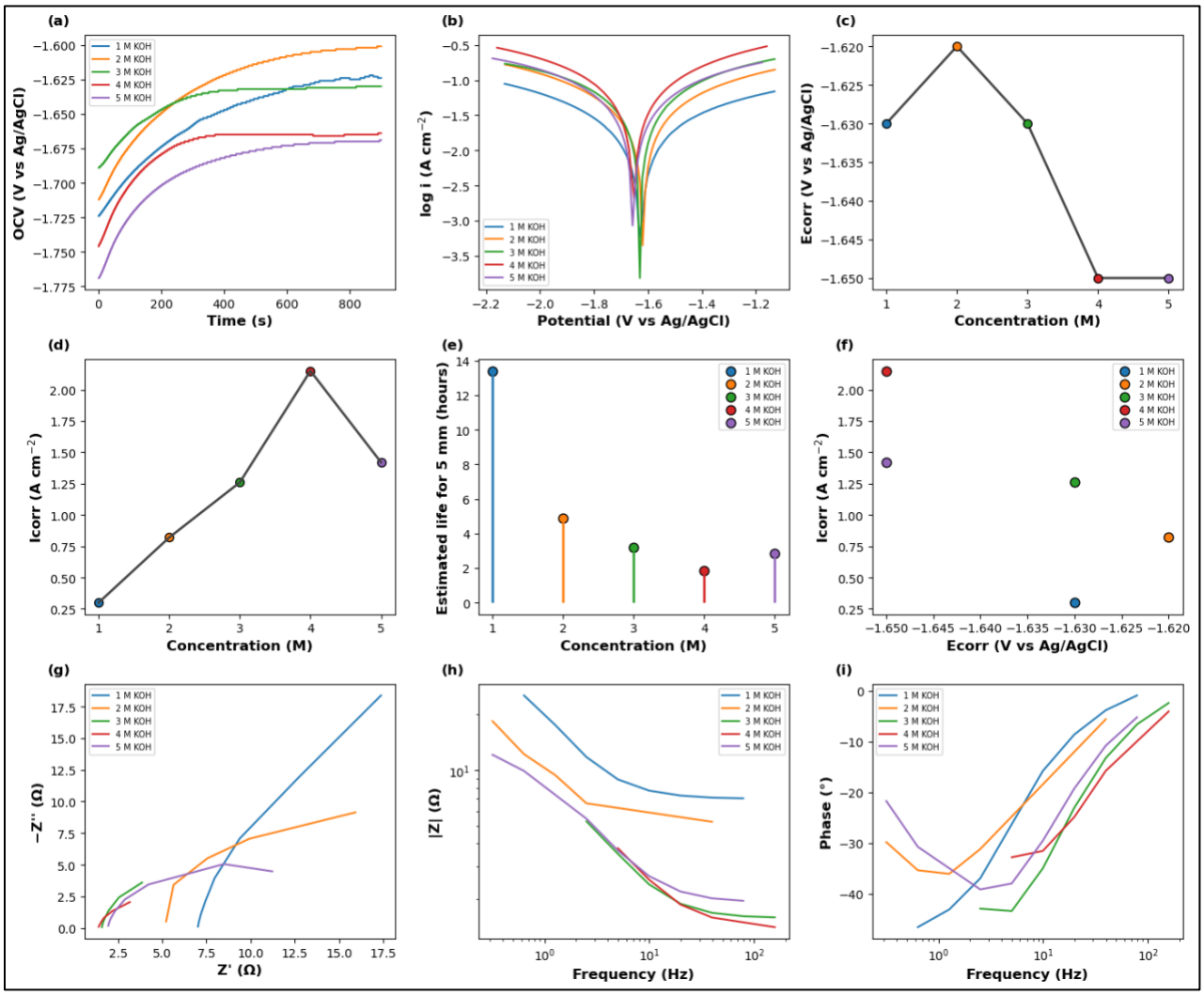


Figure 5. 4: Comprehensive electrochemical characterization of the commercial Al alloy in 1-5 M KOH, showing (a) open-circuit voltage evolution, (b) anodic and cathodic Tafel behaviours, (c) corrosion potential (Ecorr) as a function of electrolyte concentration, (d) corrosion current density (Icorr) trends, (e) estimated anode lifetime based on Icorr, (f) the relationship between Ecorr and Icorr, (g) Nyquist impedance response, (h) Bode magnitude of impedance $|Z|$ across frequency, and (i) corresponding phase-angle behaviour.

In contrast, NaOH exhibits a more systematic concentration dependence across both regimes. In the 1-5 M range (Figure 5.6a), the stabilized OCV shifts progressively toward more negative values with increasing concentration, indicating a steady enhancement in corrosive activity as hydroxide concentration increases. This monotonic trend continues in the high-concentration NaOH window (6-10 M, Figure 5.7a), where the most negative steady potentials are consistently

observed at the highest molarities. Compared with KOH at equivalent concentrations, NaOH generally stabilizes at more negative OCV values, particularly in the high-concentration regime, implying differences in the steady-state balance of anodic and cathodic reactions and in the nature or persistence of surface hydroxide films formed in the two electrolytes. Overall, the OCV behavior reveals that while both electrolytes promote rapid activation of the aluminum surface, KOH shows convergence toward a concentration-independent active state at high molarity, whereas NaOH maintains a stronger concentration sensitivity across the full range studied.

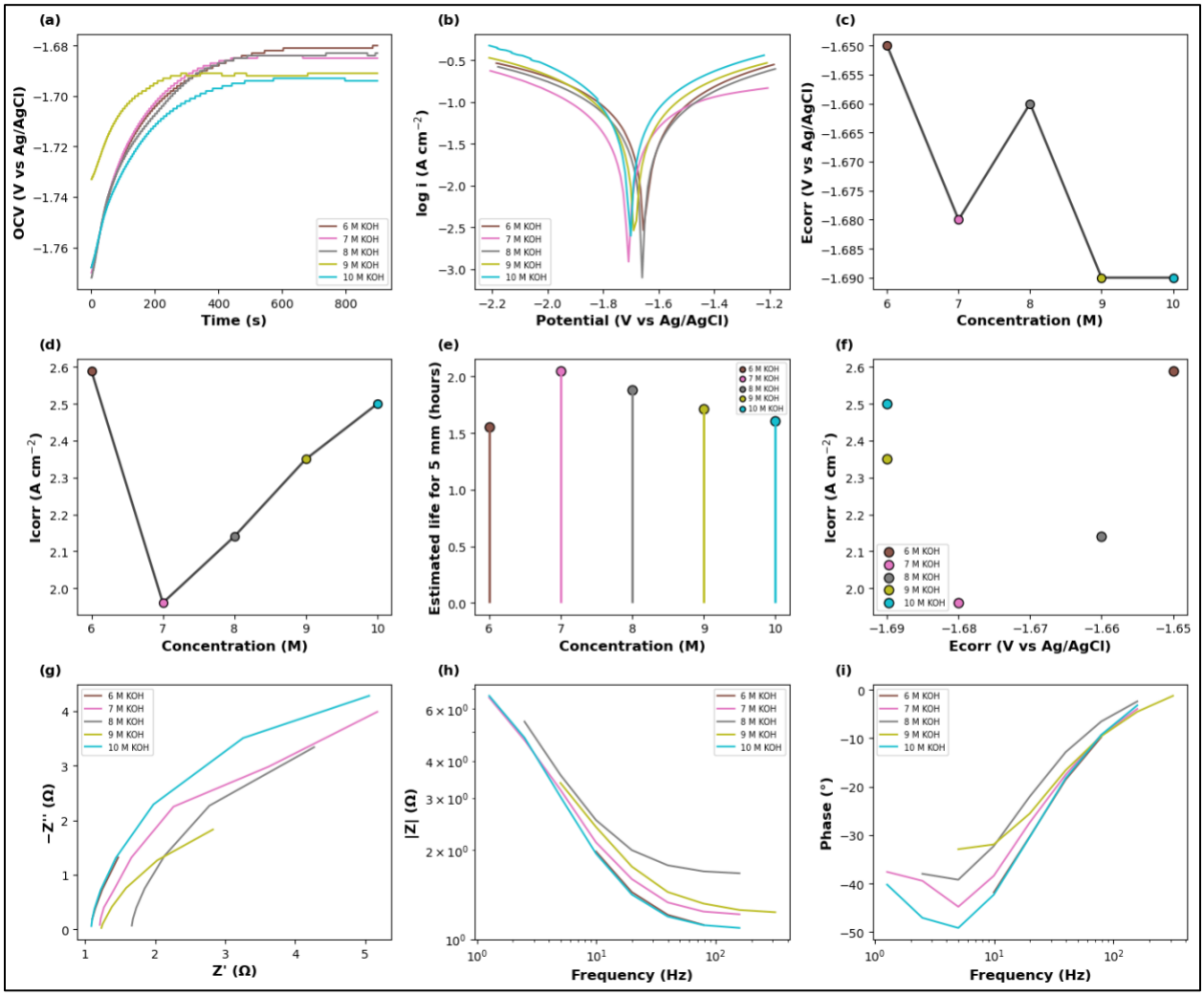


Figure 5. 5: Comprehensive electrochemical characterization of the commercial Al alloy in 6-10 M KOH, showing (a) open-circuit voltage evolution, (b) anodic and cathodic Tafel behaviours, (c) corrosion potential (Ecorr) as a function of electrolyte concentration, (d) corrosion current density (Icorr) trends, (e) estimated anode lifetime based on Icorr, (f) the relationship between Ecorr and

Icorr, (g) Nyquist impedance response, (h) Bode magnitude of impedance $|Z|$ across frequency, and (i) corresponding phase-angle behaviour.

The potentiodynamic polarization curves obtained for the commercial Al alloy in 1-5 M KOH (Figure 5.4(b)) exhibit systematic concentration-dependent changes in both anodic and cathodic branches, reflecting progressive activation of aluminum dissolution with increasing hydroxide concentration. As the KOH concentration increases from 1 to 5 M, the corrosion potential shifts toward more negative values (Figure 5.4(c)), indicating enhanced thermodynamic driving force for anodic dissolution. Similar shifts in Ecorr with increasing KOH concentration have been reported for aluminum and Al-Mg-Si alloys and are commonly attributed to accelerated chemical dissolution of the native Al_2O_3/AlOOH surface film under high OH^- activity [349].

The corrosion current density increases markedly with concentration up to 4 M KOH (Figure 5.4(d)), confirming a transition from partially inhibited dissolution at low concentration to a fully active corrosion regime at intermediate concentrations. This increase in Icorr is consistent with previous studies showing that elevated KOH concentrations enhance ionic conductivity, reduce charge-transfer resistance, and promote faster anodic aluminum oxidation coupled with hydrogen evolution [350,351]. When interpreting the KOH concentration dependence, it is also important to separate "OH^- availability" from interfacial water activity and double-layer effects. Cation-controlled solvation and electric double-layer composition can modulate the activity of "free water" participating in anodic corrosion pathways and can promote formation of more corrosion-resistant surface compounds, which directly affects the apparent activation observed in polarization responses [352]. The slight reduction in Icorr observed at 5 M relative to 4 M suggests the onset of secondary effects, such as accumulation of soluble aluminate species or partial surface blockage by corrosion products, phenomena that have also been observed at high alkalinity in earlier investigations [353,354].

The coupling between Ecorr and Icorr shown in Figure 5.4(f) indicates that anodic activation dominates the corrosion kinetics in this concentration window [355]. Comparable Ecorr-Icorr correlations have been reported in alkaline corrosion studies, where increasingly negative corrosion potentials coincide with accelerated uniform aluminum dissolution rather than localized attack [356-358].

In the 6-10 M KOH concentration window, the electrochemical behavior shifts into a regime where aggressive alkaline dissolution is governed by mass-transport and saturation-limited kinetics rather than pure charge transfer. While the rapid stabilization of Ecorr at strongly negative values in Figure 5.5(c) indicates the immediate removal of the native oxide layer, the uniformly high Icorr with modest variation observed in Figure 5.5(d) suggests that the reaction has reached a kinetic limitation [359]. This behavior is driven by the accumulation of soluble aluminate species ($Al(OH)_4^-$), coupled with increased electrolyte viscosity at higher concentrations which in-turn leading to the increased thickness of the Nernst boundary layer ($\delta \approx$ 10-100 μm) , thereby hindering the diffusion of fresh hydroxide ions to the metal surface. Simultaneously, intense hydrogen evolution leads to significant bubble adsorption, with an estimated surface coverage of 20-50%, inducing gas evolution impedance and physically blocking the active surface area [360-362]. This transition from anodic activation to transport control is further evidenced by the weak Ecorr-Icorr coupling in Figure 5.5(f), confirming that the reaction rate is throttled by the physical movement of species and interfacial blockage once a critical hydroxide threshold is exceeded.

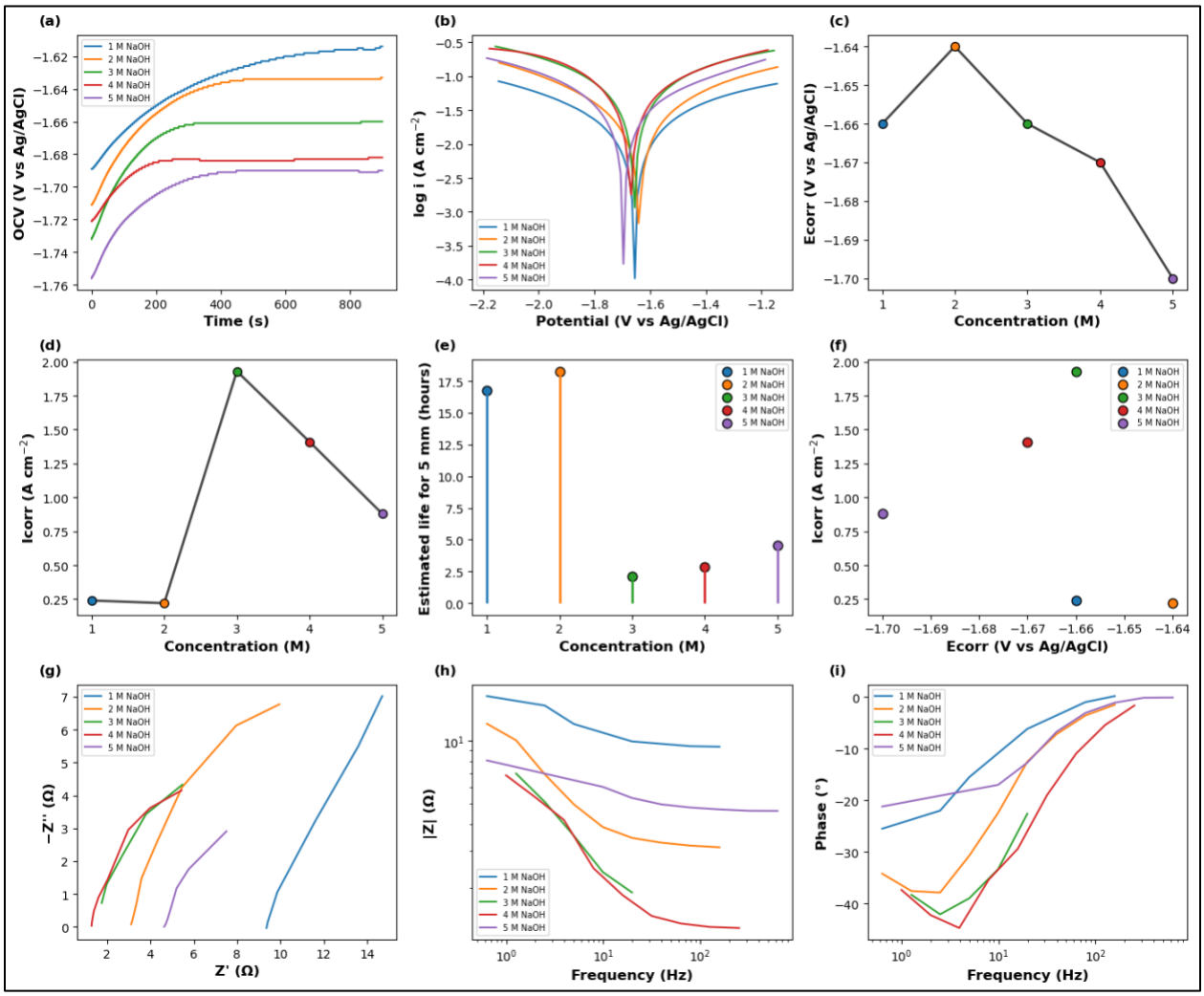


Figure 5. 6: Comprehensive electrochemical characterization of the commercial Al alloy in 1-5 M NaOH, showing (a) open-circuit voltage evolution, (b) anodic and cathodic Tafel behaviours, (c) corrosion potential (Ecorr) as a function of electrolyte concentration, (d) corrosion current density (Icorr) trends, (e) estimated anode lifetime based on Icorr, (f) the relationship between Ecorr and Icorr, (g) Nyquist impedance response, (h) Bode magnitude of impedance $|Z|$ across frequency, and (i) corresponding phase-angle behaviour.

The polarization behavior of aluminum in 1-5 M NaOH (Figure 5.6(b)) exhibits qualitatively similar trends to KOH but with clear quantitative differences. Increasing NaOH concentration drives Ecorr to more negative values (Figure 5.6(c)), reflecting progressive destabilization of the surface oxide film. However, at equivalent molarities, Ecorr values in NaOH remain consistently less negative than those measured in KOH, indicating weaker anodic

activation. The corrosion current density shows a non-monotonic dependence on concentration (Figure 5.6(d)), with a pronounced increase at intermediate concentration followed by partial suppression at higher molarity. This behavior can be attributed to competing processes, including oxide dissolution, surface reorganization, and partial re-passivation at elevated hydroxide concentrations. The longer estimated lifetimes observed at low NaOH concentrations (Figure 5.6(e)) further support the interpretation that NaOH provides a comparatively milder corrosion environment than KOH in the low-to-moderate concentration regime. The broader scatter in the Ecorr-Icorr relationship (Figure 5.6(f)) suggests greater sensitivity of corrosion kinetics to local surface conditions, indicating less stable interfacial behavior in NaOH [351].

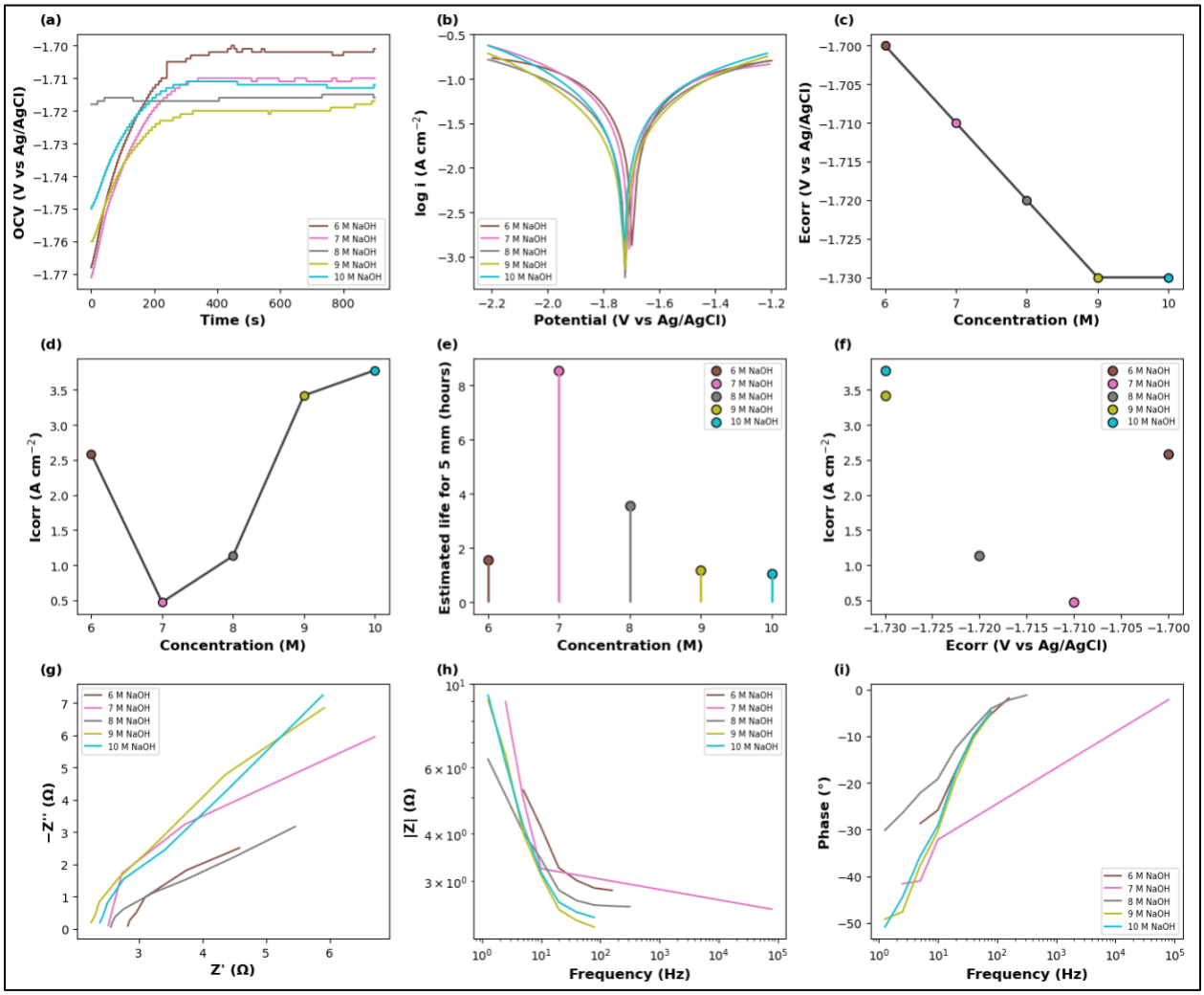


Figure 5. 7: Comprehensive electrochemical characterization of the commercial Al alloy in 6-10 M NaOH, showing (a) open-circuit voltage evolution, (b) anodic and cathodic Tafel behaviours,

(c) corrosion potential (Ecorr) as a function of electrolyte concentration, (d) corrosion current density (Icorr) trends, (e) estimated anode lifetime based on Icorr, (f) the relationship between Ecorr and Icorr, (g) Nyquist impedance response, (h) Bode magnitude of impedance $|Z|$ across frequency, and (i) corresponding phase-angle behaviour.

At higher NaOH concentrations (6-10 M), the polarization curves (Figure 5.7(b)) indicate a transition toward more active corrosion behavior. Ecorr becomes increasingly negative with concentration (Figure 5.7(c)), although the magnitude of this shift remains smaller than that observed in KOH at comparable molarities. This observation indicates that NaOH requires higher concentrations to achieve corrosion rates comparable to KOH due to differences in cation size, hydration, and interfacial transport properties [363]. The corrosion current density increases substantially at 9-10 M NaOH (Figure 5.7(d)), indicating that sufficiently high hydroxide activity can overcome surface stabilization effects and promote rapid aluminum dissolution. However, the broader Ecorr-Icorr distribution (Figure 5.7(f)) suggests less stable electrochemical behavior relative to KOH, a trend previously attributed to weaker disruption of surface passivation and less efficient charge transport in Na^+-based electrolytes [364,365].

Across the full concentration range, KOH consistently produces more negative corrosion potentials and higher corrosion current densities than NaOH at equivalent molarities (Table 5.3). This behavior cannot be explained solely by hydroxide concentration, as both electrolytes supply identical OH^- activity at the same molarity. Instead, the observed differences are attributed to cation-specific effects, where the larger ionic radius and higher mobility of K^+ facilitate faster charge transport, enhanced interfacial reactions, and accelerated hydrogen evolution kinetics [366]. The present results extend these observations across a broader concentration range and provide a unified electrochemical interpretation linking electrolyte identity to corrosion kinetics through combined Ecorr-Icorr analysis.

Table 5. 3: Comparison of corrosion potential (Ecorr) and corrosion current density (Icorr) of the commercial Al-Mg-Si alloy in KOH and NaOH electrolytes over the concentration range of 1-10 M.

Concentration (M)	Ecorr (V vs Ag/AgCl) - KOH	Icorr (A cm^{-2}) - KOH	Ecorr (V vs Ag/AgCl) - NaOH	Icorr (A cm^{-2}) - NaOH
1	-1.63	0.30	-1.66	0.24
2	-1.62	0.82	-1.64	0.22
3	-1.63	1.26	-1.66	1.93
4	-1.65	2.15	-1.67	1.41
5	-1.65	1.42	-1.70	0.88
6	-1.65	2.59	-1.70	2.59
7	-1.68	1.96	-1.71	0.47
8	-1.66	2.14	-1.72	1.13
9	-1.69	2.35	-1.73	3.42
10	-1.69	2.50	-1.73	3.78

5.4.2 Mechanistic Interpretation from Electrochemical Impedance

Electrochemical impedance spectroscopy was employed to elucidate the interfacial mechanisms governing alkaline corrosion of the commercial Al alloy and to complement the trends observed from OCV and potentiodynamic polarization measurements. The impedance response across all electrolyte concentrations and both alkaline media is well represented by an equivalent circuit consisting of the solution resistance in series with a parallel combination of charge-transfer resistance and a constant phase element representing the double-layer capacitance. This circuit captures the non-ideal capacitive behavior associated with surface roughness, evolving oxide films, and gas evolution at the aluminum-electrolyte interface.

Table 5. 4: Fitted electrochemical impedance parameters for the commercial Al alloy in KOH and NaOH electrolytes over the concentration range of 1-10 M.

Electrolyte	Concentration (M)	Rs (Ω·cm²)	Rct (Ω·cm²)	CPEdl-T	CPEdl-P
KOH	1	6.88	71.08	5.085	0.847
	2	4.983	21.46	0.025	0.891
	3	1.582	9.899	0.015	0.921
	4	1.441	4.2	0.011	0.949
	5	1.85	13.50	0.024	0.810
	6	1.038	0.01597	1.539	0.854
	7	1.172	9.597	0.019	0.860
	8	1.653	7.933	0.016	0.426
	9	1.23	5.386	0.022	0.815
	10	1.063	10.31	0.012	0.900
NaOH	1	9.22	73.13	0.038	0.615
	2	3.084	18.31	0.019	0.831
	3	1.485	12.39	0.022	0.823
	4	1.275	9.827	0.018	0.873
	5	4.65	0.0185	0.009	1.089
	6	2.829	6.202	0.011	0.927
	7	2.603	10.18	0.007	1.071
	8	2.542	3.917	0.019	0.887
	9	2.184	28.68	0.019	0.843
	10	2.313	35.49	0.021	0.827

Rs denotes solution resistance, Rct represents charge-transfer resistance, and the double-layer capacitance is represented using a constant phase element (CPEdl), where T is the magnitude parameter and P is the phase exponent.

Table 5.4 shows the values of the fitted electrochemical impedance parameters for the commercial Al alloy in KOH and NaOH electrolytes over the concentration range of 1-10 M. Across the full concentration range, the impedance spectra exhibit depressed semicircles in the Nyquist plots and broad phase-angle maxima in the Bode phase plots, indicating significant deviation from ideal capacitive behavior. This non-ideality is quantified by the CPEdl-P exponent, which remains consistently below unity for both electrolytes, confirming a heterogeneous and dynamically evolving interface. Such behavior is characteristic of aluminum corrosion in strongly alkaline environments, where continuous oxide dissolution, aluminate formation, and hydrogen evolution lead to spatially and temporally varying electrochemical conditions at the surface [367,368]. The charge-transfer resistance decreases markedly with increasing hydroxide concentration in both KOH and NaOH, consistent with the progressive activation of anodic aluminum dissolution inferred from polarization measurements. In KOH, Rct decreases rapidly from high values at low concentration to very low values at moderate-to-high molarity, reflecting the strong ability of KOH to destabilize the native Al_2O_3/AlOOH surface layer and promote facile charge transfer. This trend aligns with the increasingly negative corrosion potentials and elevated corrosion current densities observed in the polarization data, confirming that anodic activation dominates the corrosion kinetics over a broad concentration range [369]. At higher alkaline concentrations, particularly in KOH, the interpretation of Rct requires careful consideration. Extremely low fitted Rct values do not necessarily imply an absence of interfacial resistance but rather indicate that classical charge-transfer resistance becomes masked by other impedance contributions. Under these conditions, vigorous hydrogen evolution, accumulation of soluble aluminate species, and increased electrolyte viscosity contribute to gas bubble coverage, interfacial blockage, and transport limitations. These effects distort the impedance response and reduce the apparent semicircle diameter, leading to artificially low Rct values when interpreted using conventional equivalent circuit models. The persistence of non-ideal CPE behavior and the flattening of phase-angle responses at low frequencies further support a transition from pure charge-transfer control to a regime dominated by mass transport and interfacial obstruction [370].

The magnitude parameter of the constant phase element, CPEdl-T, provides additional insight into interfacial evolution. Variations in CPEdl-T across concentration reflect changes in effective double-layer capacitance, which is influenced by surface roughness, oxide film thickness, and hydrogen bubble coverage. In general, higher CPEdl-T values correspond to increased

electrochemically active surface area and thinning of surface films, consistent with enhanced anodic dissolution at elevated hydroxide concentrations. However, pronounced fluctuations in CPEdl-T at high molarity suggest that competing processes, including surface roughening and partial blockage by corrosion products or gas bubbles, act simultaneously to modulate the interfacial capacitance [371]. Comparison between KOH and NaOH reveals systematic electrolyte-dependent differences in impedance behavior that cannot be attributed solely to hydroxide concentration. At equivalent molarities, NaOH consistently exhibits higher charge-transfer resistance than KOH, indicating reduced anodic activation and slower corrosion kinetics. This finding corroborates the less negative corrosion potentials and lower corrosion current densities measured in NaOH, particularly at low-to-moderate concentrations. The CPEdl-P values in NaOH also display greater variability and, in some cases, approach or exceed unity, suggesting a less stable and more heterogeneous interfacial structure compared with KOH. Such behavior is consistent with weaker disruption of surface passivation and less efficient charge transport in Na^+-based electrolytes [352,370]. These electrolyte-specific impedance trends highlight the critical role of cation identity in governing alkaline aluminum corrosion. Although both KOH and NaOH provide identical hydroxide activity at a given molarity, the larger ionic radius, lower hydration energy, and higher mobility of K^+ facilitate enhanced interfacial transport, stronger double-layer perturbation, and more aggressive hydrogen evolution. As a result, KOH promotes lower Rct, more negative corrosion potentials, and higher corrosion currents than NaOH across the full concentration range investigated. The impedance results therefore reinforce the conclusion drawn from polarization and OCV analyses that corrosion kinetics in alkaline aluminum systems are governed by coupled hydroxide activity and cation-mediated interfacial effects. Overall, the EIS analysis provides mechanistic confirmation of the corrosion regimes inferred from DC electrochemical measurements. At low-to-moderate concentrations, corrosion is dominated by anodic activation and charge-transfer control, whereas at high alkalinity, transport limitations, surface saturation, and gas evolution increasingly govern the electrochemical response. The consistency between impedance-derived parameters and polarization behavior demonstrates the robustness of the experimental interpretation and underscores the value of EIS in resolving the complex, non-ideal interfacial processes underlying alkaline aluminum corrosion.

5.4.3 X-ray Diffraction Analysis

X-ray diffraction was employed to assess whether the electrochemical corrosion processes identified from OCV, polarization, and EIS measurements are accompanied by crystallographic degradation or formation of stable corrosion products on the commercial Al alloy.

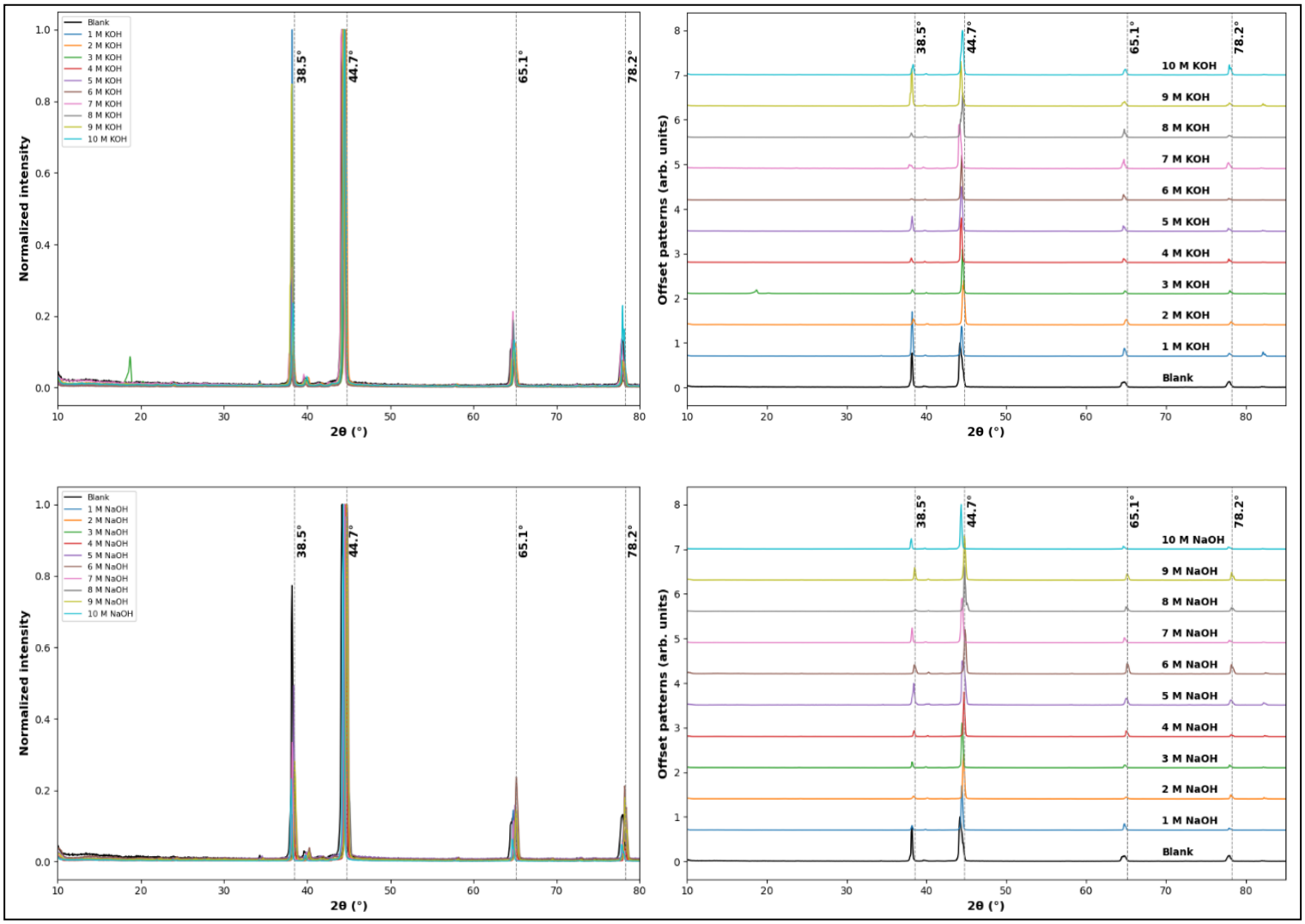


Figure 5. 8: X-ray diffraction patterns of the commercial aluminum alloy before (blank) and after exposure to KOH and NaOH electrolytes over the concentration range of 1-10 M. The normalized intensity patterns (left panels) and vertically offset patterns (right panels) show dominant reflections at approximately 38.5°, 44.7°, 65.1°, and 78.2°, corresponding to the (111), (200), (220), and (311) planes of face-centered cubic aluminum.

The XRD patterns obtained after exposure to KOH and NaOH electrolytes across the full 1-10 M concentration range are dominated by the characteristic reflections of face-centered cubic aluminum at approximately 38.5°, 44.7°, 65.1°, and 78.2°, corresponding to the (111), (200), (220), and (311) planes as shown in Figure 5.8. The persistence of these reflections with invariant peak positions across all concentrations and both electrolytes indicates that the bulk aluminum lattice remains structurally intact despite substantial electrochemical activity. No peak shifts or broadening indicative of lattice distortion or phase transformation are observed, confirming that alkaline exposure does not induce measurable crystallographic degradation of the alloy. Notably, no additional diffraction peaks associated with crystalline aluminum hydroxides, oxyhydroxides, or aluminate phases are detected under any condition. This absence suggests that corrosion products formed during alkaline exposure are predominantly amorphous, nanocrystalline, or highly hydrated, falling below the detection limit of XRD. This finding is consistent with electrochemical evidence for continuous oxide dissolution, high corrosion currents, and the lack of sustained passivation, particularly at moderate-to-high hydroxide concentrations. Minor variations in relative peak intensity observed at higher concentrations are attributed to surface roughening, preferential dissolution, and changes in near-surface texture rather than to bulk compositional changes. Such effects are expected under aggressive alkaline corrosion, where rapid anodic dissolution and hydrogen evolution continuously renew the exposed surface and inhibit the accumulation or crystallization of corrosion products. Comparison between KOH and NaOH reveals no electrolyte-specific crystalline phases, despite pronounced differences in corrosion kinetics and impedance response. The retention of the aluminum crystalline framework across all conditions provides structural validation for the mechanistic interpretations derived from polarization and EIS analyses and confirms that corrosion proceeds through continuous surface dissolution with transient, non-protective corrosion products.

5.4.4 ANN Model Performance and Predictive Accuracy

A comprehensive grid search comprising 351 ANN configurations was conducted to identify an accurate and robust predictive model for Ecorr and Icorr across NaOH and KOH concentrations. The search space systematically varied network depth, neuron allocation per layer, learning rate, and Adam β_1, while training length and batch size were held constant. Validation performance across the grid revealed substantial variability in model accuracy, with mean R^2 values ranging from 0.785 to 1.000 and an average of 0.972. Notably, 267 configurations,

corresponding to 76 percent of all tested models, achieved mean validation R^2 values exceeding 0.97, indicating that the underlying electrochemical relationships are highly learnable yet sensitive to architectural choices.

Performance trends were consistent with expected nonlinear structure in the dataset. Increasing hidden-layer depth generally improved Ecorr prediction accuracy, whereas Icorr remained robust across a wider range of architectures. Networks with non-uniform layer widths outperformed uniform configurations, demonstrating that asymmetric feature compression and expansion better captured the coupled effects of electrolyte identity, concentration, and polarization behavior. Learning rates above 0.001 and β_1 values below 0.90 tended to produce unstable convergence, confirming the importance of carefully tuned optimization dynamics when modeling strongly nonlinear corrosion responses.

Table 5. 5: ANN hyperparameter search results, including tuning grid and selected optimal configuration.

Hyperparameters	*Tuning grid*	*Optimized values*
Loss function	MSE	MSE
Hidden layers neurons	1-3 layers; neurons per layer $\in$ {20, 25, 30}	1st - 20; 2nd - 25; 3rd - 25
Learning rate (Lr)	0.00100; 0.00085; 0.00070	0.001
Beta 1	0.90; 0.92; 0.95	0.92
Beta 2	0.999	0.999
Epochs	500	500
Batch size	42	42

The best-performing configuration used a three-layer architecture with 20, 25, and 25 neurons, a learning rate of 0.001, and $\beta_1 = 0.92$. This model achieved R^2 values of 0.999888 for Ecorr and 0.999945 for Icorr, yielding a mean validation R^2 of 0.999917. Such accuracy represents an almost perfect mapping between the experimental variables and both corrosion indicators, validating the suitability of the ANN approach for predicting corrosion behavior in alkaline media.

The optimized hyperparameters are summarized in Table 5.5, confirming that relatively compact architectures can achieve high fidelity when hyperparameters are tuned systematically.

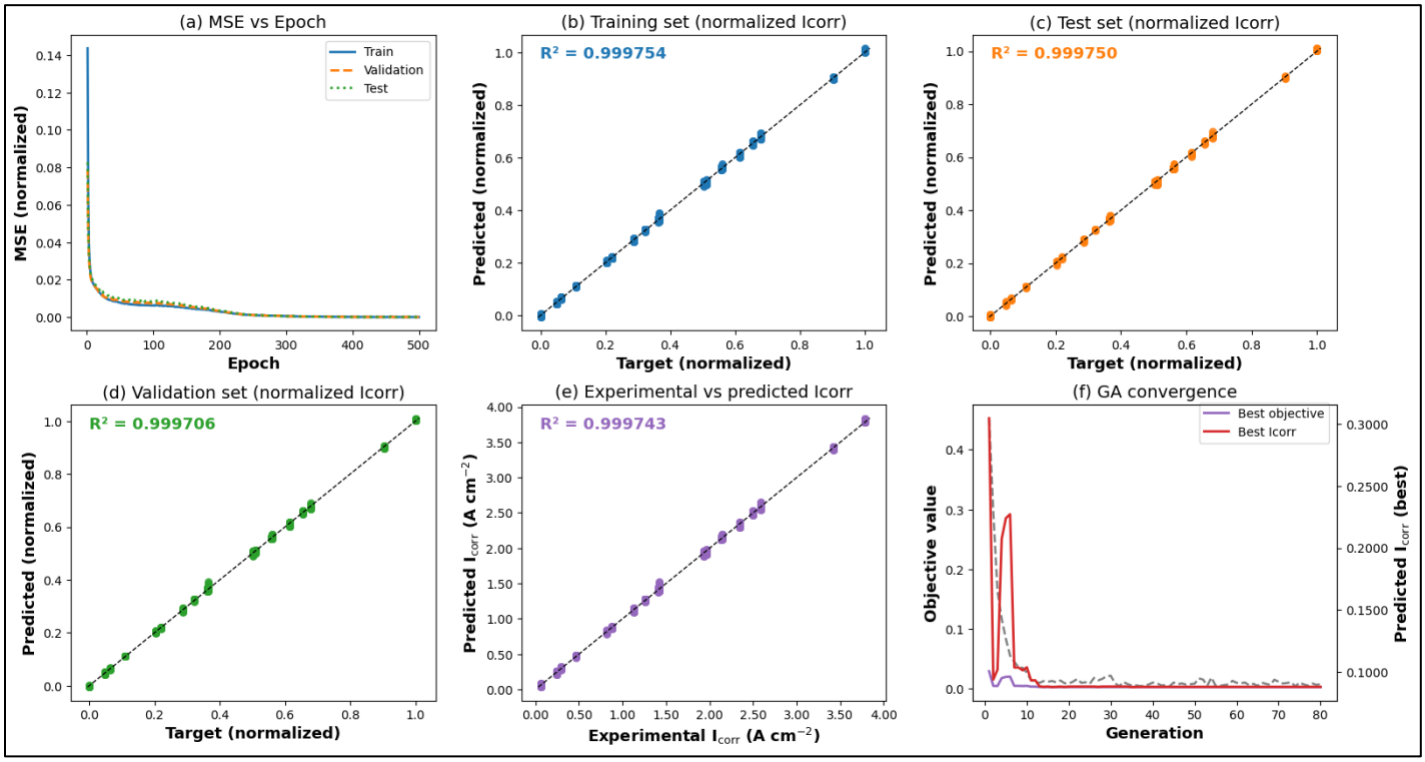


Figure 5. 9: Performance of the ANN modelling and GA optimization workflow, including (a) training and validation loss evolution, (b-e) parity plots comparing predicted and experimental/normalized Icorr, and (f) convergence of the GA showing best-objective and best-Icorr trends across generations.

The optimized three-layer ANN model demonstrated excellent predictive capability for both target variables, achieving near-perfect agreement between measured and predicted values across all data partitions. The training history (Figure 5.9(a)) shows rapid and stable convergence of the loss function, with monotonic reduction of MSE for the training, validation, and test sets throughout 500 epochs. No divergence or oscillatory behavior was observed, confirming that the selected hyperparameters ensured stable optimization. Table 5.6 shows the Summary of the optimized ANN model architecture and training configuration used for Ecorr and Icorr prediction

Scatter plots of predicted versus target Icorr values for the training, test, and validation subsets (Figures 5.9(b-d)) reveal extremely strong predictive performance, with R^2 values of 0.99975, 0.99975, and 0.99970, respectively. The points lie tightly along the line 1:1, indicating negligible systematic bias and excellent generalization across previously unseen samples. When

predictions were transformed back to physical units, the experimental-predicted comparison (Figure 5.9(e)) also maintained a very high coefficient of determination (R^2 = 0.99974), demonstrating that model accuracy remains robust in real units, not only in normalized space.

Table 5. 6: Summary of the optimized ANN model architecture and training configuration used for Ecorr and Icorr prediction.

ANN hyperparameters	**Al alloy corrosion dataset**
Feature vectors (Input)	5 (Electrolyte type, Concentration, Temperature, Voltage, Current density)
Target variables (Output)	2 (Ecorr, Icorr)
Number of hidden layers	3
Number of neurons per hidden layer	1st - 20; 2nd - 25; 3rd - 25
Activation function	ReLU for all hidden layers; Linear for output layer
Optimizer	Adam
Learning rate (optimized)	0.001
$beta_1$ (optimized)	0.92
Loss function	Mean squared error (MSE)
Epochs	500
Batch size	42

The consistently high R^2 values across all subsets and the absence of overfitting behavior confirm that the optimized ANN architecture successfully captures the nonlinear dependence of Ecorr and Icorr on electrolyte type, concentration, temperature, and polarization conditions. Together with the grid-search analysis, these results validate the ANN as a powerful predictive tool for corrosion modeling in alkaline environments.

5.4.5 GA and NSGA-II Optimization Outcomes

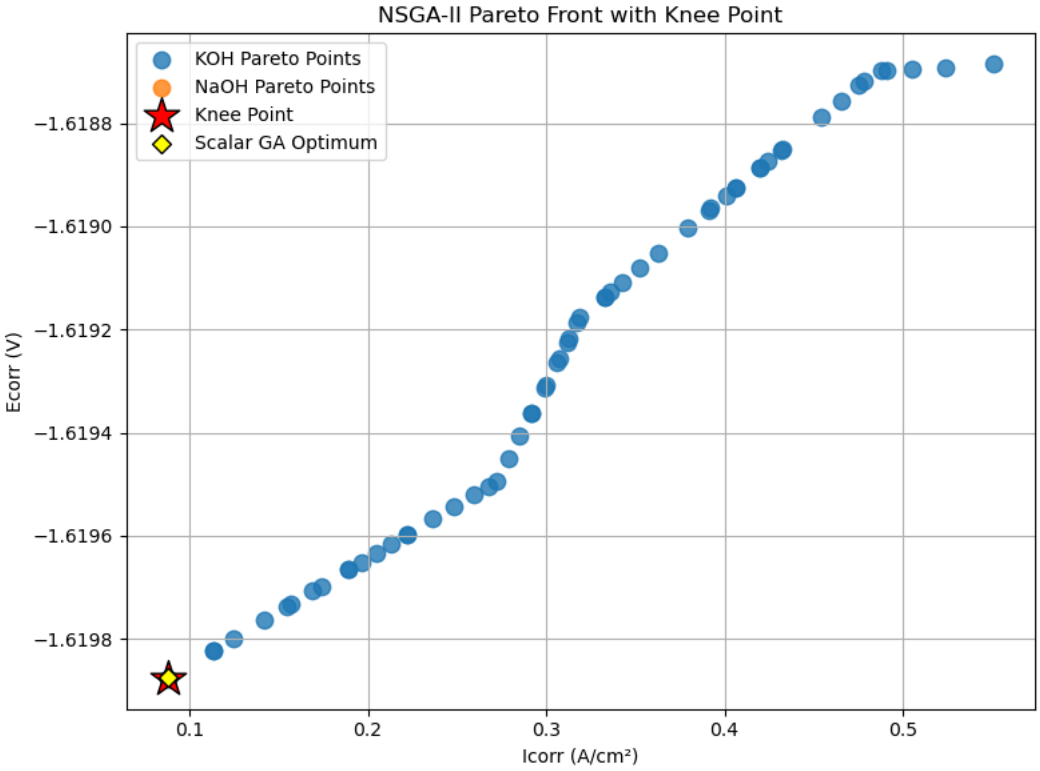


Figure 5. 10: NSGA-II Pareto front illustrating the trade-off between corrosion potential and corrosion current density, with identification of the knee point and scalar GA optimum.

Following ANN training, genetic algorithm-based optimization was applied to identify electrolyte conditions that balance corrosion thermodynamics and kinetics. A scalar GA was first employed to obtain a single optimal solution under equal weighting of Ecorr maximization and Icorr minimization, followed by NSGA-II to resolve the full trade-off structure between these two objectives without imposed weights. The resulting NSGA-II Pareto front and associated knee point are shown in Figure 5.10. The NSGA-II results reveal a smooth and continuous Pareto front for alkaline corrosion behavior, indicating a well-resolved trade-off between Ecorr and Icorr across electrolyte concentration. As shown in Figure 5.10, solutions with lower Icorr are associated with more negative Ecorr values, whereas improvements in Ecorr are accompanied by a rapid increase in corrosion current density. This monotonic but nonlinear trend reflects the fundamental electrochemical coupling between anodic dissolution kinetics and corrosion thermodynamics in alkaline aluminum systems.

The curvature of the Pareto front is particularly pronounced at low Icorr values, where relatively small increases in Icorr lead to diminishing gains in Ecorr. This behavior gives rise to a clearly identifiable knee region, which represents the transition from corrosion-limited to dissolution-dominated regimes. Beyond this point, further enhancement of Ecorr becomes increasingly costly in terms of corrosion rate, suggesting that the system enters a regime where hydroxide-driven dissolution kinetics dominate over interfacial stabilization effects.

Using the minimum-distance-to-ideal criterion, the knee point on the Pareto front was identified at a KOH concentration of approximately 1.35 M, with a predicted Ecorr of -1.6199 V and an Icorr of 0.0876 A cm^{-2}. This solution represents the least-compromise operating condition, where further reductions in corrosion current would require a disproportionate loss in corrosion potential stability. From a mechanistic perspective, the knee point corresponds to a moderate alkaline environment in which oxide film disruption and anodic dissolution are sufficiently activated to stabilize Ecorr, but transport limitations, surface saturation, and solution property effects constrain further acceleration of corrosion kinetics. This interpretation is consistent with the experimentally observed plateauing behavior in corrosion metrics at higher hydroxide concentrations, where increases in alkalinity no longer yield proportional electrochemical benefits.

Notably, the scalar GA optimum coincides almost exactly with the NSGA-II knee point, both identifying KOH at 1.35 M as the optimal electrolyte condition. The scalar GA predicts an Ecorr of -1.619876 V and an Icorr of 0.087859 A cm^{-2}, yielding a combined objective score of 0.003179. The near-identical values obtained from two fundamentally different optimization formulations provide strong validation of the ANN-based optimization framework. This agreement confirms that the equal-weight scalarization adopted in the GA does not bias the solution toward artificial extrema, but instead naturally converges toward the physically meaningful compromise identified by the Pareto geometry. In practical terms, this indicates that the knee point represents a robust optimum that is insensitive to the choice of optimization strategy, further reinforcing its relevance for corrosion-aware electrolyte selection. The combined GA and NSGA-II results demonstrate that optimal corrosion performance is achieved at intermediate hydroxide concentrations rather than at the most aggressive alkaline conditions. This finding highlights the importance of accounting for nonlinear electrochemical trade-offs when designing

aluminum electrochemical systems, particularly in applications where parasitic corrosion losses must be minimized without sacrificing electrochemical stability.

5.5 Conclusions

In this study, the corrosion behavior of a commercial Al-Mg-Si alloy in alkaline sodium hydroxide and potassium hydroxide electrolytes was systematically investigated using combined electrochemical characterization and data-driven machine learning techniques. Electrochemical measurements, including open-circuit voltage, potentiodynamic polarization, and electrochemical impedance spectroscopy, were conducted across a wide concentration range from 1 to 10 M to quantify corrosion potential and corrosion current density and to elucidate underlying corrosion mechanisms. The experimental results reveal distinct corrosion regimes governed by anodic activation at low-to-moderate alkalinity and by transport- and interfacial-limited processes at high hydroxide concentrations, with KOH consistently exhibiting more aggressive corrosion behavior than NaOH at equivalent molarities due to cation-specific interfacial effects. X-ray diffraction analysis confirms that corrosion proceeds without bulk phase transformation, indicating continuous surface dissolution accompanied by predominantly amorphous or transient surface films. To model the nonlinear dependence of corrosion behavior on electrolyte parameters, an artificial neural network was developed and trained using the experimental dataset. Systematic hyperparameter optimization resulted in an optimized ANN architecture capable of predicting both corrosion potential and corrosion current density with near-perfect accuracy, achieving coefficients of determination exceeding 0.999 for both outputs. Building on this predictive capability, genetic algorithm-based optimization was applied to identify electrolyte conditions that balance corrosion thermodynamics and kinetics. Multi-objective optimization using NSGA-II revealed a well-defined Pareto front and a robust knee-point solution corresponding to approximately 1.35 M KOH, yielding a predicted corrosion potential of −1.6199 V and a corrosion current density of 0.0876 A cm^{-2}. These results demonstrate the effectiveness of integrating electrochemical experimentation with ANN-assisted evolutionary optimization for corrosion modeling and electrolyte selection. The proposed framework enables rapid, quantitative evaluation of corrosion behavior without exhaustive experimentation and provides a foundation for corrosion-aware electrolyte optimization in aluminum-air battery systems. Future work will extend this approach to include additional operating parameters and degradation metrics, supporting the

development of digital-twin platforms for the design, optimization, and control of next-generation aluminum-based electrochemical energy systems.

Chapter 6 System-Level Modeling and Integration of Al-air Batteries in Dual-Energy-Storage Electric Vehicles

*** Chapter 6 is adapted from Shabeer Y, Madani SS, Panchal S, Fowler M. "System-Level Modeling and Integration of Al-air Batteries in Dual-Energy-Storage Electric Vehicles." World Electr. Veh. J. 2026, 17(6), 296; https://doi.org/10.3390/wevj17060296

6.1 Introduction

6.1.1. Motivation and limitations of Li-ion-only EVs

The rapid adoption of electric vehicles has been driven by the need to reduce greenhouse gas emissions, improve urban air quality, and decrease dependence on fossil fuels [372,373]. Lithium-ion (Li-ion) batteries have emerged as the dominant onboard energy storage technology due to their high round-trip efficiency, favorable power capability, and rapidly declining costs [374]. Continuous improvements in cathode chemistry, cell engineering, and battery management systems have enabled steady gains in energy density and cycle life, supporting the commercialization of long-range battery electric vehicles across multiple market segments [375].

Despite these advances, Li-ion-only architecture faces intrinsic limitations when scaled for extended driving range and diverse operating conditions. Achieving long range requires large battery packs, which increase vehicle mass, reduce payload capacity, and impose diminishing returns on efficiency [376]. The added weight also exacerbates structural requirements and braking demands, while increasing material intensity and manufacturing emissions. Furthermore, Li-ion batteries exhibit trade-offs between energy density, fast-charging capability, thermal stability, and lifetime, making it difficult to optimize a single pack for all cases without compromise [377-379].

From a systems perspective, Li-ion-only EVs are further constrained by charging infrastructure availability, charging time, and resource sustainability. High-power fast charging places significant stress on both the grid and the battery, accelerating degradation and complicating thermal management [380]. In parallel, concerns related to critical material supply chains, recycling scalability, and cost volatility motivate the exploration of complementary energy storage concepts [381,382]. These challenges collectively highlight the need for alternative or auxiliary energy solutions that can alleviate range anxiety, reduce reliance on oversized Li-ion packs, and enhance overall vehicle system robustness [383].

6.1.2. Rationale for metal-air batteries as secondary energy sources

Metal-air batteries have attracted sustained interest as auxiliary energy systems due to their exceptionally high theoretical specific energy and the decoupling of energy storage from onboard oxidant supply. By utilizing oxygen from the ambient air as the cathodic reactant, metal-air systems store energy primarily in the metal anode, enabling gravimetric energy densities that substantially exceed those of conventional rechargeable batteries [384]. This intrinsic advantage makes metal-air chemistries particularly attractive for applications where extended energy availability is required without a proportional increase in onboard mass [385].

When integrated as secondary energy sources rather than primary traction batteries, metal-air systems can complement Li-ion packs by supplying sustained low-to-moderate power over extended durations [386]. In such hybridized architectures, the metal-air battery functions as an energy reservoir that offsets Li-ion depth of discharge, reduces peak power demands, and mitigates capacity oversizing. This division of roles allows each energy storage technology to operate closer to its optimal regime, with Li-ion batteries delivering high power and dynamic response, while metal-air systems provide high energy throughput over long driving intervals [387,388]. Beyond performance considerations, metal-air batteries offer potential system-level benefits related to modularity, serviceability, and material utilization. Many metal-air chemistries are mechanically rechargeable or replaceable, enabling rapid energy replenishment through metal anode replacement rather than electrochemical charging [64,389]. This feature opens alternative pathways for range extension, reduced downtime, and decoupling of vehicle energy replenishment from grid charging constraints. As a result, metal-air batteries present a compelling case as secondary onboard energy sources within next-generation electric vehicle architecture [50].

Among metal-air chemistries, aluminum-air (Al-air) batteries are particularly attractive for EV range-extension due to their high theoretical specific energy, material abundance, and intrinsic safety. Aluminum offers a favorable combination of low cost, high volumetric availability, and established recycling infrastructure compared to alternatives such as zinc or lithium-based systems [390]. In addition, Al-air batteries operate at ambient conditions and eliminate concerns related to oxygen storage, further supporting their suitability for onboard integration as secondary energy sources. From a vehicle system's perspective, Al-air batteries are well suited for energy-dominant roles rather than high-power traction applications. Their characteristics align naturally with range-

extender and auxiliary power functions, where sustained energy delivery is prioritized over fast transient response. This operational niche distinguishes Al-air systems from other metal-air batteries that may face greater challenges related to rechargeability, material logistics, or power scalability [220]. As a result, Al-air batteries represent a practical and strategically relevant choice for hybrid energy storage architectures in electric vehicles.

To realistically assess such architectures, system-level modeling is essential. MATLAB/Simulink provides a widely adopted, modular, and control-oriented environment for vehicle powertrain simulation, enabling dynamic interaction between energy storage systems, power electronics, and driving cycles [391]. Integrating Al-air battery models within a Simulink-based virtual vehicle framework allows evaluation of power sharing, state-of-charge (SOC) evolution, and energy management strategies under transient conditions. This approach bridges the gap between electrochemical performance and vehicle-level behavior, offering a reproducible and extensible platform for assessing Al-air batteries as secondary onboard energy sources.

6.1.3. Gaps in existing metal-air electric vehicle integration studies

Prior research on metal-air batteries for electric vehicle applications has largely focused on comparative potential rather than detailed system-level integration. Several studies have evaluated different metal-air chemistries, including Al-air, zinc-air (Zn-air), and iron-air systems, as range extenders by benchmarking their theoretical energy densities, material requirements, and projected vehicle-level benefits. For example, a study from 2025 [258] systematically analyzed multiple metal-air battery technologies as onboard range extenders, highlighting their potential to supplement Li-ion batteries and extend driving range without significantly increasing vehicle mass. While such analyses provide valuable high-level insights, they are often based on assumptions and static energy balance calculations.

A common limitation in existing literature is the lack of dynamic vehicle modeling that captures the interaction between metal-air systems, Li-ion batteries, and powertrain components under realistic driving conditions. Many studies treat metal-air batteries as idealized energy sources with fixed voltage or power output, neglecting transient behavior, control strategies, and coupling with vehicle energy management systems. As a result, the implications of power limits, efficiency losses, and operational constraints on overall vehicle performance remain insufficiently explored.

Furthermore, current studies rarely address how metal-air batteries can be systematically embedded within established electric vehicle modeling frameworks . There is limited discussion on architecture selection, control logic for energy sharing, or scalability from cell-level behavior to vehicle-level performance. This gap is particularly evident in the context of commercially relevant simulation environments, where reproducibility and extensibility are critical for technology assessment. Consequently, there is a clear need for modeling approaches that bridge electrochemical characteristics with system-level vehicle simulations to enable realistic evaluation of metal-air batteries as secondary onboard energy sources.

6.1.4. Objective and contributions of the present work

The objective of this study is to establish a system-level modeling framework that enables realistic evaluation of Al-air batteries as secondary energy sources in electric vehicles. Rather than treating Al-air systems as idealized energy reservoirs, this work focuses on their dynamic integration with a Li-ion battery pack within a virtual vehicle environment. The emphasis is placed on capturing power flow, energy-sharing behavior, and operational feasibility under transient driving conditions using a modular and extensible simulation approach.

The key contributions of the present work are summarized as follows:

- Development of a modular Al-air battery subsystem suitable for integration within a MATLAB/Simulink virtual vehicle platform
- System-level coupling of Al-air and Li-ion batteries through a controlled energy-sharing architecture
- Dynamic evaluation of Al-air-assisted vehicle operation under realistic drive cycles, moving beyond static or steady-state assumptions
- Demonstration of Al-air batteries as practical range extenders and auxiliary energy sources at the vehicle system level rather than as standalone electrochemical devices

Together, these contributions address a critical gap between Al-air electrochemical research and vehicle-level performance assessment, providing a reproducible framework for future studies on hybrid energy storage architectures.

6.1.5. Layout

The remainder of this paper is structured as follows. Section 2 presents the system-level modeling framework, including the vehicle powertrain architecture, the integration of the Al-air battery within a dual-energy-storage configuration, and the associated electrochemical and control modeling approaches implemented in MATLAB/Simulink. Section 3 describes the simulation setup and evaluation scenarios, including the baseline electric vehicle configuration, standardized driving cycles, battery pack assumptions, and auxiliary load modeling. Section 4 provides the results and discussion, beginning with baseline vehicle performance and subsequently analyzing the impact of Al-air integration under both range-extender and auxiliary power unit configurations. Comparative evaluation with existing metal-air integration studies and discussion of system-level implications are also presented. Finally, Section 5 summarizes the principal findings of the study, and Section 6 outlines directions for future work.

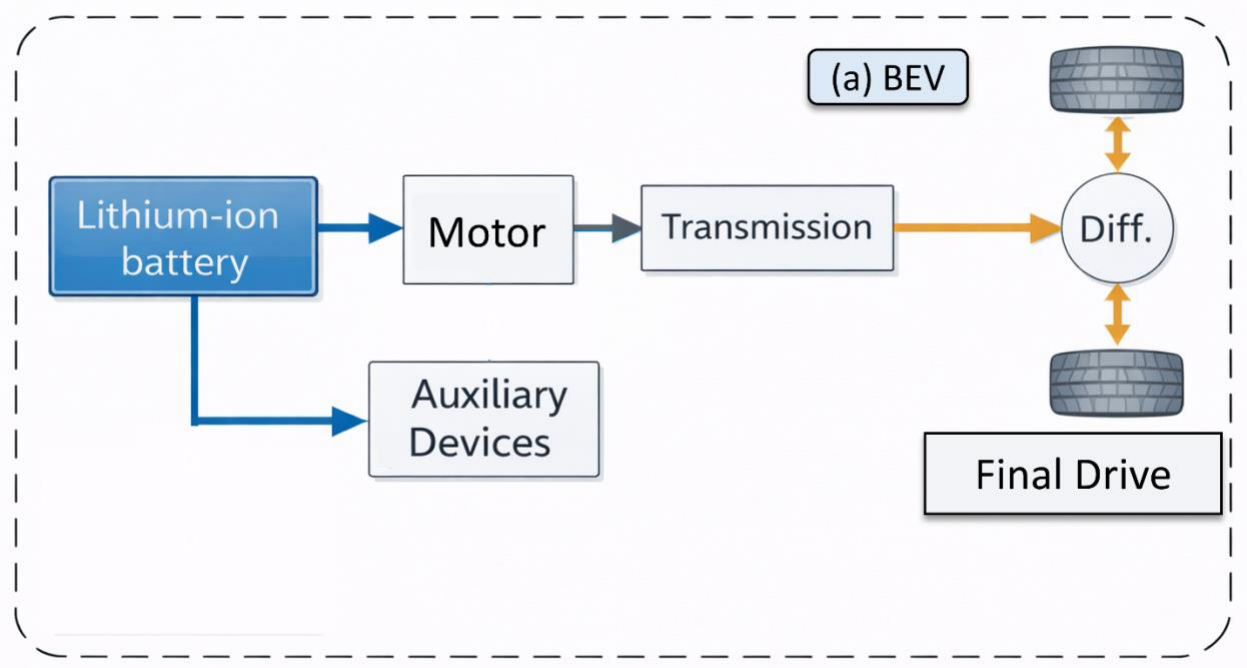
6.2 System-Level Modeling Framework

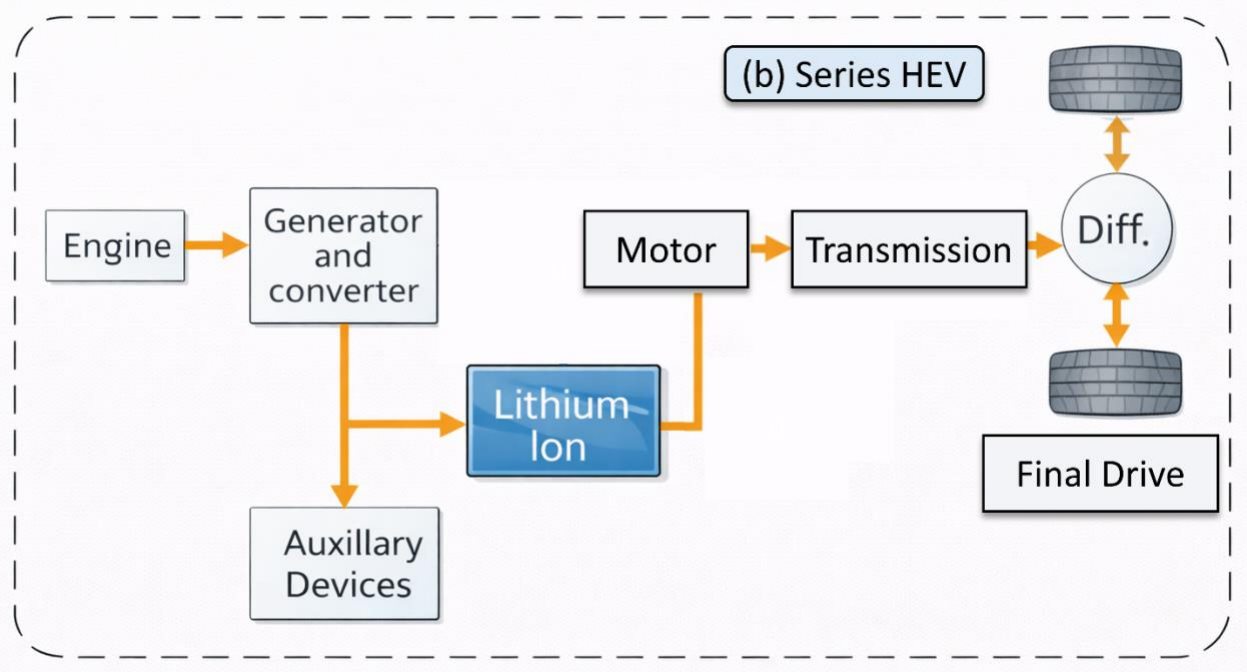
6.2.1 Vehicle Powertrain Architecture

Electric vehicle powertrain architectures have evolved in response to competing requirements for energy efficiency, driving range, cost, and operational flexibility. Modern electrified vehicles span a wide spectrum, ranging from battery electric vehicles to various hybrid electric vehicle configurations, each distinguished by how energy is stored, converted, and delivered to the drivetrain [392]. A clear understanding of these architectures is essential for contextualizing dual-energy-storage systems and range-extender concepts within electric vehicle design.

Battery electric vehicles (BEVs) (Figure 6.1a) rely exclusively on onboard electrical energy storage, typically Li-ion battery packs, to supply both traction and auxiliary loads. In BEVs, energy is converted from chemical to electrical form within the battery, conditioned by power electronics, and delivered to one or more electric motors that drive the wheels. BEVs offer high drivetrain efficiency, reduced mechanical complexity, and zero tailpipe emissions. However, their performance is constrained by battery energy density, charging time, infrastructure availability, and the mass and cost associated with large battery packs required to achieve long driving range [393].

Hybrid electric vehicles (HEVs) (Figure 6.1b) combine an internal combustion engine with one or more electric machines and an energy storage system to improve overall efficiency and operational flexibility. Depending on the coupling between mechanical and electrical power paths, HEV architectures are commonly classified as series, parallel, or series-parallel (power-split) (Figure 6.1c) configurations. In series HEVs, the engine is mechanically decoupled from the wheels and operates as a generator supplying electrical power to the traction motor or battery. Parallel HEVs allow both the engine and electric motor to directly contribute to wheel torque, while series-parallel HEVs combine these modes to enable flexible power flow at the cost of increased system complexity [394].




(b) Series HEV
Engine
Generator and converter
Motor
Transmission
Diff.
Lithium Ion
Auxillary Devices
Final Drive

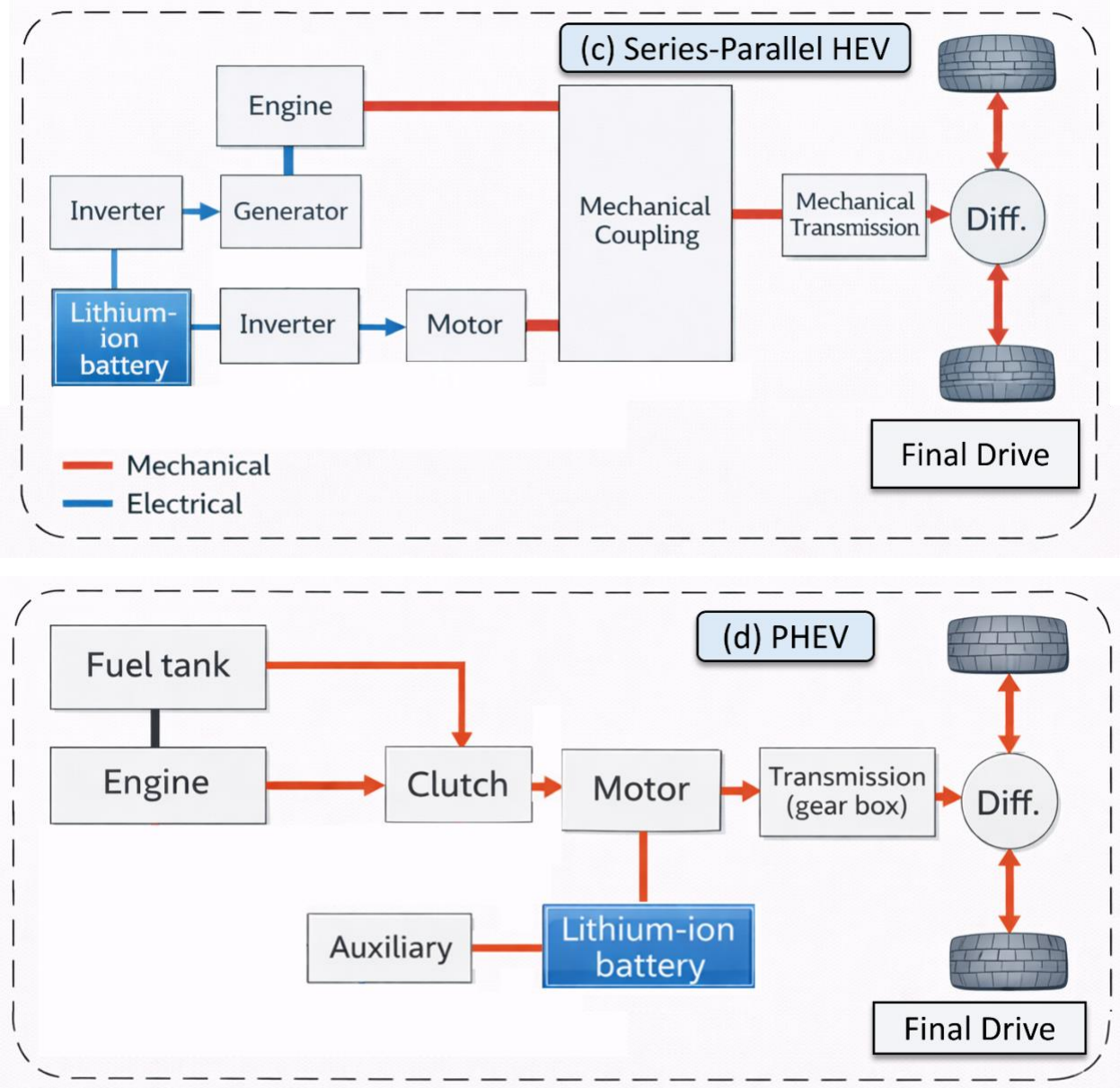


Figure 6. 1: Conventional electric vehicle powertrain architectures: (a) Battery electric vehicle (BEV) configuration and (b) series hybrid electric vehicle (HEV) configuration (c) series- parallel HEV (d) plug-in hybrid electric vehicle (PHEV)

Plug-in hybrid electric vehicles (PHEVs) (Figure 6.1d) extend the HEV concept by incorporating larger battery packs that can be charged from the grid, enabling a portion of driving to be performed in all-electric mode. A related architecture is the range-extended electric vehicle (REEV), in which the primary traction energy is supplied electrically, while a secondary onboard energy source is used exclusively to recharge the battery during operation. Conventional REEVs typically employ small internal combustion engines or fuel cells operating under near-steady

conditions to maximize efficiency. More recently, electrochemical range extenders, including metal-air batteries, have been proposed as alternatives that eliminate fuel combustion while offering high specific energy [29,395].

Recent advances in vehicle electrification have also led to hybrid architecture incorporating multiple energy storage systems with complementary characteristics. Dual-battery systems, battery-supercapacitor hybrids, and battery-fuel cell configurations have been investigated to balance energy density, power capability, efficiency, and lifetime [396-399]. Contemporary system-level studies increasingly emphasize modular architecture, control-oriented design, and compatibility with established simulation environments to facilitate consistent evaluation across vehicle platforms. Within this context, Al-air -assisted BEVs can be viewed as an extension of the REEV paradigm, where a high-energy secondary storage system augments a Li-ion battery without directly contributing to traction. This perspective motivates the modeling framework adopted in this work and provides the basis for the baseline and dual-energy-storage configurations discussed in the following subsections.

6.2.1.1 Electric Vehicle Modeling Framework

The baseline electric vehicle configuration employed in this study is based on a BEV virtual platform implemented in MATLAB/Simulink [400,401]. Figure 6.2 illustrates the structure of the baseline BEV modeling framework adopted in this work. The simulation begins with predefined driving scenarios, which specify reference speed profiles and operating conditions [402]. Environmental inputs, such as ambient effects and external disturbances, are processed alongside scenario data to inform the driver command module, which generates throttle and braking requests based on the prescribed driving task. These commands are interpreted by the vehicle controllers, which regulate powertrain operation and enforce system-level constraints. The model represents a mid-size passenger BEV and follows conventional single-energy-storage architecture, where a Li-ion battery pack supplies all traction and auxiliary power demands [403,404]. Key performance metrics, including vehicle speed, power demand, and energy consumption, are collected and routed to the visualization module for analysis. This baseline configuration serves as the reference architecture against which the proposed dual-energy-storage and Al-air -assisted configurations are evaluated and provides a modular and physics-based representation of the powertrain, enabling consistent system-level analysis under standardized

driving cycles. The vehicle model is based on the MATLAB/Simulink BEV virtual vehicle framework.

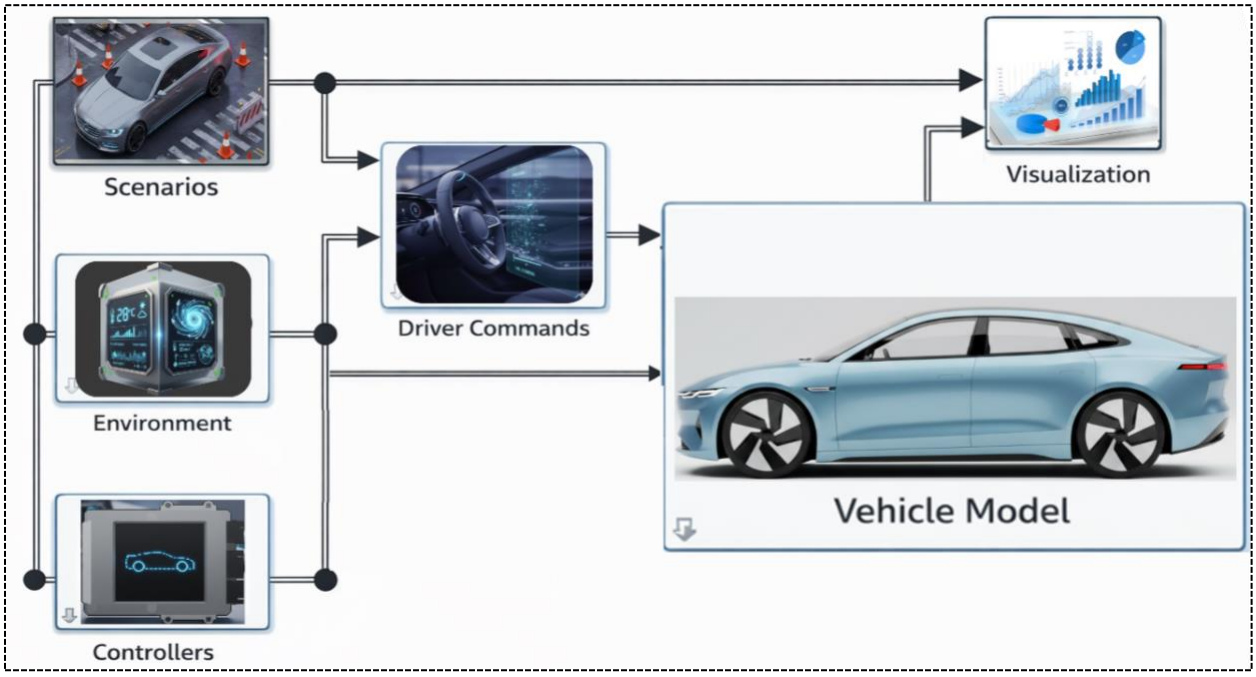


Figure 6. 2: High-Level Architecture of the Baseline BEV Modeling Framework

The architecture baseline comprises interconnected modules representing driving scenarios, environmental conditions, driver command generation, vehicle controllers, and the vehicle model itself. Simulation outputs are routed to a visualization block for post-processing and analysis. The baseline configuration includes a Li-ion battery pack, electric traction motor, inverter, drivetrain, vehicle longitudinal dynamics, and auxiliary loads. Energy flow is unidirectional from the battery to the electric motor through the power electronics, while regenerative braking is modeled to recover a portion of the kinetic energy during deceleration. The battery pack is represented using a mapped battery model with SOC-dependent voltage and internal resistance, allowing realistic prediction of battery behavior during transient operation [405].

Vehicle-level dynamics are captured using a forward-facing simulation approach, in which the driver model follows a prescribed speed profile and the powertrain responds to meet torque and power demands. This structure enables direct assessment of battery power, energy consumption, and SOC evolution under realistic operating conditions. The baseline model serves

as a reference against which the proposed dual-energy-storage configurations are evaluated, ensuring that the impact of Al-air integration is isolated from underlying vehicle and powertrain assumptions.

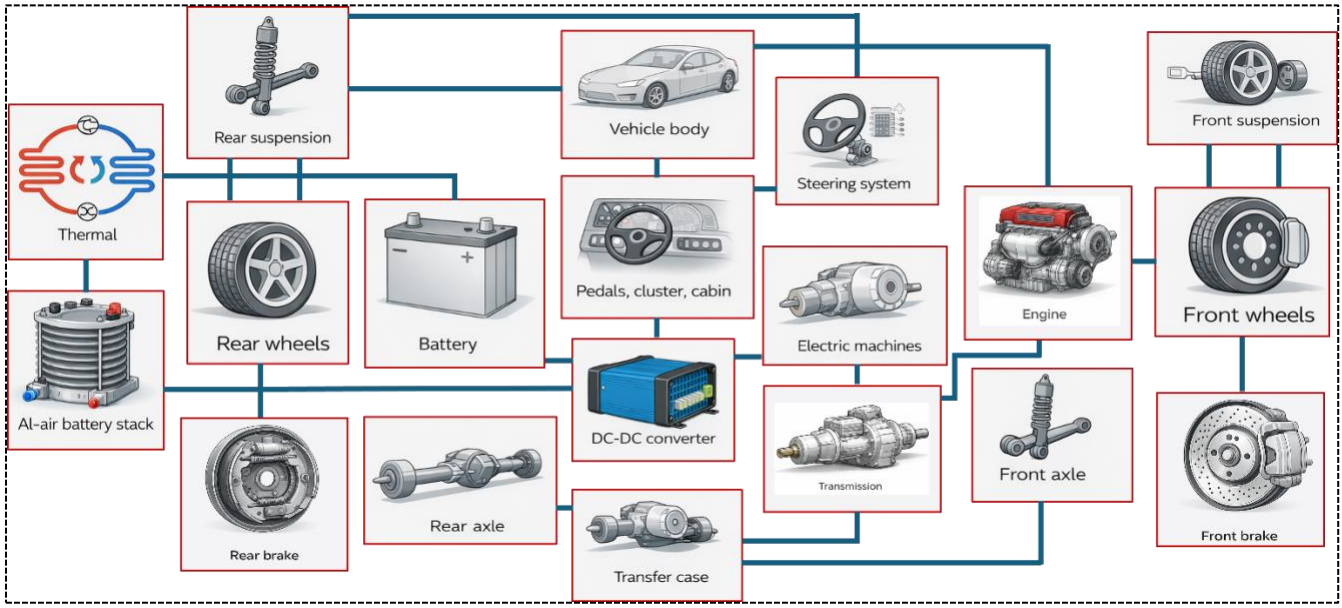


Figure 6. 3: Subsystem-level representation of the baseline BEV model, illustrating the internal powertrain, chassis, and control components implemented within the vehicle model

Figure 6.3 expands upon the high-level architecture shown in Figure 6.2 by detailing the internal structure of the vehicle model subsystem. At this level, the vehicle is decomposed into interacting powertrain, chassis, and control-related components that collectively govern longitudinal vehicle behavior. The Li-ion battery supplies electrical energy to the electric machine through the DC-DC converter and power electronics, enabling torque generation at the drivetrain. Mechanical power is transmitted through the transmission and axle assemblies to the front and rear wheels, while braking systems at each axle provide deceleration and energy dissipation [406].

In parallel, vehicle body dynamics, suspension systems, and wheel-road interactions are represented to capture realistic load transfer and road response effects. The steering system interfaces with the driver command layer to regulate directional control, while auxiliary subsystems, including thermal management, monitor and regulate operating temperatures of key components. Control signals originating from the driver and vehicle controllers propagate through this subsystem hierarchy to coordinate propulsion, braking, and stability functions [407].

This subsystem-level representation enables consistent tracking of energy flow, torque distribution, and vehicle response under transient driving conditions. By explicitly modeling the interactions between electrical, mechanical, and control domains, the framework provides a physics-based foundation for evaluating modifications to the baseline architecture. In subsequent sections, this vehicle model serves as the reference configuration against which the integration of the Al-air battery as a secondary energy source is introduced and assessed.

6.2.1.2 Dual-energy-storage-system

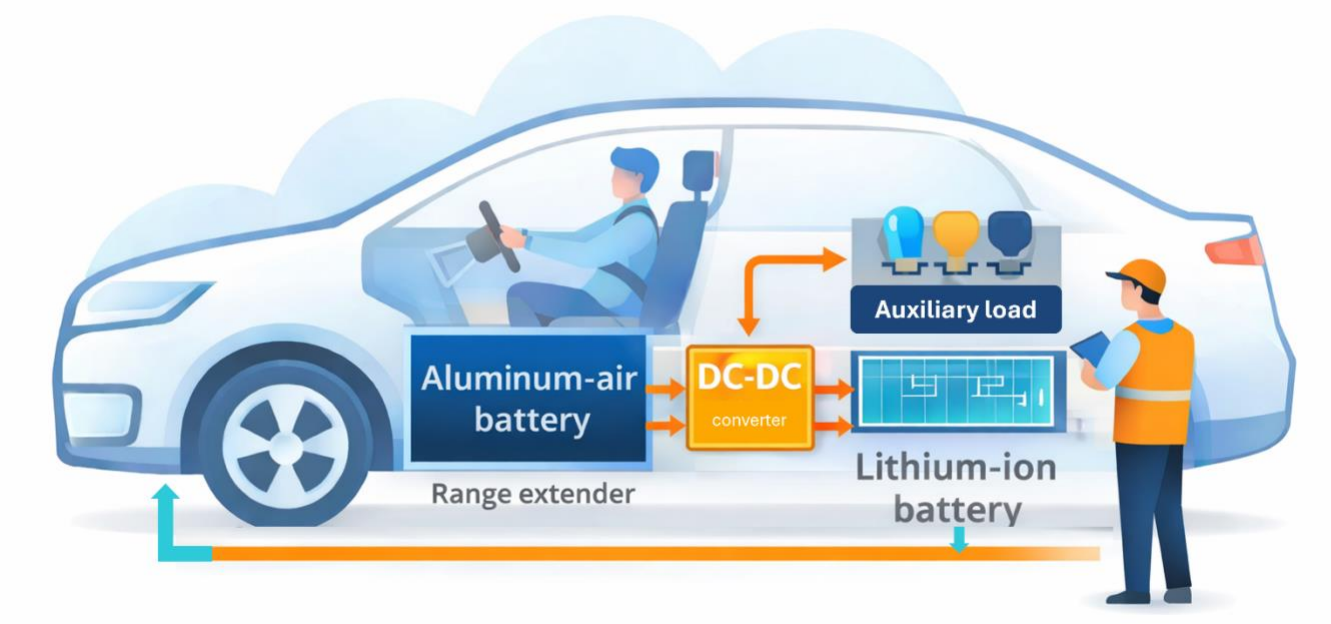


Figure 6. 4: Conceptual architecture of the dual-energy-storage electric vehicle integrating Al-air battery through a DC-DC converter for range-extender and auxiliary power operation

The proposed vehicle architecture extends the baseline BEV by integrating an Al-air battery as a secondary electrochemical energy source alongside the primary Li-ion traction battery. The Li-ion pack remains directly coupled to the electric drivetrain and is responsible for all transient propulsion demands. The Al-air system is connected to the high-voltage bus through a unidirectional DC-DC converter, enabling controlled power transfer without directly driving the traction motor. As illustrated in Figure 6.4, the Al-air battery can supply energy either to recharge the Li-ion pack or to power auxiliary loads, forming a fully electrochemical dual-energy-storage architecture in which high power density and high specific energy functions are separated between the two storage technologies.

Two operational concepts are investigated to evaluate the role of the Al-air battery within this framework. In Concept A, the Al-air system operates as a range extender and is activated when the Li-ion SOC falls below a predefined threshold. In this mode, the Al-air battery supplies charging power to the Li-ion pack via the DC-DC converter, mitigating deep discharge and extending achievable driving range. In Concept B, the Al-air battery functions as a dedicated auxiliary power unit, supplying non-traction loads such as thermal management and cabin systems. This configuration reduces auxiliary demand on the Li-ion battery and isolates traction energy from time-dependent auxiliary consumption.

Both concepts are evaluated under identical vehicle parameters and standardized drive cycles to enable consistent system-level comparison. By varying only the Al-air operating strategy while maintaining the same baseline vehicle model, the framework isolates the influence of architectural integration on energy flow, SOC evolution, aluminum consumption, and overall vehicle performance.

6.2.2 Traction Battery and Al-air Cell-Level Modeling

6.2.2.1 Baseline Traction Battery Description

The baseline traction battery is modeled using lithium iron phosphate (LFP) chemistry to reflect recent trends in commercial electric vehicle deployment. LFP cells typically exhibit a nominal voltage of approximately 3.2-3.3 V per cell, lower than nickel manganese cobalt (NMC) chemistries, but offer improved thermal stability, enhanced safety characteristics, extended cycle life, and reduced material cost due to the absence of cobalt and nickel [408,409]. The cells also have a nominal capacity of 161 Ah. A defining feature of LFP chemistry is its relatively flat open-circuit voltage (OCV) profile across a broad mid-SOC range, with steeper voltage gradients near the upper and lower SOC limits (Figure 6.5). This flat voltage plateau influences SOC estimation and results in stable voltage behavior within moderate operating windows [410-412].

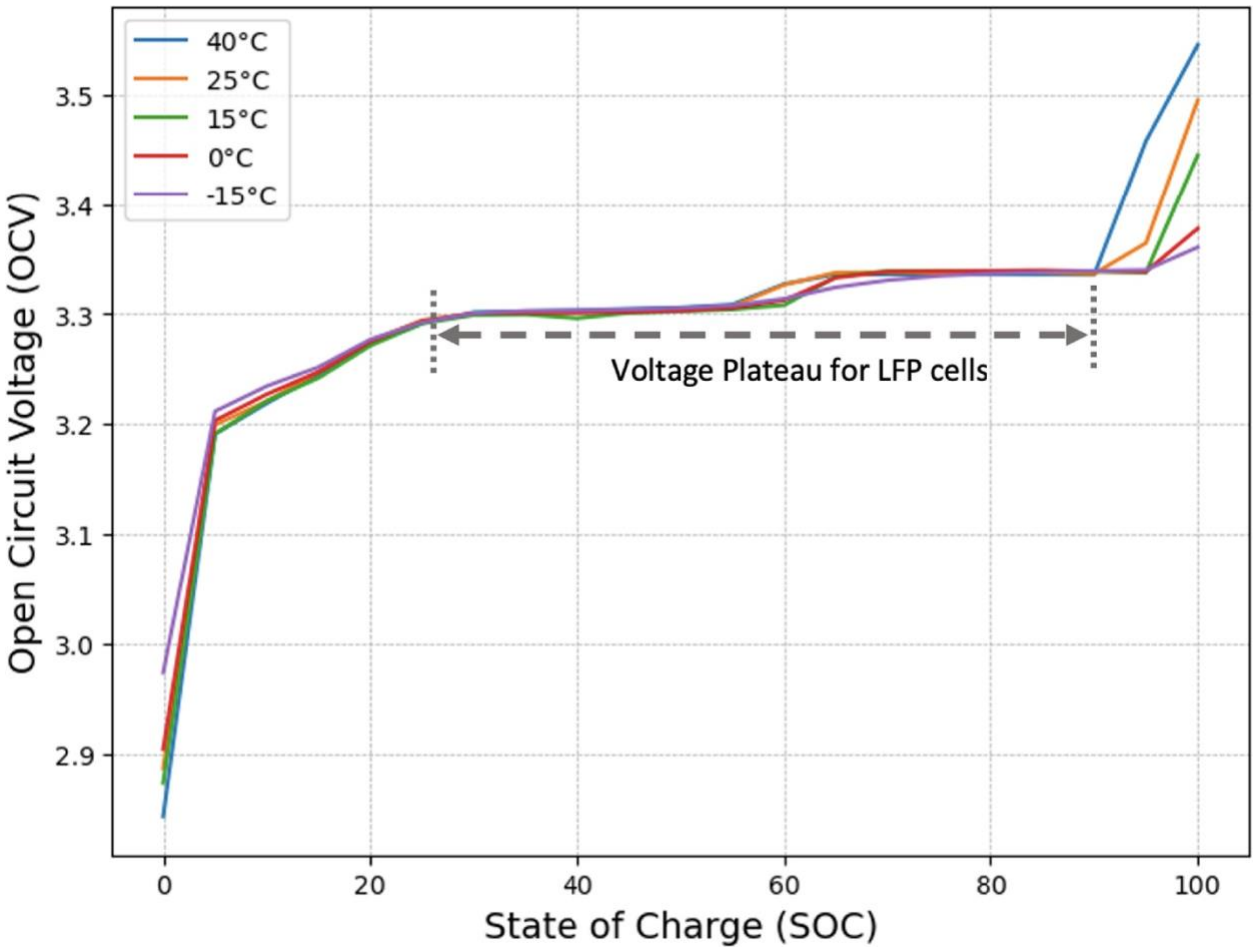


Figure 6. 5: Open circuit voltage-SOC curves of lithium iron phosphate battery at different temperatures. (Adapted from [413])

In the present study, the LFP battery pack is implemented in MATLAB/Simulink using a mapped battery model incorporating an SOC-dependent open-circuit voltage table representation. The pack voltage is determined by the number of cells connected in series (106s), while the energy capacity is scaled through parallel (1p) cell configuration. The model captures terminal voltage, pack current, internal power loss, and SOC evolution under dynamic load conditions. Under typical operating conditions, pack current responds directly to traction power demand and auxiliary loading, with voltage deviations governed by internal resistance and polarization effects. Reduced-capacity configurations are implemented by scaling the parallel cell count, thereby preserving nominal pack voltage while proportionally reducing available energy and peak power capability. This approach enables investigation of power-limited behavior and energy downsizing scenarios while maintaining consistency with realistic LFP electrochemical characteristics.

6.2.2.2 Cell-level polarization-based representation

The steady-state polarization behavior of the Al-air cell was modeled using a semi-empirical voltage loss formulation, calibrated against experimentally measured polarization data obtained in 6 M KOH at 40 °C. The experiments were conducted using a circulating electrolyte configuration with a rotating aluminum anode, an anode-cathode distance of 1.5 mm, and a geometric electrode area of 44.18 cm^2. Current density was varied from open circuit to 200 mA cm^{-2}, and the corresponding cell voltage was recorded under quasi-steady conditions [308]. The experimental polarization curve exhibits three distinct regimes. First, an abrupt voltage drop occurs immediately upon application of load, with the cell voltage decreasing from an open-circuit value of 1.469 V to 1.282 V at 20 mA cm^{-2}. This behavior indicates the presence of instantaneous losses associated with mixed electrode potentials, contact resistances, interfacial film formation, and rapid activation of parasitic reactions, which are not captured by classical activation or ohmic terms alone. Second, a near-linear voltage decrease is observed over the intermediate current density range of approximately 20 to 140 mA cm^{-2}, indicating that the dominant losses in this regime are well represented by a combination of activation overpotential and ohmic resistance. Finally, a sharp voltage collapse occurs beyond approximately 160 mA cm^{-2}, with the voltage falling to 0.263 V at 200 mA cm^{-2} [414,415]. This high-current behavior is characteristic of mass-transport and surface-coverage limitations in Al-air systems, arising from hydroxide depletion, aluminate accumulation, and hydrogen bubble coverage at the anode surface (Figure 6.6).

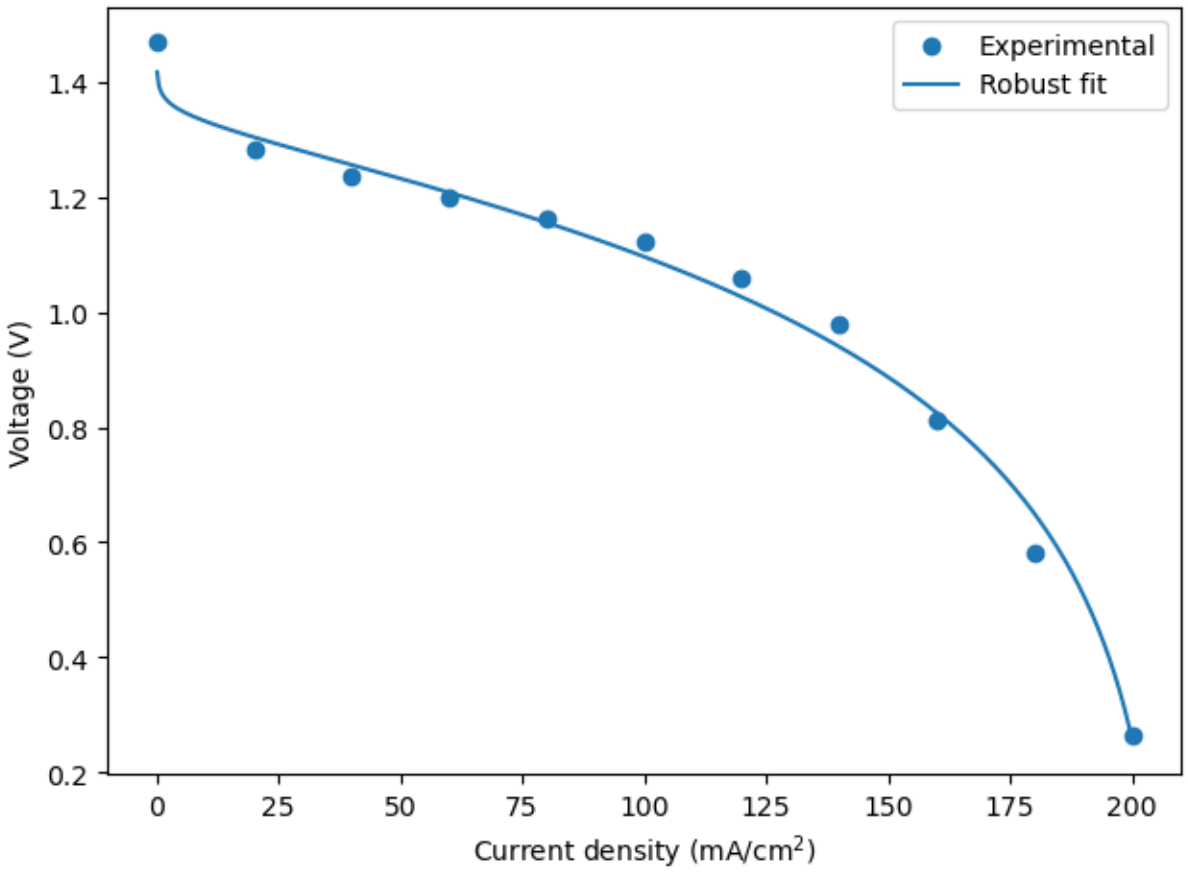


Figure 6. 6: Comparison of experimental polarization data and semi-empirical robust model fit for the Al-air cell (6 M KOH, 40 °C)

To accurately reproduce all three regimes within a single continuous formulation, the cell voltage was modeled as [416],

$$V(j) = V_{OC} - V_{\text{loss},0} - a\ln(j) - jR_0 - B\ln\left(1-\frac{j}{j_L}\right) \tag{6.1}$$

where j is the current density in A cm^{-2}. The individual terms represent distinct physical contributions:

- V_{OC} is the experimentally measured open-circuit voltage.
- $V_{\text{loss},0}$ is an instantaneous voltage loss term accounting for mixed potential effects, contact resistances, and rapid interfacial changes that occur immediately upon current drawing.

- $a\ln(j)$ represents an effective activation overpotential in Tafel form, capturing the logarithmic dependence of kinetic losses on current density.
- jR_0 is the baseline area-specific ohmic loss, encompassing electrolyte resistance across the anode-cathode gap and electronic resistances.
- $B\ln(1-j/j_L)$ is a concentration overpotential term that captures the rapid voltage decline as the current density approaches a limiting value j_L.

This formulation is widely used in metal-air and fuel-cell system modeling when a balance between physical interpretability and high-fidelity curve fitting is required, particularly for integration into system-level simulations.

The open-circuit voltage V_{OCV} was fixed at 1.469 V based on direct experimental measurement. All remaining parameters were estimated using nonlinear least-squares regression applied to the polarization data for $j > 0$. A robust loss function and a multi-start optimization strategy were employed to prevent convergence to unphysical parameter limits and to ensure stable identification of the governing loss mechanisms across the full current density range. The quality of fit was evaluated using the coefficient of determination R^2, calculated from the measured and predicted voltages over all loaded data points.

The optimized model parameters are summarized in Table 6.1. The fitted instantaneous loss $V_{\text{loss},0} = 0.1902$ V closely matches the experimentally observed voltage drop between open circuit and the first loaded point, confirming the necessity of this term for Al-air systems. The activation coefficient $a = 0.0150$ V provides an effective description of kinetic losses over the intermediate current range. The baseline area-specific resistance $R_0 = 0.0500$ Ω cm^2 corresponds to an effective electrolyte conductivity of 3.00 S cm^{-1} when combined with the measured anode-cathode distance, consistent with a highly conductive alkaline electrolyte under forced circulation.

Table 6. 1: Parameters for Al-air polarization curve model (6 M KOH, 40 °C, rotating anode, circulating electrolyte).

Parameter	Symbol	Unit	Value
Open-circuit voltage	(V_{OCV})	V	1.469
Universal gas constant	(R)	$J.mol^{-1}. K^{-1}$	8.314
Temperature	(T)	K	313.15
Faraday constant	(F)	$C.mol^{-1}$	96485
Instantaneous voltage loss (mixed potential, contact, initial IR)	($V_{loss,0}$)	V	0.1902
Activation coefficient (logarithmic term)	(a)	V	0.0150
Baseline area-specific resistance	(R_0)	Ω.cm²	0.0500
Anode-cathode distance	(L)	cm	0.15
Effective electrolyte conductivity ((\sigma = L / R_0))	(σ)	$S.cm^{-1}$	3.00
Concentration loss coefficient	(B)	V	0.3253
Limiting current density	(j_L)	$mA.cm^{-2}$	208.66
Electrode geometric area	(A)	cm²	44.18
Coefficient of determination	(R^2)	-	0.9903

The concentration overpotential parameters $B = 0.3253\text{V}$ and $j_L = 208.66\text{mA cm}^{-2}$ accurately reproduce the sharp voltage collapse observed experimentally at high current densities. The resulting model achieves an excellent fit to the data, with a coefficient of determination $R^2 = 0.9903$. The proposed semi-empirical polarization model captures the full operating behavior of the Al-air cell across activation-dominated, ohmic-dominated, and transport-limited regimes within a single continuous expression. Unlike purely mechanistic formulations, the inclusion of an instantaneous loss term and a concentration overpotential enables accurate reproduction of experimentally observed voltage discontinuities and high-current collapse without resorting to piecewise fitting.

As a result, the model is particularly well suited for implementation in system-level simulations, including range-extender and auxiliary power studies, where accurate voltage prediction over a wide current range is critical for power management, efficiency estimation, and energy consumption analysis.

6.2.2.3 Cell and Stack scaling methodology

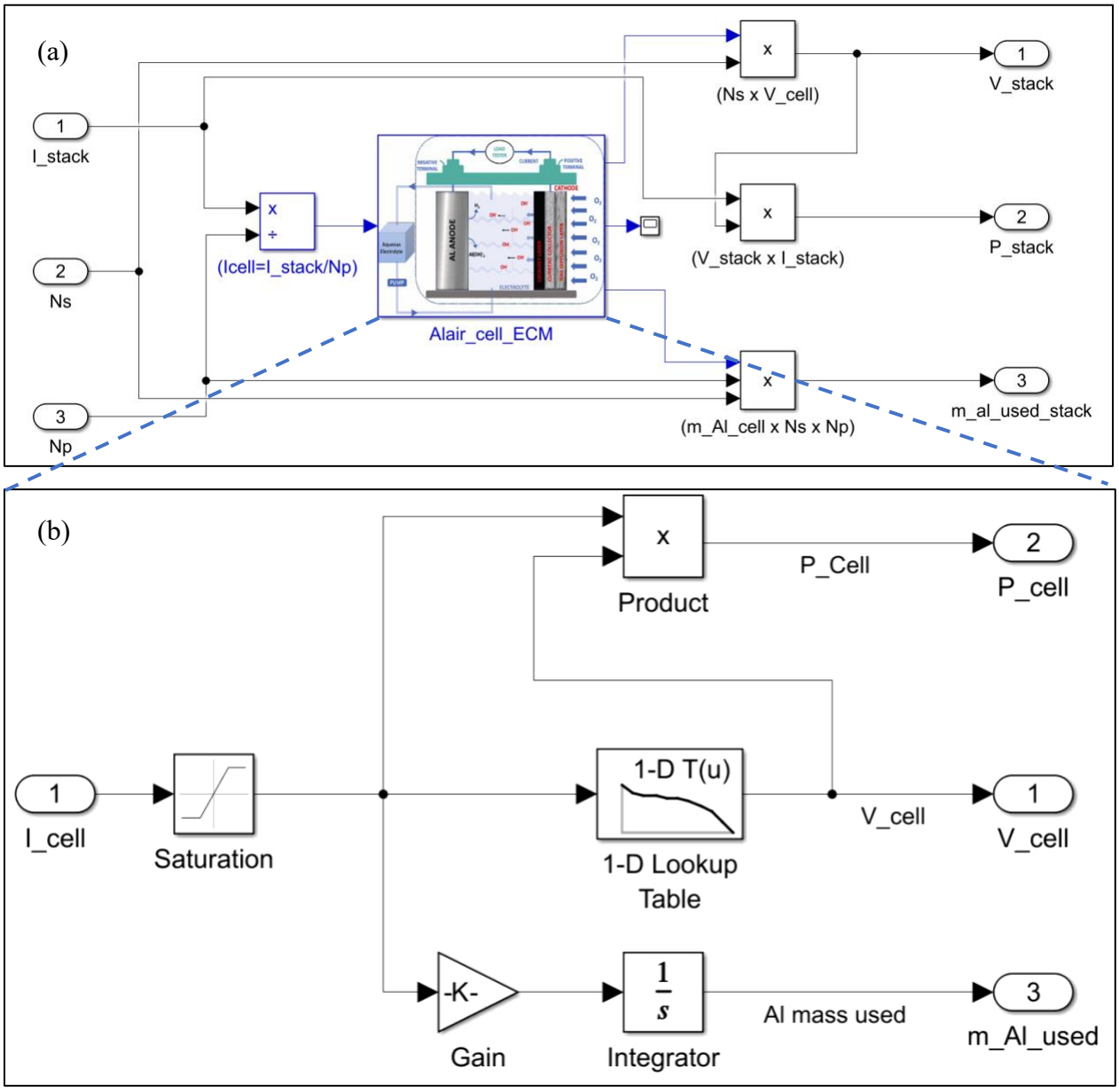


Figure 6. 7: Al-air stack model (a) and the single-cell model (b) with aluminum consumption tracking

The sub-block (Figure 6.7) implements a first-pass, polarization-based equivalent circuit representation of a single Al-air cell, coupled with a physically consistent aluminum consumption tracking model. The input to the block is the cell current, I_{cell}, which is first passed through a saturation block to enforce physically meaningful operating limits corresponding to the

experimentally characterized current density range of the 38 cm aluminum disk. This prevents extrapolation beyond the validated polarization data and ensures numerical robustness.

The saturated current is then supplied to a one-dimensional lookup table that represents the experimentally measured polarization behavior of the Al-air cell. The lookup table maps cell current directly to cell voltage, V_{cell}, implicitly capturing activation, ohmic, and mass-transport losses at a fixed electrolyte concentration and temperature. This approach mirrors the simplifications commonly adopted in metal-air system-level studies, where voltage is assumed to be a function of current (or current density) and independent of SOC over a restricted operating window.

The instantaneous electrical power delivered by the cell is computed using a product block as

$$P_{\text{cell}} = V_{\text{cell}} \cdot I_{\text{cell}} \tag{6.2}$$

and is provided as an output for subsequent pack-level scaling and energy flow calculations. This structure allows the same single-cell model to be reused for different series and parallel configurations by simple algebraic scaling at the pack level. The pack-level energy capacity of the Al-air system is estimated from the specific energy of aluminum, taken as 2.299 kWh kg^{-1}, corresponding to the theoretical electrochemical energy associated with the three-electron oxidation reaction [417]. To account for system-level losses, including polarization losses, DC-DC conversion inefficiencies, and incomplete aluminum utilization, a net electrical efficiency factor of 0.7 is applied. The effective usable energy is therefore calculated as

$$E_{\text{usable}} = m_{\text{Al}} \times 2.299 \times 0.7\text{kWh} \tag{6.3}$$

where $m_{\text{Al}}$is the initial aluminum mass in kilograms. This assumption yields an effective system-level specific energy of approximately 1.61 kWh kg^{-1}, which is used to size the Al-air pack and to estimate achievable range extension under each drive cycle. The 70% efficiency factor reflects conservative integration losses and ensures that projected vehicle range remains physically realistic rather than based on ideal electrochemical limits [418].

For the selected 100s1p configuration, each aluminum disk has a diameter of 38 cm and a thickness of 0.5 mm. The mass of a single disk is calculated from its geometric volume and the

density of aluminum. The disk radius is 0.19 m and the thickness is 0.5 mm, giving a volume per disk of

$$V = \pi r^2 t = \pi(0.19)^2(0.0005) \approx 5.67 \times 10^{-5}\ \text{m}^3 \tag{6.4}$$

Using an aluminum density of 2700 kg m^{-3}, the mass of one disk is,

$$m_{\text{disk}} = 2700 \times 5.67 \times 10^{-5} \approx 0.153\ \text{kg} \tag{6.5}$$

For 100 disks in series, the total initial aluminum mass is therefore approximately 15.3 kg. This corresponds to an effective system-level specific energy of approximately 1.61 kWh kg^{-1}. The resulting Al-air stack therefore provides roughly 24-25 kWh of usable electrical energy under realistic operating assumptions which translate to 14-15 kW of power, which is comparable to a mid-sized EV traction battery module and represents a physically plausible range-extension capacity without excessive mass or volume.

6.2.2.4 Aluminum consumption tracking

In parallel with the electrical calculations, the model tracks aluminum consumption based on Faraday's law, implemented in an equivalent specific-capacity form that is convenient for system-level simulation. The aluminum mass consumption rate is computed as

$$\dot{m}_{\text{Al}} = \frac{I_{\text{cell}}}{Q_{\text{theory}}\,\eta_{\text{util}}\,3600} \tag{6.6}$$

where $Q_{\text{theory}} \approx 2980$ Ah $\text{kg}^{-1}$is the theoretical specific capacity of aluminum for a three-electron oxidation reaction, and $\eta_{\text{util}}$is an effective utilization factor that accounts for parasitic corrosion, incomplete utilization, and non-ideal electrochemical efficiency. This formulation is mathematically equivalent to the classical Faraday expression $\dot{m} = IM/(nF\eta)$, but is more convenient for implementation in time-domain battery models.

The gain block converts the electrical current directly into a mass flow rate, $\dot{m}_{\text{Al}}$(kg s^{-1}), which is then integrated over time to yield the cumulative aluminum mass consumed,

$$m_{\text{Al,used}}(t) = \int_0^t \dot{m}_{\text{Al}}(\tau)\, d\tau \tag{6.7}$$

The utilization factor is calibrated using experimentally measured aluminum mass loss under constant-current discharge, ensuring consistency between the model and laboratory observations. This enables the Al-air system to be treated as a fuel-limited energy source whose remaining capacity is directly linked to the available aluminum mass, rather than to an abstract electrochemical state-of-charge.

6.2.3 Energy Management and Control Strategy

The proposed vehicle architecture adopts a dual energy storage system in which a Li-ion battery serves as the primary traction energy source, while an Al-air battery system is integrated as a secondary energy source operating in a range-extender mode. In this configuration, the Al-air system does not directly supply traction power to the electric drivetrain. Instead, it is coupled to the high-voltage bus through a unidirectional DC-DC converter and is used exclusively to recharge the Li-ion battery during operation. The overall energy management strategy is therefore formulated around two coupled objectives. First, the Li-ion battery SOC is regulated within a bounded operating window to avoid deep discharge while minimizing unnecessary cycling. Second, the Al-air system is enabled only when sufficient aluminum fuel remains, thereby ensuring physically meaningful energy accounting and realistic range-extender operation.

6.2.3.1 Al-air enable control logic

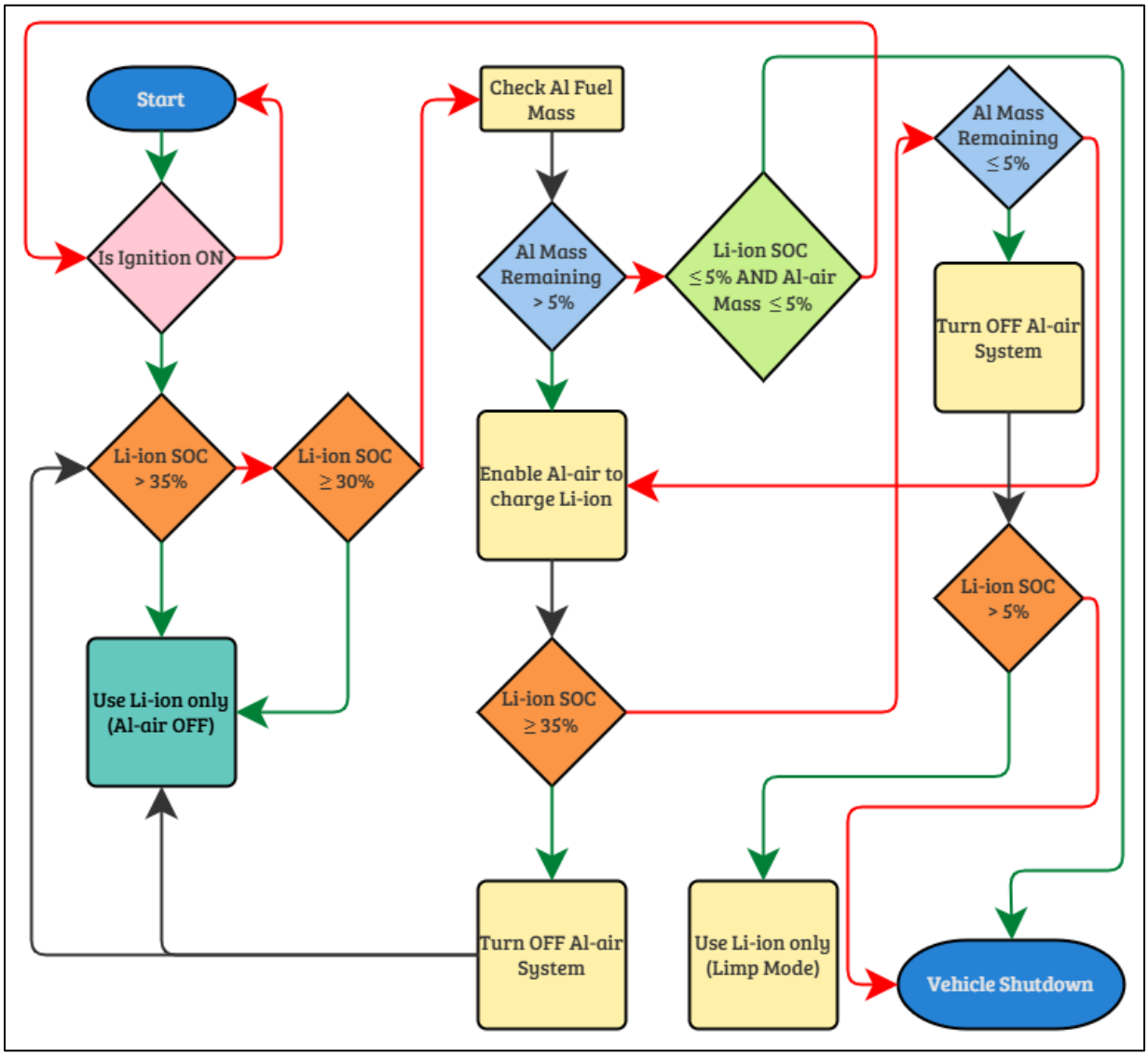


Figure 6. 8: Control logic and operational flowchart for the Al-air range extender integrated with the Li-ion battery system based on SOC thresholds and aluminum fuel availability

Under Concept A of using Al-air battery as a range extender, the Al-air battery is activated only when the Li-ion battery SOC falls below a lower threshold, and it remains active until the SOC recovers beyond an upper threshold. This hysteresis-based strategy prevents frequent on-off switching and provides stable power flow through the DC-DC converter. The control logic and operational flow chart used is shown in Figure 6.8.

In the present study, the Li-ion SOC threshold is selected as 30% for activation and 35% for deactivation. These values are chosen to represent a conservative lower operating region of the Li-ion battery, ensuring that the range-extender engages before significant depth-of-discharge (DOD) is reached, while allowing sufficient recovery before disengagement. The hysteresis band of 5% balances responsiveness and stability, particularly under transient driving conditions such as urban dynamometer driving schedule (UDDS) and highway fuel economy test (HWFET) cycles.

SOC-based logic is implemented in Simulink using a latch-type structure composed of relational operators, logical operators, and a unit delay block. As illustrated in the lower portion of the attached Simulink control diagram (Figure 6.9), the Al-air enable signal is set high when the Li-ion SOC falls below 0.30. Once enabled, the signal is latched and maintained until the SOC exceeds 0.35, at which point the Al-air system is disabled. This structure ensures deterministic behavior and avoids chattering near the threshold values.

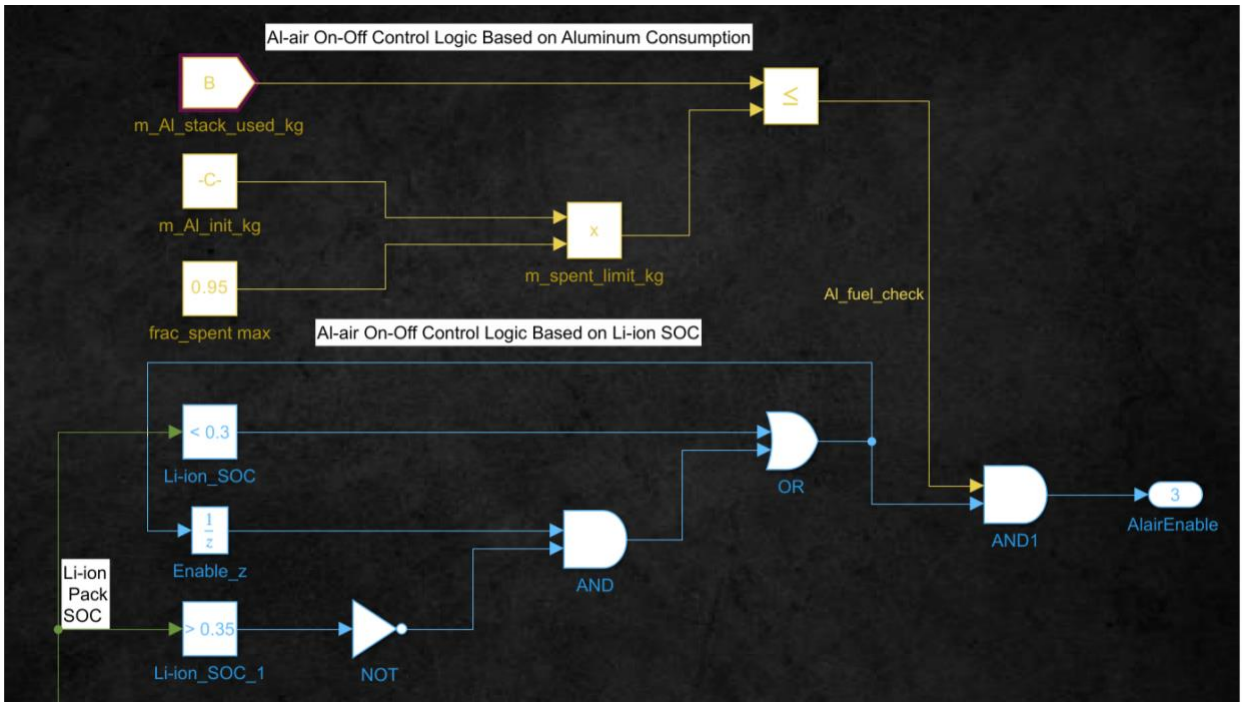


Figure 6. 9: Simulink implementation of the Al-air enable-disable control logic based on Li-ion SOC thresholds and aluminum fuel availability constraints

Unlike electrochemically rechargeable batteries, Al-air systems are mechanically rechargeable, with energy replenishment achieved through physical replacement of the aluminum anode and replenishment of electrolyte. Recent industrial developments, inspired by systems such

as those proposed by Alumapower [225,419], suggest rapid disk-replacement mechanisms and simplified electrolyte handling processes that significantly reduce service downtime. These advances motivate a control philosophy in which aluminum is treated as a consumable fuel rather than as a permanently embedded electrode. Accordingly, the Al-air enable logic is augmented with a fuel availability constraint based on the cumulative aluminum mass consumed during operation. Aluminum consumption is calculated directly from Faraday's law within the Al-air cell model and is scaled by the number of series and parallel cells to represent total pack-level consumption. The remaining aluminum mass is then inferred from the initial aluminum inventory.

To ensure realistic operation, the Al-air system is disabled once the remaining aluminum mass falls below 5% of the initial available mass. This reserve margin avoids numerical instability near complete depletion and reflects practical considerations associated with mechanical disk replacement. The resulting fuel availability signal is implemented using a relational operator that compares the cumulative aluminum mass consumed with a predefined consumption limit corresponding to 95% utilization. The final Al-air enable signal is obtained by logical AND Boolean and the SOC-based enable signal with the aluminum fuel availability flag. This structure ensures that Al-air operation is permitted only when both conditions are satisfied, namely when the Li-ion SOC is within the activation window and when sufficient aluminum fuel remains. The combined logic is clearly depicted in the attached control diagram, where the SOC-based latch is gated by the aluminum mass-based fuel check.

6.2.3.2 DC-DC Integration and Power Flow Logic

The Al-air battery is interfaced with the Li-ion battery through a unidirectional DC-DC converter operating under power-controlled mode. When enabled, the Al-air system supplies electrical power to the DC-DC converter, which regulates the charging delivered to the Li-ion battery based on the instantaneous battery voltage. This approach decouples the Al-air operating voltage from the Li-ion pack voltage and ensures compatibility across varying states of charge. In the Simulink implementation, the Al-air enables signal directly gates the current command applied to the Al-air stack. When disabled, the commanded stack current is forced to zero, resulting in zero electrical power output and zero aluminum consumption. This gating strategy guarantees internal consistency across the electrochemical, electrical, and mass-balance models, and prevents

unphysical aluminum consumption when the range-extender is inactive. Power limits imposed by the DC-DC converter are explicitly enforced through saturation blocks, ensuring that the Al-air system operates within converter rating constraints. The resulting power flow logic reflects realistic vehicle integration scenarios and allows systematic evaluation of Al-air contribution under different auxiliary and traction load conditions.

6.2.3.3 Auxiliary-load-driven operation (Concept B)

Under Concept B, the Al-air battery operates as an auxiliary power unit (APU) that supports the traction battery through a DC-DC interface. In this configuration, the Al-air stack does not directly drive the traction motor. Instead, it supplies electrical power to the Li-ion battery via a controlled DC-DC converter connected to the low-voltage busbar, thereby offsetting auxiliary and secondary electrical loads that would otherwise be drawn from the traction battery. This architecture preserves the Li-ion pack as the sole propulsion energy source while reducing its net discharge rate under sustained auxiliary demand.

For the APU configuration, a 104s1p Al-air stack is adopted to achieve a pack voltage compatible with the vehicle electrical bus while maintaining practical system dimensions. At the selected operating current density, this configuration delivers approximately 15 kW of peak electrical power, sufficient to cover high auxiliary demand scenarios *(See Section 3.2)* and provide supplemental charging support. Based on a 38 cm diameter aluminum disk with 0.5 mm thickness per cell, the total initial aluminum mass for the 104-cell stack is approximately 16 kg. Using an effective system-level specific energy of approximately 1.61 kWh kg^{-1}, derived from the theoretical aluminum energy density with a 0.7 efficiency factor, the usable electrical energy of the APU configuration is approximately 26 kWh.

To ensure physically realistic operation and avoid numerical instability near full depletion, the Al-air system is disabled when the remaining aluminum mass reaches 5% of the initial value. This cutoff represents a practical mechanical replacement threshold and ensures that the APU operates within a conservative utilization window. The resulting control strategy allows the Al-air battery to function as a fuel-limited auxiliary energy source while maintaining consistent energy accounting within the dual-energy-storage framework.

6.2.4 Simulation Setup and Scenarios

To ensure comprehensive performance assessment, the vehicle was evaluated under four standardized regulatory drive cycles: UDDS, FTP-75, HWFET, and WLTP. These cycles represent distinct driving conditions and collectively capture a wide spectrum of real-world operating profiles.

The UDDS characterizes low-speed urban operation with frequent acceleration and deceleration events, short cruising intervals, and extended idle periods. It is particularly useful for evaluating transient loading behavior, regenerative braking effectiveness, and dynamic current oscillations within the battery pack. The federal test procedure (FTP-75) extends the UDDS framework by incorporating additional cold-start and transient phases, providing a more comprehensive representation of urban driving emissions and energy consumption. Although similar in structure to UDDS, FTP-75 introduces additional variability in transient intensity and cycle duration [420,421]. The HWFET represents steady-state highway driving conditions with higher average vehicle speeds and smoother acceleration patterns. This cycle is critical for assessing sustained power demand, steady discharge behavior, and long-duration thermal loading of the battery pack. The worldwide harmonized light vehicles test procedure (WLTP) incorporates a broader range of operating conditions, including low-, medium-, high-, and extra-high-speed segments. Compared to earlier regulatory cycles, WLTP exhibits greater dynamic variability and higher peak speed demands, thereby offering a more representative approximation of modern real-world driving behavior [422,423].

For each drive cycle, the vehicle model was operated in closed-loop speed control mode, wherein the driver block tracks the prescribed reference speed profile. Battery pack voltage, current, power, and internal power loss were recorded for subsequent analysis. Vehicle speed tracking performance was monitored to ensure adherence to the target cycle, particularly under reduced-capacity battery scenarios where power limitations may arise. This baseline simulation framework establishes the reference electrical and vehicle-level performance metrics necessary for evaluating battery downsizing effects and the integration of the Al-air range extender architecture in subsequent sections.

6.2.4.1 Initial SOC and Range

The baseline vehicle range was determined using an energy-based approach derived from the total battery discharge energy and the corresponding distance traveled over each driving cycle. The total chemical energy withdrawn from the Li-ion pack was calculated by integrating the instantaneous battery discharge power over time, including internal resistive losses, such that [424]

$$E_{\text{batt}} = \frac{1}{3600}\int_0^T (P_{\text{batt}}(t) + P_{\text{loss}}(t))\, dt \tag{6.8}$$

where $P_{\text{batt}}(t)$is the terminal battery power, $P_{\text{loss}}(t)$represents internal power loss, and $T$is the cycle duration. The total distance traveled during the cycle was computed as [425]

$$D = \int_0^T v(t)\, dt \tag{6.9}$$

where $v(t)$denotes the vehicle speed. The specific energy consumption was then obtained as [426]

$$\text{Wh/km} = \frac{E_{\text{batt}} \times 1000}{D} \tag{6.10}$$

and the full-cycle vehicle range was estimated by scaling this consumption with the usable battery energy E_{usable} [427],

$$\text{Range} = \frac{E_{\text{usable}}}{\text{Wh/km}} \tag{6.11}$$

This methodology ensures that the calculated range reflects the total electrochemical energy depletion of the battery pack under each prescribed driving cycle.

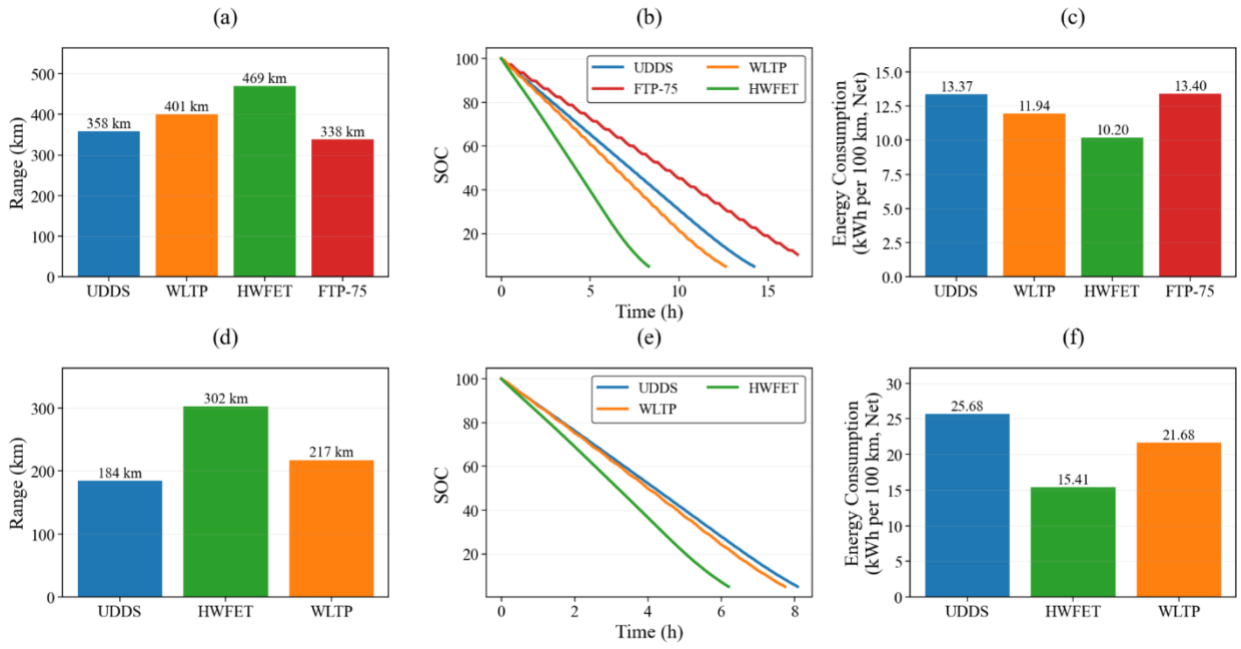


Figure 6. 10: Comparative performance of baseline and auxiliary electric vehicle configurations under standard driving cycles: range, SOC evolution, and energy consumption

Figure 6.10 confirms that electric vehicle performance is strongly influenced by driving cycle characteristics. Under the baseline configuration, the HWFET cycle yields the highest range (469 km) and lowest specific energy consumption (10.20 kWh per 100 km), while the urban-intensive UDDS and FTP-75 cycles exhibit higher consumption and reduced range. The smoother velocity profile and lower transient loading in highway operation reduce resistive and dynamic losses, resulting in improved overall efficiency. The SOC depletion profiles further support this observation. Under highway conditions, SOC decreases more gradually, reflecting lower average power demand. In contrast, frequent acceleration and deceleration events in urban cycles increase instantaneous current draw and cumulative energy losses, leading to faster SOC depletion.

For the auxiliary configuration, the apparent increase in specific energy consumption, particularly under UDDS, may initially appear counterintuitive. However, this effect is primarily mathematical rather than physical. Energy consumption expressed in kWh per 100 km is normalized by distance. When total achievable distance decreases due to reduced battery capacity, even modest differences in absolute energy usage can lead to a disproportionately larger kWh per 100 km value. Thus, the increase in specific consumption under the auxiliary configuration reflects

distance normalization effects combined with higher relative internal resistance losses at reduced capacity, rather than a fundamental deterioration in drivetrain efficiency.

Additionally, the relatively small range difference between UDDS and FTP-75 in the baseline configuration warrants clarification. Although FTP-75 is formally temperature-dependent and includes cold-start characteristics, the present simulations were conducted without thermal variation. Ambient temperature and battery thermal behavior were held constant, and no additional cold-start penalties were modeled. Consequently, the expected temperature-induced efficiency differences inherent to FTP-75 are not captured in this study, leading to performance results that closely resemble those of UDDS. For the UDDS cycle with a duration of 1369 s, the total battery discharge energy was 50.422 kWh, of which 2.531 kWh was recovered through regenerative braking, resulting in a net battery energy consumption of 47.891 kWh. For the WLTP cycle with a duration of 1800 s, the corresponding discharge energy was 49.795 kWh, with 1.931 kWh recovered via regeneration, yielding a net battery energy consumption of 47.864 kWh. The near-identical net energy consumption in the two cases, differing by less than 0.03 kWh, indicates that the overall energetic demand of the two cycles is comparable for the modeled vehicle and powertrain configuration. Despite the similarity in net battery energy consumption, the extrapolated driving range differs significantly, with approximately 360 km obtained for UDDS and 400 km for WLTP. This difference is attributed primarily to the longer duration and higher average speed of the WLTP cycle, which results in a greater distance covered per cycle for nearly the same net energy expenditure. In other words, while the UDDS cycle exhibits slightly higher regenerative energy recovery due to its more frequent stop-and-go nature, the increased distance traveled during the WLTP cycle leads to a lower effective energy consumption per kilometer. Consequently, the higher WLTP-based range does not reflect a fundamental improvement in vehicle efficiency but rather arises from the inherent characteristics of the drive cycle, particularly its speed profile and total distance covered for a given energy input. Overall, the findings emphasize two key system-level insights. First, driving cycle aggressiveness significantly affects energy consumption and range. Second, reduced battery capacity magnifies distance-normalization effects in specific energy metrics. These considerations are critical when evaluating auxiliary or hybrid energy storage architectures, particularly when interpreting kWh per 100 km as a comparative performance metric across different capacity configurations.

6.2.4.2 Drive cycle and Battery Pack Characteristics

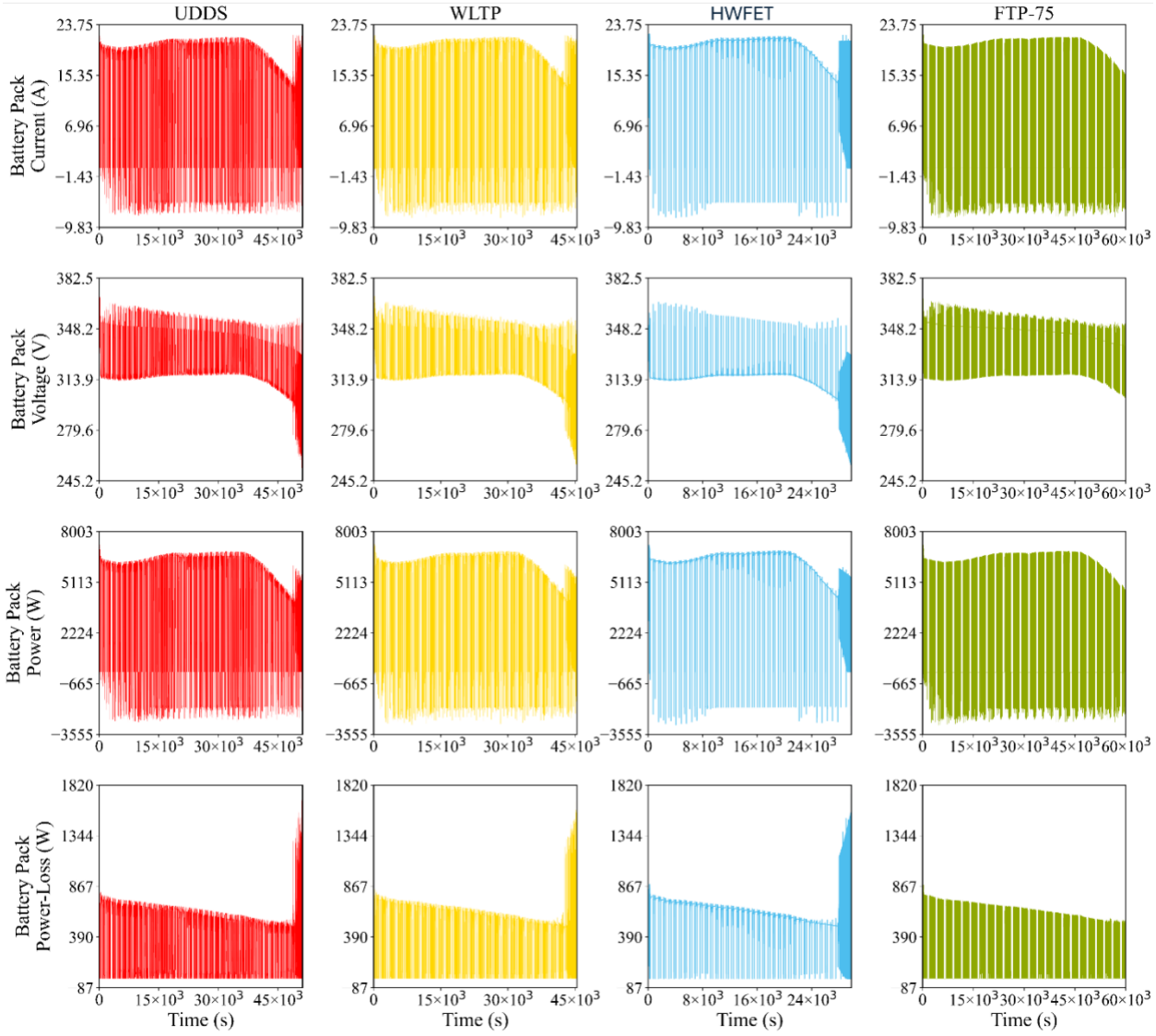


Figure 6. 11: Baseline Li-ion battery pack electrical response under standard driving cycles (UDDS, WLTP, HWFET, FTP-75)

Figure 6.11 presents the baseline Li-ion battery pack response under four standard driving cycles, namely UDDS, WLTP, HWFET, and FTP-75. The multi-panel layout illustrates battery pack current, voltage, power, and internal power loss as functions of time for each cycle. The results provide a comparative view of how distinct driving profiles influence battery loading characteristics, dynamic response, and energy dissipation behavior. The battery current profiles exhibit clear cycle-dependent characteristics. The UDDS and FTP-75 cycles show frequent high-amplitude current oscillations associated with repeated acceleration and deceleration events typical

of urban driving. The WLTP profile demonstrates moderate but sustained current demand, reflecting its mixed driving structure. In contrast, the HWFET cycle exhibits comparatively smoother and more sustained current behavior, consistent with steady highway operation. Peak current magnitudes are broadly similar across cycles, but the temporal distribution of current demand differs significantly, with urban cycles producing more transient spikes.

The battery voltage trends inversely follow current demand, as expected from internal resistance effects. Under higher discharge currents, voltage drops are more pronounced, particularly during aggressive acceleration segments in UDDS and FTP-75. The HWFET cycle maintains a relatively stable voltage profile over most of the duration, with gradual decline toward the end, indicating sustained but less transient loading. The observed voltage depression during high-power intervals confirms the dominant influence of internal ohmic and polarization effects under dynamic conditions. Battery pack power traces reflect the combined influence of current demand and voltage variation. Urban-oriented cycles generate highly fluctuating power profiles with frequent high positive discharge peaks and regenerative events. The HWFET cycle produces comparatively smoother power demand, with sustained discharge levels during steady cruising. Maximum discharge power levels appear comparable across cycles, but urban cycles demonstrate greater intermittency and higher instantaneous variability.

The battery power-loss profiles reveal the internal resistive dissipation behavior. Power losses increase with discharge current magnitude, consistent with quadratic current dependence. Urban cycles exhibit larger transient loss peaks due to repeated high-current events, whereas HWFET demonstrates more gradual variation in internal losses. Notably, the end-of-cycle regions show elevated loss spikes corresponding to higher instantaneous discharge events and lower terminal voltages. Overall, the results demonstrate that urban and transient-heavy driving cycles impose higher dynamic stress on the battery pack, characterized by frequent current oscillations, deeper voltage excursions, and larger instantaneous internal losses. In contrast, highway operation induces smoother but sustained loading. These distinctions have direct implications for thermal management, degradation assessment, and energy efficiency evaluation in subsequent range-extender and downsizing studies.

6.2.5 Auxiliary Power Demand

Auxiliary power demand in electric vehicles arises from non-traction electrical consumers, including cabin heating, ventilation, and air-conditioning systems, thermal management of the battery and power electronics, cooling pumps and fans, lighting, infotainment, sensors, and onboard control electronics. In contrast to traction power, which scales strongly with vehicle speed and driving dynamics, auxiliary loads are primarily time-dependent and persist regardless of vehicle motion. As a result, auxiliary power consumption can impose a disproportionate penalty on vehicle energy use, particularly during low-speed or stop-and-go operation and plays a critical role in determining effective driving range [428].

In conventional internal combustion engine vehicles, auxiliary electrical loads are supplied by an alternator driven by the engine, effectively decoupling auxiliary power demand from traction energy storage. In battery electric vehicles, however, all auxiliary loads are typically supplied via a DC-DC converter from the traction battery, directly reducing the energy available for propulsion. Reported values in the literature indicate that baseline non-HVAC auxiliary loads, comprising electronics, control units, pumps, and lighting, generally fall in the range of 0.2-0.5 kW. Cabin air-conditioning under moderate to hot ambient conditions typically requires 1-3 kW on average, while cabin heating can impose substantially higher demands of approximately 2-6 kW, particularly for vehicles employing resistive heating in cold climates as listed in Table 6.2. Consequently, many system-level EV studies represent auxiliary power demand using an equivalent constant load to capture its cumulative impact on energy consumption and range [429-431].

Table 6. 2: Representative auxiliary power demands reported in the literature [432,433].

Auxiliary load category	Typical reported range	Representative use case
Non-HVAC electronics and controls	0.2-0.5 kW	ECUs, sensors, lighting, pumps
Cabin air-conditioning (cooling)	1-3 kW (average)	Moderate to hot ambient conditions
Cabin heating	2-6 kW	Cold climates, resistive heating
Common values in system-level EV studies	0.5-2 kW	Nominal operating assumptions
Adopted value in this study	3.0 kW	High-end, worst-case average auxiliary load

Motivated by this architectural coupling between auxiliary power demand and traction energy in battery electric vehicles, this study proposes an alternative system-level concept in which a metal-air battery, specifically an Al-air battery, is employed as a dedicated auxiliary power unit. In this configuration, the Al-air system supplies electrical power exclusively to non-traction loads through a dedicated DC-DC interface, thereby offloading auxiliary energy demand from the Li-ion traction battery. This approach leverages the high specific energy and fuel-like characteristics of metal-air batteries while avoiding the need for high transient power capability, which is not required for auxiliary loads. To examine a conservative and practically relevant operating condition, a constant auxiliary load of approximately 3 kW is adopted. This value lies at the upper end of reported average HVAC cooling demands and within the lower bound of heating-dominated scenarios, representing a high-end but realistic average auxiliary load rather than a transient peak.

Urban, Highway and WLTP drive cycles are therefore simulated under the assumption that all auxiliary power demand, fixed at 3 kW, is supplied by the Al-air auxiliary power unit rather than the traction battery and their respective electrical response of the battery pack is shown in Figure 6.12. This framework enables a direct assessment of how decoupling auxiliary loads from the Li-ion battery influences energy consumption and driving range under contrasting driving conditions. In particular, the Urban cycle highlights the sensitivity of range to time-dependent auxiliary loads at low average speeds, while the Highway cycle illustrates the reduced relative impact of auxiliary energy consumption due to higher distance traveled per unit time. By treating the metal-air system as a dedicated auxiliary energy source rather than a traction range extender, this study introduces and quantitatively evaluates a distinct integration pathway for metal-air batteries in electric vehicles, offering new insight into their potential role as onboard auxiliary power units under high auxiliary demand conditions.

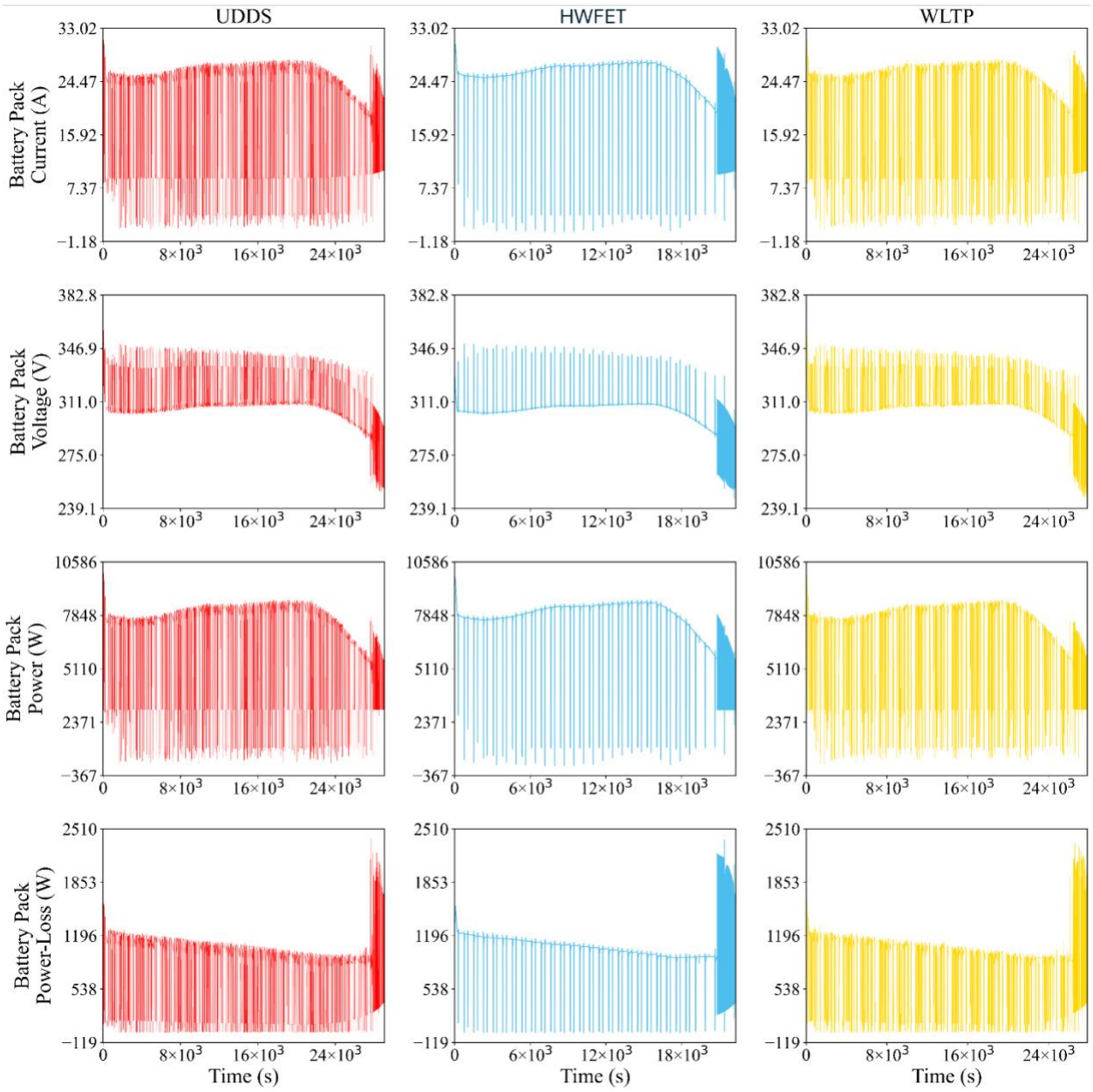


Figure 6. 12: Baseline Li-ion battery pack response under constant 3000 W auxiliary load (UDDS, HWFET, WLTP)

Figure 6.12 illustrates the battery pack electrical response under a constant 3000 W auxiliary load for UDDS, HWFET, and WLTP, compared with the baseline case without auxiliary consumption. While the fundamental cycle-dependent characteristics remain consistent, the auxiliary load shifts the battery operating point to a higher sustained discharge regime across all cycles.

Relative to baseline operation, the current profiles exhibit an elevated mean discharge level, with dynamic oscillations now superimposed on a non-zero discharge floor. This effect is particularly evident during low-traction intervals, where the battery continues to supply auxiliary demand. Voltage trajectories show a steeper overall decline and deeper instantaneous depressions, reflecting increased internal resistive effects due to higher average current. Similarly, power traces demonstrate an upward shift in net discharge power, and regenerative events are partially offset by the auxiliary load.

Internal power losses are correspondingly elevated throughout the cycle duration, consistent with the quadratic dependence on current. Overall, the constant auxiliary demand increases average loading, accelerates voltage depletion, and amplifies internal dissipation, indicating greater electrochemical and thermal stress compared to baseline operation without auxiliary consumption.

6.3 Results and Discussions

This section first establishes the performance characteristics of the baseline BEV configuration prior to integration of the Al-air range extender. The baseline system consists of a Li-ion traction battery supplying all propulsion and auxiliary loads under standard driving cycles. Vehicle electrical behavior, speed tracking capability, energy consumption, and achievable range are evaluated to provide a consistent reference for subsequent comparisons.

In addition to the nominal baseline configuration, two reduced-energy Li-ion pack cases were investigated, corresponding to 50% and 65% reductions in total pack energy. These scenarios were introduced to examine the feasibility of compensating reduced Li-ion capacity through Al-air range extension. However, downsizing the Li-ion pack not only reduces stored energy but also reduces available peak power, thereby imposing power limitations on the propulsion system. As a result, under high-demand driving segments, the vehicle was unable to fully track the prescribed drive cycle speed, leading to reduced achievable vehicle speed in certain regions.

The degree of power limitation was quantified using a root-mean-square error (RMSE) metric between the reference drive cycle speed and the simulated vehicle speed. The RMSE was calculated as

$$\text{RMSE} = \sqrt{\frac{1}{N}\sum_{k=1}^{N}\left(v_{\text{ref},k} - v_k\right)^2} \tag{6.12}$$

where $v_{\text{ref},k}$ is the target cycle speed and $v_k$is the simulated vehicle speed at time step k. An increase in RMSE relative to the nominal baseline indicates degradation in tracking performance due to power constraints. In the reduced pack configurations, elevated RMSE values were observed, particularly during high-acceleration and high-speed segments, confirming that the system entered a power-limited operating regime [434]. Consequently, reductions in achievable range for the downsized cases reflect both decreased energy capacity and incomplete adherence to the target drive cycle. These baseline and reduced-capacity results from the reference framework against which the Al-air-assisted configurations are evaluated in subsequent sections.

6.3.1 SOC depletion behavior and Range

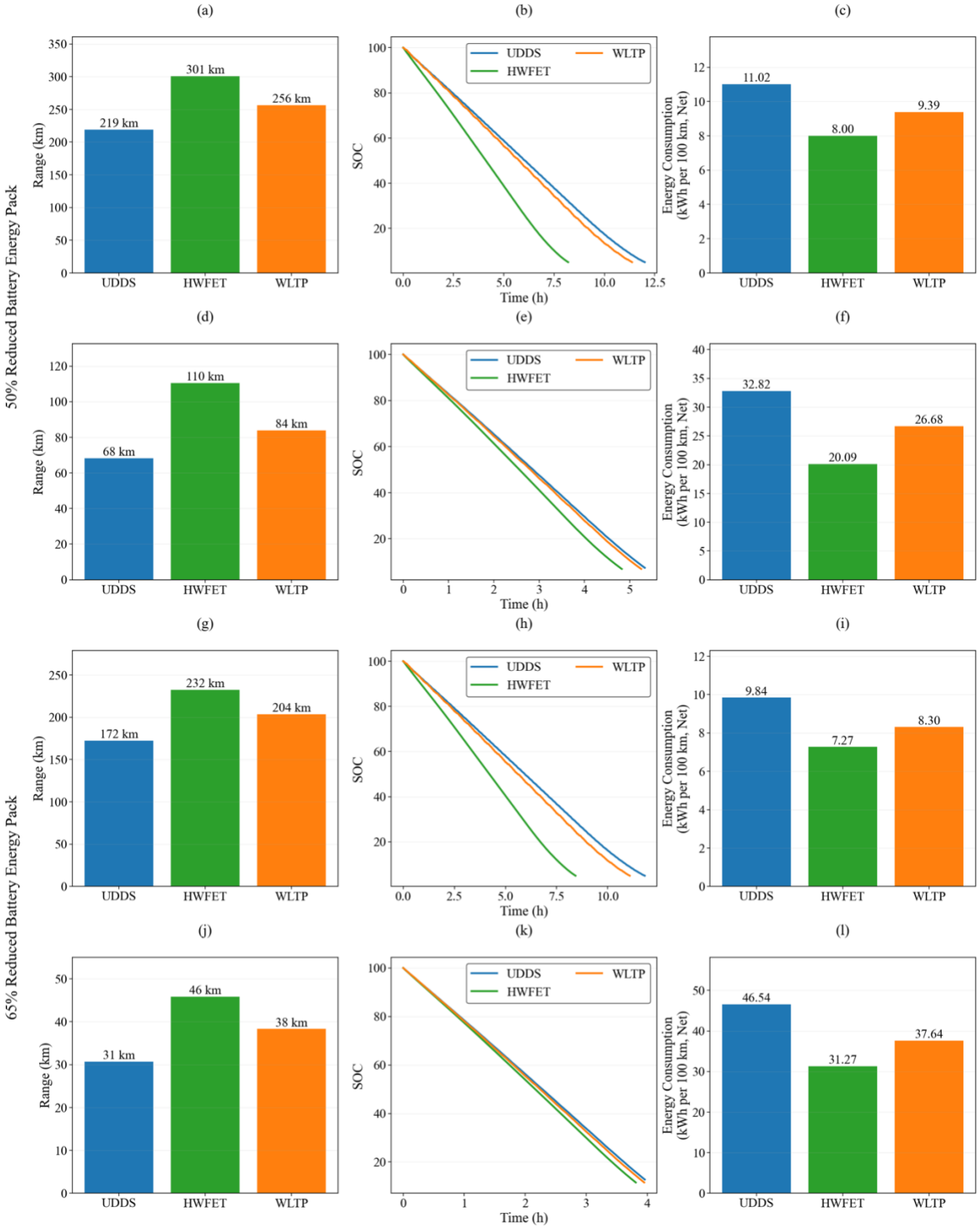


Figure 6. 13: Performance comparison of reduced-capacity Li-ion packs (50% and 65%) under baseline (a,b,c,g,h,i) and under constant 3000 W auxiliary load (d,e,f,j,k,l) across standard driving cycles.

Figure 6.13 compares reduced-capacity Li-ion packs (50% and 65%) under baseline operation and under a constant 3 kW auxiliary load across UDDS, HWFET, and WLTP cycles. Under baseline conditions, range scales are approximately proportionally with available energy. HWFET consistently delivers the highest range due to steady-speed operation and lower transient losses, followed by WLTP, while UDDS yields the lowest range because frequent acceleration events increase peak current demand and internal resistive losses. SOC depletion remains nearly linear across cycles, indicating traction-dominated discharge behavior in the absence of auxiliary loading.

The introduction of a constant 3 kW auxiliary load significantly accelerates SOC depletion and reduces achievable range across all drive cycles. The penalty is most pronounced in UDDS, where auxiliary power represents a larger fraction of total power demand during low-speed operation. Consequently, energy consumption per 100 km increases substantially under auxiliary loading due to the very low total distance covered (Table 6.3), particularly for the smaller pack configuration. These results underscore the importance of supplemental energy strategies such as the proposed Al-air range extender and auxiliary configurations.

Table 6. 3: Energy consumption and achievable range of baseline and reduced-capacity Li-ion configurations under standard drive cycles.

Drive Cycle	Distance (km)	Net Energy (kWh)	Discharge (kWh)	Regen (kWh)	Net (kWh/100 km)	Discharge-Only (kWh/100 km)
Baseline - Full Capacity						
UDDS	358.200	47.891	50.422	2.531	13.370	14.076
WLTP	400.846	47.864	49.795	1.931	11.941	12.422
HWFET	469.416	47.874	48.343	0.469	10.199	10.299
FTP-75	338.471	45.359	47.673	2.314	13.401	14.085
Baseline - Full Capacity + 3 kW Auxiliary Load						
UDDS	183.989	47.240	47.240	0.000	25.675	25.675

HWFET	302.159	46.561	46.561	0.000	15.409	15.409
WLTP	217.288	47.120	47.120	0.000	21.685	21.685
50% Energy Capacity Reduced						
UDDS	218.993	24.126	24.501	0.375	11.017	11.188
HWFET	300.647	24.036	24.099	0.063	7.995	8.016
WLTP	256.462	24.093	24.493	0.401	9.394	9.551
65% Energy Capacity Reduced						
UDDS	172.447	16.968	17.062	0.094	9.839	9.894
HWFET	232.435	16.896	16.917	0.021	7.269	7.278
WLTP	203.645	16.912	17.036	0.124	8.304	8.365
50% Reduced + 3 kW Auxiliary Load						
UDDS	68.123	22.356	22.356	0.000	32.818	32.818
HWFET	110.476	22.193	22.193	0.000	20.088	20.088
WLTP	83.900	22.385	22.385	0.000	26.681	26.681
65% Reduced + 3 kW Auxiliary Load						
UDDS	30.685	14.280	14.280	0.000	46.538	46.538
HWFET	45.870	14.344	14.344	0.000	31.271	31.271
WLTP	38.311	14.420	14.420	0.000	37.640	37.640

6.3.2 Battery Pack Characteristics

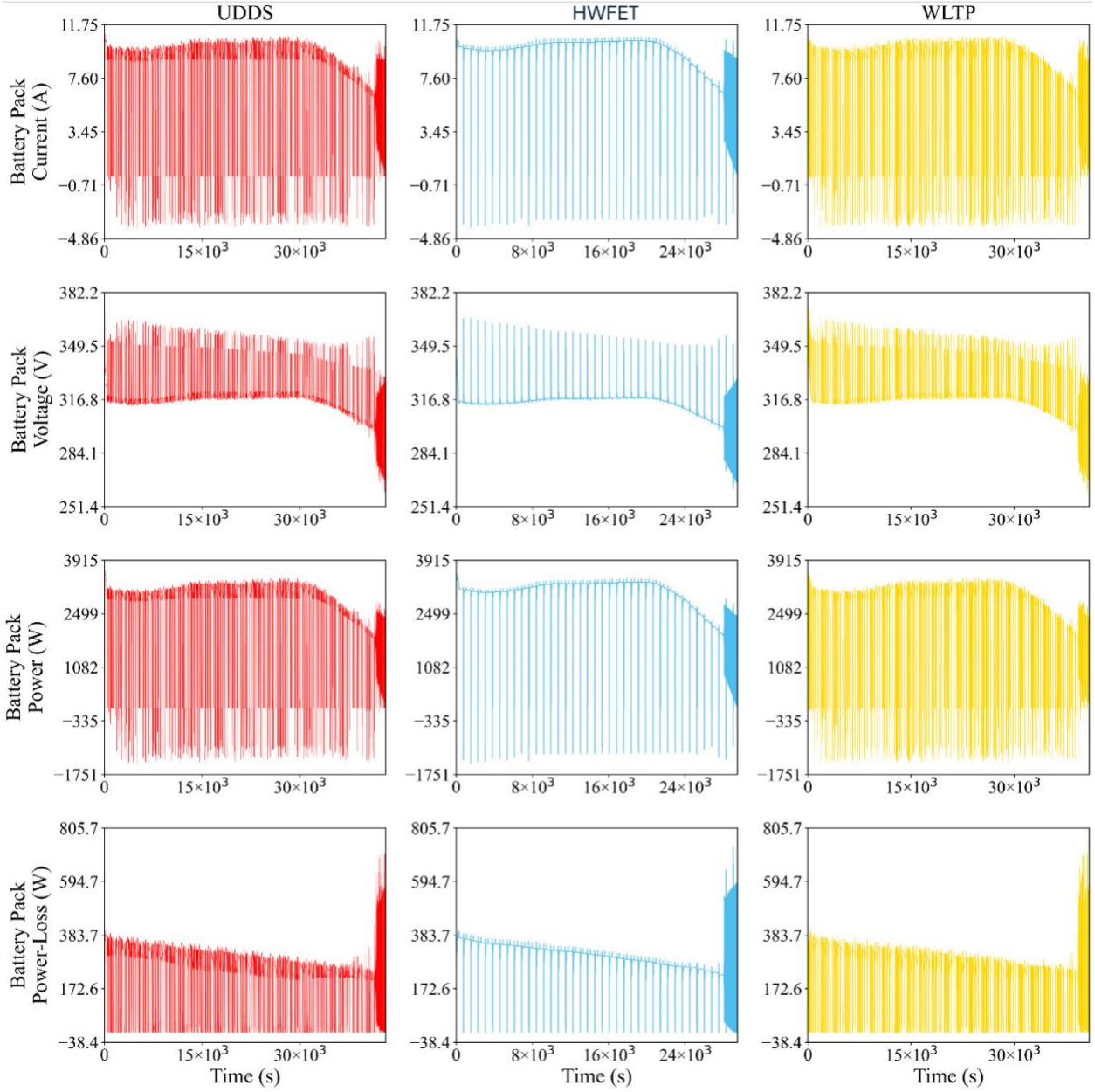


Figure 6. 14: Electrical response of the baseline Li-ion battery pack with 50% reduction in total energy capacity under UDDS, HWFET, AND WLTP driving cycles

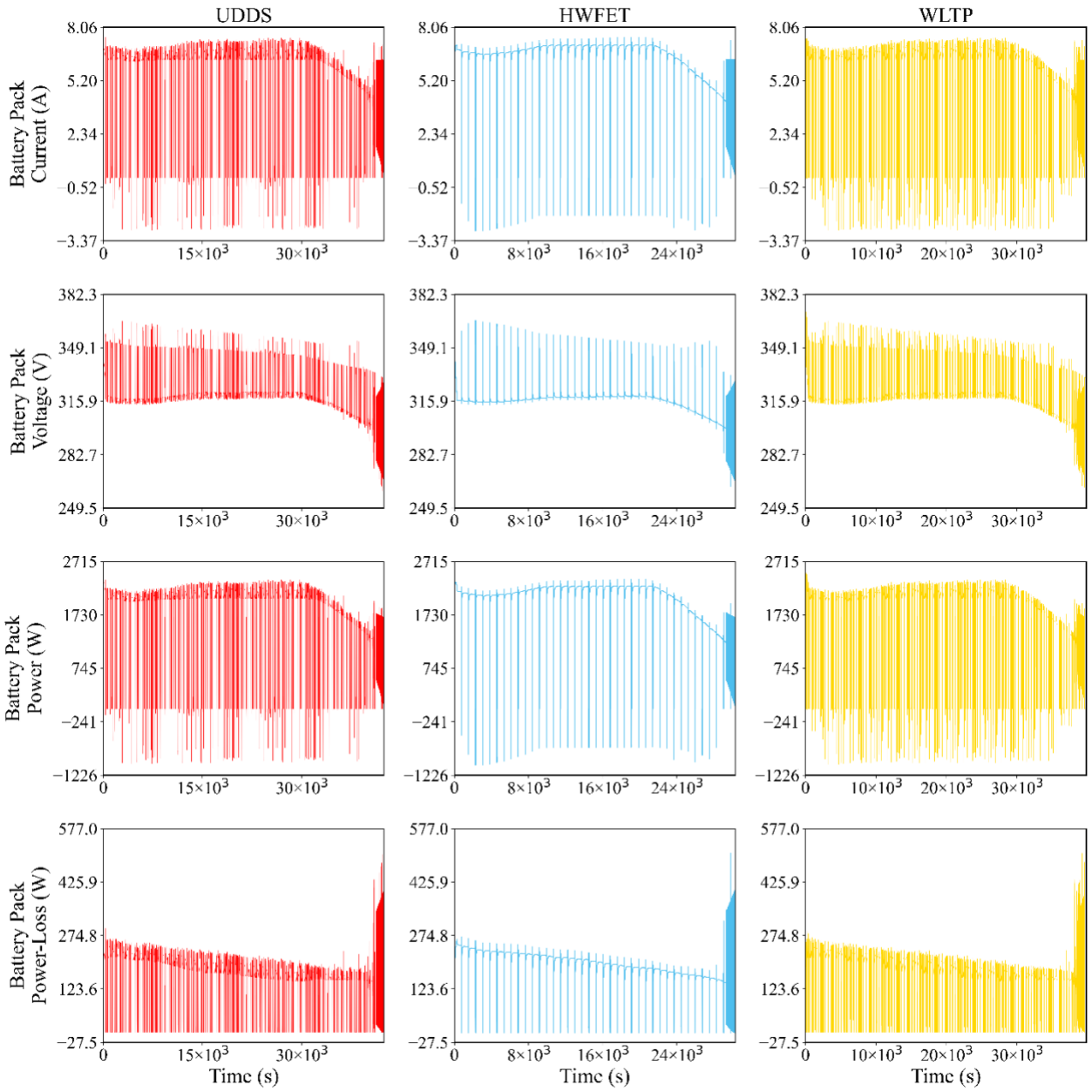


Figure 6. 15: Electrical response of the baseline Li-ion battery pack with 65% reduction in total energy capacity under UDDS, HWFET, AND WLTP driving cycles

Figures 6.14 and 6.15 illustrate the detailed electrical response of the reduced-capacity Li-ion packs (50% and 65%) under baseline operation. Across all drive cycles, the pack current profiles reflect the transient nature of traction demand, with UDDS and WLTP exhibiting higher fluctuation amplitudes compared to the smoother HWFET cycle. As capacity is reduced from 50% to 65%, the same power demand translates into higher effective C-rates, which is evident from

increased current magnitudes and more pronounced voltage sag toward the end of discharge. The voltage trajectories show progressive drop as SOC decreases, with sharper declines near end-of-discharge due to increased internal resistance effects. Correspondingly, pack power traces follow the drive-cycle power demand, while the internal power-loss plots reveal elevated resistive losses during high-current events, particularly in UDDS where acceleration spikes are frequent.

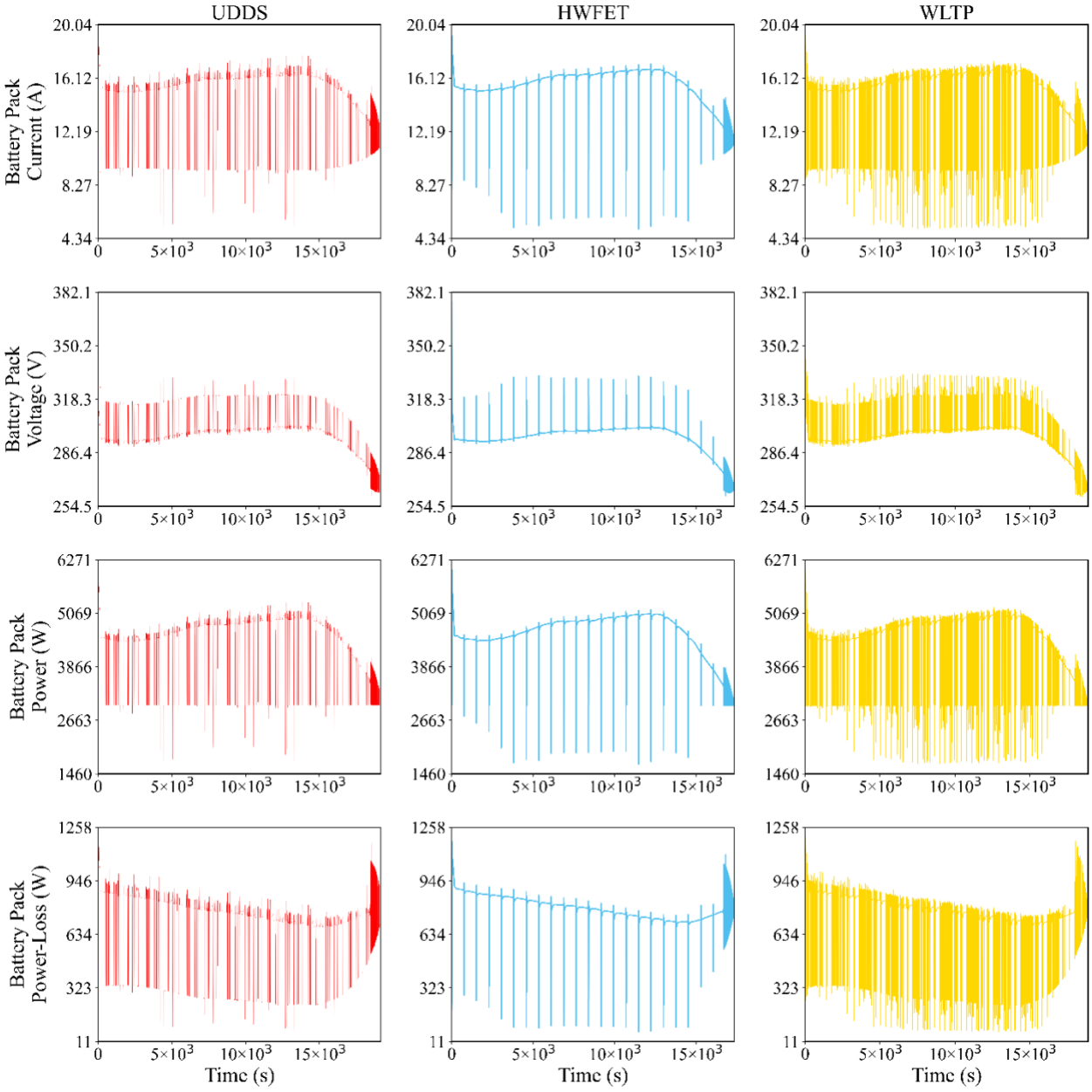


Figure 6. 16: Electrical response of the baseline Li-ion battery pack with 50% reduction in total energy capacity under constant 3000 w auxiliary load (UDDS, HWFET, WLTP)

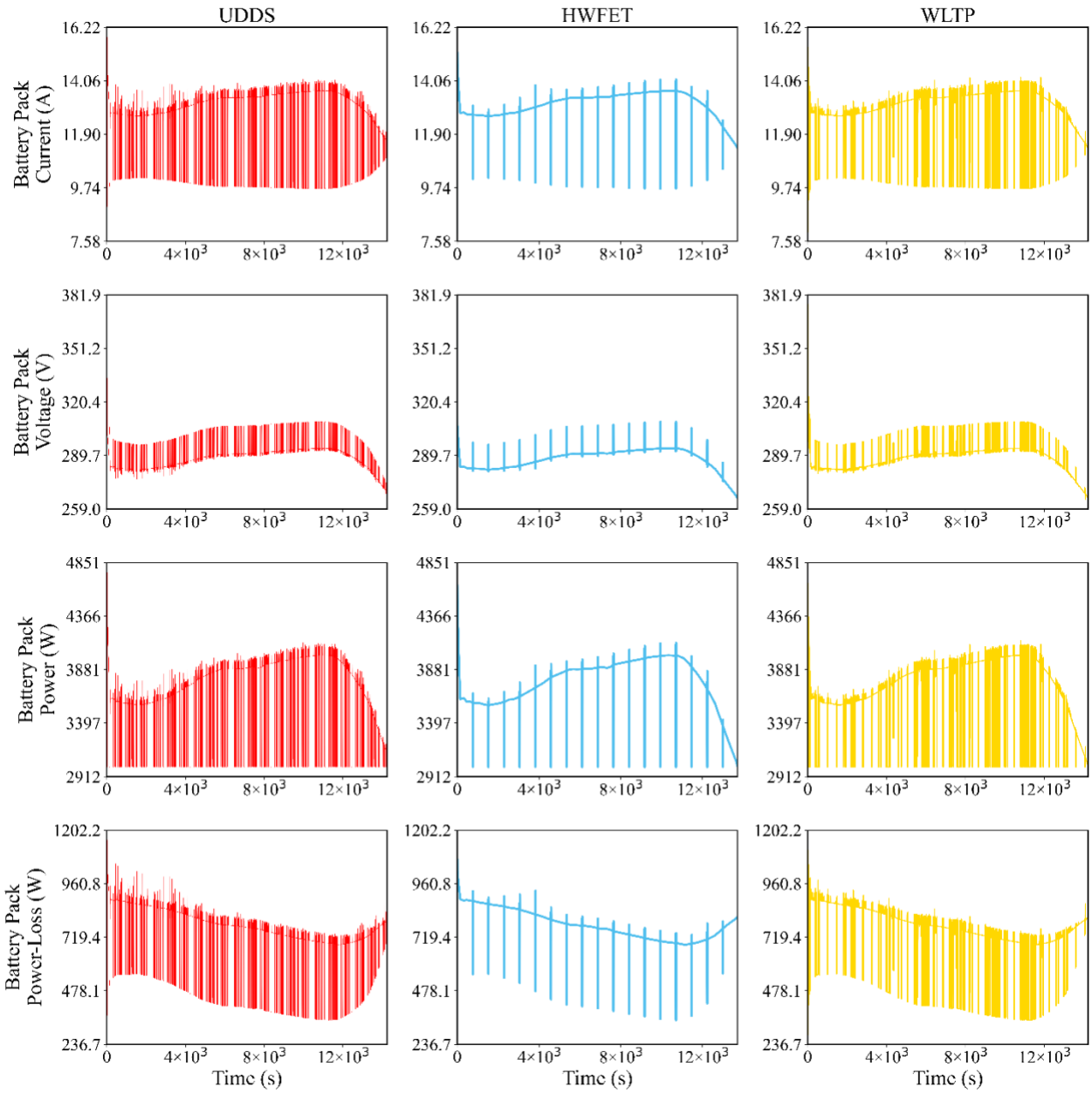


Figure 6. 17: Electrical response of the baseline Li-ion battery pack with 65% reduction in total energy capacity under constant 3000 w auxiliary load (UDDS, HWFET, WLTP)

Figures 6.16 and 6.17 show the electrical response when a constant 3 kW auxiliary load is superimposed on traction demand. The auxiliary load introduces a steady current offset across the entire drive cycle, resulting in higher baseline current levels and consistently lower terminal voltages compared to baseline operation. This shift increases cumulative resistive losses and accelerates voltage decay near end-of-discharge, especially for the 65% capacity case. The effect

is most pronounced in UDDS, where auxiliary power constitutes a larger fraction of total instantaneous demand during low-speed segments. The combined traction and auxiliary loading produces a more rapid transition into the nonlinear voltage-drop region, highlighting how fixed auxiliary demand amplifies internal loss mechanisms in downsized battery configurations and stresses pack voltage stability under dynamic driving conditions.

The RMSE was computed between the prescribed drive-cycle speed and the simulated vehicle speed over the full duration of each cycle. The nominal baseline full-capacity Li-ion configuration was used as the reference speed trace. Reduced-capacity packs and auxiliary-loaded configurations were compared against this reference to quantify deviations caused by power limitations. RMSE therefore represents the average magnitude of speed tracking error over the entire drive cycle and are shown in Table 6.4.

Table 6. 4: Root-mean-square error between reference and simulated vehicle speed under reduced-capacity Li-ion configurations and auxiliary loading.

Configuration	UDDS (km h^{-1})	HWFET (km h^{-1})	WLTP (km h^{-1})
Baseline Li-ion pack with 50% reduction in total energy capacity	11.84	20.76	13.63
Baseline Li-ion pack with 65% reduction in total energy capacity	15.13	29.65	18.88
Full-capacity Li-ion + 3 kW auxiliary	12.27	19.88	15.36
50% reduced energy Li-ion + 3 kW auxiliary	25.35	45.38	31.48
65% reduced energy Li-ion + 3 kW auxiliary	28.44	52.41	34.66

The RMSE results reveal a clear and systematic degradation in speed tracking performance as Li-ion capacity is reduced and auxiliary loading is introduced. Downsizing the traction battery increases RMSE across all driving cycles, indicating that reduced parallel configuration limits peak

power capability and results in larger deviations from the prescribed speed trace. The effect is most pronounced under HWFET conditions, where sustained high-speed operation imposes continuous propulsion demand and exposes power limitations more severely than in UDDS or WLTP. The introduction of a constant 3 kW auxiliary load further amplifies this degradation, particularly in the reduced-capacity cases. For the 65% reduced energy configuration under HWFET, RMSE exceeds 50 km h^{-1}, signifying substantial and sustained speed deficit relative to the reference cycle. These results demonstrate that battery downsizing not only reduces stored energy and achievable range but also induces a power-constrained operating regime, especially under highway and combined traction-auxiliary loading conditions.

6.3.3 Impact of Al-air Integration

Table 6. 5: Energy Consumption and Performance Metrics for Al-air Enabled Range-Extender Configurations with Reduced Li-ion Energy Capacity.

Drive Cycle	Distance (km)	Net Energy (kWh)	Discharge (kWh)	Regen (kWh)	Net (kWh/100 km)	Discharge-Only (kWh/100 km)
50% Reduced Energy Capacity + Al-air Range Extender						
UDDS	417.038	18.570	42.184	23.613	4.453	10.115
HWFET	583.305	19.453	39.742	20.289	3.335	6.813
WLTP	490.098	18.661	41.891	23.230	3.808	8.547
65% Reduced Energy Capacity + Al-air Range Extender						
UDDS	379.295	9.888	34.111	24.222	2.607	8.993
HWFET	522.709	10.604	32.766	22.163	2.029	6.269
WLTP	450.218	9.982	33.805	23.823	2.217	7.508

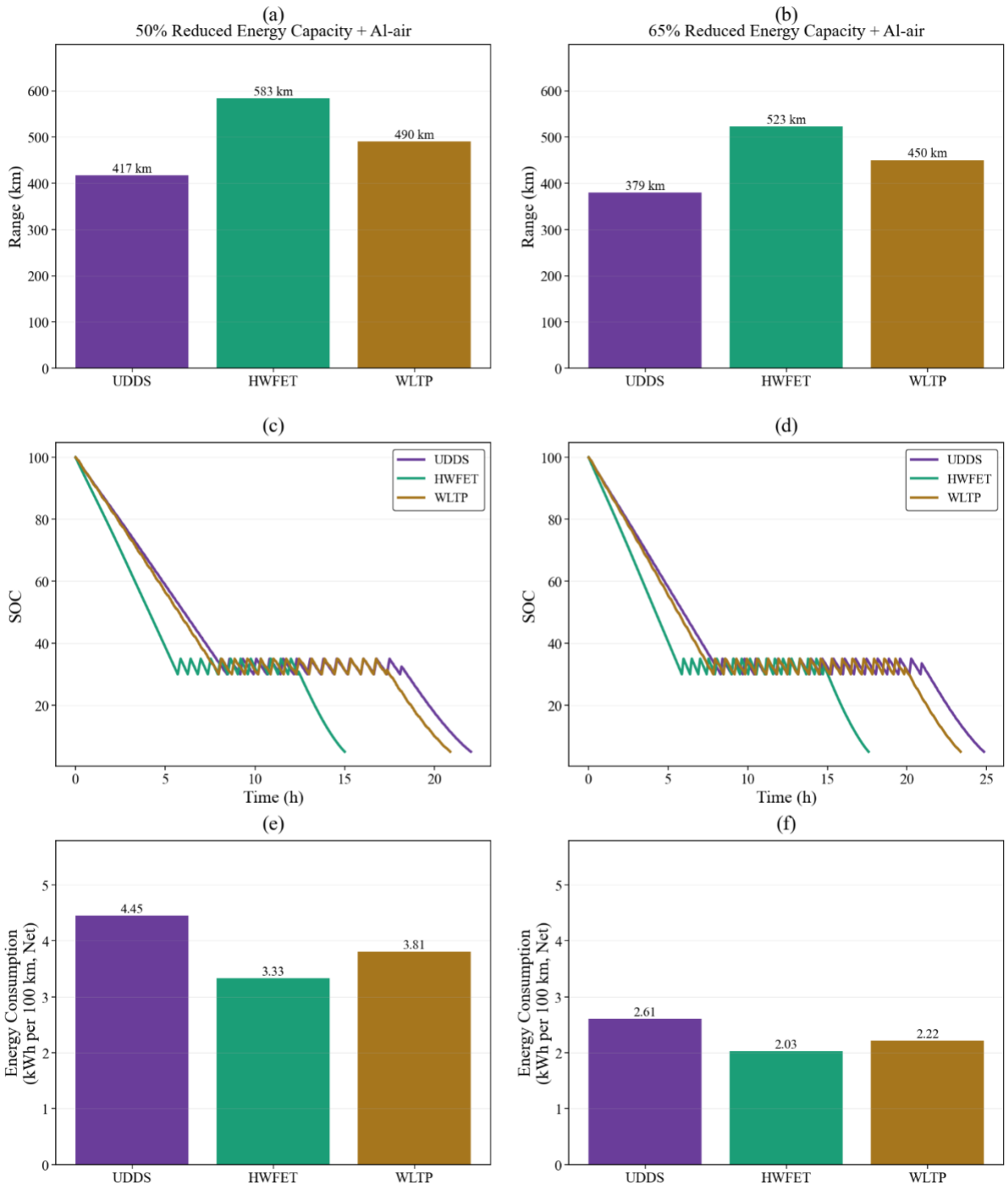


Figure 6. 18: Range performance, state-of-charge evolution, and net energy consumption for reduced Li-ion energy capacity configurations integrated with an Al-air range extender under UDDS, HWFET, and WLTP drive cycles

Figure 6.18 presents a comprehensive comparison of the 50% and 65% reduced Li-ion energy capacity configurations integrated with the Al-air range extender across three standardized driving cycles. Figure 6.18 combines range performance (panels a-b), SOC evolution (panels c-d), and net energy consumption (panels e-f), enabling simultaneous evaluation of performance, efficiency, and operational behavior.

The addition of the Al-air range extender enables substantial range recovery in both reduced-capacity configurations. For the 50% reduced case, the achieved ranges are approximately 417 km (UDDS), 583 km (HWFET), and 490 km (WLTP). For the 65% reduced case, ranges of approximately 379 km (UDDS), 523 km (HWFET), and 450 km (WLTP) are obtained. Notably, even with a 65% reduction in Li-ion energy capacity, the hybrid system surpasses the baseline full-capacity Li-ion range in all drive cycles. This demonstrates that Al-air integration effectively compensates for aggressive Li-ion downsizing while significantly reducing system mass. The HWFET cycle consistently yields the highest range due to its steady-speed profile and lower transient power demand, whereas UDDS produces the lowest range because of frequent accelerations and higher dynamic load fluctuations.

The SOC profiles clearly illustrate the role of the Al-air system as a range extender. In both configurations, the Li-ion SOC decreases initially, after which it stabilizes within a narrow operating window. This stabilization indicates that the Al-air module actively supplements the power demand, preventing deep Li-ion discharge. The oscillatory behavior observed during mid-range SOC reflects charge-sustaining operation under varying load conditions. In the 65% reduced case, the SOC plateau occurs earlier compared to the 50% reduced case, confirming stronger reliance on the Al-air subsystem due to the smaller Li-ion capacity. Importantly, deep Li-ion discharge is avoided until the later stages of operation, suggesting reduced Li-ion stress and potential cycle life benefits.

The net Li-ion energy consumption values decrease significantly with Li-ion downsizing. In the 50% reduced configuration, net consumption ranges between 3.33 and 4.45 kWh per 100 km, while in the 65% reduced case it further decreases to 2.03-2.61 kWh per 100 km. This reduction reflects the increasing contribution of the Al-air system to propulsion energy. HWFET again shows the lowest energy consumption, consistent with its smoother velocity profile. The reduced Li-ion energy throughput in the 65% configuration suggests that Li-ion degradation

mechanisms associated with deep cycling may be mitigated, which is advantageous for long-term durability.

Overall, the results confirm that aggressive Li-ion downsizing coupled with Al-air augmentation enables substantial mass reduction without sacrificing long-range capability. Among the evaluated configurations, the 65% reduced Li-ion integrated with the Al-air range extender provides the most favorable balance between range extension, reduced Li-ion utilization, and overall system efficiency.

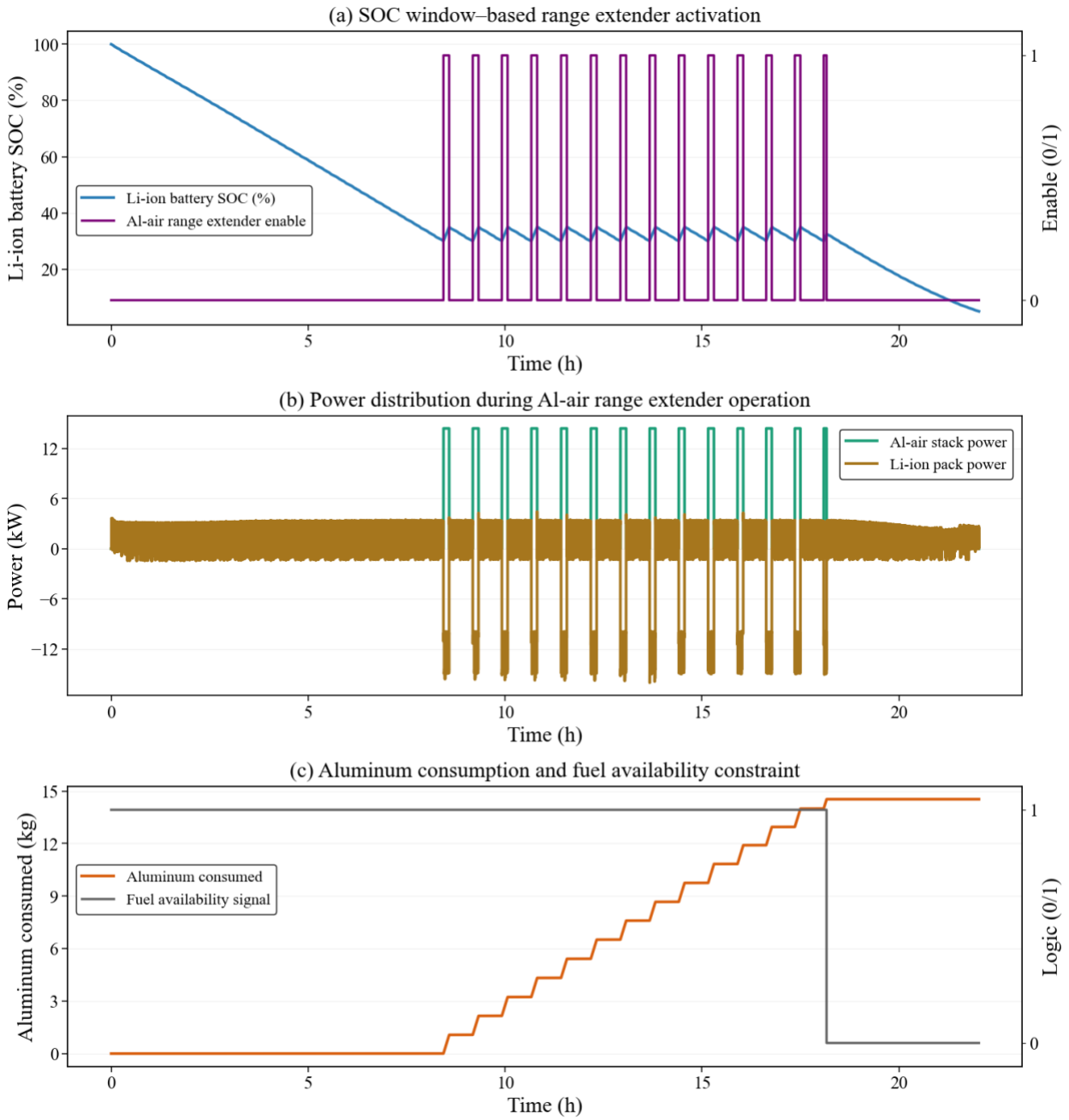


Figure 6. 19: Operational validation of SOC-window-controlled aluminum-air range extender and fuel consumption behavior

Figure 6.19 validates the SOC-based activation strategy of the Al-air range extender. As the Li-ion battery discharges and reaches the lower SOC threshold (~30-35%), the Al-air system periodically activates, producing short charging pulses that maintain the battery SOC within the control window. Correspondingly, the Al-air stack delivers positive power during these intervals,

reducing the net discharge demand on the Li-ion battery. Aluminum consumption increases stepwise during each activation event, reflecting electrochemical fuel utilization. Once the aluminum fuel limit is reached, the fuel-availability signal deactivates the system, confirming correct implementation of the SOC-based control and fuel-constraint logic.

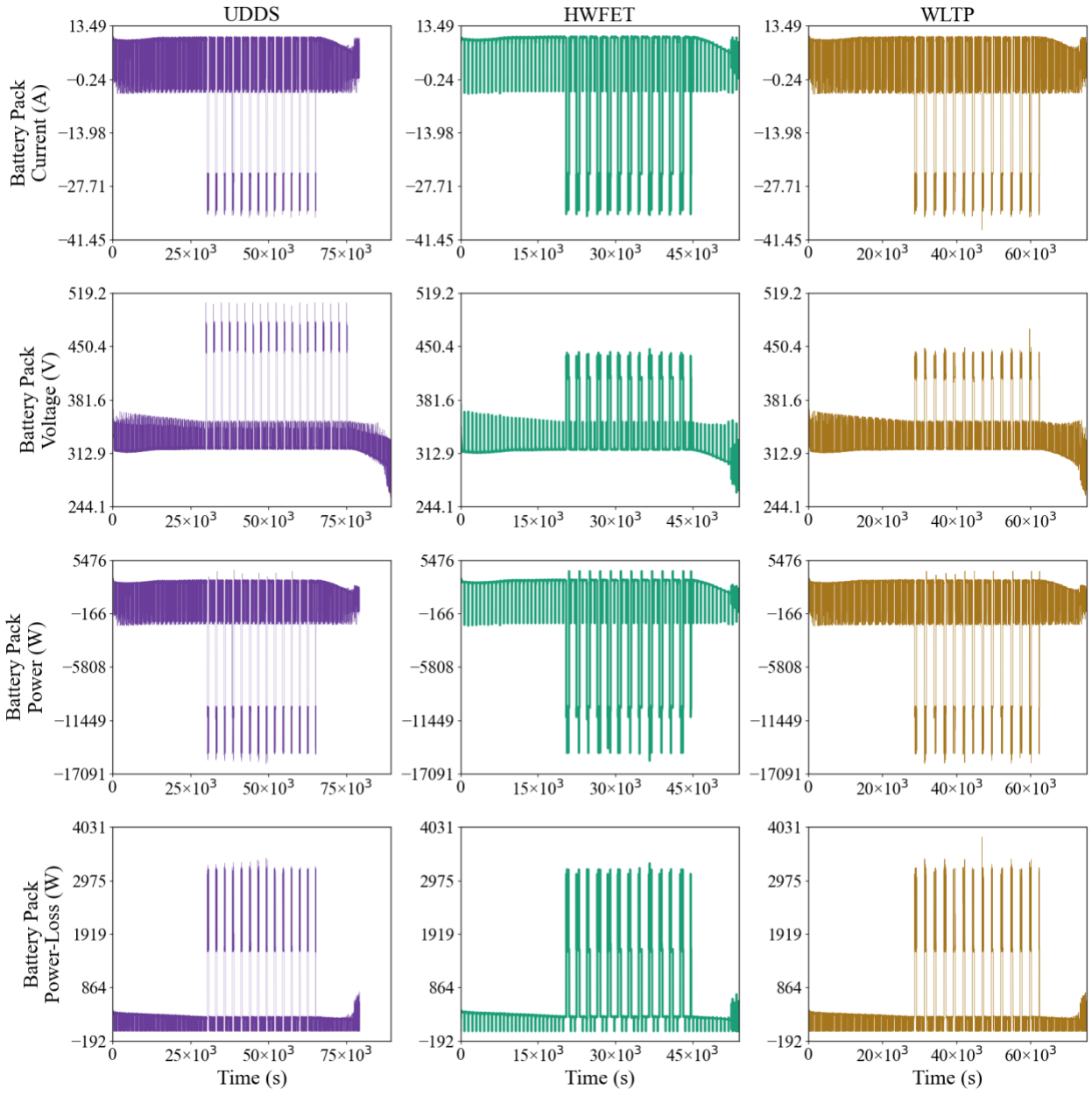


Figure 6. 20: Battery pack current, voltage, power, and power loss profiles under Al-air assisted operation with 50% reduced Li-ion energy capacity

Figure 6.20 presents the temporal profiles of battery pack current, voltage, power, and power loss for the 50% reduced Li-ion energy capacity configuration assisted by the Al-air range extender under the UDDS, HWFET, and WLTP driving cycles. These results provide insight into the dynamic interaction between the Li-ion battery and the aluminum-air system during vehicle operation.

Across all three drive cycles, the Li-ion battery remains the primary traction energy source, as indicated by the predominantly negative battery current and power values corresponding to discharge. However, once the Li-ion SOC approaches the predefined lower control threshold, the Al-air range extender is periodically activated. These activation events manifest as distinct transient pulses in the battery current and power profiles, corresponding to short-duration charging intervals supplied by the Al-air stack. During these intervals, the battery current momentarily shifts toward stronger negative peaks, indicating increased electrochemical activity associated with the charging process. Concurrently, the battery voltage profile exhibits noticeable upward excursions during these charging pulses, reflecting the temporary increase in pack voltage due to the additional charging contribution from the Al-air system.

The magnitude and frequency of these pulses vary with the driving cycle. The UDDS cycle, characterized by frequent accelerations and decelerations typical of urban driving, produces more irregular power fluctuations but relatively moderate charging pulses from the Al-air stack. In contrast, the HWFET cycle, which represents steady highway driving conditions, shows more pronounced and consistent charging pulses due to the smoother and more sustained load profile. The WLTP cycle, which contains a mix of low-, medium-, and high-speed phases, exhibits intermediate behavior, combining steady traction demand with periodic dynamic load changes.

The battery power-loss profiles further reveal the electrochemical implications of these charging events. During Al-air activation periods, the internal resistive losses of the Li-ion battery increase significantly, resulting in pronounced peaks in the power-loss plots. These peaks correspond to the elevated transient currents experienced during the charging pulses. Nevertheless, outside of these activation windows, the battery operates within a relatively stable loss regime, suggesting that the system effectively limits the duration of high-current events.

Overall, the results demonstrate that the SOC-window control strategy successfully stabilizes the Li-ion battery operation despite the 50% reduction in available energy capacity. The

Al-air range extender compensates for the reduced battery energy by providing periodic charging support, thereby preventing rapid SOC depletion and maintaining vehicle operability across all driving cycles. Importantly, the relatively moderate magnitude of the current and power pulses indicates that the Li-ion battery is not excessively stressed under this configuration, suggesting that the 50% reduced capacity case represents a feasible balance between battery downsizing and range-extender utilization.

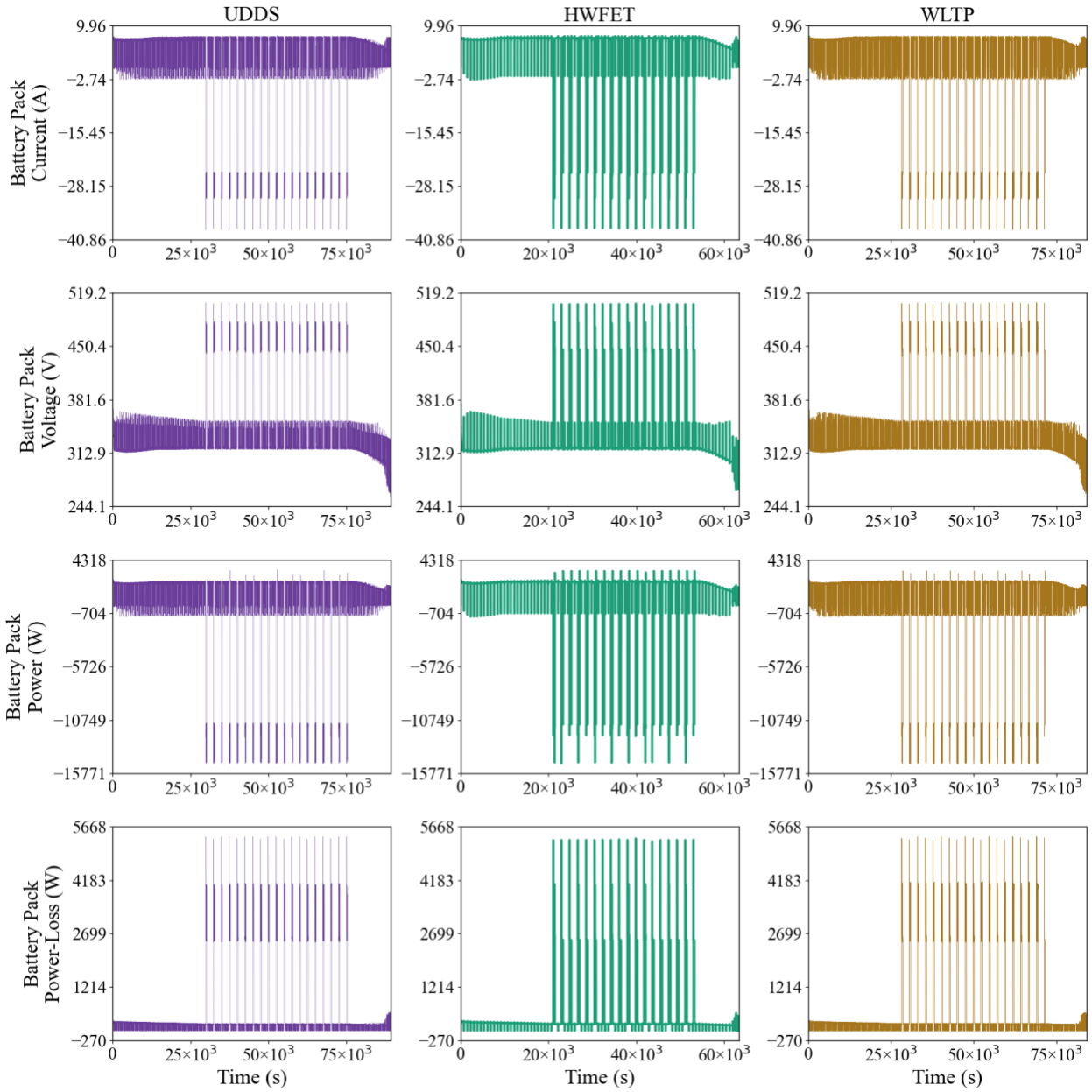


Figure 6. 21: Battery pack current, voltage, power, and power loss profiles under Al-air assisted operation with 65% reduced Li-ion energy capacity

Figure 6.21 illustrates the corresponding battery response for the 65% reduced Li-ion energy capacity configuration assisted by the Al-air range extender. This scenario represents a more aggressive reduction in the primary battery energy storage and therefore provides insight into the operational limits of the dual-energy-storage architecture.

Compared with the 50% reduction case, the Li-ion battery exhibits noticeably stronger dependence on the Al-air system. The battery current and power profiles reveal larger and more frequent transient charging pulses, indicating that the Al-air stack must operate more intensively to maintain the SOC within the control window. Because the Li-ion battery stores less total energy in this configuration, the SOC approaches the lower threshold more rapidly, triggering more frequent activation of the range extender.

This behavior is particularly evident in the HWFET cycle, where the steady highway power demand causes the Li-ion SOC to decline more rapidly in the absence of supplemental energy input. Consequently, the Al-air system produces repeated high-amplitude charging pulses to restore the SOC toward the upper boundary of the control window. These pulses appear as pronounced spikes in both the battery current and power plots. Similar patterns are observed in the UDDS and WLTP cycles, although the transient load fluctuations inherent to those cycles lead to more irregular pulse timing.

The voltage profiles provide further evidence of this increased interaction between the two energy systems. During each charging interval, the battery voltage rises sharply as the Al-air stack injects electrical energy into the Li-ion pack. Because these charging events occur more frequently in the 65% reduction scenario, the voltage oscillations become more pronounced and periodic throughout the simulation.

The battery power-loss profiles also reflect the increased operational burden imposed on the Li-ion battery. Higher and more frequent current transients lead to larger peaks in internal resistive losses, indicating elevated electrochemical stress during charging events. While the system remains stable and operational across all drive cycles, the increased magnitude and

frequency of these loss peaks suggest that further reductions in Li-ion capacity could lead to diminished efficiency or accelerated battery degradation if not carefully managed.

Despite these challenges, the results demonstrate that the Al-air range extender effectively compensates for the substantial reduction in Li-ion energy capacity, allowing the vehicle to maintain continuous operation across all evaluated driving cycles. However, the increased reliance on the range extender highlights the importance of appropriately balancing Li-ion battery capacity and range-extender capability. From a system-level perspective, the 65% reduction case illustrates the operational limits of aggressive battery downsizing, where the benefits of mass reduction must be weighed against increased power fluctuations, higher internal losses, and greater dependence on the auxiliary energy source.

Together, Figures 6.20 and 6.21 confirm that the proposed control strategy enables stable dual-energy operation across a range of battery capacity reductions. At moderate reductions (50%), the Al-air system provides supplementary energy with limited impact on battery stress, whereas deeper reductions (65%) significantly increase the reliance on the range extender, highlighting important design trade-offs for hybrid metal-air BEV architectures.

Table 6. 6: Mass breakdown and total range for reduced-energy Li-ion configurations with and without Al-air range extender.

Drive Cycle	Li-ion Pack Mass (kg)	Al-air Pack Mass (kg)	Total System Mass (kg)	Total Range Achieved (km)
Baseline, full energy capacity (58 kWh)				
UDDS	326	0	326	358.200
HWFET	326	0	326	469.416
WLTP	326	0	326	400.846
50% reduced energy capacity (29 kWh)				
UDDS	163	0	163	218.993
HWFET	163	0	163	300.647
WLTP	163	0	163	256.462
65% reduced energy capacity (20.3 kWh)				
UDDS	114	0	114	172.447
HWFET	114	0	114	232.435

WLTP	114	0	114	203.645
50% reduced energy capacity + Al-air range extender				
UDDS	163	34	197	417.038
HWFET	163	34	197	583.305
WLTP	163	34	197	490.098
65% reduced energy capacity + Al-air range extender				
UDDS	114	34	148	379.295
HWFET	114	34	148	522.709
WLTP	114	34	148	450.218

From a purely mass-based perspective, the optimal configuration in each driving cycle depends on the required target range. The lightest architecture overall is the 65% reduced energy capacity Li-ion configuration, with a total pack mass of 114 kg. However, this configuration provides limited driving range, achieving approximately 172 km under UDDS, 232 km under HWFET, and 204 km under WLTP conditions. Therefore, while it is the minimum-mass solution, it is only suitable for short-range applications.

When extended range is required, the 65% reduced energy capacity combined with the Al-air range extender emerges as the most mass-efficient high-range configuration across all drive cycles. This configuration results in a total system mass of approximately 148 kg, which is still significantly lower than the baseline 58 kWh Li-ion pack mass of 326 kg. Despite the reduced Li-ion capacity, the addition of the Al-air pack enables ranges of approximately 379 km (UDDS), 523 km (HWFET), and 450 km (WLTP). Notably, this configuration achieves comparable or superior range relative to the baseline vehicle while reducing total system mass by more than 50%.

The 50% reduced energy capacity combined with the Al-air range extender provides the highest absolute range in all cycles, reaching approximately 417 km (UDDS), 583 km (HWFET), and 490 km (WLTP). However, this comes at a higher total mass of approximately 197 kg. While still substantially lighter than the baseline configuration, it does not offer the same mass efficiency as the 65% reduced plus Al-air option when range-to-mass performance is considered.

Overall, if the objective is to maximize driving range while minimizing total system mass, the 65% reduced energy capacity Li-ion pack integrated with the Al-air range extender represents

the optimal configuration across UDDS, HWFET, and WLTP cycles. It delivers substantial range recovery with minimal mass addition and consistently outperforms the baseline full-capacity Li-ion system in mass efficiency.

Table 6. 7: Pack capital cost assumptions and total CAPEX for configurations evaluated.

Configuration	Li-ion energy (kWh)	Al-air energy (kWh)	Li-ion pack cost (USD)	Al-air pack cost (USD)	Total pack cost (USD)
Baseline, full energy capacity Li-ion	58.0	0.0	10,000 to 25,000	0	10,000 to 25,000
50% reduced energy capacity Li-ion	29.0	0.0	5,000 to 12,500	0	5,000 to 12,500
65% reduced energy capacity Li-ion	20.3	0.0	3,500 to 8,750	0	3,500 to 8,750
50% reduced energy capacity Li-ion + Al-air range extender	29.0	24.6	5,000 to 12,500	5,000 to 12,000	10,000 to 24,500
65% reduced energy capacity Li-ion + Al-air range extender	20.3	24.6	3,500 to 8,750	5,000 to 12,000	8,500 to 20,750

Using the assumed low-volume, fully integrated system costs, the baseline full-capacity Li-ion configuration remains the simplest solution but is not cost-optimal when judged purely on pack CAPEX. With a 58 kWh pack cost spanning 10,000 to 25,000 USD, the baseline represents the highest single-component investment among Li-ion-only cases. In contrast, reducing Li-ion energy capacity to 50% or 65% lowers the estimated Li-ion pack CAPEX proportionally, yielding ranges of approximately 5,000 to 12,500 USD and 3,500 to 8,750 USD, respectively. From a cost-only perspective, the reduced-capacity Li-ion configurations therefore minimize pack CAPEX, although they also reduce the achievable driving range.

When Al-air is introduced as a range extender, the total pack CAPEX increases due to the additional Al-air module, assumed here to span 5,000 to 12,000 USD for the 24.6 kWh system including stack, balance-of-plant, and power electronics. Under these assumptions, the combined 50% reduced Li-ion plus Al-air configuration results in a total pack CAPEX of approximately 10,000 to 24,500 USD, overlapping with the baseline full Li-ion cost range. As a result, this

configuration is not consistently cost-advantaged relative to the baseline when CAPEX alone is considered, even though it enables substantially higher driving range than the reduced Li-ion-only case.

In comparison, the 65% reduced Li-ion plus Al-air configuration provides the most favorable cost balance among the hybrid options. Its total pack CAPEX is estimated at 8,500 to 20,750 USD, which is lower than the baseline full-capacity Li-ion pack across most of the assumed range while still offering large range recovery relative to the reduced Li-ion-only case. This makes the 65% reduced plus Al-air configuration the most cost-efficient hybrid architecture under the adopted system-level pricing assumptions, as it achieves substantial range extension without exceeding the baseline CAPEX envelope. If the objective is to obtain extended driving range while maintaining total pack CAPEX at or below the baseline cost envelope, the 65% reduced Li-ion plus Al-air range extender provides the best cost-based trade-off.

When both total system mass and pack capital expenditure are considered simultaneously, the 65% reduced energy capacity Li-ion configuration integrated with the Al-air range extender emerges as the most balanced option. This architecture results in a total system mass of approximately 148 kg, which is substantially lower than the baseline full-capacity Li-ion system at 326 kg and also lower than the 50% reduced plus Al-air configuration at approximately 197 kg. Despite the significant reduction in Li-ion capacity, the addition of the Al-air module restores and extends the driving range beyond the baseline vehicle in all evaluated drive cycles.

In the UDDS cycle, the 65% reduced Li-ion-only configuration achieves approximately 172 km, whereas the addition of the Al-air range extender increases the range to approximately 379 km, corresponding to an additional 207 km of driving range. Under HWFET conditions, range increases from approximately 232 km to 523 km, yielding an additional 291 km. Similarly, in the WLTP cycle, range improves from approximately 204 km to 450 km, providing an additional 246 km. Notably, these values also exceed the baseline full-capacity Li-ion ranges (358 km UDDS, 469 km HWFET, and 401 km WLTP), demonstrating that substantial range recovery is achieved with a significantly lighter system.

From a cost perspective, assuming system-level pack costs of 10,000 to 25,000 USD for the 58 kWh Li-ion baseline and 5,000 to 12,000 USD for the 24.6 kWh Al-air pack, the total CAPEX of the 65% reduced plus Al-air configuration spans approximately 8,500 to 20,750 USD.

This range generally remains within or below the baseline cost envelope while delivering large range gains relative to the reduced Li-ion-only case.

Accordingly, when evaluated on combined mass, cost, and range criteria, the 65% reduced Li-ion pack supplemented by the Al-air range extender represents the most favorable trade-off among the configurations studied. It reduces system mass by more than 50% relative to the baseline, controls total pack CAPEX within the baseline range, and adds between approximately 207 and 291 km of additional driving range depending on the drive cycle.

6.3.4 Aluminum-air as an Auxiliary Power Unit

To further investigate the system-level integration of Al-air technology, the Al-air subsystem was evaluated as an APU supplying vehicle auxiliary loads while the Li-ion battery remained the primary traction energy source. In this configuration, auxiliary electrical demands were supported by the Al-air stack, reducing the load imposed on the traction battery during vehicle operation. Simulations were conducted using the MATLAB/Simulink virtual vehicle framework under the UDDS, HWFET, and WLTP drive cycles. The electrical response of the Li-ion battery, including current, voltage, power, and power loss, was analyzed to assess the influence of auxiliary load support (Figure 6.22). The resulting vehicle range and battery SOC evolution were also examined to quantify the impact of the Al-air auxiliary power (Figure 6.23).

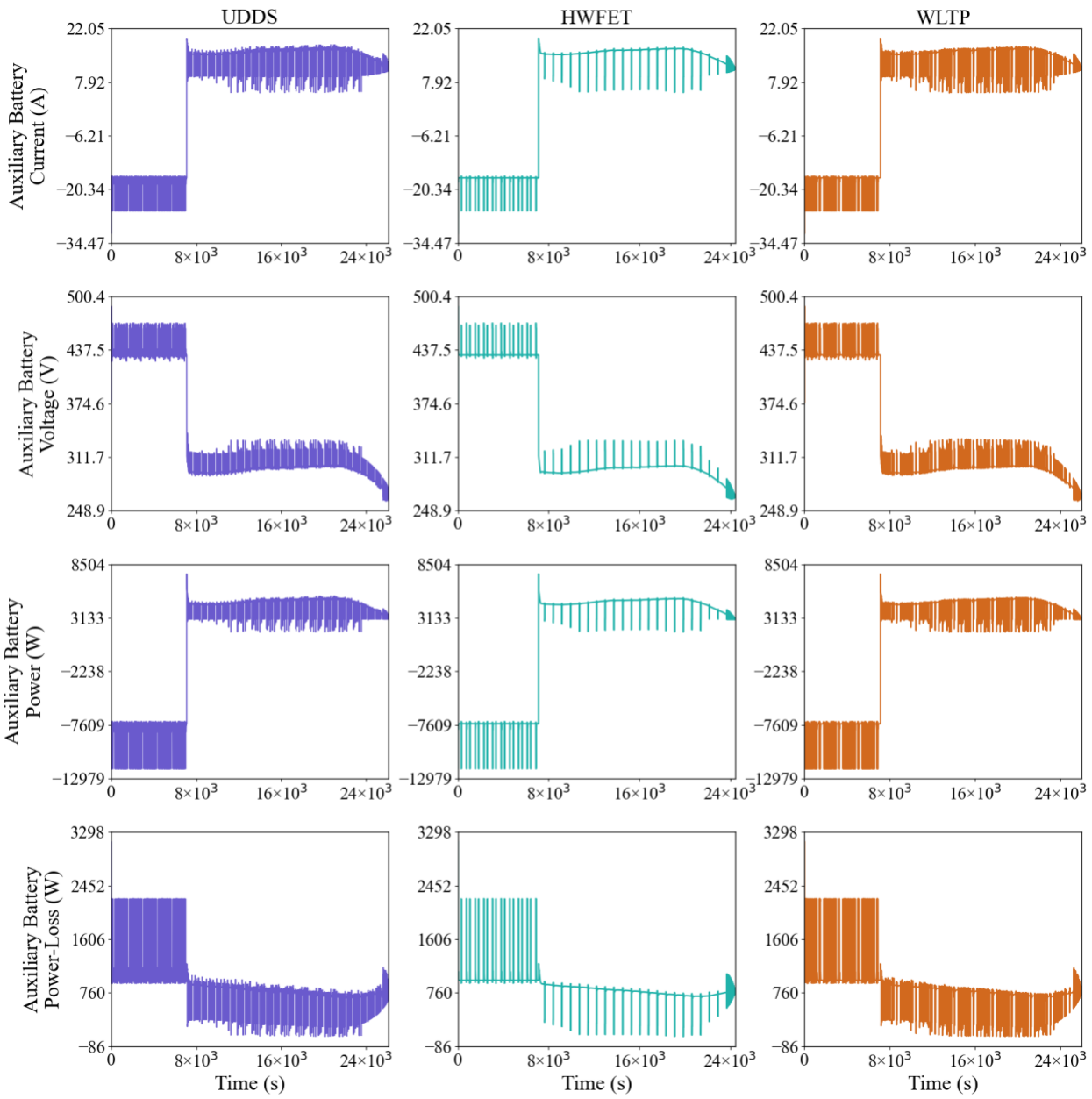


Figure 6. 22: Lithium-ion battery electrical response when auxiliary loads are supplied by the aluminum-air auxiliary power unit under UDDS, HWFET, and WLTP drive cycles, showing battery current, voltage, power, and power loss profiles.

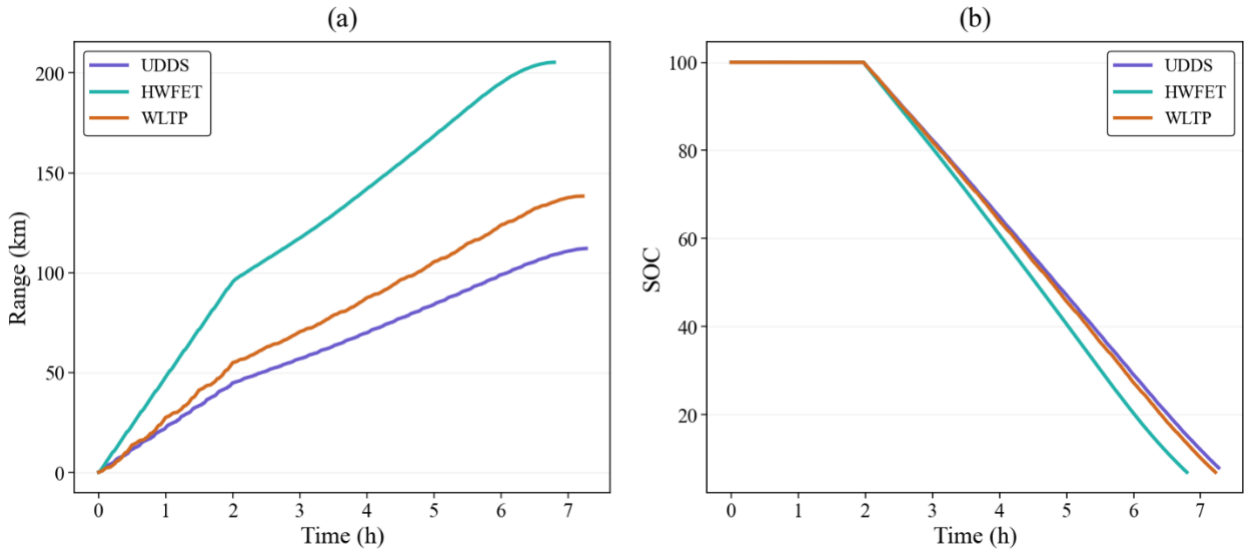


Figure 6. 23: Vehicle range and lithium-ion battery state-of-charge evolution for the aluminum-air auxiliary power unit configuration under UDDS, HWFET, and WLTP drive cycles.

The baseline configuration with a constant 3000 W auxiliary load places a continuous electrical demand on the Li-ion battery, requiring it to supply both propulsion and auxiliary power throughout the drive cycle. As shown in Figure 6.22, this results in sustained discharge currents and elevated battery power output across the UDDS, HWFET, and WLTP cycles. The increased current demand leads to higher internal resistive losses, reflected in the battery power loss profiles. Correspondingly, the battery voltage gradually decreases over time as the state of charge declines, while the SOC curves exhibit a nearly linear depletion throughout the driving duration. Under this baseline configuration with a 50% reduced battery energy capacity, the achievable vehicle ranges are 68 km for UDDS, 110 km for HWFET, and 84 km for WLTP, with the longest range observed in the HWFET cycle due to its relatively steady driving conditions and lower transient load fluctuations.

When the auxiliary load is supplied by the Al-air APU, the electrical burden on the Li-ion battery is significantly reduced. As shown in Figure 6.22, the battery current and power profiles exhibit lower sustained discharge levels compared with the baseline case, indicating that a portion of the auxiliary energy demand is offloaded to the Al-air subsystem. This reduction in battery load decreases internal power losses and moderates the voltage drop during operation, resulting in a slower rate of SOC depletion across all drive cycles. The reduced auxiliary load on the traction battery allows a larger portion of the stored Li-ion energy to be dedicated to propulsion.

The system-level benefit of this configuration is reflected in the substantial improvement in vehicle range. Compared with the baseline case, the Al-air APU configuration increases the achievable range from 68 km to 112 km in UDDS, from 110 km to 206 km in HWFET, and from 84 km to 138 km in WLTP. These correspond to absolute improvements of 44 km, 96 km, and 54 km, respectively, representing relative range increases of approximately 64.7%, 87.3%, and 64.3%. The largest improvement occurs in the HWFET cycle, where the longer driving duration amplifies the energy savings associated with auxiliary load offsetting. Overall, these results demonstrate that integrating an Al-air subsystem as an auxiliary power unit can significantly mitigate auxiliary load penalties, improving energy utilization and substantially extending the achievable driving range of the vehicle.

6.3.5 Comparison with Literature Metal-Air Range Extenders

Earlier vehicle-level work on metal-air range extenders has focused predominantly on Zn-air systems, largely because Zn-air is the most mature aqueous metal-air chemistry and is one of the few systems that can be electrically regenerated. Sherman et al. [435] presented one of the clearest dual-energy-storage EV studies in this area by coupling a small Li-ion pack with a larger Zn-air secondary pack in a full vehicle model. In that work, the Zn-air battery was not used for direct traction support, but rather as a reserve energy source that extended range while limiting cycling of the metal-air pack. Their study showed that a properly controlled Zn-air-assisted architecture could outperform a single-pack BEV in range while also reducing cost pressure on the Li-ion system, thereby establishing the dual-ESS concept as a practical pathway for metal-air integration in vehicles.

A key feature of the Zn-air vehicle literature is that it consistently treats the metal-air battery as an energy-dominant but power-limited device. Sherman et al. [435] explicitly emphasized the low power density and limited cycle life of Zn-air batteries as the main reasons they are unsuitable as standalone EV traction batteries, while still identifying them as attractive range extenders because of their lower expected cost and higher energy density relative to Li-ion batteries. The same study also noted that metal-air systems generally face low voltage, low current density, self-discharge, and side reactions, and further pointed out that Al-air batteries, although highly energy dense, are not electrically rechargeable and would require replacement or off-board recycling rather than conventional charging. This framing is important because it closely aligns

with the present work, where the Al-air battery is likewise assigned a secondary energy role rather than a primary propulsion role.

The broader comparative review by Shabeer et al. [258] reinforces this distinction between Zn-air and Al-air. That review identifies aluminum as an attractive anode because of its very high theoretical specific energy and volumetric energy density, as well as its abundance, safety, and low cost, but it also highlights corrosion and parasitic reactions in aqueous electrolytes as major barriers to practical implementation. In contrast, the review notes that Zn-air has lower theoretical specific energy than Al-air but retains a critical practical advantage in that zinc-based aqueous metal-air systems can be electrically recharged, whereas aqueous Al-air systems remain mechanically rechargeable. Thus, the literature positions Zn-air as the more mature rechargeable chemistry, but Al-air as the more compelling candidate when the objective is maximum onboard energy storage in a fuel-like range-extender role.

From a modeling perspective, Clark et al. [436] reviewed the wider toolbox available for metal-air battery design, with particular emphasis on Zn-air systems. Their review showed that most established modeling work has concentrated on Zn-air because of its relative maturity, and that the main technical challenges remain electrolyte instability, hydrogen evolution, electrode shape change, passivation, air-electrode degradation, and the need for suitable continuum models to bridge materials behavior and cell-level performance. This is an important observation for the present study. Much of the existing metal-air literature has advanced either at the material scale or at the cell scale, whereas vehicle-level integration studies remain comparatively limited. The present work addresses that gap by embedding an experimentally informed Al-air model within a full MATLAB/Simulink EV framework and by explicitly evaluating control logic, SOC evolution, power flow, and drive-cycle-dependent operation.

Taken together, the attached literature suggests clear progression. Sherman et al. [435] established the feasibility of dual-ESS metal-air-assisted EVs using Zn-air as a secondary pack. Clark et al. [436] clarified that multi-scale modeling is essential for capturing the coupled electrochemical and transport limitations of metal-air systems. Shabeer et al. [258] then positioned Al-air as a particularly promising range-extender chemistry because of its superior theoretical energy potential, despite its mechanical recharge requirement and corrosion-related challenges. Relative to these studies, the present work advances literature by translating Al-air from a largely

conceptual or comparative candidate into a dynamically integrated vehicle subsystem, and by assessing both range-extender and auxiliary-power-unit roles within a reproducible system-level EV simulation environment.

6.3.6 Practical Implications and Limitations

Although the system-level simulations demonstrate the potential of Al-air batteries as supplemental energy sources in EVs, several practical constraints must be considered when interpreting the results. A primary limitation of metal-air systems is their relatively low power density compared with conventional Li-ion batteries. Al-air cells are typically optimized for high energy density rather than rapid transient power delivery, and their performance is governed by electrochemical reaction kinetics, mass transport through the air cathode, and electrolyte conductivity. As a result, these systems are better suited to sustained or moderate power operation rather than high-power traction demands. The architecture adopted in this work addresses this constraint by assigning the Li-ion battery full responsibility for propulsion while the Al-air subsystem operates as a secondary energy source, either as a range extender or as an auxiliary power unit. Even within this framework, power limitations remain an important design consideration, because excessive current densities can lead to severe polarization losses, electrode passivation, and accelerated degradation of the air electrode.

System-level efficiency is another important consideration for practical implementation. In Al-air batteries, the theoretical electrochemical energy stored in aluminum cannot be fully converted into usable electrical energy due to several loss mechanisms. Polarization losses associated with activation overpotentials, ohmic resistance, and concentration limitations reduce the operating cell voltage under load. Additional efficiency penalties arise from parasitic side reactions, most notably hydrogen evolution at the aluminum anode, which consumes active material without contributing to useful electrical output. Electrolyte management also plays a critical role in overall system efficiency. As aluminum oxidizes, aluminate species accumulate in the alkaline electrolyte, altering ionic conductivity and potentially limiting mass transport near the electrode surface. In practical systems, circulation or periodic replacement of electrolyte may be required to maintain stable electrochemical conditions, which introduces additional balance-of-plant complexity. Hydrogen generation further necessitates appropriate gas management strategies

to ensure safe operation, including controlled venting or recombination systems to prevent pressure buildup and mitigate safety risks.

These constraints highlight several implications for the continued development of Al-air batteries for vehicle applications. Effective hydrogen management and electrolyte control will be essential for maintaining stable long-duration operation, particularly under variable load conditions encountered in real driving cycles. Advances in corrosion inhibitors, electrolyte additives, and improved air cathode catalysts may help suppress parasitic reactions and enhance coulombic efficiency. At the system level, improvements in stack design, optimized current distribution, and enhanced thermal and fluid management strategies will be necessary to increase practical power density while maintaining high energy efficiency. The results of the present study therefore illustrate both the promise and the limitations of Al-air technology: while its high specific energy makes it attractive as a secondary onboard energy source, successful integration into electric vehicles will depend on continued progress in electrochemical stability, system engineering, and operational management of electrolyte and gas byproducts.

6.4 Conclusions

In conclusion, this detailed simulation study shows that incorporating a high-specific-energy Al-air battery alongside a Li-ion pack can substantially improve EV performance at the vehicle level. Operating the Al-air battery as a range extender (Concept A) enabled a 65%-downsized Li-ion pack to **s**urpas**s** the driving range of a full-capacity Li-ion baseline, while reducing total battery system mass by more than half and keeping capital costs within the baseline range. Likewise, using the Al-air system as an APU (Concept B) to supply auxiliary loads relieved the Li-ion pack of parasitic demands, translating into range increases of 44-96 km (up to ~87% improvement) under standard cycles. These results confirm that high-energy-density but mechanically rechargeable chemistries like Al-air can be effectively harnessed as secondary energy sources in dual-storage architecture. By bridging the gap between the Al-air battery's theoretical energy advantage and real-world vehicle integration, the proposed hybrid configuration overcomes key Li-ion pack limitations. It thus offers a viable path toward dramatically extending EV range and efficiency without incurring prohibitive weight or cost, underlining the promise of Al-air integration in next-generation electric vehicle designs.

6.5 Future Work

While the present study demonstrates the feasibility of integrating Al-air batteries as secondary energy sources in electric vehicles through system-level simulation, several avenues remain for further development and validation. One important direction involves the implementation of higher-fidelity electrochemical models for the Al-air cell and stack. The current study employs a semi-empirical polarization-based representation calibrated to experimental discharge data. While this approach is well suited for system-level vehicle simulations, it does not explicitly capture detailed electrochemical phenomena such as electrolyte transport limitations, aluminum surface passivation, hydrogen evolution kinetics, and air-cathode degradation. Future work will therefore focus on developing physics-informed models that couple electrochemical reaction kinetics, electrolyte chemistry, and mass transport processes to enable more accurate prediction of cell performance across varying operating conditions. A second important step is experimental validation of the proposed Al-air-assisted vehicle architecture. Although the present framework integrates experimentally derived polarization data, the system-level interaction between the Al-air subsystem, Li-ion battery pack, and vehicle powertrain has been evaluated only through simulation. Experimental validation using laboratory-scale Al-air stacks operating under controlled current profiles representative of vehicle drive cycles would provide valuable insight into practical system behavior. Such testing would enable validation of aluminum consumption rates, hydrogen generation characteristics, and overall energy conversion efficiency under dynamic operating conditions. Future work will also investigate optimization of pack sizing and energy management strategies for dual-energy-storage architectures. The results presented here illustrate that different combinations of Li-ion capacity and Al-air energy storage can significantly influence vehicle range, system mass, and operational behavior. A systematic optimization framework incorporating vehicle dynamics, electrochemical constraints, and control strategies could identify optimal pack configurations for different vehicle classes and driving conditions. In addition, advanced control strategies that dynamically regulate Al-air power output based on load demand, battery SOC, and remaining aluminum fuel may further improve system efficiency and reduce transient stress on the Li-ion battery. These research directions will help bridge the gap between system-level modeling and practical implementation of Al-air batteries in electric vehicle architectures, supporting the development of next-generation hybrid electrochemical energy systems capable of combining high power capability with extremely high onboard energy density.

Chapter 7 Conclusions and Future Work

This thesis presents a comprehensive multiscale investigation of aluminum-air (Al-air) batteries, spanning techno-economic evaluation, experimental performance characterization, corrosion modeling, and system-level integration within electric vehicle (EV) architectures. The central objective was to establish a unified framework linking electrochemical behavior to practical system-level performance, thereby evaluating the feasibility of Al-air batteries as viable energy storage and range-extending solutions.

From a techno-economic perspective, the analysis conducted in Chapter 3 demonstrates that metal-air batteries, particularly Al-air systems, offer a substantial advantage in gravimetric energy density compared to conventional lithium-ion batteries. While typical Li-ion battery packs operate in the range of 150-250 Wh kg^{-1}, Al-air systems exhibit theoretical energy densities exceeding 2000 Wh kg^{-1}, with practical system-level values approaching 700-900 Wh kg^{-1} under optimized conditions. When integrated into EV architectures, this translates to a significant potential for range extension, with modeled scenarios indicating improvements on the order of 2-5× compared to baseline Li-ion configurations, depending on system design and operating conditions. However, the analysis also reveals that these benefits are constrained by system-level considerations, including auxiliary components, electrolyte management, and overall cost, highlighting the importance of integrated techno-economic evaluation.

Experimental investigations in Chapter 4 provide detailed insights into the performance of Al-air batteries under varying electrolyte compositions and operating conditions. The results demonstrate that alkaline electrolytes, particularly in the range of 6-8 M concentration, achieve optimal performance by balancing ionic conductivity and electrochemical kinetics. Peak power densities exceeding 500 mW cm^{-2} were observed under controlled conditions, while discharge tests at moderate current densities (e.g., ~80-100 mA cm^{-2}) exhibited stable voltage profiles in the range of 1.0-1.2 V. However, the experiments also confirm that increasing electrolyte concentration beyond optimal levels leads to accelerated parasitic corrosion and hydrogen evolution, resulting in diminished efficiency. These findings establish a clear trade-off between performance and degradation, emphasizing the need for controlled optimization of operating conditions.

Chapter 5 advances the understanding of corrosion behavior through the development of a predictive modeling framework based on artificial neural networks (ANN) coupled with genetic algorithm (GA) and multi-objective optimization (NSGA-II). The ANN models achieved high

predictive accuracy, with coefficient of determination (R^2) values approaching unity ($R^2 > 0.99$) for both corrosion potential (Ecorr) and corrosion current density (Icorr). The optimization framework successfully identified operating regimes that simultaneously maximize Ecorr and minimize Icorr, demonstrating the capability to navigate complex, multidimensional parameter spaces. This represents a significant advancement over conventional empirical approaches, enabling systematic prediction and optimization of corrosion kinetics under varying electrolyte and temperature conditions.

At the system level, Chapter 6 demonstrates the integration of Al-air batteries within a dual-energy storage EV architecture using MATLAB/Simulink. The results show that Al-air systems can effectively function as range extenders, providing supplemental energy when the state-of-charge (SOC) of the primary Li-ion battery falls below a predefined threshold. Simulation results under standard driving cycles (UDDS, WLTP, and HWFET) indicate that Al-air integration can mitigate rapid SOC depletion and extend driving range, particularly in reduced-capacity Li-ion configurations (e.g., 50% and 35% baseline energy). The system-level analysis further highlights the importance of control strategies, such as SOC window-based activation, in ensuring stable and efficient operation.

Overall, the findings of this thesis demonstrate that while Al-air batteries offer significant advantages in energy density and potential range extension, their practical implementation is governed by complex interactions between electrochemical performance, corrosion behavior, and system-level constraints. The integration of experimental characterization, data-driven modeling, and vehicle-level simulation provides a comprehensive framework for evaluating and optimizing Al-air battery systems.

In summary, this thesis establishes that Al-air batteries are not merely high-energy theoretical systems, but viable candidates for practical energy applications when supported by optimized electrochemical design, predictive modeling, and intelligent system integration.

While this thesis provides a comprehensive foundation for the development and integration of Al-air batteries, several avenues for future research remain to further advance the technology toward practical deployment.

First, the development of higher-fidelity electrochemical models is essential to capture the dynamic interactions between corrosion, mass transport, and electrode kinetics. Future work

should focus on coupling equivalent circuit models with physics-based formulations to improve predictive accuracy while maintaining computational efficiency.

Second, further investigation into electrolyte engineering and additive design is required to mitigate parasitic corrosion and hydrogen evolution. The incorporation of corrosion inhibitors, electrolyte additives, and hybrid electrolyte systems may provide pathways to enhance anode stability and improve overall system efficiency.

Third, the ANN-GA framework developed in this thesis can be extended to include broader datasets and additional input parameters, such as flow conditions, electrode geometry, and long-term degradation effects. Integration with explainable AI techniques, such as SHAP analysis, can further enhance interpretability and provide deeper insight into the governing factors influencing corrosion behavior.

Fourth, future studies should focus on experimental validation of system-level integration, including the development of prototype dual-energy storage systems and real-world testing under dynamic operating conditions. This would enable validation of simulation results and provide critical insight into practical challenges such as thermal management, electrolyte circulation, and mechanical refueling.

Fifth, the incorporation of life cycle assessment (LCA) and sustainability analysis will be crucial to evaluate the environmental impact of Al-air systems relative to existing battery technologies. This includes assessment of aluminum production, electrolyte usage, recycling strategies, and overall system lifecycle emissions.

Finally, continued collaboration with industry, particularly in the development of advanced Al-air system architectures such as rotating electrode designs and galvanic generator configurations, will be essential to bridge the gap between laboratory research and commercialization.

References

[1] Wang X, Dong X, Zhang Z, Wang Y. Transportation carbon reduction technologies: A review of fundamentals, application, and performance. Journal of Traffic and Transportation Engineering (English Edition) 2024;11:1340-77. https://doi.org/10.1016/J.JTTE.2024.11.001.

[2] Jannesar Niri A, Poelzer GA, Zhang SE, Rosenkranz J, Pettersson M, Ghorbani Y. Sustainability challenges throughout the electric vehicle battery value chain. Renewable and Sustainable Energy Reviews 2024;191:114176. https://doi.org/10.1016/J.RSER.2023.114176.

[3] Sciatti F, Tamburrano P, Distaso E, Amirante R, Radogna A V., Morciano A, et al. A comprehensive overview of lithium-ion batteries for electric vehicles: Materials, performance, safety, recycling, and emerging technologies. J Energy Storage 2026;144:119694. https://doi.org/10.1016/J.EST.2025.119694.

[4] Camuamba E, Damásio B, Mendonça S. Assessing critical mineral occurrence in battery technologies. Resources Policy 2025;111:105755. https://doi.org/10.1016/J.RESOURPOL.2025.105755.

[5] Rai S, Prachi P, Kant CR, Jha R. Metal-air batteries: From fundamental mechanisms to practical applications. J Alloys Compd 2025;1033:180805. https://doi.org/10.1016/J.JALLCOM.2025.180805.

[6] Haruna K, Musa A, Olabintan AB, Saleh TA. Emerging frontiers in aluminum-air batteries: Advances, challenges, and prospects for lightweight, high-energy-density storage. J Energy Storage 2026;149:120152. https://doi.org/10.1016/J.EST.2025.120152.

[7] Mahmoudi H, Alam A, Theato P, Gaele MF, Gargiulo P, Li H, et al. Additives for Aluminum-Air Batteries: A Review. Small 2026;22:e14913. https://doi.org/10.1002/SMLL.202514913.

[8] Huang Y, Wang C, Lyu H, Allen MG, Allen SAB. Micro aluminum-air batteries for extended operational duration of small-scale quadrotors. Scientific Reports 2025 15:1 2025;15:44431-. https://doi.org/10.1038/s41598-025-23776-4.

[9] Karthikeyan N, Vijayalakshmi KA. Air Cathode Built From Rice Husk Derived Air Plasma Exposed SiO2@Al-Doped Cadmium Oxide Employed in Aluminum Air Batteries and Supercapacitor. ChemNanoMat 2026;12:e202500424. https://doi.org/10.1002/CNMA.202500424.

[10] Pourzolfaghar H, Chen YC, Dalan AK, Khadem Hosseini R, Liao CP, Hosseini S, et al. Inorganic-organic hybrid additive modulation for inhibiting the hydrogen evolution reaction in aluminum-air batteries. J Energy Storage 2026;151. https://doi.org/10.1016/J.EST.2025.120250.

[11] Tian H, Zhang J, Fan B, Yang B, Li H, Zhao J. Interfacial engineering of neutral aluminum-air batteries via synergistic organic-inorganic composite additive for balancing discharge activation and corrosion suppression. J Power Sources 2026;665:239002. https://doi.org/10.1016/J.JPOWSOUR.2025.239002.

[12] Liu X, Dong Y, Ma J, Huang J, Wang Z, Cheng S, et al. Synergistic interface engineering with anionic imidazole and stannate for hydrogen evolution suppression in aluminum-air batteries. J Power Sources 2026;667:239325. https://doi.org/10.1016/J.JPOWSOUR.2026.239325.

[13] Cruz Orellana SN, Acevedo-Peña P, Díaz-Góngora JAI, Reguera E. Ligand-engineered MOF-derived composites for dual energy storage in aluminum-air batteries and asymmetric supercapacitors. Journal of Physics and Chemistry of Solids 2026;215:113730. https://doi.org/10.1016/J.JPCS.2026.113730.

[14] Prawin Babu L, Jafferson JM, Radha R. 3D-Printed AlSi10Mg Lattice Anodes in Aluminum-Air Batteries: Effects of Electrolyte and Structure. Results in Engineering 2026;29. https://doi.org/10.1016/J.RINENG.2026.109553.

[15] Zheng Z, Wang L, Yang X, Lu Y. Effect of interface regulation on the performance and lifetime of cathode catalyst FeMo2S4@NC in aluminum-air batteries. Applications of Surface Science 2026;727. https://doi.org/10.1016/J.APSUSC.2026.166016.

[16] Østergaard PA, Duic N, Noorollahi Y, Kalogirou S. Latest progress in Sustainable Development using renewable energy technology. Renew Energy 2020;162:1554-62. https://doi.org/10.1016/j.renene.2020.09.124.

[17] Gaele MF, Di Palma TM. Polymer Electrolytes for Al-Air Batteries: Current State and Future Perspectives. Energy & Fuels 2022;36:12875-95. https://doi.org/10.1021/acs.energyfuels.2c02453.

[18] Gouveia J, Mendes A, Monteiro R, Mata TM, Caetano NS, Martins AA. Life cycle assessment of a vanadium flow battery. Energy Reports 2020;6:95-101. https://doi.org/10.1016/J.EGYR.2019.08.025.

[19] Aldhafeeri T, Tran MK, Vrolyk R, Pope M, Fowler M. A Review of Methane Gas Detection Sensors: Recent Developments and Future Perspectives. Inventions 2020, Vol 5, Page 28 2020;5:28. https://doi.org/10.3390/inventions5030028.

[20] Shittu E, Suman R, Ravikumar MK, Shukla AK, Zhao G, Patil S, et al. Life cycle assessment of soluble lead redox flow battery. J Clean Prod 2022;337:130503. https://doi.org/10.1016/j.jclepro.2022.130503.

[21] GSR 2025 | RENEWABLES 2025 GLOBAL STATUS REPORT n.d. https://www.ren21.net/gsr-2025/ (accessed April 5, 2026).

[22] Branco H, Castro R, Setas Lopes A. Battery energy storage systems as a way to integrate renewable energy in small isolated power systems. Energy for Sustainable Development 2018;43:90-9. https://doi.org/10.1016/j.esd.2018.01.003.

[23] Tooryan F, HassanzadehFard H, Collins ER, Jin S, Ramezani B. Smart integration of renewable energy resources, electrical, and thermal energy storage in microgrid applications. Energy 2020;212:118716. https://doi.org/10.1016/J.ENERGY.2020.118716.

[24] Legala A, Kubesh M, Chundru V, Conway G, AI XL-E and, 2024 undefined. Machine learning modeling for fuel cell-battery hybrid power system dynamics in a Toyota Mirai 2 vehicle under various drive cycles. *Energy and AI*, *17*, 100415. https://doi.org/10.1016/j.egyai.2024.100415.

[25] Narassimhan E, Myslikova Z, Sims Gallagher - K, Luh S, Kannan R, McKenna R, et al. Review—Electromobility: Batteries or Fuel Cells? J Electrochem Soc 2015;162:A2605. https://doi.org/10.1149/2.0211514JES.

[26] Neubauer, J., & Wood, E. (2014). The impact of range anxiety and home, workplace, and public charging infrastructure on simulated battery electric vehicle lifetime utility. *Journal of power sources*, *257*, 12-20. https://doi.org/10.1016/j.jpowsour.2014.01.075.

[27] Singer M. Consumer views on plug-in electric vehicles--National Benchmark Report 2016.

[28] Li, W., Long, R., Chen, H., & Geng, J. (2017). A review of factors influencing consumer intentions to adopt battery electric vehicles. *Renewable and Sustainable Energy Reviews*, *78*, 318-328. https://doi.org/10.1016/j.rser.2017.04.076.

[29] Tran MK, Bhatti A, Vrolyk R, Wong D, Panchal S, Fowler M, et al. A Review of Range Extenders in Battery Electric Vehicles: Current Progress and Future Perspectives. World

Electric Vehicle Journal 2021, Vol 12, Page 54 2021;12:54. https://doi.org/10.3390/wevj12020054.

[30] Cano, Z. P., Banham, D., Ye, S., Hintennach, A., Lu, J., Fowler, M., & Chen, Z. (2018). Batteries and fuel cells for emerging electric vehicle markets. *Nature energy*, *3*(4), 279-289. https://doi.org/10.1038/s41560-018-0108-1.

[31] Zackrisson M, Fransson K, Hildenbrand J, Lampic G, O'Dwyer C. Life cycle assessment of lithium-air battery cells. J Clean Prod 2016;135:299-311. https://doi.org/10.1016/J.JCLEPRO.2016.06.104.

[32] Zhang, X., Li, Z., Luo, L., Fan, Y., & Du, Z. (2022). A review on thermal management of lithium-ion batteries for electric vehicles. Energy, 238, 121652. https://doi.org/10.1016/j.energy.2021.121652

[33] O'hayre RP, Colella WG, Prinz FB, Adams RH, John W. Fuel cell fundamentals. 2016.

[34] Alaswad, A., Baroutaji, A., Achour, H., Carton, J., Al Makky, A., & Olabi, A. G. (2016). Developments in fuel cell technologies in the transport sector. *International Journal of Hydrogen Energy*, *41*(37), 16499-16508. https://doi.org/10.1016/j.ijhydene.2016.03.164

[35] Ramasubramanian, B., Rao, R. P., Chellappan, V., & Ramakrishna, S. (2022). Towards sustainable fuel cells and batteries with an AI perspective. *Sustainability*, *14*(23), 16001. https://doi.org/10.3390/su142316001

[36] Welcome to the Lithium-ion Age Global lithium S&D analysis highlights opportunity for high-quality assets 2016.

[37] Placke T, Kloepsch R, Dühnen S, Winter M. Lithium ion, lithium metal, and alternative rechargeable battery technologies: the odyssey for high energy density. SpringerT Placke, R Kloepsch, S Dühnen, M WinterJournal of Solid State Electrochemistry, 2017•Springer 2017;21:1939-64. https://doi.org/10.1007/s10008-017-3610-7.

[38] Li M, Lu J, Chen Z, Amine K. 30 years of lithium-ion batteries. Wiley Online LibraryM Li, J Lu, Z Chen, K AmineAdvanced Materials, 2018•Wiley Online Library 2018;30. https://doi.org/10.1002/adma.201800561.

[39] Fit for 55: MEPs back objective of zero emissions for cars and vans in 2035 | News | European Parliament n.d. https://www.europarl.europa.eu/news/en/press-room/20220603IPR32129/fit-for-55-meps-back-objective-of-zero-emissions-for-cars-and-vans-in-2035 (accessed March 29, 2026).

[40] Global EV Outlook 2024 - Analysis - IEA n.d. https://www.iea.org/reports/global-ev-outlook-2024 (accessed April 5, 2026).

[41] Yu, X., Chen, R., Gan, L., Li, H., & Chen, L. (2023). Battery safety: From lithium-ion to solid-state batteries. *Engineering*, *21*, 9-14. https://doi.org/10.1016/j.eng.2022.06.022

[42] Feng, X., Ren, D., He, X., & Ouyang, M. (2020). Mitigating thermal runaway of lithium-ion batteries. *Joule*, *4*(4), 743-770. https://doi.org/10.1016/j.joule.2020.02.010

[43] Deng, D. (2015). Li-ion batteries: basics, progress, and challenges. Energy Science & Engineering, 3(5), 385-418. https://doi.org/10.1002/ese3.95.

[44] Mokhtar M, Talib MZM, Majlan EH, Tasirin SM, Ramli WMFW, Daud WRW, et al. Recent developments in materials for aluminum-air batteries: A review. Journal of Industrial and Engineering Chemistry 2015;32:1-20. https://doi.org/10.1016/J.JIEC.2015.08.004.

[45] Wen H, Liu Z, Qiao J, Chen R, Zhao R, Wu J, et al. High energy efficiency and high power density aluminum-air flow battery. Int J Energy Res 2020;44:7568-79. https://doi.org/10.1002/ER.5485;REQUESTEDJOURNAL:JOURNAL:1099114X;PAGE:STRING:ARTICLE/CHAPTER.

[46] Hou J, Yang M, Wang D, Zhang J, Hou J, Zhang J, et al. Fundamentals and challenges of lithium ion batteries at temperatures between− 40 and 60° C. Wiley Online LibraryJ Hou, M Yang, D Wang, J ZhangAdvanced Energy Materials, 2020•Wiley Online Library 2020;10. https://doi.org/10.1002/aenm.201904152.

[47] Bandhauer TM, Garimella S, Fuller TF. A Critical Review of Thermal Issues in Lithium-Ion Batteries. J Electrochem Soc 2011;158:R1. https://doi.org/10.1149/1.3515880/XML.

[48] Costa CM, Barbosa JC, Gonçalves R, Castro H, Campo FJD, Lanceros-Méndez S. Recycling and environmental issues of lithium-ion batteries: Advances, challenges and opportunities. Energy Storage Mater 2021;37:433-65. https://doi.org/10.1016/j.ensm.2021.02.032.

[49] Liu Q, Pan Z, Wang E, An L, Sun G. Aqueous metal-air batteries: Fundamentals and applications. Energy Storage Mater 2020;27:478-505. https://doi.org/10.1016/j.ensm.2019.12.011.

[50] Li Y, Lu J. Metal-Air Batteries: Will They Be the Future Electrochemical Energy Storage Device of Choice? ACS Energy Lett 2017;2:1370-7. https://doi.org/10.1021/acsenergylett.7b00119.

[51] Hardwick, L. J., & De León, C. P. (2018). Rechargeable multi-valent metal-air batteries. *Johnson Matthey Technology Review*, *62*(2), 134-149. https://doi.org/10.1595/205651318X696729

[52] Fu J, Paul Cano Z, Gyu Park M, Yu A, Fowler M, Chen Z, et al. Electrically Rechargeable Zinc-Air Batteries: Progress, Challenges, and Perspectives. Advanced Materials 2017;29:1604685. https://doi.org/10.1002/ADMA.201604685.

[53] Buckingham, R., Asset, T., & Atanassov, P. (2021). Aluminum-air batteries: A review of alloys, electrolytes and design. *Journal of Power Sources*, *498*, 229762. https://doi.org/10.1016/j.jpowsour.2021.229762

[54] Feng, Y., Xiong, W., Zhang, J., Wang, R., & Wang, N. (2016). Electrochemical discharge performance of the Mg–Al–Pb–Ce–Y alloy as the anode for Mg–air batteries. *Journal of Materials chemistry A*, *4*(22), 8658-8668. https://doi.org/10.1039/C6TA02574A

[55] Zhang T, Tao Z, Horizons JC-M, 2014 undefined. Magnesium-air batteries: from principle to application. PubsRscOrgT Zhang, Z Tao, J ChenMaterials Horizons, 2014. https://doi.org/10.1039/c3mh00059a.

[56] Arafat, Y., Azhar, M. R., Zhong, Y., Tadé, M. O., & Shao, Z. (2021). Metal-free carbon based air electrodes for Zn-air batteries: Recent advances and perspective. *Materials Research Bulletin*, *140*, 111315. https://doi.org/10.1016/j.materresbull.2021.111315

[57] Bi X, Jiang Y, Chen R, Du Y, Zheng Y, Yang R, et al. Rechargeable zinc-air versus lithium-air battery: from fundamental promises toward technological potentials. Wiley Online Library. 2024;14. https://doi.org/10.1002/AENM.202302388.

[58] Li L, Chang Z wen, Zhang XB. Recent progress on the development of metal-air batteries. Wiley Online Library 2017;1. https://doi.org/10.1002/ADSU.201700036.

[59] Li T, Peng X, Cui P, Shi G, Yang W, Chen Z, et al. Recent progress and future perspectives of flexible metal-air batteries. Wiley Online Library 2021;2:519-53. https://doi.org/10.1002/SMM2.1076.

[60] Survey USG. Mineral commodity summaries 2024. Mineral Commodity Summaries 2024. https://doi.org/10.3133/MCS2024.

[61] Alemu MA, Getie MZ, Worku AK. Advancement of electrically rechargeable multivalent metal-air batteries for future mobility. Springer 2023;29:3421-35. https://doi.org/10.1007/S11581-023-05131-7.

[62] Wang C, Yu Y, Niu J, Liu Y, Bridges D, Liu X, et al. Recent Progress of Metal-Air Batteries—A Mini Review. Applied Sciences 2019, Vol 9, Page 2787 2019;9:2787. https://doi.org/10.3390/APP9142787.

[63] Ren X, Society YW-J of the AC, 2013 undefined. A low-overpotential potassium-oxygen battery based on potassium superoxide. ACS Publications 2013;135:2923-6. https://doi.org/10.1021/JA312059Q.

[64] Han X, Li X, White J, Zhong C, Deng Y, Hu W, et al. Metal-Air Batteries: From Static to Flow System. Adv Energy Mater 2018;8:1801396. https://doi.org/10.1002/aenm.201801396.

[65] Cheng F, Reviews JC-CS, 2012 undefined. Metal-air batteries: from oxygen reduction electrochemistry to cathode catalysts. PubsRscOrg 2012;41:2172-92. https://doi.org/10.1039/c1cs15228a.

[66] Cheng, J., Zhang, L., Yang, Y. S., Wen, Y. H., Cao, G. P., & Wang, X. D. (2007). Preliminary study of single flow zinc–nickel battery. *Electrochemistry Communications*, *9*(11), 2639-2642. https://doi.org/10.1016/j.elecom.2007.08.016

[67] Fu J, Zhang J, Song X, Zarrin H, Tian X, Qiao J, et al. A flexible solid-state electrolyte for wide-scale integration of rechargeable zinc-air batteries. PubsRscOrg 2016;9:663. https://doi.org/10.1039/c5ee03404c.

[68] Li F, Zhang T, Science HZ-E& E, 2013 undefined. Challenges of non-aqueous Li-O 2 batteries: electrolytes, catalysts, and anodes. PubsRscOrg 2010. https://doi.org/10.1039/c3ee00053b.

[69] Yadegari H, Sun Q, Sun X, Yadegari H, Sun Q, Sun X. Sodium-oxygen batteries: a comparative review from chemical and electrochemical fundamentals to future perspective. Wiley Online Library 2016;28:7065-93. https://doi.org/10.1002/ADMA.201504373.

[70] Zhang X. Metal-air batteries: fundamentals and applications. 2018.

[71] Liu Q, Chang Z, Li Z, Zhang X. Flexible metal-air batteries: Progress, challenges, and perspectives. Wiley Online LibraryWiley Online Library 2018;2. https://doi.org/10.1002/SMTD.201700231.

[72] McCloskey BD, Scheffler R, Speidel A, Bethune DS, Shelby RM, Luntz AC. On the Efficacy of Electrocatalysis in Nonaqueous Li-O2 Batteries. ACS Publications 2011;133:18038-41. https://doi.org/10.1021/JA207229N.

[73] Peng Z, Freunberger SA, Chen Y, Bruce PG. A Reversible and Higher-Rate Li-O2 Battery. ScienceOrg 2012;337:563-6. https://doi.org/10.1126/SCIENCE.1223985.

[74] Chen Y, Freunberger SA, Peng Z, Fontaine O, Bruce PG. Charging a Li-O2 battery using a redox mediator. NatureCom 2013. https://doi.org/10.1038/NCHEM.1646.

[75] Xu, J. J., Wang, Z. L., Xu, D., Zhang, L. L., & Zhang, X. B. (2013). Tailoring deposition and morphology of discharge products towards high-rate and long-life lithium-oxygen batteries. *Nature communications*, *4*(1), 2438. https://doi.org/10.1038/ncomms3438.

[76] Zhang T, communications HZ-N, 2013 undefined. A reversible long-life lithium-air battery in ambient air. NatureCom 2013. https://doi.org/10.1038/ncomms2855.

[77] Tu, K. N., & Gusak, A. N. (2020). Mean-time-to-failure equations for electromigration, thermomigration, and stress migration. *IEEE Transactions on Components, Packaging and Manufacturing Technology*, *10*(9), 1427-1431. doi: 10.1109/TCPMT.2020.3003003.

[78] Ye L, Liao M, Zhao T, Sun H, Zhao Y, Sun X, et al. A sodiophilic interphase-mediated, dendrite-free anode with ultrahigh specific capacity for sodium-metal batteries. Wiley Online Library 2019;131:17210-6. https://doi.org/10.1002/ANGE.201910202.

[79] Olabi, A. G., Sayed, E. T., Wilberforce, T., Jamal, A., Alami, A. H., Elsaid, K., ... & Abdelkareem, M. A. (2021). Metal-air batteries—a review. *Energies*, *14*(21), 7373. https://doi.org/10.3390/en14217373

[80] Arai, H. (2021). Introduction—General features of metal-air batteries. In *Electrochemical Power Sources: Fundamentals, Systems, and Applications* (pp. 1-10). Elsevier. https://doi.org/10.1016/B978-0-444-64333-9.00001-1

[81] Arai H, Ikezawa A. Electrochemical Devices | Metal-Air Batteries. Encyclopedia of Electrochemical Power Sources: Volume 1-7, Second Edition 2024;1:V1:292-V1:300. https://doi.org/10.1016/B978-0-323-96022-9.00147-X.

[82] Arai, H. (2015). Metal Storage/Metal Air (Zn, Fe, Al, Mg). In *Electrochemical Energy Storage for Renewable Sources and Grid Balancing* (pp. 337-344). Elsevier. https://doi.org/10.1016/B978-0-444-62616-5.00018-8

[83] Zhang, X. B. (Ed.). (2018). *Metal-air batteries: fundamentals and applications*. John Wiley & Sons.

[84] Park M, Young Kim K, Seo H, Eun Cheon Y, Hyun Koh J, Sun H, et al. Practical challenges associated with catalyst development for the commercialization of Li-air batteries.

JecstOrgM Park, KY Kim, H Seo, YE Cheon, JH Koh, H Sun, TJ KimJournal of Electrochemical Science and Technology, 2014•jecstOrg 2014;5:1-18. https://doi.org/10.5229/JECST.2014.5.1.1.

[85] Suryatna A, Raya I, Thangavelu L, Alhachami FR, Kadhim MM, Altimari US, et al. A review of high-energy density lithium-air battery technology: investigating the effect of oxides and nanocatalysts. Wiley Online Library 2022;2022. https://doi.org/10.1155/2022/2762647.

[86] Li J, Hou L, Yu M, Li Q, Zhang T, Sun H. Review and recent advances of oxygen transfer in Li-air batteries. Wiley Online Library 2021;8:3588-603. https://doi.org/10.1002/CELC.202100560.

[87] Jilani A, Awan Z, Taqvi SAA, Khan F, Alshahrani T. Recent Advances in the Development of Li-Air Batteries, Experimental and Predictive Approaches-Prospective, Challenges, and Opportunities. Wiley Online Library 2024;11:95-114. https://doi.org/10.1002/CBEN.202300036.

[88] Manthiram A, Li L. Hybrid and aqueous lithium-air batteries. Wiley Online Library 2015;5. https://doi.org/10.1002/AENM.201401302.

[89] Zhang Z, Xiao X, Zhu X, Tan P. Addressing transport issues in non-aqueous Li-air batteries to achieving high electrochemical performance. Springer 2023;6:18. https://doi.org/10.1007/S41918-022-00157-3.

[90] Luntz AC, McCloskey BD. Nonaqueous Li-air batteries: a status report. ACS Publications 2014;114:11721-50. https://doi.org/10.1021/CR500054Y.

[91] Feng N, He P, Zhou H. Critical Challenges in Rechargeable Aprotic Li-O2 Batteries. Wiley Online LibraryN Feng, P He, H ZhouAdvanced Energy Materials, 2016•Wiley Online Library 2016;6. https://doi.org/10.1002/AENM.201502303.

[92] Shu C, Wang J, Long J, Liu H-K, Dou S-X, Shu CZ, et al. Understanding the reaction chemistry during charging in aprotic lithium-oxygen batteries: existing problems and solutions. Wiley Online LibraryC Shu, J Wang, J Long, HK Liu, SX DouAdvanced Materials, 2019•Wiley Online Library 2019;31. https://doi.org/10.1002/ADMA.201804587.

[93] Zhang T, Imanishi N, Takeda Y, Yamamoto O. Aqueous Lithium/Air Rechargeable Batteries. Chem Lett 2011;40:668-73. https://doi.org/10.1246/CL.2011.668.

[94] Imanishi, N., & Yamamoto, O. (2014). Rechargeable lithium–air batteries: characteristics and prospects. *Materials today*, *17*(1), 24-30. https://doi.org/10.1016/j.mattod.2013.12.004

[95] Imanishi, N., & Yamamoto, O. (2019). Perspectives and challenges of rechargeable lithium–air batteries. *Materials Today Advances*, *4*, 100031. https://doi.org/10.1016/j.mtadv.2019.100031

[96] Chen P, Bai F, Deng J wen, Liu B, Zhang T. Recent progresses and challenges in aqueous lithium-air batteries relating to the solid electrolyte separator: A mini-review. FrontiersinOrg 2022;10. https://doi.org/10.3389/FCHEM.2022.1035691/FULL.

[97] Imanishi, N., Hasegawa, S., Zhang, T., Hirano, A., Takeda, Y., & Yamamoto, O. (2008). Lithium anode for lithium-air secondary batteries. *Journal of Power Sources*, *185*(2), 1392-1397. https://doi.org/10.1016/j.jpowsour.2008.07.080

[98] Wang, Y., & Zhou, H. (2010). A lithium-air battery with a potential to continuously reduce O2 from air for delivering energy. *Journal of Power Sources*, *195*(1), 358-361. https://doi.org/10.1016/j.jpowsour.2009.06.109

[99] Zhang T, Imanishi N, Hasegawa S, Hirano A, Xie J, Takeda Y, et al. Li/polymer electrolyte/water stable lithium-conducting glass ceramics composite for lithium-air secondary batteries with an aqueous electrolyte. IopscienceIopOrg 2008;155:A965. https://doi.org/10.1149/1.2990717/META.

[100] He, P., Wang, Y., & Zhou, H. (2010). A Li-air fuel cell with recycle aqueous electrolyte for improved stability. *Electrochemistry Communications*, *12*(12), 1686-1689. https://doi.org/10.1016/j.elecom.2010.09.025

[101] Hasegawa S, Imanishi N, Zhang T, Xie J, Hirano A, Takeda Y, et al. Study on lithium/air secondary batteries—Stability of NASICON-type lithium ion conducting glass-ceramics with water. J Power Sources 2009;189:371-7. https://doi.org/10.1016/J.JPOWSOUR.2008.08.009.

[102] Li, L., Zhao, X., & Manthiram, A. (2012). A dual-electrolyte rechargeable Li-air battery with phosphate buffer catholyte. *Electrochemistry Communications*, *14*(1), 78-81. https://doi.org/10.1016/j.elecom.2011.11.007

[103] Shimonishi Y, Zhang T, Johnson P, Imanishi N, Hirano A, Takeda Y, et al. A study on lithium/air secondary batteries—Stability of NASICON-type glass ceramics in acid

solutions. J Power Sources 2010;195:6187-91. https://doi.org/10.1016/J.JPOWSOUR.2009.11.023.

[104] Ding, F., Xu, W., Shao, Y., Chen, X., Wang, Z., Gao, F., ... & Zhang, J. G. (2012). H+ diffusion and electrochemical stability of Li1+ x+ yAlxTi2− xSiyP3− yO12 glass in aqueous Li/air battery electrolytes. *Journal of Power Sources*, *214*, 292-297. https://doi.org/10.1016/j.jpowsour.2012.04.058

[105] Bidault, F., Brett, D. J. L., Middleton, P. H., & Brandon, N. P. (2009). Review of gas diffusion cathodes for alkaline fuel cells. *Journal of Power Sources*, *187*(1), 39-48. https://doi.org/10.1016/j.jpowsour.2008.10.106

[106] He P, Zhang T, Jiang J, Zhou H. Lithium-air batteries with hybrid electrolytes. ACS PublicationsP He, T Zhang, J Jiang, H ZhouThe Journal of Physical Chemistry Letters, 2016•ACS Publications 2016;7:1267-80. https://doi.org/10.1021/ACS.JPCLETT.6B00080.

[107] Manthiram A, Yu X, Materials SW-NR, 2017 undefined. Lithium battery chemistries enabled by solid-state electrolytes. NatureComA Manthiram, X Yu, S WangNature Reviews Materials, 2017•natureCom 2017. https://doi.org/10.1038/natrevmats.2016.103.

[108] Choudhury S, Stalin S, Deng Y, Archer LA. Soft colloidal glasses as solid-state electrolytes. ACS PublicationsS Choudhury, S Stalin, Y Deng, LA ArcherChemistry of Materials, 2018•ACS Publications 2018;30:5996-6004. https://doi.org/10.1021/ACS.CHEMMATER.8B02227.

[109] Wu, Y., Li, Y., Wang, Y., Liu, Q., Chen, Q., & Chen, M. (2022). Advances and prospects of PVDF based polymer electrolytes. *Journal of Energy Chemistry*, *64*, 62-84. https://doi.org/10.1016/j.jechem.2021.04.007

[110] Wang HF, Wang XX, Li F, Xu JJ. Fundamental Understanding and Construction of Solid-State Li− Air Batteries. Wiley Online LibraryHF Wang, XX Wang, F Li, JJ XuSmall Science, 2022•Wiley Online Library 2022;2. https://doi.org/10.1002/SMSC.202200005.

[111] Vadhva P, Gill TE, Cruddos JH, Said S, Siniscalchi M, Narayanan S, et al. Engineering solution-processed non-crystalline solid electrolytes for Li metal batteries. ACS Publications 2023;35:1168-76. https://doi.org/10.1021/ACS.CHEMMATER.2C03071.

[112] Raj H, Fabre T, Lachal M, Neveu A, Jean J, Steil MC, et al. Stabilizing the NASICON solid electrolyte in an inert atmosphere as a function of physical properties and sintering

conditions for solid-state battery fabrication. ACS Publications 2023;6:1197-207. https://doi.org/10.1021/ACSAEM.2C02464.

[113] Xu A, Wang R, Yao M, Cao J, Li M, Yang C, et al. Electrochemical properties of an Sn-doped LATP ceramic electrolyte and its derived sandwich-structured composite solid electrolyte. MdpiCom. https://doi.org/10.3390/nano12122082

[114] Zhang, H., Yu, Z., Cheng, J., Chen, H., Huang, X., & Tian, B. (2023). Halide/sulfide composite solid-state electrolyte for Li-anode based all-solid-state batteries. *Chinese Chemical Letters*, *34*(11), 108228. https://doi.org/10.1016/j.cclet.2023.108228

[115] Hamao N, Societies KH-J of AC, 2022 undefined. Fabrication of single-grain-layered garnet-type electrolyte sheets by a precursor method. Taylor & Francis 2022;10:1-8. https://doi.org/10.1080/21870764.2021.1974782.

[116] Sun J, Zhao N, Li Y, Guo X, Feng X, Liu X, et al. A rechargeable Li-air fuel cell battery based on garnet solid electrolytes. NatureCom 2017. https://doi.org/10.1038/srep41217.

[117] Lu J, Electronics YL-J of MSM in, 2021 undefined. Perovskite-type Li-ion solid electrolytes: a review. Springer 2021;32:9736-54. https://doi.org/10.1007/S10854-021-05699-8.

[118] Hashishin T, Shimomura H, Kamiyama R, Matsuda M. Analcime with high sodium ion conduction as a solid electrolyte. ACS Publications 2022;126:19480-6. https://doi.org/10.1021/ACS.JPCC.2C05802.

[119] Cao, W., Yang, Y., Deng, J., Li, Y., Cui, C., & Zhang, T. (2021). Localization of electrons within interlayer stabilizes NASICON-type solid-state electrolyte. *Materials Today Energy*, *22*, 100875. https://doi.org/10.1016/j.mtener.2021.100875

[120] Xu Z, Liu Z, Gu Z, Zhao X, Guo D, Yao X. Polyimide-based solid-state gel polymer electrolyte for lithium-oxygen batteries with a long-cycling life. ACS Publications 2023;15:7014-22. https://doi.org/10.1021/ACSAMI.2C22694.

[121] Hamao, N., Yamaguchi, Y., & Hamamoto, K. (2021). Densification of a NASICON-type LATP electrolyte sheet by a cold-sintering process. *Materials*, *14*(16), 4737. https://doi.org/10.3390/ma14164737

[122] Zhu, Q., Ma, J., Li, S., & Mao, D. (2023). Solid-state electrolyte for lithium-air batteries: A review. *Polymers*, *15*(11), 2469. https://doi.org/10.3390/polym15112469

[123] Sun Z, Lu H, Fan L, Hong Q, Leng J, Chen C. Performance of Al-air batteries based on Al-Ga, Al-In and Al-Sn alloy electrodes. IopscienceIopOrg 2015;162:A2116-22. https://doi.org/10.1149/2.0681510JES/META.

[124] Zhang Z, Xiong L, Wang S, Xie Y, You W, Du X. A review of the Al-gas batteries and perspectives for a "Real" Al-air battery. J Power Sources 2023;580:233375. https://doi.org/10.1016/J.JPOWSOUR.2023.233375.

[125] Elia GA, Marquardt K, Hoeppner K, Fantini S, Lin R, Knipping E, et al. An Overview and Future Perspectives of Aluminum Batteries. Advanced Materials 2016;28:7564-79. https://doi.org/10.1002/ADMA.201601357;ISSUE:ISSUE:DOI.

[126] Chen L, Li B, Zhu L, Deng X, Sun X, Liu Y, et al. A PVA/LiCl/PEO interpenetrating composite electrolyte with a three-dimensional dual-network for all-solid-state flexible aluminum-air batteries. RSC Adv 2021;11:39476-83. https://doi.org/10.1039/D1RA07180G.

[127] Haynes W. CRC handbook of chemistry and physics. CRC Press; 2016. https://doi.org/10.1201/9781315380476/CRC-HANDBOOK-CHEMISTRY-PHYSICS-WILLIAM-HAYNES.

[128] Hu Y, Sun D, Luo B, Wang L. Recent Progress and Future Trends of Aluminum Batteries. Energy Technology 2019;7:86-106. https://doi.org/10.1002/ENTE.201800550;CSUBTYPE:STRING:SPECIAL;PAGE:STRING:ARTICLE/CHAPTER.

[129] Bogolowski N, Drillet J-F. An Electrically Rechargeable Al-Air Battery with Aprotic Ionic Liquid Electrolyte. ECS Trans 2017;75:85. https://doi.org/10.1149/07522.0085ECST.

[130] Revel R, Audichon T, Gonzalez S. Non-aqueous aluminium-air battery based on ionic liquid electrolyte. J Power Sources 2014;272:415-21. https://doi.org/10.1016/J.JPOWSOUR.2014.08.056.

[131] Wang D, Gao X, Chen Y, Jin L, Kuss C, Bruce PG. Plating and stripping calcium in an organic electrolyte. Nature Materials 2017 17:1 2017;17:16-20. https://doi.org/10.1038/nmat5036.

[132] Carlin RT, Osteryoung RA. Aluminum Anodization in a Basic Ambient Temperature Molten Salt. J Electrochem Soc 1989;136:1409. https://doi.org/10.1149/1.2096931.

[133] Schröder D, Janek J, Adelhelm P. Nonlithium Aprotic Metal/Oxygen Batteries Using NA, K, MG, or CA as Metal Anode. Encyclopedia of Electrochemistry 2010:1-29. https://doi.org/10.1002/9783527610426.BARD110018;WGROUP:STRING:PUBLICATION.

[134] Xiao N, Ren X, McCulloch WD, Gourdin G, Wu Y. Potassium Superoxide: A Unique Alternative for Metal-Air Batteries. Acc Chem Res 2018;51:2335-43. https://doi.org/10.1021/ACS.ACCOUNTS.8B00332.

[135] Deyab MA, Mohsen Q. Improved battery capacity and cycle life in iron-air batteries with ionic liquid. Renewable and Sustainable Energy Reviews 2021;139:110729. https://doi.org/10.1016/J.RSER.2021.110729.

[136] McKerracher RD, Poncedeleon C, Wills RGA, Shah AA, Walsh FC. A review of the iron-air secondary battery for energy storage. Wiley Online Library 2015;80:323-35. https://doi.org/10.1002/CPLU.201402238.

[137] Zhao X, Xu N, Li X, Gong Y, Huang K. Energy storage characteristics of a new rechargeable solid oxide iron-air battery. RSC Adv 2012;2:10163-6. https://doi.org/10.1039/C2RA21992A.

[138] Arai Hajime, Garche J, Colmenares Luis. Electrochemical power sources : fundamentals, systems and applications : metal-air batteries : present and perspectives 2021.

[139] Sun Q, Dai L, Luo T, Wang L, Liang F, Liu S. Recent advances in solid-state metal-air batteries. Carbon Energy 2023;5:e276. https://doi.org/10.1002/CEY2.276;ISSUE:ISSUE:DOI.

[140] Zhao X, Gong Y, Li X, Xu N, Huang K. Performance of Solid Oxide Iron-Air Battery Operated at 550°C. J Electrochem Soc 2013;160:A1241-7. https://doi.org/10.1149/2.085308JES/PDF.

[141] Zhao X, Gong Y, Li X, - al, Jin X, White RE, et al. Understanding the High-Temperature Solid-Oxide Iron-Air Redox Battery Operated with an Oxygen Shuttle Mechanism: A Computational Study. J Electrochem Soc 2015;162:A1476. https://doi.org/10.1149/2.0401508JES.

[142] Girishkumar G, McCloskey B, Luntz AC, Swanson S, Wilcke W. Lithium−Air Battery: Promise and Challenges. Journal of Physical Chemistry Letters 2010;1:2193-203. https://doi.org/10.1021/JZ1005384.

[143] Lu J, Li L, Park JB, Sun YK, Wu F, Amine K. Aprotic and Aqueous Li-O2 Batteries. Chem Rev 2014;114:5611-40. https://doi.org/10.1021/CR400573B.

[144] Kowalczk I, Read J, Salomon M. Li-air batteries: A classic example of limitations owing to solubilities. DegruyterbrillCom 2007;79:851-60. https://doi.org/10.1351/PAC200779050851/HTML.

[145] Geng D, Ding N, Hor TSA, Chien SW, Liu Z, Wuu D, et al. From lithium-oxygen to lithium-air batteries: challenges and opportunities. Wiley Online Library Wiley Online Library 2016;6. https://doi.org/10.1002/AENM.201502164.

[146] Grande L, Paillard E, Hassoun J, Park JB, Lee YJ, Sun YK, et al. The lithium/air battery: Still an emerging system or a practical reality? Advanced Materials 2015;27:784-800. https://doi.org/10.1002/ADMA.201403064;REQUESTEDJOURNAL:JOURNAL:15214095;WGROUP:STRING:PUBLICATION.

[147] Staniewicz RJ. A Study of the Calcium-Thionyl Chloride Electrochemical System. J Electrochem Soc 1980;127:782-9. https://doi.org/10.1149/1.2129758/PDF.

[148] Weinrich H, Durmus YE, Tempel H, Kungl H, Eichel RA. Silicon and Iron as Resource-Efficient Anode Materials for Ambient-Temperature Metal-Air Batteries: A Review. Materials 2019, Vol 12, Page 2134 2019;12:2134. https://doi.org/10.3390/MA12132134.

[149] Xu X, Hui KS, Dinh DA, Hui KN, Wang H. Recent advances in hybrid sodium-air batteries. Mater Horiz 2019;6:1306-35. https://doi.org/10.1039/C8MH01375F.

[150] Faktorovich-Simon E, Natan A, Peled E, Golodnitsky D. Oxygen redox processes in PEGDME-based electrolytes for the Na-air battery. Journal of Solid State Electrochemistry 2017 22:4 2017;22:1015-22. https://doi.org/10.1007/S10008-017-3843-5.

[151] Ju H, Lee J. High-temperature liquid Sn-air energy storage cell. Journal of Energy Chemistry 2015;24:614-9. https://doi.org/10.1016/J.JECHEM.2015.08.006.

[152] Skyllas-Kazacos M, Cao L, Kazacos M, Kausar N, Mousa A. Vanadium Electrolyte Studies for the Vanadium Redox Battery-A Review. ChemSusChem 2016;9:1521-43. https://doi.org/10.1002/CSSC.201600102;PAGE:STRING:ARTICLE/CHAPTER.

[153] Skyllas-Kazacos M, Grossmith F. Efficient Vanadium Redox Flow Cell. J Electrochem Soc 1987;134:2950-3. https://doi.org/10.1149/1.2100321/PDF.

[154] Andrés CMC, Pérez de la Lastra JM, Andrés Juan C, Plou FJ, Pérez-Lebeña E. Superoxide Anion Chemistry—Its Role at the Core of the Innate Immunity. International Journal of

Molecular Sciences 2023, Vol 24, Page 1841 2023;24:1841. https://doi.org/10.3390/IJMS24031841.

[155] Wu WF, Yan X, Zhan Y. Recent progress of electrolytes and electrocatalysts in neutral aqueous zinc-air batteries. Chemical Engineering Journal 2023;451:138608. https://doi.org/10.1016/J.CEJ.2022.138608.

[156] Li Y, Dai H. Recent advances in zinc-air batteries. Chem Soc Rev 2014;43:5257-75. https://doi.org/10.1039/C4CS00015C.

[157] Xu M, Ivey DG, Xie Z, Qu W. Rechargeable Zn-air batteries: Progress in electrolyte development and cell configuration advancement. J Power Sources 2015;283:358-71. https://doi.org/10.1016/J.JPOWSOUR.2015.02.114.

[158] Ocon JD, Kim JW, Abrenica GHA, Lee JK, Lee J. Quasi-perpetual discharge behaviour in p-type Ge-air batteries. Physical Chemistry Chemical Physics 2014;16:22487-94. https://doi.org/10.1039/C4CP02134G.

[159] Pan J, Xu YY, Yang H, Dong Z, Liu H, Xia BY. Advanced Architectures and Relatives of Air Electrodes in Zn-Air Batteries. Advanced Science 2018;5:1700691. https://doi.org/10.1002/ADVS.201700691;PAGEGROUP:STRING:PUBLICATION.

[160] Lv XW, Wang Z, Lai Z, Liu Y, Ma T, Geng J, et al. Rechargeable Zinc-Air Batteries: Advances, Challenges, and Prospects. Small 2024;20:2306396. https://doi.org/10.1002/SMLL.202306396;ISSUE:ISSUE:DOI.

[161] Li Y, Gong M, Liang Y, Feng J, Kim JE, Wang H, et al. Advanced zinc-air batteries based on high-performance hybrid electrocatalysts. Nature Communications 2013 4:1 2013;4:1805-. https://doi.org/10.1038/ncomms2812.

[162] Wang HF, Tang C, Zhang Q. A Review of Precious-Metal-Free Bifunctional Oxygen Electrocatalysts: Rational Design and Applications in Zn−Air Batteries. Adv Funct Mater 2018;28:1803329. https://doi.org/10.1002/ADFM.201803329;JOURNAL:JOURNAL:10990712;PAGE:STRING:ARTICLE/CHAPTER.

[163] Yu P, Wang L, Sun F, Xie Y, Liu X, Ma J, et al. Co Nanoislands Rooted on Co-N-C Nanosheets as Efficient Oxygen Electrocatalyst for Zn-Air Batteries. Advanced Materials 2019;31:1901666. https://doi.org/10.1002/ADMA.201901666;ISSUE:ISSUE:DOI.

[164] Han X, Ling X, Wang Y, Ma T, Zhong C, Hu W, et al. Spatial Isolation of Zeolitic Imidazole Frameworks-Derived Cobalt Catalysts: From Nanoparticle, Atomic Cluster to Single Atom. Angew Chem Int Ed 2019;58:5359-64. https://doi.org/10.1002/ANIE.201901109.

[165] Shang H, Zhou X, Dong J, Li A, Zhao X, Liu Q, et al. Engineering unsymmetrically coordinated Cu-S1N3 single atom sites with enhanced oxygen reduction activity. Nature Communications 2020 11:1 2020;11:3049-. https://doi.org/10.1038/s41467-020-16848-8.

[166] Zhang J, Zhou Q, Tang Y, Zhang L, Li Y. Zinc-air batteries: are they ready for prime time? Chem Sci 2019;10:8924-9. https://doi.org/10.1039/C9SC04221K.

[167] Deiss E, Holzer F, Haas O. Modeling of an electrically rechargeable alkaline Zn-air battery. Electrochim Acta 2002;47:3995-4010. https://doi.org/10.1016/S0013-4686(02)00316-X.

[168] Hong W, Li H, Wang B. A Horizontal Three-Electrode Structure for Zinc-Air Batteries with Long-Term Cycle Life and High Performance. Int J Electrochem Sci 2016;11:3843-51. https://doi.org/10.1016/S1452-3981(23)17441-4.

[169] Ma H, Wang B, Fan Y, Hong W. Development and Characterization of an Electrically Rechargeable Zinc-Air Battery Stack. Energies 2014, Vol 7, Pages 6549-6557 2014;7:6549-57. https://doi.org/10.3390/EN7106549.

[170] Li PC, Chien YJ, Hu CC. Novel configuration of bifunctional air electrodes for rechargeable zinc-air batteries. J Power Sources 2016;313:37-45. https://doi.org/10.1016/J.JPOWSOUR.2016.02.063.

[171] Nazir G, Rehman A, Lee JH, Kim CH, Gautam J, Heo K, et al. A Review of Rechargeable Zinc-Air Batteries: Recent Progress and Future Perspectives. Nano-Micro Letters 2024 16:1 2024;16:138-. https://doi.org/10.1007/S40820-024-01328-1.

[172] Park MG, Lee DU, Seo MH, Cano ZP, Chen Z. 3D Ordered Mesoporous Bifunctional Oxygen Catalyst for Electrically Rechargeable Zinc-Air Batteries. Small 2016;12:2707-14. https://doi.org/10.1002/SMLL.201600051;WGROUP:STRING:PUBLICATION.

[173] Liu Q, Liu R, He C, Xia C, Guo W, Xu ZL, et al. Advanced polymer-based electrolytes in zinc-air batteries. EScience 2022;2:453-66. https://doi.org/10.1016/J.ESCI.2022.08.004.

[174] Leong KW, Wang Y, Ni M, Pan W, Luo S, Leung DYC. Rechargeable Zn-air batteries: Recent trends and future perspectives. Renewable and Sustainable Energy Reviews 2022;154:111771. https://doi.org/10.1016/J.RSER.2021.111771.

[175] Wu M, Zhang G, Tong H, Liu X, Du L, Chen N, et al. Cobalt (II) oxide nanosheets with rich oxygen vacancies as highly efficient bifunctional catalysts for ultra-stable rechargeable Zn-air flow battery. Nano Energy 2021;79:105409. https://doi.org/10.1016/J.NANOEN.2020.105409.

[176] Huang S, Zhang H, Zhuang J, Zhou M, Gao M, Zhang F, et al. Redox-Mediated Two-Electron Oxygen Reduction Reaction with Ultrafast Kinetics for Zn-Air Flow Battery. Adv Energy Mater 2022;12:2103622. https://doi.org/10.1002/AENM.202103622;REQUESTEDJOURNAL:JOURNAL:16146840;WGROUP:STRING:PUBLICATION.

[177] Zhang Y, Deng YP, Wang J, Jiang Y, Cui G, Shui L, et al. Recent Progress on Flexible Zn-Air Batteries. Energy Storage Mater 2021;35:538-49. https://doi.org/10.1016/J.ENSM.2020.09.008.

[178] Fang W, Zhao J, Zhang W, Chen P, Bai Z, Wu M. Recent progress and future perspectives of flexible Zn-Air batteries. J Alloys Compd 2021;869:158918. https://doi.org/10.1016/J.JALLCOM.2021.158918.

[179] Liu H, Xie W, Huang Z, Yao C, Han Y, Huang W. Recent Advances in Flexible Zn-Air Batteries: Materials for Electrodes and Electrolytes. Small Methods 2022;6:2101116. https://doi.org/10.1002/SMTD.202101116;PAGE:STRING:ARTICLE/CHAPTER.

[180] Zhang L, Shao Q, Zhang J. An overview of non-noble metal electrocatalysts and their associated air cathodes for Mg-air batteries. Materials Reports: Energy 2021;1:100002. https://doi.org/10.1016/J.MATRE.2020.11.001.

[181] Raghavan P, Das A, Jabeen Fatima MJ. Advanced Technologies for Rechargeable Batteries: Metal Ion, Hybrid, and Metal-Air Batteries, Volume 2. Advanced Technologies for Rechargeable Batteries: Metal Ion, Hybrid, and Metal-Air Batteries, Volume 2 2024:1-374. https://doi.org/10.1201/9781003310174/ADVANCED-TECHNOLOGIES-RECHARGEABLE-BATTERIES-PRASANTH-RAGHAVAN-AKHILA-DAS-JABEEN-FATIMA/RIGHTS-AND-PERMISSIONS.

[182] Chen X, Venezuela J, Shi Z, Wang L, Dargusch M. Ultra-high-purity Mg-Ge anodes enable a long-lasting, high energy-density Mg-air battery. Nano Energy 2024;122:109269. https://doi.org/10.1016/J.NANOEN.2024.109269.

[183] Li L, Chen H, He E, Wang L, Ye T, Lu J, et al. High-energy-density magnesium-air battery based on dual-layer gel electrolyte. Wiley Online LibraryL Li, H Chen, E He, L Wang, T Ye, J Lu, Y Jiao, J Wang, R Gao, H Peng, Y ZhangAngewandte Chemie, 2021•Wiley Online Library 2021;133:15445-50. https://doi.org/10.1002/ANGE.202104536.

[184] Huang X, Liu Y, Park W, Zhao Z, Li J, Lim CK, et al. Stretchable magnesium-air battery based on dual ions conducting hydrogel for intelligent biomedical applications. InfoMat 2023;5:e12388. https://doi.org/10.1002/INF2.12388;CTYPE:STRING:JOURNAL.

[185] Guo Z, Zhao S, Li T, Su D, Guo S, Wang G. Recent Advances in Rechargeable Magnesium-Based Batteries for High-Efficiency Energy Storage. Adv Energy Mater 2020;10:1903591. https://doi.org/10.1002/AENM.201903591;JOURNAL:JOURNAL:16146840;REQUESTEDJOURNAL:JOURNAL:16146840;ISSUE:ISSUE:DOI.

[186] Li CS, Sun Y, Gebert F, Chou SL. Current Progress on Rechargeable Magnesium-Air Battery. Adv Energy Mater 2017;7:1700869. https://doi.org/10.1002/AENM.201700869;CSUBTYPE:STRING:SPECIAL;PAGE:STRING:ARTICLE/CHAPTER.

[187] Peled E, Golodnitsky D, Mazor H, Goor M, Avshalomov S. Parameter analysis of a practical lithium- and sodium-air electric vehicle battery. J Power Sources 2011;196:6835-40. https://doi.org/10.1016/J.JPOWSOUR.2010.09.104.

[188] Qin L, Xiao N, Zhang S, Chen X, Wu Y. From K-O2 to K-Air Batteries: Realizing Superoxide Batteries on the Basis of Dry Ambient Air. Wiley Online Library 2020;59:10498-501. https://doi.org/10.1002/ANIE.202003481.

[189] Mao P, Arandiyan H, Mofarah SS, Koshy P, Pozo-Gonzalo C, Zheng R, et al. A comprehensive review of cathode materials for Na-air batteries. Energy Advances 2023;2:465-502. https://doi.org/10.1039/D2YA00340F.

[190] Qin L, Ao H, Wu Y. Feasibility of achieving two-electron K-O2 batteries. Faraday Discuss 2024;248:60-74. https://doi.org/10.1039/D3FD00085K.

[191] Yu W, Lau KC, Lei Y, Liu R, Qin L, Yang W, et al. Dendrite-free potassium-oxygen battery based on a liquid alloy anode. ACS Publications 2017;9:31871-8. https://doi.org/10.1021/ACSAMI.7B08962.

[192] Wang T, Han Y, Xu P, Feng X, Ji W, Arandiyan H. In-situ generating highly efficient sites for multifunctional water splitting/Zn-air battery over hierarchically architectured Fe2Ni3

nanoalloy/N-incorporated carbon matrix. Chemical Engineering Journal 2022;450:138245. https://doi.org/10.1016/J.CEJ.2022.138245.

[193] Lutz L, Alves Dalla Corte D, Tang M, Salager E, Deschamps M, Grimaud A, et al. Role of Electrolyte Anions in the Na-O2 Battery: Implications for NaO2 Solvation and the Stability of the Sodium Solid Electrolyte Interphase in Glyme Ethers. Chemistry of Materials 2017;29:6066-75. https://doi.org/10.1021/ACS.CHEMMATER.7B01953.

[194] Yadegari H, Sun X. Sodium-Oxygen Batteries: Recent Developments and Remaining Challenges. Trends Chem 2020;2:241-53. https://doi.org/10.1016/J.TRECHM.2019.12.003.

[195] Kang Y, Wang S, Zhu S, Gao H, Hui KS, Yuan CZ, et al. Iron-modulated nickel cobalt phosphide embedded in carbon to boost power density of hybrid sodium-air battery. Appl Catal B 2021;285:119786. https://doi.org/10.1016/J.APCATB.2020.119786.

[196] Xu C, Zhang K, Zhang D, Chang S, Liang F, Yan P, et al. Reversible hybrid sodium-CO2 batteries with low charging voltage and long-life. Nano Energy 2020;68:104318. https://doi.org/10.1016/J.NANOEN.2019.104318.

[197] Enterría M, Reynaud M, Paredes JI, Medinilla L, Younesi R, Ortiz-Vitoriano N. Driving the sodium-oxygen battery chemistry towards the efficient formation of discharge products: The importance of sodium superoxide quantification. Journal of Energy Chemistry 2022;68:709-20. https://doi.org/10.1016/J.JECHEM.2021.12.014.

[198] Duan C, Li X, Wang D, Wang Z, Sun H, Zheng R, et al. Nanosized high entropy spinel oxide (FeCoNiCrMn)3O4 as a highly active and ultra-stable electrocatalyst for the oxygen evolution reaction. Sustain Energy Fuels 2022;6:1479-88. https://doi.org/10.1039/D1SE02038B.

[199] Cohn, G., Starosvetsky, D., Hagiwara, R., Macdonald, D. D., & Ein-Eli, Y. (2009). Silicon–air batteries. *Electrochemistry Communications*, *11*(10), 1916-1918. https://doi.org/10.1016/j.elecom.2009.08.015

[200] Zhong X, Zhang H, Liu Y, Bai J, Liao L, Huang Y, et al. High-capacity silicon-air battery in alkaline solution. ChemSusChem 2012;5:177-80. https://doi.org/10.1002/CSSC.201100426;ISSUE:ISSUE:DOI.

[201] Park DW, Kim S, Ocon JD, Abrenica GHA, Lee JK, Lee J. Controlled Electrochemical Etching of Nanoporous Si Anodes and Its Discharge Behavior in Alkaline Si-Air Batteries. ACS Appl Mater Interfaces 2015;7:3126-32. https://doi.org/10.1021/AM507360E.

[202] Durmus YE, Aslanbas Ö, Kayser S, Tempel H, Hausen F, de Haart LGJ, et al. Long run discharge, performance and efficiency of primary Silicon-air cells with alkaline electrolyte. Electrochim Acta 2017;225:215-24. https://doi.org/10.1016/J.ELECTACTA.2016.12.120.

[203] Schalinski R, Schweizer SL, Wehrspohn RB. The Role of Silicate Enrichment on the Discharge Duration of Silicon-Air Batteries. ChemSusChem 2023;16:e202300077. https://doi.org/10.1002/CSSC.202300077;REQUESTEDJOURNAL:JOURNAL:1864564X;ISSUE:ISSUE:DOI.

[204] Montiel Guerrero SS, Durmus YE, Tempel H, Roth C, Kungl H, van Waasen S, et al. Unveiling the Potential of Silicon-Air Batteries for Low-Power Transient Electronics: Electrochemical Insights and Practical Application. Batter Supercaps 2024;7:e202300573. https://doi.org/10.1002/BATT.202300573;REQUESTEDJOURNAL:JOURNAL:25666223;WGROUP:STRING:PUBLICATION.

[205] Yang W tian, Yu J, Li D xin, Hu S qiu, Ding X, Chen F yu, et al. Performance of silicon-air batteries using industrial silicon as anode. Journal of Materials Science: Materials in Electronics 2023 34:9 2023;34:800-. https://doi.org/10.1007/S10854-023-10191-6.

[206] Lu YT, Neale AR, Hu CC, Hardwick LJ. Divalent Nonaqueous Metal-Air Batteries. Front Energy Res 2021;8:602918. https://doi.org/10.3389/FENRG.2020.602918/FULL.

[207] Ocon JD, Kim JW, Uhm S, Mun BS, Lee J. An etched nanoporous Ge anode in a novel metal-air energy conversion cell. Physical Chemistry Chemical Physics 2013;15:6333-8. https://doi.org/10.1039/C3CP50885D.

[208] Ye L, Liao M, Zhang K, Zheng M, Jiang Y, Cheng X, et al. A rechargeable calcium-oxygen battery that operates at room temperature. Nature 2024 626:7998 2024;626:313-8. https://doi.org/10.1038/s41586-023-06949-x.

[209] Fang C, Tang X, Wang J, Yi Q. Performance of iron-air battery with iron nanoparticle-encapsulated C-N composite electrode. Frontiers in Energy 2024;18:42-53. https://doi.org/10.1007/S11708-023-0913-5/METRICS.

[210] Liu Y, Sun Q, Li W, Adair KR, Li J, Sun X. A comprehensive review on recent progress in aluminum-air batteries. Green Energy & Environment 2017;2:246-77. https://doi.org/10.1016/J.GEE.2017.06.006.

[211] Liu X, Jiao H, Wang M, Song W li, Xue J, Jiao S. Current progresses and future prospects on aluminium-air batteries. International Materials Reviews 2022;67:734-64. https://doi.org/10.1080/09506608.2021.2006968.

[212] Goel P, Dobhal D, Sharma RC. Aluminum-air batteries: A viability review. J Energy Storage 2020;28:101287. https://doi.org/10.1016/J.EST.2020.101287.

[213] Mori R. Recent Developments for Aluminum-Air Batteries. Electrochemical Energy Reviews 2020 3:2 2020;3:344-69. https://doi.org/10.1007/S41918-020-00065-4.

[214] Mori R. Rechargeable Aluminum-Air Battery Using Various Air-Cathode Materials and Suppression of Byproducts Formation on Both Anode and Air Cathode. ECS Trans 2017;80:377. https://doi.org/10.1149/08010.0377ECST.

[215] Zhao Q, Yu H, Fu L, Wu P, Li Y, Li Y, et al. Electrolytes for aluminum-air batteries: advances, challenges, and applications. Sustain Energy Fuels 2023;7:1353-70. https://doi.org/10.1039/D2SE01744J.

[216] Xu Y, Zhao Y, Ren J, Zhang Y, Peng H. An All-Solid-State Fiber-Shaped Aluminum-Air Battery with Flexibility, Stretchability, and High Electrochemical Performance. Angew Chem Int Ed 2016;55:7979-82. https://doi.org/10.1002/anie.201601804.

[217] Yang S, Knickle H. Design and analysis of aluminum/air battery system for electric vehicles. J Power Sources 2002;112:162-73. https://doi.org/10.1016/S0378-7753(02)00370-1.

[218] Tang Y, Lu L, Roesky HW, Wang L, Huang B. The effect of zinc on the aluminum anode of the aluminum-air battery. J Power Sources 2004;138:313-8. https://doi.org/10.1016/J.JPOWSOUR.2004.06.043.

[219] Garcia-Garcia FJ, Skeldon P, Thompson GE, Smith GC. The effect of nickel on alloy microstructure and electrochemical behaviour of AA1050 aluminium alloy in acid and alkaline solutions. Electrochim Acta 2012;75:229-38. https://doi.org/10.1016/J.ELECTACTA.2012.04.106.

[220] Ryu J, Park M, Cho J. Advanced Technologies for High-Energy Aluminum-Air Batteries. Advanced Materials 2019;31:1804784. https://doi.org/10.1002/adma.201804784.

[221] Phinergy demonstrates aluminum-air battery capable of fueling an electric vehicle for 1000 miles n.d. https://phys.org/news/2013-03-phinergy-aluminum-air-battery-capable-fueling.html (accessed April 5, 2026).

[222] Vegh JM, Alonso JJ. Design and optimization of short-range aluminum-air powered aircraft. 54th AIAA Aerospace Sciences Meeting 2016;0. https://doi.org/10.2514/6.2016-1026.

[223] Rewatkar P, Goel S. Catalyst-mitigated arrayed aluminum-air origami fuel cell with ink-jet printed custom-porosity cathode. Energy 2021;224:120017. https://doi.org/10.1016/J.ENERGY.2021.120017.

[224] Huang H, Liu P, Ma Q, Tang Z, Wang M, Hu J. Enabling a high-performance saltwater Al-air battery via ultrasonically driven electrolyte flow. Ultrason Sonochem 2022;88:106104. https://doi.org/10.1016/J.ULTSONCH.2022.106104.

[225] GT Sheerin - US Patent 10 978,758, 2021 undefined. Air metal battery having a rotating anode and a cathode assembly. Google Patents

[226] Xu N, Wang D, Xu Z. CORROSION AND ELECTROCHEMICAL PROPERTIES OF Sn/Mg-MODIFIED ALUMINUM ALLOYS AFTER HEAT TREATMENT FOR METAL-AIR BATTERIES. Materiali in Tehnologije 2026;60:111-20. https://doi.org/10.17222/MIT.2025.1585.

[227] Kim D, Chung Y, Jeong SK. Enhanced Electrochemical Performance of Aluminum-Air Batteries via Gallium Alloying. Key Eng Mater 2024;993:9-14. https://doi.org/10.4028/P-PS19EU.

[228] Rahmanian M, Yasri NG, Roberts EPL. Polarization-Driven Hydrogen Evolution and Metal Dissolution in Electrocoagulation. ACS ES&T Water 2026;6:922-35. https://doi.org/10.1021/ACSESTWATER.5C01000.

[229] Nwanonenyi SC, Daniyan AA, Idris MB, Ige OO. Corrosion control through sacrificial anodes: A review of aluminium alloys in oil and gas applications. Hybrid Advances 2025;11:100571. https://doi.org/10.1016/J.HYBADV.2025.100571.

[230] Eren Civan F, Ahmed Zabara M, Katırcı G. Temperature-Dependent Electrochemical Impedance Spectroscopy of Batteries 2026. https://doi.org/10.1021/acselectrochem.5c00512.

[231] Madani SS, Shabeer Y, Nair AS, Fowler M, Panchal S, Ziebert C, et al. Advances in Battery Modeling and Management Systems: A Comprehensive Review of Techniques, Challenges,

and Future Perspectives. Batteries 2025, Vol 11, Page 426 2025;11:426. https://doi.org/10.3390/BATTERIES11110426.

[232] Dewangan SK, Jain S, Lee H, Youn G, Jain R, Baghel VS, et al. Neural network-enabled prediction and optimization of mechanical properties and biocompatibility in high-entropy alloys: A data-driven approach to metallurgical innovation. Journal of Materials Research and Technology 2026;42:3313-29. https://doi.org/10.1016/J.JMRT.2026.04.026.

[233] Yang Q, Zhao L, Xiao J, Wen R, Zhang F, Zhang D. Machine learning-assisted prediction and optimization of solid oxide electrolysis cell for green hydrogen production. Green Chemical Engineering 2025;6:154-68. https://doi.org/10.1016/J.GCE.2024.04.004.

[234] Zheng B, Deng Z, Luo Z, Mao S, Ouyang M, Han X, et al. A comprehensive review of lithium-ion battery modelling research and prospects: in-depth analysis of current research and future directions. Appl Energy 2025;401:126688. https://doi.org/10.1016/J.APENERGY.2025.126688.

[235] Cai C, Gong Y, Fotouhi A, Auger DJ. A novel hybrid electrochemical equivalent circuit model for online battery management systems. J Energy Storage 2024;99:113142. https://doi.org/10.1016/J.EST.2024.113142.

[236] Azad FS, Rahman A, Barman S Das, Chowdhury P, Ali MS, Farrok O. Towards efficient energy management systems for electric vehicles: advances in control techniques and applications. Energy Conversion and Management: X 2025;28:101326. https://doi.org/10.1016/J.ECMX.2025.101326.

[237] Masri J, Ismail M, Obaid A. Power Flow Simulation and Thermal Performance Analysis of Electric Vehicles Under Standard Driving Cycles. Energies 2025, Vol 18, Page 3737 2025;18:3737. https://doi.org/10.3390/EN18143737.

[238] Mahmoud M, Adhari OHK, Sayed ET, Abdelkareem MA, Olabi AG. Advances in hybrid renewable energy systems coupled with mechanical energy storage: Progress and challenges. Results in Engineering 2026;29:108994. https://doi.org/10.1016/J.RINENG.2026.108994.

[239] Isilti A, Tate JE. Technical performance evolution of BEVs: range, consumption and weight projections to 2050. Transp Res D Transp Environ 2026;152:105172. https://doi.org/10.1016/J.TRD.2025.105172.

[240] Waseem M, Lakshmi GS, Ahmad M, Suhaib M. Energy storage technology and its impact in electric vehicle: Current progress and future outlook. Next Energy 2025;6:100202. https://doi.org/10.1016/J.NXENER.2024.100202.

[241] Soto JDLC, Castillo UC, Soto JDLC, Castillo UC. Fuel Cell as Range Extender in Battery Electric Vehicles for Supply Chain Fleets. Sustainable Supply Chain Management 2016. https://doi.org/10.5772/62792.

[242] Mevawalla A, Shabeer Y, Tran MK, Panchal S, Fowler M, Fraser R. Thermal Modelling Utilizing Multiple Experimentally Measurable Parameters. Batteries 2022, Vol 8, Page 147 2022;8:147. https://doi.org/10.3390/BATTERIES8100147.

[243] Shittu E, Suman R, Krishnamoorthy Ravikumar M, Kumar Shukla A, Zhao G, Patil S, et al. Life cycle assessment of soluble lead redox flow battery. J Clean Prod 2022;337:130503. https://doi.org/10.1016/j.jclepro.2022.130503.

[244] Madhavan PV, Zeng X, Shahgaldi S, Li X. Investigation of Cr2SiC Ceramic MAX Phase Coated Metallic Bipolar Plates in Ex-situ Conditions for Proton Exchange Membrane Fuel Cells. Int J Hydrogen Energy 2024;96:1232-42. https://doi.org/10.1016/j.ijhydene.2024.11.373.

[245] Moradizadeh L, Madhavan PV, Chellehbari YM, Gupta A, Li X, Shahgaldi S. Porous transport layers with low Pt loading having Nb-Ta alloy as interlayer for proton exchange membrane water electrolyzers. Int J Hydrogen Energy 2024;94:1114-29. https://doi.org/10.1016/j.ijhydene.2024.11.192.

[246] Zackrisson M, Avellán L, Orlenius J. Life cycle assessment of lithium-ion batteries for plug-in hybrid electric vehicles - Critical issues. J Clean Prod 2010;18:1519-29. https://doi.org/10.1016/J.JCLEPRO.2010.06.004.

[247] Legala A, Zhao J, Li X. Machine learning modeling for proton exchange membrane fuel cell performance. Energy and AI 2022;10. https://doi.org/10.1016/j.egyai.2022.100183.

[248] Legala A, Shahgaldi S, Li X. Data-based modelling of proton exchange membrane fuel cell performance and degradation dynamics. Energy Convers Manag 2023;296. https://doi.org/10.1016/j.enconman.2023.117668.

[249] Nayak PK, Yang L, Brehm W, Adelhelm P. From Lithium-Ion to Sodium-Ion Batteries: Advantages, Challenges, and Surprises. Angew Chem Int Ed 2018;57:102-20. https://doi.org/10.1002/ANIE.201703772.

[250] Wen J, Yu Y, Chen C. A Review on Lithium-Ion Batteries Safety Issues: Existing Problems and Possible Solutions. Materials Express 2012;2:197-212. https://doi.org/10.1166/MEX.2012.1075.

[251] Goodenough JB, Kim Y. Challenges for Rechargeable Li Batteries. Chemistry of Materials 2010;22:587-603. https://doi.org/10.1021/cm901452z.

[252] Rahman MdA, Wang X, Wen C. High Energy Density Metal-Air Batteries: A Review. J Electrochem Soc 2013;160:A1759-71. https://doi.org/10.1149/2.062310JES/XML.

[253] Narayanan SR, Prakash GKS, Manohar A, Yang B, Malkhandi S, Kindler A. Materials challenges and technical approaches for realizing inexpensive and robust iron-air batteries for large-scale energy storage. Solid State Ion 2012;216:105-9. https://doi.org/10.1016/J.SSI.2011.12.002.

[254] Hartmann P, Bender CL, Vračar M, Dürr AK, Garsuch A, Janek J, et al. A rechargeable room-temperature sodium superoxide (NaO2) battery. Nature Materials 2012 12:3 2012;12:228-32. https://doi.org/10.1038/nmat3486.

[255] Lee JS, Kim ST, Cao R, Choi NS, Liu M, Lee KT, et al. Metal-Air Batteries with High Energy Density: Li-Air versus Zn-Air. Adv Energy Mater 2011;1:34-50. https://doi.org/10.1002/AENM.201000010.

[256] Ramasubramanian B, Dalapati GK, Reddy MVV, Zaghib K, Chellappan V, Ramakrishna S. Progress and Complexities in Metal-Air Battery Technology. Energy Technology 2024. https://doi.org/10.1002/ente.202301375.

[257] Moon S, 한국부식학회지 SP-, 1997 undefined. A Review of Aluminium/Air Battery. J-CstOrg n.d.

[258] Shabeer Y, Madani SS, Panchal S, Mousavi M, Fowler M. Different Metal-Air Batteries as Range Extenders for the Electric Vehicle Market: A Comparative Study. Batteries 2025;11:35. https://doi.org/10.3390/BATTERIES11010035.

[259] Li Q, Bjerrum NJ. Aluminum as anode for energy storage and conversion: A review. J Power Sources 2002;110:1-10. https://doi.org/10.1016/S0378-7753(01)01014-X.

[260] Crompton T. Battery reference book. 2000.

[261] Buckingham R, Asset T, Atanassov P. Electrochemical Performance in Alkaline Electrolyte of Aluminum Alloy 6061 As Anode in Aluminum-Air Battery Applications. ECS Meeting Abstracts 2021;MA2021-02:8-8. https://doi.org/10.1149/MA2021-0218MTGABS/META.

[262] Wang L, Wang W, Yang G, Liu D, Xuan J, Wang H, et al. A hybrid aluminum/hydrogen/air cell system. Int J Hydrogen Energy 2013;38:14801-9. https://doi.org/10.1016/J.IJHYDENE.2013.09.036.

[263] Pan W, Wang Y, Kwok HYH, Leung DYC. Aluminum-air battery with cotton substrate: Controlling the discharge capacity by electrolyte pre-deposition. Green Energy & Environment 2023;8:757-66. https://doi.org/10.1016/J.GEE.2021.05.003.

[264] Sheerin, Geoffrey T. "Air metal battery having a rotating anode and a cathode assembly." U.S. Patent No. 10,978,758. 13 Apr. 2021.

[265] Sheerin, Geoffrey, Robert James Alexander, and William Terence D'Silva. "Control system and design for adynamic adaptive intelligent multi-cell air battery." U.S. Patent Application No. 18/043,361.

[266] Aaron D, Tang Z, Papandrew AB, Zawodzinski TA. Polarization curve analysis of all-vanadium redox flow batteries. J Appl Electrochem 2011;41:1175-82. https://doi.org/10.1007/S10800-011-0335-7/TABLES/2.

[267] Varsan Madhavan P, Shahgaldi S, Li X. Ex-situ Characterization of Nb-Ti Alloy/Pt Coated Stainless Steel Bipolar Plates for Proton Exchange Membrane Fuel Cells. Energy Convers Manag 2024;311:118536. https://doi.org/10.1016/J.ENCONMAN.2024.118536.

[268] Usui H, Chiku M, Shin-Ichi Y, Kuratani K, Fukami K, Tsuchiya H. Electrochemical Polarization Part 2: Electrochemical Devices. Electrochemistry 2022;90:102004-102004. https://doi.org/10.5796/ELECTROCHEMISTRY.22-66086.

[269] Sheng Y, Hu F, Wu Y, Li D, Ji W, Chen Y. Electrochemical oscillation during galvanostatic charging and discharging of Zr-modified Li 4 Ti 5 O 12 in Li-ion batteries. RSC Adv 2024;14:21799-807. https://doi.org/10.1039/D4RA03331K.

[270] Huld FT, Mæhlen JP, Keller C, Lai SY, Eleri OE, Koposov AY, et al. Revealing Silicon's Delithiation Behaviour through Empirical Analysis of Galvanostatic Charge-Discharge Curves. Batteries 2023;9:251. https://doi.org/10.3390/BATTERIES9050251/S1.

[271] Lu CT, Zhu ZY, Chen SW, Chang YL, Hsueh KL. Effects of Cell Design Parameters on Zinc-Air Battery Performance. Batteries 2022, Vol 8, Page 92 2022;8:92. https://doi.org/10.3390/BATTERIES8080092.

[272] Chu I, Zhang M, Ong S, Modeling YM-H of M, 2020 undefined. Battery electrodes, electrolytes, and their interfaces. SpringerIH Chu, M Zhang, SP Ong, YS MengHandbook

of Materials Modeling: Applications: Current and Emerging Materials, 2020•Springer 2018. https://doi.org/10.1007/978-3-319-50257-1_96-1.

[273] Logan BE, Zikmund E, Yang W, Rossi R, Kim K-Y, Saikaly PE, et al. Impact of Ohmic Resistance on Measured Electrode Potentials and Maximum Power Production in Microbial Fuel Cells 2018. https://doi.org/10.1021/acs.est.8b02055.

[274] Thorne, R. J., Sommerseth, C., Svensson, A. M., Sandnes, E., Lossius, L. P., Linga, H., & Ratvik, A. P. (2014). Understanding anode overpotential. In *Light Metals 2014* (pp. 1213-1217). Cham: Springer International Publishing.

[275] Reddy TB, LD. Linden's handbook of batteries.

[276] Examine Effect of Diffusion Coefficient and Volume Fraction on Battery Terminal Voltage n.d. https://www.mathworks.com/help/simscape-battery/ug/examine-effect-diffusion-coefficient-and-volume-fraction-on-terminal-voltage.html (accessed January 5, 2025).

[277] Hu T, Li K, Fang Y, Su L, Song Z, Shen H, et al. Experimental research on temperature rise and electric characteristics of aluminum air battery under open-circuit condition for new energy vehicle. Int J Energy Res 2019;43:1099-110. https://doi.org/10.1002/ER.4329.

[278] Zuo Y, Yu Y, Zuo C, Ning C, Liu H, Gu Z, et al. Low-Temperature Performance of Al-air Batteries. Energies 2019, Vol 12, Page 612 2019;12:612. https://doi.org/10.3390/EN12040612.

[279] Cai Y, Tong Y, Liu Y, Li X, Chen B, Liu F, et al. Study on Thermal Effect of Aluminum-Air Battery. Nanomaterials 2023;13:646. https://doi.org/10.3390/NANO13040646.

[280] Du P, Liu D, Chen X, Xie H, Qu X, Wang D, et al. Research progress towards the corrosion and protection of electrodes in energy-storage batteries. Energy Storage Mater 2023;57:371-99. https://doi.org/10.1016/J.ENSM.2023.02.028.

[281] Cunningham J, Gross M, Han P, Keveevivitchai W, Liu S, Mefford T, et al. Aluminum/Air Battery Experiment 2015.

[282] Wong AA, Aziz MJ. Method for Comparing Porous Carbon Electrode Performance in Redox Flow Batteries 2020. https://doi.org/10.1149/1945-7111/aba54d.

[283] Wlodarczyk JK, Schärer RP, Friedrich KA, Schumacher JO. Upscaling of Reactive Mass Transport through Porous Electrodes in Aqueous Flow Batteries 2024. https://doi.org/10.1149/1945-7111/ad258e.

[284] Wen H, Liu Z, Qiao J, Chen R, Zhao R, Wu J, et al. High energy efficiency and high power density aluminum-air flow battery. Int J Energy Res 2020;44:7568-79. https://doi.org/10.1002/er.5485.

[285] Wang Z, Wu Z, Liu Y, Zhang J, Yang Y, … JX-A at S. Hydrogen Evolution and Electrochemical Behavior of Aluminum in Al-Air Batteries with Concentrated Naoh Electrolytes. PapersSsrnCom. https://ssrn.com/abstract=4923394

[286] Gilliam RJ, Graydon JW, Kirk DW, Thorpe SJ. A review of specific conductivities of potassium hydroxide solutions for various concentrations and temperatures. Int J Hydrogen Energy 2007;32:359-64. https://doi.org/10.1016/J.IJHYDENE.2006.10.062.

[287] Ahmadpour A, Rashidi H, Jaber M, Mahboub D, Farmad MR. Comparing the Performance of KOH with NaOH-Activated Anthracites in terms of Methane Storage. https://doi.org/10.1260/0263-6174.31.8.729

[288] Mennilli F, Jin L, Rossi M, Comodi G. Assessment of a NaOH-based alkaline electrolyser's performance: System modelling and operating parameters optimisation A R T I C L E I N F O 2024. https://doi.org/10.1016/j.ijhydene.2024.08.175.

[289] Yu J, Ni L. Naoh as Aqueous Electrolyte to Improve the Performance of Electric Double-Layer Capacitors - a Molecular Dynamics Study 2024. https://doi.org/10.2139/SSRN.4998752.

[290] Zhou C, Bhonge K, Cho KT. Analysis of the effect of hydrogen-evolving side reaction in the aqueous aluminum-air battery. Electrochim Acta 2020;330. https://doi.org/10.1016/J.ELECTACTA.2019.135290.

[291] Rani B, Yadav JK, Saini P, Pandey AP, Dixit A. Aluminum-air batteries: current advances and promises with future directions. RSC Adv 2024;14:17628-63. https://doi.org/10.1039/D4RA02219J.

[292] Lv C, Li Y, Zhu Y, Zhang Y, Kuang J, Zhao Q, et al. Quasi-Solid-State Aluminum-Air Batteries with Ultra-high Energy Density and Uniform Aluminum Stripping Behavior. Advanced Science 2023;10:2304214. https://doi.org/10.1002/ADVS.202304214.

[293] Zuo Y, Yu Y, Shi H, Wang J, Zuo C, Dong X. Inhibition of Hydrogen Evolution by a Bifunctional Membrane between Anode and Electrolyte of Aluminum-Air Battery. Membranes (Basel) 2022;12:407. https://doi.org/10.3390/MEMBRANES12040407.

[294] Nayem SMA, Islam S, Mohamed M, Shaheen Shah S, Ahammad AJS, Aziz MA. A Mechanistic Overview of the Current Status and Future Challenges of Aluminum Anode and Electrolyte in Aluminum-Air Batteries. The Chemical Record 2024;24:e202300005. https://doi.org/10.1002/TCR.202300005.

[295] Avoundjian A, Galvan V, Gomez FA. An Inexpensive Paper-Based Aluminum-Air Battery. Micromachines (Basel) 2017;8:222. https://doi.org/10.3390/MI8070222.

[296] Liu Y, Wu Z, Qin Z, Liu Y, Hu W. Recent progress in inhibition of hydrogen evolution reaction in alkaline Al-air batteries. National Science Open 2024;3:20240037. https://doi.org/10.1360/NSO/20240037.

[297] Chen LD, Nørskov JK, Luntz AC. Al-air batteries: Fundamental thermodynamic limitations from first-principles theory. Journal of Physical Chemistry Letters 2015;6:175-9. https://doi.org/10.1021/JZ502422V/SUPPL_FILE/JZ502422V_SI_001.PDF.

[298] Timilsina RR, Zhang J, Rahut DB, Patradool K, Sonobe T. Global drive toward net-zero emissions and sustainability via electric vehicles: an integrative critical review. Energy, Ecology and Environment 2024 10:2 2025;10:125-44. https://doi.org/10.1007/S40974-024-00351-7.

[299] Muratori M, Arent D, Bazilian MD, Bistline J, Borlaug B, Brown A, et al. Trends and 2025 insights on the rise of electric vehicles in the USA. Nature Reviews Clean Technology 2025 1:12 2025;1:827-45. https://doi.org/10.1038/s44359-025-00108-3.

[300] Schulthoff M, Anstett P, Lange J, Arend D, Gencer E, Kaltschmitt M. Federal Transformation costs of e-mobility in Germany: Effectiveness and efficiency of EV incentives between 2015 and 2023. Transp Res Interdiscip Perspect 2025;31:101435. https://doi.org/10.1016/J.TRIP.2025.101435.

[301] Ludin NA, Phoumin H, Junedi MM, Alyssa N, Affandi A, Ludin NA, et al. Comparative Environmental Evaluation of Electric Vehicle Charging Technologies, Infrastructure and Charging Stations in Malaysia: Towards a Sustainable Energy Transition 2025:143-64. https://doi.org/10.1007/978-981-96-6019-3_7.

[302] Song Y, Li Y, Jiang J, Ye B. The industrial prospect of electric vehicles—time delay stochastic evolutionary game evidence from the U.S., China, the EU, and Japan. Humanities and Social Sciences Communications 2025 12:1 2025;12:901-. https://doi.org/10.1057/s41599-025-05342-5.

[303] Koech AK, Mwandila G, Mulolani F. A review of improvements on electric vehicle battery. Heliyon 2024;10:e34806. https://doi.org/10.1016/J.HELIYON.2024.E34806.

[304] Pol VG. Lithium-Ion Battery Critical Materials Sustainability. ACS Energy Lett 2025;10:2553-8. https://doi.org/10.1021/ACSENERGYLETT.5C01018.

[305] Zhang S, Zhu X, Wang Z, Wang L, Zhang Z, Liu Y, et al. The Significance of Enhancing the Reliability of Lithium-Ion Batteries in Reducing Electric Vehicle Field Safety Accidents. Batter Supercaps 2025;8:e202400355. https://doi.org/10.1002/BATT.202400355;WEBSITE:WEBSITE:CHEMISTRY-EUROPE;REQUESTEDJOURNAL:JOURNAL:25666223;WGROUP:STRING:PUBLICATION.

[306] Qahtan TF, Alade IO, Rahaman MS, Alansi AM, Saleh TA. Trends in metal-air battery research: Clusters, and future directions. J Alloys Compd 2025;1022:179617. https://doi.org/10.1016/J.JALLCOM.2025.179617.

[307] Dilshad M, Li T, Lee SL, Qin L. Next-Generation Aluminum-Air Batteries: Integrating New Materials and Technologies for Superior Performance. ACS Appl Energy Mater 2025;8:3248-75. https://doi.org/10.1021/ACSAEM.4C02926.

[308] Shabeer Y, Madani SS, Panchal S, Fowler M. Performance optimization of high energy density aluminum-air batteries: Effects of operational parameters and electrolyte composition. Future Batteries 2025;6:100082. https://doi.org/10.1016/J.FUB.2025.100082.

[309] Tan WC, Koh ZH, Low FS, Thiam HS, Wu JS, Chen WH, et al. Optimization of air cathode composition for enhanced performance in aluminum-air batteries. Chemical Engineering Journal 2025;519:165168. https://doi.org/10.1016/J.CEJ.2025.165168.

[310] Wan Y, Qiang Y, Liu S, Gao Y, Jin Y, Wu J, et al. Multi-center corrosion inhibition strategy for enhanced interfacial stability and longevity of aluminum-air batteries. Chemical Engineering Journal 2025;521:166814. https://doi.org/10.1016/J.CEJ.2025.166814.

[311] Pahlevan SM, Hosseini SMS, Goli A. Sustainable supply chain network design using products' life cycle in the aluminum industry. Environmental Science and Pollution Research 2021 2021:1-25. https://doi.org/10.1007/S11356-020-12150-8.

[312] Tian S, Di Y, Dai M, Chen W, Zhang Q. Comprehensive assessment of energy conservation and CO2 emission reduction in future aluminum supply chain. Appl Energy 2022;305:117796. https://doi.org/10.1016/J.APENERGY.2021.117796.

[313] Obot IB, Bahraq AA, Qamar M, Ahmad R. Sustainable additives to mitigate the self-corrosion of aluminium metal in alkaline solution: Electrochemical and theoretical investigations. Mater Today Commun 2025;42:111325. https://doi.org/10.1016/J.MTCOMM.2024.111325.

[314] Li S, Miao D, Liu Y, Qu J, Yan W. Constructing composite protective interphase in situ for high-performance aluminum-air batteries. J Power Sources 2025;640:236750. https://doi.org/10.1016/J.JPOWSOUR.2025.236750.

[315] Ma Y, Huang J, Gao S, Li L, Yi Z, Xiao D, et al. Super-Concentrated Alkali Hydroxide Electrolytes for Rechargeable Zn Batteries. Angew Chem Int Ed 2025;64:e202425261. https://doi.org/10.1002/ANIE.202425261;WGROUP:STRING:PUBLICATION.

[316] Hu T, Fang Y, Su L, Li K. A novel experimental study on discharge characteristics of an aluminum-air battery. Int J Energy Res 2019;43:1839-47. https://doi.org/10.1002/ER.4421;ISSUE:ISSUE:DOI.

[317] Wu S, Zhang Q, Sun D, Luan J, Shi H, Hu S, et al. Understanding the synergistic effect of alkyl polyglucoside and potassium stannate as advanced hybrid corrosion inhibitor for alkaline aluminum-air battery. Chemical Engineering Journal 2020;383:123162. https://doi.org/10.1016/J.CEJ.2019.123162.

[318] Zhu C, Yan L, Han Y, Luo L, Guo J, Xiang B, et al. Synergistic modulation of alkaline aluminum-air battery based on localized water-in-salt electrolyte towards anodic self-corrosion. Chemical Engineering Journal 2024;485:149600. https://doi.org/10.1016/J.CEJ.2024.149600.

[319] Corrosion of metallic anodes in aqueous batteries - Energy & Environmental Science (RSC Publishing) DOI:10.1039/D5EE00075K n.d. https://pubs.rsc.org/en/content/articlehtml/2012/40/d5ee00075k (accessed December 16, 2025).

[320] Investigation of commercial aluminum alloys as anode materials for alkaline aluminum-air batteries - Sustainable Energy & Fuels (RSC Publishing) DOI:10.1039/D2SE01341J n.d. https://pubs.rsc.org/en/content/articlehtml/2023/se/d2se01341j (accessed December 16, 2025).

[321] Buckingham R, Asset T, Atanassov P. Electrochemical Performance in Alkaline Electrolyte of Aluminum Alloy 6061 As Anode in Aluminum-Air Battery Applications. ECS Meeting Abstracts 2021;MA2021-02:8. https://doi.org/10.1149/MA2021-0218MTGABS.

[322] Sitanggang RB, Nur'aini S, Widiyastuti W, Nurtono T, Setyawan H. Anodization - Deposition of aluminum alloy 6061 as the potential anode material for aluminum air battery. Next Materials 2025;9:101170. https://doi.org/10.1016/J.NXMATE.2025.101170.

[323] Elboughdiri N, Kriaa K, Barah OO, Sanusi YS, Alaneme GU, Maatki C. Optimized NaOH and KOH treatments for interfacial and mechanical enhancement of agro-marine ash reinforced aluminum composites. Scientific Reports 2025 15:1 2025;15:37226-. https://doi.org/10.1038/s41598-025-21038-x.

[324] Che S, Liu H, Li K, Li B, Li X. Advances in high-performance aluminum-air batteries: A comprehensive review of electrode and electrolyte engineering strategies. Journal of Electroanalytical Chemistry 2025;996:119400. https://doi.org/10.1016/J.JELECHEM.2025.119400.

[325] Amodu OS, Odunlami MO, Akintola JT, Ojumu T V., Ayanda OS. Artificial neural network and response surface methodology for optimization of corrosion inhibition of mild steel in 1 M HCl by Musa paradisiaca peel extract. Heliyon 2022;8:e11955. https://doi.org/10.1016/j.heliyon.2022.e11955.

[326] Coelho LB, Zhang D, Van Ingelgem Y, Steckelmacher D, Nowé A, Terryn H. Reviewing machine learning of corrosion prediction in a data-oriented perspective. Npj Materials Degradation 2022 6:1 2022;6:8-. https://doi.org/10.1038/s41529-022-00218-4.

[327] McCafferty E. Validation of corrosion rates measured by the Tafel extrapolation method. Corros Sci 2005;47:3202-15. https://doi.org/10.1016/J.CORSCI.2005.05.046.

[328] Middlemiss LA, Rennie AJR, Sayers R, West AR. Characterisation of batteries by electrochemical impedance spectroscopy. Energy Reports 2020;6:232-41. https://doi.org/10.1016/J.EGYR.2020.03.029.

[329] Mehdizadeh Chellehbari Y, Madhavan PV, Johar M, Moradizadeh L, Gupta A, Li X, et al. Machine learning-assisted optimization of NbTa alloy coating thickness via DC magnetron sputtering for SS316L bipolar plates in PEMFCs. ETransportation 2025;26:100500. https://doi.org/10.1016/J.ETRAN.2025.100500.

[330] Chepino, B. G., Yacoub, R. R., Aula, A., Saleh, M., & Sanjaya, B. W. (2023). Effect of minmax normalization on ORB data for improved ANN accuracy. *Journal of Electrical Engineering, Energy, and Information Technology (J3EIT)*, *11*(2), 29.

[331] Kunstner, F., Milligan, A., Yadav, R., Schmidt, M., & Bietti, A. (2024). Heavy-tailed class imbalance and why adam outperforms gradient descent on language models. *Advances in Neural Information Processing Systems*, *37*, 30106-30148. https://doi.org/10.52202/079017-0948

[332] Liu, X., Qi, H., Jia, S., Guo, Y., & Liu, Y. (2025). Recent advances in optimization methods for machine learning: a systematic review. *Mathematics*, *13*(13), 2210. https://doi.org/10.3390/math13132210

[333] Chicco D, Warrens MJ, Jurman G. The coefficient of determination R-squared is more informative than SMAPE, MAE, MAPE, MSE and RMSE in regression analysis evaluation. PeerJ Comput Sci 2021;7:1-24. https://doi.org/10.7717/PEERJ-CS.623/SUPP-1.

[334] Zhang Z, Wu F, Wu A, Zhang Z, Wu F, Wu A. Research on Multi-Objective Process Parameter Optimization Method in Hard Turning Based on an Improved NSGA-II Algorithm. Processes 2024, Vol 12, 2024;12. https://doi.org/10.3390/PR12050950.

[335] Pereira JLJ, Oliver GA, Francisco MB, Cunha SS, Gomes GF. A Review of Multi-objective Optimization: Methods and Algorithms in Mechanical Engineering Problems. Archives of Computational Methods in Engineering 2021 29:4 2021;29:2285-308. https://doi.org/10.1007/S11831-021-09663-X.

[336] Giovannelli T, Raimundo MM, Vicente LN. Pareto sensitivity, most-changing sub-fronts, and knee solutions 2025.

[337] He M, Wang X, Chen H, Li X. A Knee Point-Driven Many-Objective Evolutionary Algorithm with Adaptive Switching Mechanism. Wiley Online LibraryM He, X Wang, H Chen, X LiJournal of Applied Mathematics, 2024•Wiley Online Library 2024;2024. https://doi.org/10.1155/2024/4737604.

[338] Xia D-H, Song S, Qin Z, - al, Lan C, Wang Y, et al. Review of Artificial Neural Networks (ANN) applied to corrosion monitoring. J Phys Conf Ser 2012;364:012114. https://doi.org/10.1088/1742-6596/364/1/012114.

[339] Salem H, Kabeel AE, El-Said EMS, Elzeki OM. Predictive modelling for solar power-driven hybrid desalination system using artificial neural network regression with Adam

optimization. Desalination 2022;522:115411. https://doi.org/10.1016/J.DESAL.2021.115411.

[340] Wang Y, Xiao Z, Cao G. A convolutional neural network method based on Adam optimizer with power-exponential learning rate for bearing fault diagnosis. Journal of Vibroengineering 2022;24:666-78. https://doi.org/10.21595/JVE.2022.22271.

[341] Shantal M, Othman Z, Abu Bakar A. Missing data imputation using correlation coefficient and min-max normalization weighting. Intelligent Data Analysis 2025;29:372-84. https://doi.org/10.3233/IDA-230140.

[342] Hodson TO. Root-mean-square error (RMSE) or mean absolute error (MAE): when to use them or not. Geosci Model Dev 2022;15:5481-7. https://doi.org/10.5194/GMD-15-5481-2022.

[343] Wang W, Lu Y. Analysis of the Mean Absolute Error (MAE) and the Root Mean Square Error (RMSE) in Assessing Rounding Model. IOP Conf Ser Mater Sci Eng 2018;324:012049. https://doi.org/10.1088/1757-899X/324/1/012049.

[344] Lambora A, Gupta K, Chopra K. Genetic Algorithm- A Literature Review. Proceedings of the International Conference on Machine Learning, Big Data, Cloud and Parallel Computing: Trends, Prespectives and Prospects, COMITCon 2019 2019:380-4. https://doi.org/10.1109/COMITCON.2019.8862255.

[345] Al-Majali BH, Zobaa AF. Analyzing bi-objective optimization Pareto fronts using square shape slope index and NSGA-II: A multi-criteria decision-making approach. Expert Syst Appl 2025;272:126765. https://doi.org/10.1016/J.ESWA.2025.126765.

[346] Verma S, Pant M, Snasel V. A Comprehensive Review on NSGA-II for Multi-Objective Combinatorial Optimization Problems. IEEE Access 2021;9:57757-91. https://doi.org/10.1109/ACCESS.2021.3070634.

[347] Moghadam Z, Shabani-Nooshabadi M, Behpour M. Electrochemical performance of aluminium alloy in strong alkaline media by urea and thiourea as inhibitor for aluminium-air batteries. J Mol Liq 2017;242:971-8. https://doi.org/10.1016/J.MOLLIQ.2017.07.119.

[348] Boukerche I, Djerad S, Benmansour L, Tifouti L, Saleh K. Degradability of aluminum in acidic and alkaline solutions. Corros Sci 2014;78:343-52. https://doi.org/10.1016/J.CORSCI.2013.10.019.

[349] Reena Kumari PD, Nayak J, Nityananda Shetty A. Corrosion behavior of 6061/Al-15 vol. pct. SiC(p) composite and the base alloy in sodium hydroxide solution. Arabian Journal of Chemistry 2016;9:S1144-54. https://doi.org/10.1016/J.ARABJC.2011.12.003.

[350] Musicco N, Gelfi M, Iora P, Venturelli M, Artioli N, Montorsi L, et al. A review of hydrogen generation methods via aluminum-water reactions. International Journal of Thermofluids 2025;27:101152. https://doi.org/10.1016/J.IJFT.2025.101152.

[351] Porciúncula CB, Marcilio NR, Tessaro IC, Gerchmann M. Production of hydrogen in the reaction between aluminum and water in the presence of NaOH and KOH. Brazilian Journal of Chemical Engineering 2012;29:337-48. https://doi.org/10.1590/S0104-66322012000200014.

[352] Chung Y, Lee S, Yoon S, Choi WK, Jeong SK. Mitigating anodic corrosion in aluminum-air batteries: Effects of alkali metal cation size on electrochemical performance. Appl Surf Sci 2025;681:161533. https://doi.org/10.1016/J.APSUSC.2024.161533.

[353] Harchegani R. Strategies to Improve the Electrochemical Performance of Aluminum Anodes in Primary Alkaline Aluminum-Air Batteries 2023.

[354] Buryakovskaya OA, Vlaskin MS. Hydrogen Recovery from Waste Aluminum-Plastic Composites Treated with Alkaline Solution. Materials 2022, Vol 15, Page 8699 2022;15:8699. https://doi.org/10.3390/MA15238699.

[355] Xiao, F., Zhang, H., Kong, L., Zheng, Y., & Hu, X. (2022). Effect of pH on corrosion behavior of Al-Mg-Si alloy in NaCl solution. *International Journal of Electrochemical Science*, *17*(11), 221162. https://doi.org/10.20964/2022.11.62

[356] Correa O V, De Souza JAB, De Oliveira MCL, Antunes RA. Influence of aging time on the corrosion behavior of 6061 Al alloy in alkaline solution 2014.

[357] Wei W, González S, Hashimoto T, Prasath Babu R, Thompson GE, Zhou X. Effect of low temperature sensitization on the susceptibility to intergranular corrosion in AA5083 aluminum alloy. Wiley Online Library 2016;67:331-9. https://doi.org/10.1002/MACO.201508589.

[358] Nyby C, Guo X, Saal JE, Chien SC, Gerard AY, Ke H, et al. Electrochemical metrics for corrosion resistant alloys. Sci Data 2021;8:58. https://doi.org/10.1038/S41597-021-00840-Y.

[359] Wang Z, Wu Z, Liu Y, Zhang J, Yang Y, Xu J, et al. Hydrogen evolution and electrochemical behavior of Al in Al-air batteries with concentrated NaOH electrolytes. Corrosion Communications 2025. https://doi.org/10.1016/J.CORCOM.2024.10.002.

[360] Shao HB, Wang JM, Wang XY, Zhang JQ, Cao CN. Anodic dissolution of aluminum in KOH ethanol solutions. Electrochem Commun 2004;6:6-9. https://doi.org/10.1016/J.ELECOM.2003.10.007.

[361] Chen Y, Qi DM, Wang HP, Xu Z, Yi CX, Zhang Z. Corrosion Behavior of Aluminum Bronze under Thin Electrolyte Layers Containing Artificial Seawater. Int J Electrochem Sci 2015;10:9056-72. https://doi.org/10.1016/S1452-3981(23)11160-6.

[362] Niverty S, Kalsar R, Seffens RJ, Guzman AD, Roosendaal TJ, Strange L, et al. Probing corrosion using a simple and versatile in situ multimodal corrosion measurement system. Scientific Reports 2023 13:1 2023;13:16695-. https://doi.org/10.1038/s41598-023-42249-0.

[363] Das S, Manna SS, Pathak B. Recent Trends in Electrode and Electrolyte Design for Aluminum Batteries. ACS Omega 2020;6:1043-53. https://doi.org/10.1021/ACSOMEGA.0C04163.

[364] Fadhilah N, Wahyuono RA, Rois MF, Risanti DD. Resolving two pathways of Al(OH)3 formation in hydrogen production from aluminum water reaction. Int J Hydrogen Energy 2025;143:112-20. https://doi.org/10.1016/J.IJHYDENE.2025.05.311.

[365] Li Z, Duan Z, Zheng M. Comparative study of corrosions of aluminum alloys 2024 and 6101 at various pH values. Nanomaterials and Energy 2020;9:82-8. https://doi.org/10.1680/JNAEN.19.00057.

[366] Xhanari K, Finšgar M, Xhanari K, Finšgar M. Organic corrosion inhibitors for aluminum and its alloys in chloride and alkaline solutions: A review. Arabian Journal of Chemistry 2019;12:4646-63. https://doi.org/10.1016/J.ARABJC.2016.08.009.

[367] Fabris R, Masi G, Bignozzi MC, Fabris R, Masi G, Bignozzi MC. Corrosion Behavior of Aluminum Alloys in Different Alkaline Environments: Effect of Alloying Elements and Anodization Treatments. Coatings 2024, Vol 14, 2024;14. https://doi.org/10.3390/COATINGS14020240.

[368] Khan AR, Zhang HJ, Jun Z, Eldin SM, Alsaiari NS, Katubi KM. Electrochemical corrosion resistance of aluminum alloy 6101 with cerium-based coatings in an alkaline environment. Front Chem 2022;10:1066958. https://doi.org/10.3389/FCHEM.2022.1066958/BIBTEX.

[369] Gelman D, Lasman I, Elfimchev S, Starosvetsky D, Ein-Eli Y. Aluminum corrosion mitigation in alkaline electrolytes containing hybrid inorganic/organic inhibitor system for power sources applications. J Power Sources 2015;285:100-8. https://doi.org/10.1016/J.JPOWSOUR.2015.03.048.

[370] El-sayed A, Abdelsamie M, Elrouby M. Tracing the impact of CO2 on the electrochemical and charge-discharge behavior for Al-Mg alloy in KOH and LiOH electrolytes for battery applications. Scientific Reports 2024 14:1 2024;14:7714-. https://doi.org/10.1038/s41598-024-57638-2.

[371] Zhao J, Zhao T, Zhang Y, Zhang Z, Chen Z, Wang J, et al. Corrosion Behavior of the 2024 Aluminum Alloy in the Atmospheric Environment of the South China Sea Islands. Coatings 2024, Vol 14, 2024;14. https://doi.org/10.3390/COATINGS14030331.

[372] Singh M, Yuksel T, Michalek JJ, Azevedo IML. Ensuring greenhouse gas reductions from electric vehicles compared to hybrid gasoline vehicles requires a cleaner U.S. electricity grid. Scientific Reports 2024 14:1 2024;14:1639-. https://doi.org/10.1038/s41598-024-51697-1.

[373] Madani SS, Shabeer Y, Fowler M, Panchal S, Ziebert C, Chaoui H, et al. Digital twin technologies for battery systems: advancements, applications, and future directions. Frontiers in Batteries and Electrochemistry 2026;5:1764210. https://doi.org/10.3389/fbael.2026.1764210.

[374] Alfaro-Algaba M, Ramirez FJ. Review of upstream processes for Li-ion batteries recycling: Safety and economic concerns. J Clean Prod 2025;501:145327. https://doi.org/10.1016/j.resconrec.2019.104461.

[375] Yang X, Zhang H, Liu Q, Jiang G. The Li-ion battery industry and its challenges. Nature Reviews Chemistry 2025 9:8 2025;9:497-8. https://doi.org/10.1038/s41570-025-00742-2.

[376] Maghsoudi R, Ghezi A, Jamalpour S, Tamsilian Y, Tohidian M, Shahebrahimi Y. Advantages, Limitations, and Industrial Applications of Lithium-Ion Batteries. Nanostructured Materials for Energy Storage I-IV 2024:793-820. https://doi.org/10.1002/9783527838851.ch22.

[377] Khan MI, Gilani R, Hafeez J, Ayoub R, Zahoor I, Saira G. Advantages and disadvantages of lithium-ion batteries. Nanostructured Lithium-Ion Battery Materials: Synthesis, Characterization, and Applications 2025:47-64. https://doi.org/10.1016/B978-0-443-13338-1.00017-4.

[378] Guo Y, Guo C, Li P, Song W, Huang W, Yan J, et al. Improving the fast-charging capability of NbWO-based Li-ion batteries. Nature Communications 2025 16:1 2025;16:2441-. https://doi.org/10.1038/s41467-025-57576-1.

[379] Teng Z, Lv C. Detection toward early-stage thermal runaway gases of Li-ion battery by semiconductor sensor. Front Chem 2025;13:1586903. https://doi.org/10.3389/fchem.2025.1586903.

[380] Geng S, Zhang Y, Xie B, Shi A, Ning Y, Lou S, et al. Challenges and Opportunities for Fast-Charging Batteries. The Journal of Physical Chemistry C 2023;127:15021-34. https://doi.org/10.1021/acs.jpcc.3c01927.

[381] Dixit M, Witherspoon B, Muralidharan N, Mench MM, Kweon CBM, Sun YK, et al. Insights into the Critical Materials Supply Chain of the Battery Market for Enhanced Energy Security. ACS Energy Lett 2024;9:3780-9. https://doi.org/10.1021/acsenergylett.4c01300.

[382] Miao Y, Liu L, Xu K, Li J. High concentration from resources to market heightens risk for power lithium-ion battery supply chains globally. Environmental Science and Pollution Research 2023 30:24 2023;30:65558-71. https://doi.org/10.1007/s11356-023-27035-9.

[383] Chakraborty P, Parker R, Hoque T, Cruz J, Du L, Wang S, et al. Addressing the range anxiety of battery electric vehicles with charging en route. Scientific Reports 2022 12:1 2022;12:5588-. https://doi.org/10.1038/s41598-022-08942-2.

[384] Wang YJ, Fan H, Ignaszak A, Zhang L, Shao S, Wilkinson DP, et al. A comprehensive review of metal-air batteries: Mechanistic aspects, advantages and challenges. Catal Today 2025;451:115229. https://doi.org/10.1016/j.cej.2018.04.208.

[385] Park J, Son Y. Recent Progress of Materials Design and Engineering of Aqueous Metal-Air Batteries. Korean Journal of Chemical Engineering 2025 42:7 2025;42:1491-505. https://doi.org/10.1007/s11814-025-00456-7.

[386] Nsanzimana JMV, Cai L, Jiang Z, Xia BY, Maiyalagan T. Engineering Bifunctional Catalytic Microenvironments for Durable and High-Energy-Density Metal-Air Batteries. Nano-Micro Letters 2025 17:1 2025;17:294-. https://doi.org/10.1007/s40820-025-01799-w.

[387] Meng NQ, Fan YX, Cai JS. Zn-air batteries for electric vehicles. Tungsten 2022 6:1 2022;6:164-73. https://doi.org/10.1007/s42864-022-00149-2.

[388] Yan L, Chen J, Yang C, Ning J, Hu Y. Achieving High Energy Efficiency: Recent Advances in Zn-Air-Based Hybrid Battery Systems. Small Science 2024;4:2300094. https://doi.org/10.1002/smsc.202300094.

[389] Aremo B, Oyinseye SI, Akinwole IE, Ayodeji SA, Abass GF. Mechanically rechargeable zinc-air battery for off-grid and remote power applications. Future Batteries 2025;5:100029. https://doi.org/10.1016/j.fub.2025.100029.

[390] Zhang Y, Lv C, Zhu Y, Kuang J, Wang H, Li Y, et al. Challenges and Strategies of Aluminum Anodes for High-Performance Aluminum-Air Batteries. Small Methods 2024;8:2300911. https://doi.org/10.1002/smtd.202300911.

[391] Soni Y, Katake V, Mullapudi D, Chaskar M. Automated Evaluation of Drive File Simulation Accuracy. SAE Technical Papers 2026. https://doi.org/10.4271/2026-26-0528.

[392] Ali Qasem Mohammed S, Saleh Hakami S, Kassas M, Almuhaini MM. Critical Review on Powertrain Technologies for Electric Vehicles: Classification, Broadly Adopted Topologies, and Future Challenges. IEEE Access 2025;13:71755-72. https://doi.org/10.1109/ACCESS.2025.3561577.

[393] Wang Z, Zhou J, Rizzoni G. A review of architectures and control strategies of dual-motor coupling powertrain systems for battery electric vehicles. Renewable and Sustainable Energy Reviews 2022;162:112455. https://doi.org/10.1016/j.rser.2022.112455.

[394] Ezugwu EO, Bhattacharya I, Ayomide AI, Antony Dhason MV, Soyoye BD, Banik T. Powertrain in Battery Electric Vehicles (BEVs): Comprehensive Review of Current Technologies and Future Trends Among Automakers. World Electric Vehicle Journal 2025, Vol 16, Page 573 2025;16:573. https://doi.org/10.3390/wevj16100573.

[395] Chakraborty S, Vu HN, Hasan MM, Tran DD, El Baghdadi M, Hegazy O. DC-DC Converter Topologies for Electric Vehicles, Plug-in Hybrid Electric Vehicles and Fast Charging Stations: State of the Art and Future Trends. Energies 2019, Vol 12, Page 1569 2019;12:1569. https://doi.org/10.3390/en12081569.

[396] Garse KM, Bairwa KN, Roy A. Modelling Techniques and Power Management Strategies for Dual Battery Systems in Electric Vehicles - A Review. Journal of Mines, Metals and Fuels 2025:2439-50. https://doi.org/10.18311/jmmf/2025/49311.

[397] Jiang H, Xu L, Li J, Hu Z, Ouyang M. Energy management and component sizing for a fuel cell/battery/supercapacitor hybrid powertrain based on two-dimensional optimization algorithms. Energy 2019;177:386-96. https://doi.org/10.1016/j.energy.2019.04.110.

[398] Rand DAJ. Hybrid battery/supercapacitor energy storage system for the electric vehicles. J Power Sources 2018;374:237-48. https://doi.org/10.1016/0378-7753(79)85001-6.

[399] Bhattacharya S, Anagnostou D, Schwane P, Bauer C, Kallo J, Willich C. A Flexible DC-DC Converter with Multi-Directional Power Flow Capabilities for Power Management and Delivery Module in a Hybrid Electric Aircraft. Energies (Basel) 2022;15:105999. https://doi.org/10.3390/en15155495.

[400] Shin J, Kim W, Yoo K, Kim H, Han M. Vehicular level battery modeling and its application to battery electric vehicle simulation. J Power Sources 2023;556:232531. https://doi.org/10.1016/j.jpowsour.2022.232531.

[401] Detailed Battery Electric Vehicle (BEV) Model - MATLAB & Simulink n.d. https://www.mathworks.com/help/sps/ug/detailed-battery-electric-vehicle-model.html (accessed March 11, 2026).

[402] Bin Ahmad MS, Pesyridis A, Sphicas P, Mahmoudzadeh Andwari A, Gharehghani A, Vaglieco BM. Electric Vehicle Modelling for Future Technology and Market Penetration Analysis. Front Mech Eng 2022;8:896547. https://doi.org/10.3389/fmech.2022.896547.

[403] Ahmed S, Imtiaz MA, Ahmad B, Ahmed J, Soomro AA, Majeed MK, et al. NEXT-LEVEL SYSTEM DESIGN: ADVANCED AND HIGH-PERFORMANCE SYSTEM ARCHITECTURES FOR THE FUTURE OF ELECTRIC VEHICLES. Spectrum of Engineering Sciences 2025:262-82. https://doi.org/10.5281/zenodo.15393826.

[404] El Hadraoui H, Zegrari M, Hammouch FE, Guennouni N, Laayati O, Chebak A. Design of a Customizable Test Bench of an Electric Vehicle Powertrain for Learning Purposes Using Model-Based System Engineering. Sustainability 2022, Vol 14, Page 10923 2022;14:10923. https://doi.org/10.3390/su141710923.

[405] Wang Y, Tian J, Sun Z, Wang L, Xu R, Li M, et al. Attention-based two-level architecture for electric vehicle battery capacity prediction with condition standardization. J Energy Storage 2026;152:120720. https://doi.org/10.1016/j.rser.2020.110015.

[406] Nikzadfar K, Stone T, Caine J, Abbasian M, Babaie M, Goswami R, et al. Battery Electric Vehicles: Technologies, Challenges and Future Prospects for Sustainable Transportation.

Energy, Environment, and Sustainability 2025;Part F885:99-185. https://doi.org/10.1007/978-981-96-6624-9_4.

[407] Chandran M, Palanisamy K, Benson D, Sundaram S. A Review on Electric and Fuel Cell Vehicle Anatomy, Technology Evolution and Policy Drivers towards EVs and FCEVs Market Propagation. Chemical Record 2022;22:e202100235. https://doi.org/10.1002/tcr.202100235.

[408] Shen H, Wang H, Li M, Li C, Zhang Y, Li Y, et al. Thermal Runaway Characteristics and Gas Composition Analysis of Lithium-Ion Batteries with Different LFP and NCM Cathode Materials under Inert Atmosphere. Electronics 2023, Vol 12, Page 1603 2023;12:1603. https://doi.org/10.3390/electronics12071603.

[409] Wang R, Liu G, Wang C, Ji Z, Yu Q. A comparative study on mechanical-electrical-thermal characteristics and failure mechanism of LFP/NMC/LTO batteries under mechanical abuse. ETransportation 2024;22:100359. https://doi.org/10.1016/j.etran.2024.100359.

[410] Kim N, Shamim N, Crawford A, Viswanathan V V., Sivakumar BM, Huang Q, et al. Comparison of Li-ion battery chemistries under grid duty cycles. J Power Sources 2022;546:231949. https://doi.org/10.1016/j.jpowsour.2022.231949.

[411] Meng E, Sun J, Huang Y, Tang H. Morphology Evolution and Improved Electrochemical Properties of LiFePO4 Cathode Materials for Li-ion Batteries. Int J Electrochem Sci 2022;17:221225. https://doi.org/10.20964/2022.12.25.

[412] Steger F, Krogh J, Meegahapola L, Schweiger HG. Calculating Available Charge and Energy of Lithium-Ion Cells Based on OCV and Internal Resistance. Energies 2022, Vol 15, Page 7902 2022;15:7902. https://doi.org/10.3390/en15217902.

[413] Boulanger T, Eldesoky A, Buechele S, - al, Black W, Azam S, et al. Addressing the OCV-SOC Flat Region in LFP Cells for SOC Estimations Using EIS Measurements. J Electrochem Soc 2026;173:020503. https://doi.org/10.1149/1945-7111/ae33fc.

[414] Liu Z, Zhao J, Cai Y, Xu B. Design and research on discharge performance for aluminum-air battery. AIP Conf Proc 2017;1794:40006. https://doi.org/10.1063/1.4971943.

[415] Katsoufis P, Katsaiti M, Mourelas C, Andrade TS, Dracopoulos V, Politis C, et al. Study of a Thin Film Aluminum-Air Battery. Energies 2020, Vol 13, Page 1447 2020;13:1447. https://doi.org/10.3390/en13061447.

[416] Xie J, He P, Zhao R, Yang J. Numerical Modeling and Analysis of the Performance of an Aluminum-Air Battery with Alkaline Electrolyte. Processes 2020, Vol 8, Page 658 2020;8:658. https://doi.org/10.3390/PR8060658.

[417] Egan DR, Ponce De León C, Wood RJK, Jones RL, Stokes KR, Walsh FC. Developments in electrode materials and electrolytes for aluminium-air batteries. J Power Sources 2013;236:293-310. https://doi.org/10.1016/j.jpowsour.2013.01.141.

[418] Xue Y, Yuan J, Yu X, Sun S, Zhang H, Zhou W, et al. Air-breathing cathode for aluminum-air battery: From architecture to fabrication and evaluation. Materials Science and Engineering: R: Reports 2025;163:100942. https://doi.org/10.1016/j.mser.2025.100942.

[419] Sheerin G, Alexander R, WT D'Silva - US Patent App. 18/043 361, 2023 undefined. Control system and design for adynamic adaptive intelligent multi-cell air battery. Google Patents n.d.

[420] Yang J Di, Millichamp J, Suter T, Shearing PR, Brett DJL, Robinson JB. A Review of Drive Cycles for Electrochemical Propulsion. Energies 2023, Vol 16, Page 6552 2023;16:6552. https://doi.org/10.3390/en16186552.

[421] Lee S, Eom I, Lee B, Won J. Driving Characteristics Analysis Method Based on Real-World Driving Data. Energies 2024, Vol 17, Page 185 2023;17:185. https://doi.org/10.3390/en17010185.

[422] Yong JY, Ramachandaramurthy VK, Tan KM, Mithulananthan N. Component-level energy consumption and range analysis of battery electric vehicles under urban and highway driving conditions. Appl Therm Eng 2025;274:126797. https://doi.org/10.1016/j.rser.2015.04.130.

[423] Lee G, Park J, Park S, Yoon SH. Study on the Necessity of Real-World Driving Tests for Passenger Electric Vehicles. International Journal of Automotive Technology 2024 25:6 2024;25:1323-30. https://doi.org/10.1007/s12239-024-00108-5.

[424] Fiori C, Ahn K, Rakha HA. Power-based electric vehicle energy consumption model: Model development and validation. Appl Energy 2016;168:257-68. https://doi.org/10.1016/j.apenergy.2016.01.097.

[425] Gołębiewski W, Lisowski M. Theoretical analysis of electric vehicle energy consumption according to different driving cycles. IOP Conf Ser Mater Sci Eng 2018;421:022010. https://doi.org/10.1088/1757-899X/421/2/022010.

[426] Donkers A, Yang D, Viktorović M. Influence of driving style, infrastructure, weather and traffic on electric vehicle performance. Transp Res D Transp Environ 2020;88:102569. https://doi.org/10.1016/j.trd.2020.102569.

[427] Larminie J, Lowry J, Wiley J. Electric vehicle technology explained. 2012.

[428] Li J, Wang Y, Chen J, Zhang X. Study on energy management strategy and dynamic modeling for auxiliary power units in range-extended electric vehicles. Appl Energy 2017;194:363-75. https://doi.org/10.1016/j.apenergy.2016.09.001.

[429] Badin F, Le Berr F, Briki H, Dabadie JC, Petit M, Magand S, et al. Evaluation of EVs energy consumption influencing factors, driving conditions, auxiliaries use, driver's aggressiveness. 2013 World Electric Vehicle Symposium and Exhibition, EVS 2014 2014. https://doi.org/10.1109/EVS.2013.6914723.

[430] Unni K, Thale S. Influence of Auxiliary Loads on the Energy Consumption of Electric Vehicle - A Case Study. 2021 IEEE Transportation Electrification Conference, ITEC-India 2021 2021. https://doi.org/10.1109/ITEC-India53713.2021.9932456.

[431] Yang X, Niu D, Sun L, Wang K, De G. Participation of electric vehicles in auxiliary service market to promote renewable energy power consumption: Case study on deep peak load regulation of auxiliary thermal power by electric vehicles. Energy Sci Eng 2021;9:1465-76. https://doi.org/10.1002/ese3.907.

[432] Liu K, Wang J, Yamamoto T, Morikawa T. Exploring the interactive effects of ambient temperature and vehicle auxiliary loads on electric vehicle energy consumption. Appl Energy 2018;227:324-31. https://doi.org/10.1016/j.apenergy.2017.08.074.

[433] Wang C, Zheng P, Bauman J. A Review of Electric Vehicle Auxiliary Power Modules: Challenges, Topologies, and Future Trends. IEEE Trans Power Electron 2023;38:11233-44. https://doi.org/10.1109/TPEL.2023.3288393.

[434] Ehsani M, Gao Y, Longo S, Ebrahimi K. Modern electric, hybrid electric, and fuel cell vehicles. CRC Press; 2018. https://doi.org/10.1201/9780429504884.

[435] Sherman SB, Cano ZP, Fowler M, Chen Z, Sherman SB, Cano ZP, et al. Range-extending Zinc-air battery for electric vehicle. AIMS Energy 2018 1:121 2018;6:121-45. https://doi.org/10.3934/energy.2018.1.121.

[436] Clark S, Latz A, Horstmann B. A Review of Model-Based Design Tools for Metal-Air Batteries. Batteries 2018, Vol 4, Page 5 2018;4:5. https://doi.org/10.3390/batteries4010005.